High Pressure Solid State Chemistry of C-N-H and Ti-N Systems

A thesis presented to the University College London in partial fulfillment of the requirements for the degree of Doctor of Philosophy

Ashkan Salamat

University College London

October 2009

Declaration

I hereby declare that the work described within this thesis is entirely my own, except where specifically acknowledged in the text.

Ashkan Salamat – Thesis submitted October 2009

Abstract

This thesis presents the use of molecular precursors for the synthesis of solid-state materials through the application of extreme conditions. The main tool for the exploration of these materials was the diamond anvil cell which generated static pressures of up to 85 GPa. Combined with the use of high-power lasers, it provides a powerful and efficient technique for high-pressure-high-temperature synthesis of solid-state materials. The work presented here is an investigation into the synthesis and recovery of new materials within two solid-state systems, C-N-H and Ti-N-O. Crystallographic analysis of these systems is a challenging process, made more difficult by their relatively light elemental composition and the use of the diamond anvil cell. In both cases a systematic experimental and analytical strategy was adopted to enable the extraction of the best data possible, both qualitatively and statistically.

Two C-N-H systems were investigated: C_2N_3H and $C_6N_9H_3.HCl$. Synchrotron X-ray diffraction and Raman scattering data are reported for the new dense tetrahedrally bonded phase C_2N_3H with a defective wurtzite structure. This is synthesised by laser heating from an organic precursor, dicyandiamide, $C_2N_4H_4$ at high-pressure in a diamond anvil cell. This work confirms the structure deduced in previous work from electron diffraction experiments on samples recovered to ambient conditions.

The graphitic layered compound $C_6N_9H_3.HCl$ was subjected to pressures up to 70 GPa in a diamond anvil cell and its structural behaviour was examined using synchrotron X-ray diffraction. The use of laser heating experiments revealed the synthesis of a new carbon nitride phase which is recoverable to ambient conditions.

The second group of systems explored was those based on Ti-O-N. Amorphous or nano-crystalline precursors were used to attempt the synthesis of Ti_3N_4. The high-pressure and temperature behaviour of these materials was examined using synchrotron X-ray diffraction and Raman spectroscopy, in a laser-heated diamond anvil cell.

In addition, the high-pressure studies of $Ti_{2.85}O_4N$, a recently discovered titanium oxynitride phase, are reported here up to 70 GPa. Using synchrotron angle dispersive techniques two high-pressure phases are observed and an attempt to elucidate these structures are reported.

Table of Contents

Table of Figures:

Table of Tables:

Table of Abbreviation

APS	Advanced Photon Source
CCD	charge couple device
DAC	diamond anvil cell
DCDA	dicyandiamide
DFT	density functional theorem
DLS	Diamond Light Source
E	energy
e	particle charge
EELS	electron energy-loss spectroscopy
EOS	equation of state
ESRF	European Synchrotron Radiation Facility
F	normalised pressure
f	Eulerian strain
FTIR	Fourier-transform infrared
FWHM	full width half maximum
h	Planck's constant
HP	high-pressure
HPHT	high-pressure high-temperature
IR	infrared
K_0	zero pressure bulk modulus
K_0'	pressure derivative
λ	wavelength
LH	laser heating
m	particle mass
v	frequency
nano-SIMS	nano-secondary ion mass spectrometry
Nd:YAG	neodymium doped yttrium aluminium garnet
Nd:YLF	neodymium doped yttrium lithium fluoride
NMR	nuclear magnetic resonance
P	pressure
ppm	part per million
PTM	pressure transmitting medium

SEM	scanning electron microscope
SRS	Synchrotron Radiation Source
T	temperature
T_c	superconductivity temperature
TEM	transmission electron microscope
UCL	University College London
UV	ultra-violet
V	volume
V_0	volume at zero pressure
WC	tungsten carbide
XRD	X-ray diffraction
2θ	scattering angle

Units

Å	Ångtroms	($1x10^{-10}$ metres)
cm^{-1}	wavenumber	
ºC	Celsius	
eV	electron volts	
KeV	kilo-electron volts	($1x10^{3}$ volts)
GeV	giga-electron volts	($1x10^{9}$ volts)
GPa	giga pascal	($1x10^{9}$ pascal)
K	Kelvin	
m	metre	
mm	millimetre	($1x10^{-3}$ metre)
μm	micrometre	($1x10^{-6}$ metre)
nm	nanometre	($1x10^{-9}$ metre)
mW	milliwatt	($1x10^{-3}$ Watt)
W	Watt	

Acknowledgements

I would like to thank my supervisor Professor Paul F. McMillan for taking me on board in his group and giving me the opportunity to work in such an interesting and multidisciplinary field. His constant enthusiasm and encouragement have enabled me to find my feet and take pride in my work. I would also like to thank my second supervisor Dr Dewi Lewis for his support throughout the first year of my PhD and my introduction into theoretical science.

I would specially like to thank Dr Raul Quesada Cabrera and Dr Dominik Daisenberger for having taught me everything they know and spending many hours with me at synchrotron runs. Their friendship has been as indispensable as their knowledge. In addition, I would like to acknowledge Dr Simon Jacques for his friendship and counsel. Dr Steve Firth and Dr Andrea Sella for the endless advice and help. Also Vesna Middelkoop for her role as artistic director and Stuart M. Turner for his help with all things crystallographic.

Dr Andrew Hector from Southampton University participated with the TixNy and the bismuth pyrochlores projects and provided the samples. Dr Geoff Hyett provided the samples and was involved in the analysis and discussions of the Ti_3O_4N project. Dr Furio Corà contributed to both of the C-N-H projects and Aisha Rahman carried out calculations for the work on the C_2N_3H system. Katherine Woodhead participated in the project of the synthesis of C_2N_3H. I would like to thank James Percival, Jim Stevenson, Roy Northeast and Robert Gollay from the UCL chemistry and physics workshop for their work on the gas loading vessel and various other jobs throughout the years. Many have given their help and support towards this project at various synchrotrons and laboratories and are personally acknowledged.

A personal thanks to my friends within the chemistry department, not in any order; Rachael Hazael, John Kilmartin, Caroline Knapp, Keith Butler, Dr Victoria Lees and Dr Edward Bailey. Also to Dr Alan Taylor for believing in me and dragging me through my undergraduate studies. Dr Nazila Kamaly for getting me to study chemistry and the rest of my loving family.

I would like to dedicate this thesis to my father and mother Massoud and Nasrin. Thank you for all you love, patience and sacrifice. A final thank you to my favourite three: Donya, Nicholas and Michael.

Publications

A. Salamat, K. Woodhead. P. F. McMillan, R. Quesada Cabrera, A. Rahman, D. Adriaens F. Corá. Tetrahedrally bonded dense C_2N_3H with a defective wurtzite structure: X-ray diffraction and Raman scattering results at high pressure and ambient conditions. Physical Review B **80**, 104106 (2009).

R. Quesada Cabrera, **A. Salamat**, O. I. Barkalov, O. Leynaud, P. Hutchins. D. Daisenberger, D. Machon, A. Sella, D. W. Lewis, P. F. McMillan. Pressure-induced structural transformations of the Zintl phase sodium silicide. Journal of Solid State Chemistry **182**, 2535 (2009).

A. Salamat, G. Hyett, R. Quesada Cabrera, P. F. McMillan, I. P. Parkin. High pressure behaviour and polymorphism of titanium oxynitride phase, $Ti_{2.85}O_4N$. Journal of Physical Chemistry C **114**, 8546 (2010).

1 Introduction

Much of the pioneering research in high-pressure science was carried out by Percy W. Bridgman in the first part of the twentieth century. This early work involved the use of mechanical presses to achieve pressures of up to 2 GPa and undertook the study of many different types of compounds including solids, metals, organics and polymers [1, 2]. However, it was the development of the diamond anvil cell (DAC) in 1958 that enabled high-pressure studies to be carried out on a hand held scale. Much of the early work carried in developing the DAC was by a joint collaboration by Weir *et al.* [3] and Van Valkunberg which often led to the destruction of many diamonds and cells. Work carried out in the National Bureau of Standards laboratory and Chicago with confiscated diamonds enabled the expensive research of DAC development to be conducted at a rate that would not have been possible without this opportunity for the scientists to experiment with such numbers of precious stones [4]. A history of the development of the DAC, high-pressure research and the search for the synthesis of diamond is given by R. Hazen [5].

Advancements in the application of extreme conditions were initially made in geology [6, 7] and mineralogy but are now a powerful discipline in condensed matter and solid-state chemistry and physics [8-10]. The fundamental concept behind this new and exciting field of extreme conditions science is forcing the systems under observation to undergo a volume change which leads to phase and structural transformations [11]. When applied to solid-state chemistry, these techniques can bring fundamental changes to structural, thermal, optical or mechanical properties of matter and an overall lowering of the energy of the system, permitting new material synthesis [12, 13]. As systems adopt new low energy configurations, a range of transformations can occur, including ionisation, polymerisation, phase transitions, condensation, amorphisation and metallisation [14-17]. The application of high-pressure to solid-state chemistry also creates the potential of removing the use of solvent, catalyst or radical initiators used in synthetic routes [18].

In the present work we have chosen to focus on the solid-state chemistry of new high-density materials, specifically in the C-N and Ti-N systems. These systems are expected to possess useful properties including high hardness and wide electronic band gaps [19]. The essence of this work has been the

investigation of light elemental systems, specifically carbon and titanium nitride based materials. Research in the field of C-N systems has been spurred by theoretical predictions that the sp^3-bonded forms of carbon nitride with stoichiometry C_3N_4 could be superhard, comparable to the incompressibility and hardness of diamond [20, 21]; this has led to several thousand publications being reported on this system [22-25]. Formation of these materials has been reported in thin films produced by vapour deposition techniques [24, 26, 27]; however, the materials are generally nanocrystalline and they have not yet been fully characterised [28]. There have also been several attempts to form dense carbon nitride phases using high-pressure high-temperature methods. The structures and compositions of phases reported to have been synthesised in these studies are generally not known, and the materials synthesised have not been recoverable to ambient conditions [29, 30]. However, high-P,T synthesis methods have already produced a number of well-characterised dense systems with a X_3N_4 stoichiometry for both group IV and XIV elements (X = Zr, Hf and Si, Ge). There has been much interest in synthesising analogous C-N and Ti-N based materials including the spinel form of Ti_3N_4 as predicted by *ab initio* calculations [31].

Titanium nitrides already form an important series of high-hardness materials with important applications within industry due to their unique properties of biocompatibility, chemical resistance and low coefficient of friction [32-34]. With a rich number of valuable properties including high hardness and an attractive gold appearance, there are currently many applications for this material such as machine tools, microelectronics, surgical tools, implants, as well as jewellery [32, 35, 36]. Therefore, searching for new polymorphs within this chemical system is important and potentially rewarding.

Recent work carried out at UCL has identified a new oxynitrides, $Ti_{2.85}O_4N$, using a synthetic route of atmospheric pressure chemical vapour deposition (CVD) [37], a technique more normally associated with thin film synthesis and industrial scale up, than with materials discovery [38]. This material may have photocatalytic properties and so its further characterisation is valuable.

This thesis presents an exploration and identification of crystalline phases within the C-N-H and Ti-N-O solid-state systems, firstly describing the tools and techniques instrumental in the synthesis and investigation of these

systems: the diamond anvil cell, Raman spectroscopy and synchrotron X-ray diffraction. Following this, I present my work within the C-N-H system, reporting on the synthesis and characterisation of sp^3-bonded carbon nitride C_2N_3H and the graphitic layered compound $C_6N_9H_3.HCl$, in addition to discussing other phases potentially formed. Subsequently, the synthesis and investigation of amorphous nanocrystalline composite Ti_xN_y materials, and the exploration of the phase diagram of a new titanium oxynitride phase, $Ti_{2.85}O_4N$, are described. In all cases the materials presented have been synthesised at high-pressure and recovered to ambient conditions which is central for material design. Fundamental to the success of this work has been adopting a systematic strategy both experimentally and analytically to be able to successfully synthesis and analyse these new solid-state systems.

2 Experimental Techniques

In this chapter an outline of the different experimental and analytical techniques will be given. Fundamental to all the work reported here is the use of the diamond anvil cell and the application of extreme pressure to our systems. In the search for discovery of new solid-state systems, the application of pressure has been combined with *in situ* laser heating to allow the full exploration of the P-T landscape. Both of these techniques are described in the first part of this chapter.

In order to probe the diamond anvil cell samples in the laboratory at UCL, Raman spectroscopy was used. Following a general review of the Raman effect, and a description of the optical set-up at UCL, the techniques developed for this study are provided.

The main techniques for monitoring reactions and samples (*in situ*) for the bulk of the work presented here are synchrotron radiation and angle dispersive X-ray diffraction. Work was carried out both at the newly constructed UK synchrotron Diamond Light Source, Didcot, at the extreme conditions station I15, and at the European Synchrotron Radiation Facility (ESRF), Grenoble, at the high-pressure beamline ID27. The focus of the latter part of this section will be on the set up of these two high-pressure stations. An overview of the basics of X-ray diffraction is provided along with a discussion of powder diffraction analysis using Le Bail and Rietveld refinement techniques.

2.1 Diamond Anvil Cell

2.1.1 Introduction

The diamond anvil cell (DAC) incorporates two gem-quality diamonds encapsulating a reaction chamber where very high pressures, now reaching 300 GPa, have become routine. The introduction of the megabar pressure scale resulted from the work carried out by Mao *et al.* and the pioneering work regarding cell design and pressure calibration [39, 40]. Work by Ruoff *et al.* has reported studies of metals up to 560 GPa [41], however experiments above 400 GPa are far less common, and generally not reproduced. This is generally due to the several factors regarding the theoretical and experimental elastic limits of diamond and reliable methods of enabling the pressure inside the DAC to be correctly estimated. Bradley *et al.* have reported the diamond phase of carbon stable up to 800 GPa using ramp-wave compression [42]. However, the current nominal limit for DAC work is generally accepted to be ~300 GPa although at these elevated pressures it is very difficult to measure the DAC pressure. This is because the most popular standard of pressure calibration, the ruby scale, discussed in detail later, reaches its limit of precision at ~2-2.5 Mbar and therefore other, more demanding techniques for calculating pressure inside the DAC are required [43, 44].

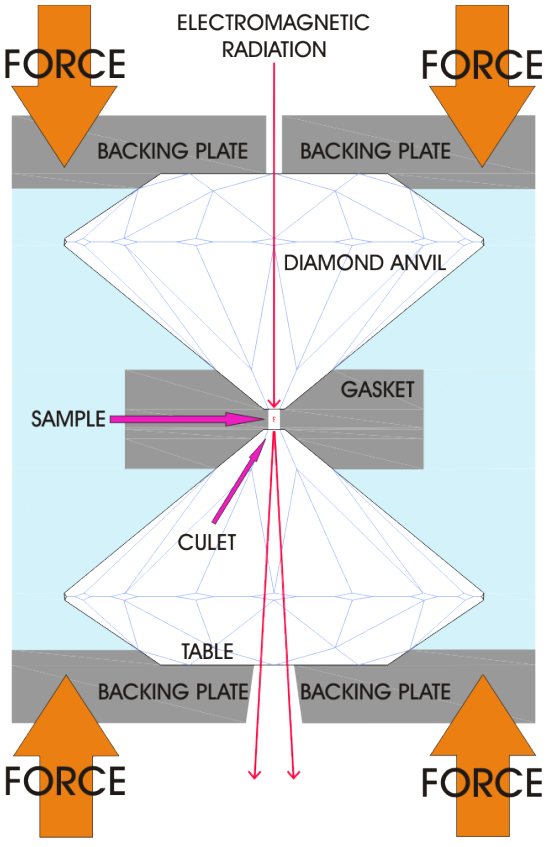

FIG. 1: A schematic of the diamond anvil cell cross section. Applying an even force to the backing plates of the diamond anvils translates to a pressure being generated in the sample chamber. The sample is held in place by the metal gasket and the aperture of the backing plates allows for access to the sample for *in situ* measurements.

A schematic of a DAC is shown in FIG. 1. The reaction chamber is enclosed by a gasket and pressed between the culets of two opposing diamonds which are attached to a backing plate. A micro sized sample is inserted into a micro-drilled hole in the gasket. The whole is encapsulated by a cell with two parts: in the case of the cylindrical cells this consists of a piston and a cylinder, although this is not necessary with all designs of DACs such as the Merrill-Bassett designs. Each diamond and its backing plate sits inside either the piston or cylinder, which may then be brought together and the cell closed. Force may be applied to the diamonds in the closed cell by a gas or mechanical means. The small area of the culet translates a moderate force into a large amount of pressure which is related by the relationship: Pressure = Force / Area. Dunstan *et al.* provide a full description of the components of the cell and preparation for experiments [45-48].

The provision of an aperture in the backing plates, and the optical transparency of diamond, enables photons to reach and pass through the sample and are described later on in detail. This is enormously advantageous as it allows access to the sample *in situ* and at pressure for probing, laser heating and visual observation. Vibrational spectroscopy such as Raman and infrared may be used to investigate the sample [49]; the use of crystallographic analysis using X-ray diffraction is also a powerful method for structural studies of systems under ultra-high pressures [50, 51].

Single-crystal diffraction analysis became possible as a result of the studies carried out single crystal experiments on ice VI [52]. Initially, the samples compressed and analysed in the DAC were fluids and powders, but Merrill and Bassett developed a miniature cell which provided a wider aperture for improved 3D resolution for single-crystal diffraction work [53].

Improvements to the design of the DAC have also led to the standard method commonly adopted for high-pressure research. Examples of these are the introduction of a metal gasket to surround the sample and prevent it from slipping out [54], the advancement of hydrostatic limits and utilisation of the ruby scale for calibrating the pressure [55, 56].

2.1.2 Different Types of Cells

FIG. 2: A photograph of various diamond anvil cell devices used in this work. (left) The cell is referred to as a Mao symmetrical cell which consists of a four-screw piston-cylinder set-up. (middle) This cell is of a similar set-up to the Mao cell and is designed and built by EasyLab Technologies Ltd, UK. (right) A membrane cell (EasyLab Technologies Ltd, UK) in which pressure is generated by pumping gas in an expandable membrane which pushes the piston half of the cell into the cylinder half.

The DACs used in the works presented here are based on the symmetrical Mao DAC or a membrane-driven DAC. Both types of cell consist of a piston-cylinder configuration with opposing diamond anvils seated onto backing plates with conical apertures. The method in which these two types of DACs generate a force, leading to an increase of pressure inside the sample chamber, are based on two different principles. The Mao cell has a screw driven mechanism based on four screws which are arranged in a clockwise and anticlockwise manner and as they are tightened the piston and cylinder are bought closer together. The number of turns determine the force generated and the resulting increase in pressure. Using this type of DAC can be difficult in reaching pressures greater than 100 GPa since turning the screws the same amount with every turn is very difficult. One method of ensuring an even distance between the piston and cylinder is by using a caliper to measure the distances at each of the screws as well as the use of a torch wrench. However, even with these precautions it is difficult to achieve a homogeneous force.

The membrane cell in addition to having the capabilities of being closed using a four screw mechanism, similar to the symmetrical cell described, also

has an expandable diaphragm which is attached to the piston half the cell. This can be expanded using an external flow of gas from a control box and pushes the piston into the cylinder. This method of generating pressure provides a more controlled approach to achieving the desired pressure point as well as a more even force onto the piston. The advantage of being able to externally control the gas pressure flowing into the membrane is that the DAC does not need to be moved or repositioned during experiments. This minimises the need for realignment or re-calibration and is also fundamental for doing background subtractions during XRD, where the DAC must remain stationary throughout the whole experiment [57-59].

2.1.3 Basic Principles and Components of Diamond Anvil Cell

2.1.3.1 Diamond Anvils

Diamond has unique properties in that it is an extremely hard and incompressible material and is also transparent and very resistant to chemical attack [60]. This makes it ideal for anvils in high-pressure experiments. Single crystal, gem quality diamonds are selected with specific properties and are characterised by their carat, cut, clarity and colour (the 'four Cs'). Its optical transparency to a wide range of the electromagnetic spectrum means that different types of light may be shone onto the sample during *in situ* high pressure experiments. This not only provides an in situ analytical approach but also allows the use of high power lasers for HPHT research.

Diamonds are specially selected for their optical properties when used in spectroscopic experiments. When selecting diamonds for Raman spectroscopy the requirement is low luminescence of diamonds. [61]. It is possible to measure the Raman to background ratio by comparing the intensity of the second order peak of diamond to its relative background (FIG. 3). This is done by measuring the maximum intensity of second order peak and the intensity of the background baseline nearby. Then the diamond is removed and a background pattern is taken using the same exposure time. The wavenumber (x-axis) of the position of the first two peaks is measured on the background pattern and subtracted from the first set of values. Ratios in the order of 10:1 are ideal

for Raman experiments. Some diamonds measured can have values as high as 30:1.

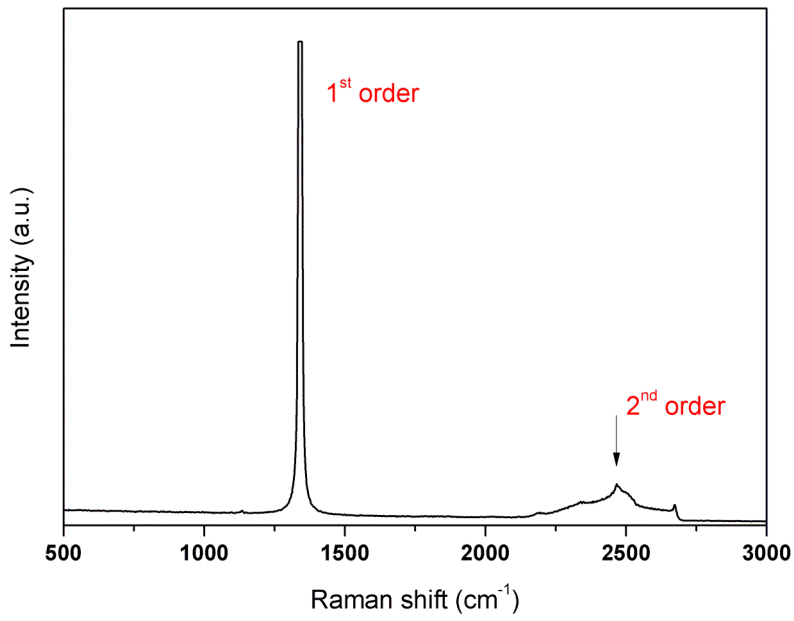

FIG. 3: The Raman spectra of diamond showing the 1st and 2nd order peaks. The Raman to background ratio is calculated by using the intensity of the 2nd order peaks and dividing by the baseline following a background subtraction.

2.1.3.2 Backing Plates

The diamond anvils are mounted and attached onto backing plates, which are in turn held in place within the two halves of a DAC. The backing plate has a conical aperture drilled into one side which allows *in situ* optical access to the sample chamber allowing the scattered signal to be recorded. The half angle of the conical opening is the limiting factor in the maximum observable 2θ range. For the experiments carried out in this work the backing plates used provided an observable 2θ range of 30 degrees. Developments with the Boehler-Almax design of backing plates which have the diamond girdle sitting inside the packing plate increasing the conical aperture to 120 degrees [62]. The maximum amount of strain experienced within the DACs is in the culets of the diamonds. With a fraction of this carried on to the backing plates it is possible to use a range of materials made specific to the experiment. For the experiments reported here tungsten carbide and beryllium backing plates were used.

Tungsten carbide is ideal for higher pressures and excellent in cleaning up the scattering x-rays. Beryllium is a very light element and is virtually transparent to x-rays allowing a wider range of the total scattering angle observed. When using Be backing plates a method of having a tungsten carbide plate on the half facing the incident beam was preferred as alignment of the DAC to a synchrotron beam was conducted. FIG. 4 illustrates a number of different backing plates used for experiments throughout this thesis.

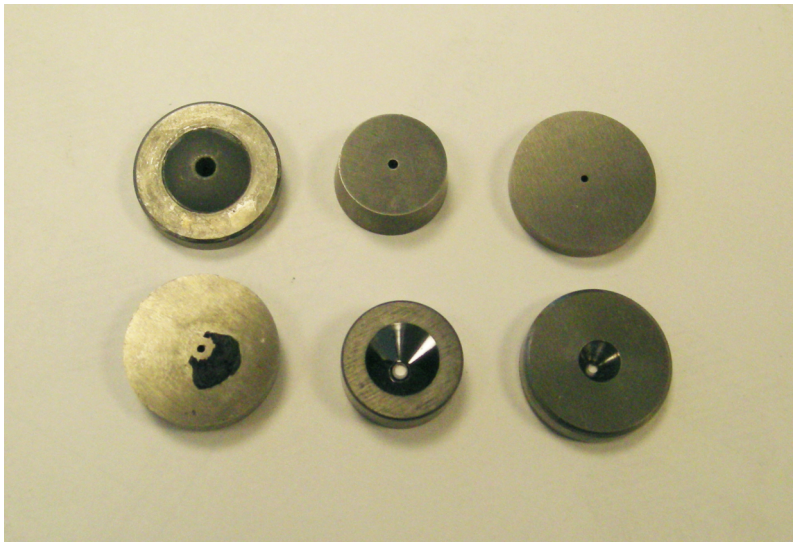

FIG. 4: An assortment of different backing plates for various types of diamond anvil cells. The bottom row shows the exiting aperture of the backing plates.

2.1.3.3 Gasket

A drilled gasket is used as a chamber to contain the sample between the two opposing anvils (FIG. 5). This method prevents the sample from being squeezed out laterally as the two diamond anvils are brought closer together during high-pressure experiments. In addition, it acts to prevent the anvils coming into contact with one another and also allows for the containment of different pressure transmitting mediums. By having a defined chamber, the sample can be placed in a desired configuration to allow the PTM to encapsulate it and ensure hydrostatic conditions. During high-pressure experiments gaskets are under a great amount of strain and deformation often occurs. Any structural failure of the gasket, or major warping of the drilled hole, could lead to the termination of the experiment and damage, if not the destruction, to one or both of the diamond anvils.

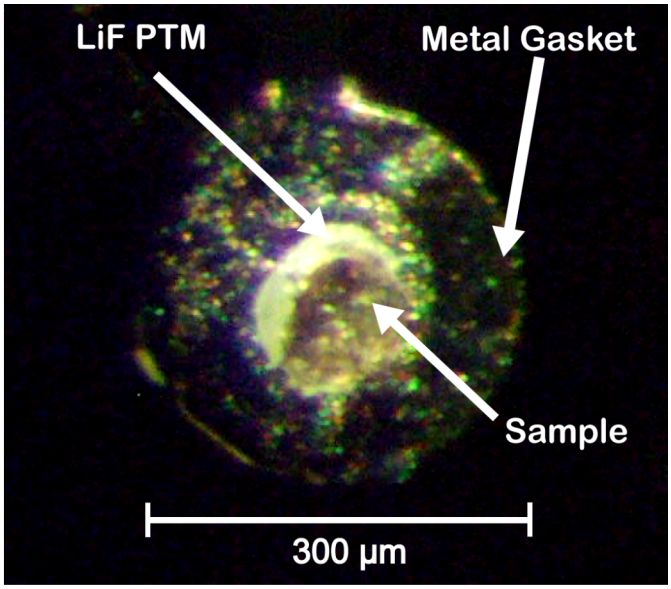

FIG. 5: An optical micrograph of the sample chamber defined by a drilled metal gasket. The image is taken looking through the top diamond and is of the sample chamber in a closed DAC.

A number of different materials have been investigated as gaskets for HP experiments. Low Z compounds such as beryllium can be used as gaskets as their transparency for X-rays allows for the co-axial probing of samples. This consists of probing the sample perpendicular to the axis of compression through the transparent low Z compound backing plate using a radial diffraction technique [63]. The requirement of extreme condition experiments at the limit of the DAC has encouraged the development of new gasket materials and designs [64-67]. For routine experiments in the high-pressure laboratory stainless steel, rhenium or tungsten gaskets are used, mainly because of the their low chemical reactivity and high strength.

All of the experiments presented in this thesis have been carried out using rhenium gaskets as this provided an option for investigating a larger pressure range as well as the option for laser heating. The rhenium gaskets are pre-indented in the DAC to a thickness of ~30 μm which equates to a pressure of 20 GPa. This can be carried either using a trial and error process or by placing ruby dust on a culet and taking the DAC up to a pressure of 20 GPa. The gasket is drilled with a diameter relative to the size of diamond culet used. This was usually a hole diameter of 80-100 μm for 300 μm culet size with the hole size nominally a third of the size of the culet diameter. The drilling is carried out

using a spark eroder which uses a electric discharge to produce a spark which melts through the conducting metal [68]. A more recent method for drilling has been using a constant pulsed laser which can provide a more accurate approach for making holes only a few microns in diameter.

2.1.4 Glove Box Loadings

FIG. 6: A photograph of a glove box at UCL, designed and modified specifically for diamond anvil cell loadings.

Due to the nature of the very small sample sizes (~50x50x10 μm) involved in DAC work traces of any contamination or oxidation would have a significant effect on the experiments and results. In the systems examined in this work all the loadings have been carried out in a clean, inert environment to safeguard the quality of work. This has mostly consisted of using a specially setup glove box designed for such types of loadings, as well as some work being carried out in a glove bag. Exceptions to glove box loadings have been when using gas PTMs which have to be cryogenically loaded, a procedure which is not possible in a glove box. The standard conditions required in a general-purpose glove box are usually to have both the water and oxygen content lower than 1 ppm. The

presence of water contamination can be magnified when using crystallographic probe techniques, especially when working with a X-ray beam size greater than 10x10 μm. A smaller beam size would allow the user to map the sample and potentially identify a pure region of sample.

Glove box loadings are, however, generally difficult and extremely challenging for DAC work. The confinement of the rubber gloves of the box can affect manual dexterity and the effects of static build up make moving very small fragments of sample very difficult. The glove box itself has to be modified to accommodate the use of DAC work. These amendments must include the incorporation of a microscope, appropriate for DAC loadings, and adequate lighting with both transmission and reflective optical paths.

Before loading, the sample can be compressed between two tungsten carbide cubes or another DAC and then picked apart and loaded with the PTM. When the loading is finished the top half of the cell can be brought out of the glove box and cleaned thoroughly before closing the DAC and screwing the cell tight enough to ensure it is closed but still at low pressure.

All samples taken into the glove box should be dry and under vacuum. The following precautions should also be taken to minimise the contamination of the sample and glove box:

- Use spectroscopic grade materials, packed under argon.
- Open chemicals only in the glove box with seal intact.
- Store salts for PTM in a glove box.

In addition, salts should not be taken from a laboratory environment into the glove box even after a length of time in an oven. This is crucial when using amorphous reactants or for melt experiments as any presence of water would be deleterious.

2.1.5 Pressure Transmitting Medium

The pressure transmitting medium (PTM) is a substance that is packed around the sample in the DAC and is there to homogenise the stresses and strains acting upon the sample whilst under a mechanical force. A truly hydrostatic environment would consist of having the sample enclosed by a pressure transmitting medium which would be fluid and therefore not support

any shear. However, unless the experimental pressure is below the hydrostatic limit of the PTM, the PTM will solidify. The choice of PTM with low shear strength can support a more homogeneous environment around the sample. This can minimise the effects of deviatoric and uniaxial stress, both of which have been reported extensively relative to high-pressure research [69, 70]. The presence of these stresses can affect the shape of the Debye-Scherrer rings which can make solving the crystal structure difficult if not impossible.

Specifically in the case of using powdered samples, a truly hydrostatic environment is difficult as it is the grain-grain contacts within the solid material that dictate the stresses seen in the analytical results [71]. These non-hydrostatic effects can be seen as peak broadening and asymmetrical contribution in diffraction (FIG. 7) and spectroscopy data [72]. Additional effects can be seen in a lowering of the transition pressure for phase transitions [73]. However, the contact between the grains of a powder sample can be very important when attempting synthesis inside the DAC. These points can act as nucleation sites during a reaction and may be very beneficial for carrying out HP chemistry. Therefore the presence of a PTM for carrying out synthesis in a DAC would probably only act as a thermal insulator during LH. For attempting to calculate mechanical properties or an EOS, it is important to have hydrostatic conditions not only around the sample but also around any pressure markers to improve the precision of the experiment

Medium	Hydrostatic limit (GPa) (Approx)
Helium	12. 1
4:1 Methanol–ethanol	9.8
Neon	4.8
Nitrogen	3
Argon	1.9

TABLE 1: The approximate hydrostatic limit of various PTMs as given by Angel *et al.* [74] and Klotz *et al.* [75].

It is therefore vital to select the correct PTM for the experiment [76]. Importantly for the work reported here, in particular concerning light elemental systems, the atomic number of the PTM plays a decisive role in the choice of

PTM. The weakly X-ray scattering C-N-H systems are easily dominated by the presence of any heavier system, such as a PTM, and the choice of PTM has been based on its mass rather than its "hydrostatic effect". An additional function of the PTM is to provide thermal insulation to the diamond windows during laser heating experiments. As diamond is such an excellent thermal conductor, the sample must not be in contact with the diamond during the LH runs in order to keep the hot spot localised on the sample and not dissipate through to the diamonds, risking the experiment.

The most important PTMs for glove box loadings are soft solid media such as the Group I halides, e.g. NaCl and CsI. Although these are solids, and therefore do not provide a true hydrostatic environment, they are considerably softer than many minerals and ceramics and can therefore be useful [77]. For loading in an inert environment the salts are purchased as spectroscopic grade quality and are only ever opened in the glove box to prevent any contamination with water.

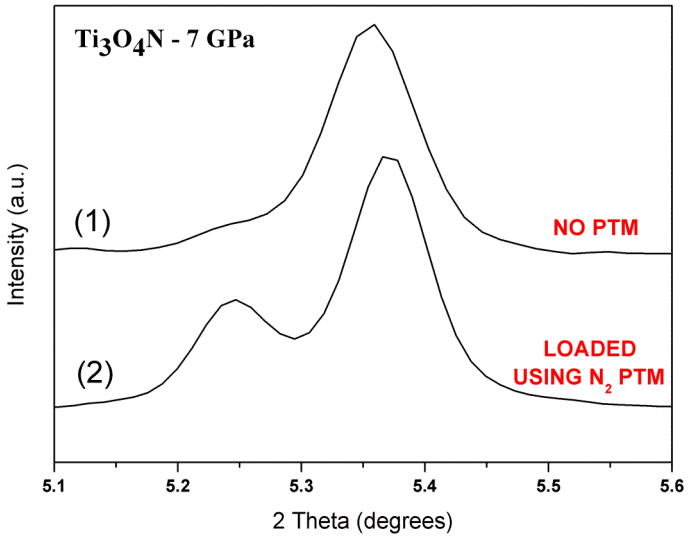

FIG. 7: A comparison of two XRD patterns taken of $Ti_{2.85}O_4N$ both at 7 GPa. (1) The pattern is of just the sample with no PTM. The main peak at 5.35 degrees is broader then that seen in pattern 2. Also the shoulder at 5.24 degrees seen in pattern 2 is not clearly visible in the non-hydrostatic pattern (1).

The use of solid PTM materials is ideal in glove box loadings and also makes them an excellent candidate for LH experiments. In particular, sodium chloride and lithium fluoride were used when opting for a solid PTM. NaCl has been well tested for LH-DAC experiments, but it has strong diffraction lines that

can mask key reflections of the desired system. The situation is further complicated by the B1-B2 transition that occurs at P~27 GPa but with considerable hysteresis during decompression [78]. LiF is less well established as a PTM for LH-DAC synthesis studies; however, we found it performed well during the C_2N_3H experiments and its use enabled us to complete the set of diffraction data unobservable using NaCl. It is considerably lighter than NaCl and remains as a single phase up to 100 GPa [79].

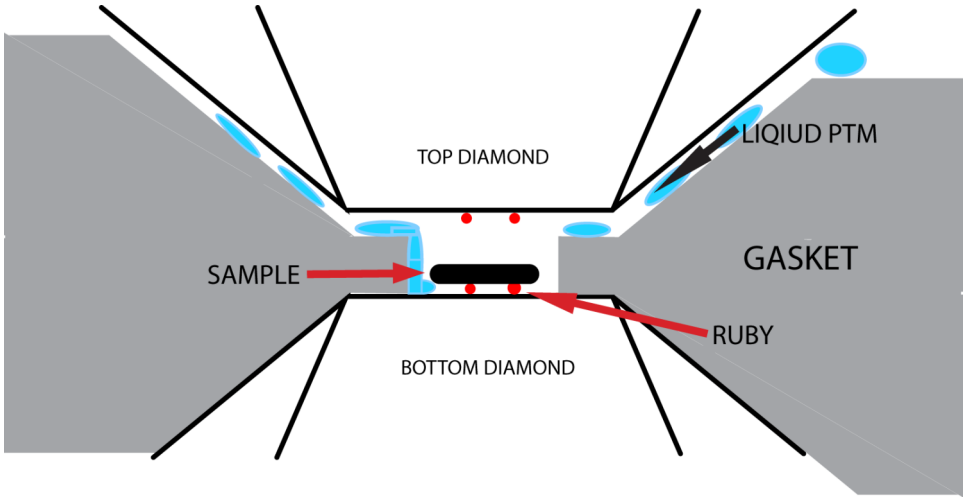

FIG. 8: A schematic illustrating the setup for cryogenically loading a PTM into a DAC. The sample is first compressed in either another DAC or using tungsten carbide blocks, to ensure a compact load. It is then mounted on a tripod of ruby dust, with attention paid to making sure the sample is elevated above the diamond culet. Ruby is placed in a similar formation on the opposing diamond and the cell is closed as usual except for a small gap of a few microns between the top diamond and the sides of the gasket wall. The placement of ruby is to prevent any contact between the sample and either one of the diamond culets. The flow of PTM into the sample chamber must be smooth enough to prevent washing away the sample on its mount.

Other PTMs include cryogenically-cooled gases such as nitrogen, argon and neon. The sample preparation for this type of loading is slightly different from using salt PTMs since the sample has to be elevated above the diamonds for the condensed liquid medium to be able to flow under and around the sample. This improves the overall contact of the PTM with the sample and isolates the sample from the diamonds for LH experiments. Ruby is usually used at UCL for elevating the sample above the diamond culets although other

materials are available. To load the PTM, the cell is placed in a polystyrene box igloo and the gaseous PTM is pumped through a reservoir of liquid nitrogen and condensed onto the DAC. This method allows clean PTM to be loaded, minimising the presence of water, as well as bringing the DAC to thermal equilibrium as the cryogenically cooled gas slowly fills the polystyrene box in which the DAC rests. Once the DAC is submerged in liquid PTM the cell is left for about 15 minutes and then closed with the PTM trapped in the sample chamber. It is important at this stage to close the cell tight enough to ensure the PTM does not leak out of the DAC but also it is imperative not to close the DAC too tightly and risk a large jump in pressure or damage to the diamonds. This method also enables the loadings of active PTMs which act as reactants as in the synthesis of γ-Si_3N_4 at high pressures from Si and N_2 PTM [80].

2.1.6 Gas Loading System

During the first year of my PhD, I carried out research on using carbon dioxide as a reactant to explore the synthesis of new materials [81-84]. The vapour pressure of CO_2 is above room pressure and to liquidify its triple point occurs at a pressure of 5.2 atm and at 216.6K (-56.4^{o}C). Therefore, a gas pressure vessel was designed and built at UCL for these purposes, to allow different gases to be pumped into a chamber at pressure, and cooled whilst being able to shut the DAC closed inside (FIG. 9).

The gas loading system consists of a stainless steel vessel of 16–20 mm walls with a two valve neck and a lid with a 20 mm thick window. An inlet valve is inside the vessel which allows a membrane DAC to be attached and closed from the outside using a valve outside the vessel to which a gas regulator may be attached. The membrane cell is prepared in the usual manner but left slightly open when placed in the vessel. A gap of 5 to 30 μm is left between the two diamond culets to enable the condensation of the gas to flow into the sample chamber. Once the vessel has been filled with the liquid medium, a gas regulator used to pump helium into the membrane of the cell, forcing the membrane to shut the DAC and isolating the sample.

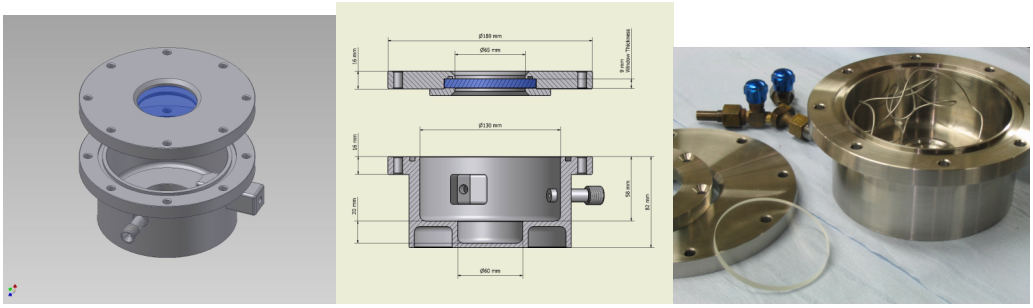

FIG. 9: A series of schematics illustrating the development of the gas loading system and a photograph (right) showing the final constructed device.

During my work I have also cryogenically loaded CO_2 along with different minerals where the CO_2 acts as both the thermal insulator and a reactant as part of the synthesis. The gas loading system was used at UCL and the ESRF in attempts to study and synthesis novel CO_2 phases and metal carbonates. Some new results obtained are now being analysed and are not reported in this thesis.

2.1.7 In situ Determination of Pressure in a Diamond Anvil Cell

2.1.7.1 The Ruby Scale

The use of ruby fluorescence is a precise and relatively simple method for making *in situ* pressure measurements in the DAC [55, 85]. A fluorescence system is used to measure the shift in wavelength of the sharp-line (R-line) luminescence of ruby grains (Cr^{3+}:Al_2O_3) which are loaded into the sample chamber of the DAC (FIG. 10). The first use of a ruby fluorescence system for measuring pressure within a DAC was described by Barnett *et al.* [86]. At UCL, the Raman system is used to measure the ruby fluorescence; its micro-focussing capabilities permit the use of very small ruby fragments (~1 μm). In contrast, large-scale facilities such as synchrotron sources often do not provide users with a micro-focusing fluorescence system and so larger grains of ruby are required. This can lead to extreme fluorescence which floods the Raman signal; additionally, greater amounts of ruby can contaminate XRD patterns.

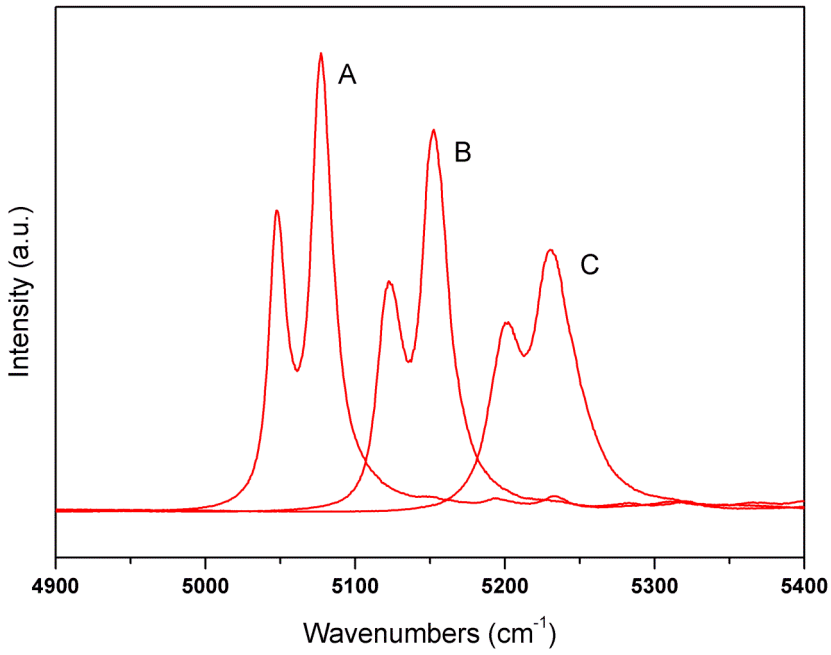

FIG. 10: Emission spectrum from the fluorescence of ruby packed in NaCl. Pattern A is at 5 GPa, Pattern B at 16 GPa and Pattern C is at 36 GPa. The loss of hydrostatic conditions can be observed from the general broadening and merging of the doublet peaks as seen in the progression from A to C.

The ambient emission spectrum of ruby consists of a doublet line, R_1 and R_2, which are due to an electronic transition. The wavelength of the ruby R_1 line has been shown to increase linearly as a function of pressure up to 29.1 GPa [56]. The ruby scale versus pressure was originally calibrated using the Decker equation of state of NaCl [87, 88] and has since then been revised a number of times to ever increasing pressures [89, 90]. Bell and Mao first reached the one Mega-bar benchmark [91] using ruby as an internal calibration and subsequently other authors have reached even higher pressures [92]. In addition to pressure measurements the full width at half maximum (FWHM) and the separation between the R_1 and R_2 lines are sensitive indicators of hydrostatic conditions in the sample chamber (FIG. 10).

2.1.7.2 Other Pressure Calibrants

An earlier method of pressure determination, and one that is still in use now, are sensors such as NaCl, CsCl and Au inside the sample chamber. By using X-ray diffraction the EOS of the sensor can be applied to determine the pressure in the sample chamber, or at least the pressure felt by the environment of the sensor [93-97]. For infrared spectroscopy different pressure sensors can be used in the form of ionic molecular salts such as $NaNO_3$, $MgCO_3$, $BaSO_4$ [98-100].

2.1.8 Laser and Resistive Heating in the Diamond Anvil Cell

2.1.8.1 Laser Heating in the Diamond Anvil Cell

The application of LH in the DAC was been well demonstrated [101-103] and provides an excellent approach for the synthesis and exploration of solid-state systems over a very wide range of pressure and temperature. The high transparency of diamonds for IR and near IR radiation allows *in situ* heating of samples inside the DAC. The heating is carried out by the absorption of focused intense radiation by the sample. The heat generated occurs via several processes, such as charge transfer or light scattering mechanisms, allowing temperatures up to 6000 K to be generated. Currently, there are two common types of lasers used in high-pressure for LH in high-pressure research and which are used throughout the work reported here. The first of these are continuous-wave solid state lasers which are targeted at semiconductors and metals [104] and have a power source of wavelength $\lambda = 1.064$ μm. These near IR lasers are either Nd:YAG (yttrium-aluminum-garnet) or the more recently Nd:YLF (yttrium-lithium-fluoride) and they are available at a number of high-pressure beamlines at various synchrotrons sources as well as in the laboratory [105-109]. The absorption of these lasers by materials with the appropriate band gap is generally weak and a very tight focus of the light is required. This often leads to a very small laser spot with minimal penetration of the material, resulting in extremely large temperature gradients across the sample chamber.

These effects may be minimised with the employment of multimode lasers, double-sided laser heating etc. which allow the temperature to be homogeneous through the depth of the sample [105, 110] Another method of delocalising the heat and improving the temperature gradient is by soft focusing the laser spot prior to an increase in laser power. This consists of getting the sample to couple with the laser spot and then defocusing the spot as the power of the laser is increased accordingly whilst maintaining the coupling mechanism.

An alternative to solid-state lasers is the CO_2 laser [111] (wavelength λ= 10.6 μm), used particularly for heating minerals and oxides and organic materials [80]. These compounds are highly absorbent at the larger emission wavelengths of the CO_2 gas laser. The absorption by SiO_2 of this wavelength of light makes glass objectives unusable and the laser is focused with a ZnSe lens [112]. In contrast to the use of solid-state lasers, the CO_2 laser heating technique provides a greater penetration depth, often greater than the sample thickness and thus removing the need for double-sided focusing. In addition, the focal size of the laser spot can measure up to ~50 μm in diameter and thus making steering and focusing much easier than the previously described near-IR source. At UCL we have a 50 W and a 150 W CO_2 laser (Synrad®) available and both were used in the work reported here. The lower-powered, smaller laser was used for annealing samples at pressure whilst the 150 W laser was predominantly used for synthesis. For LH with the membrane DAC a copper cooling jacket (FIG. 11) was designed and built to minimise heat transfer to and expansion of the membrane.

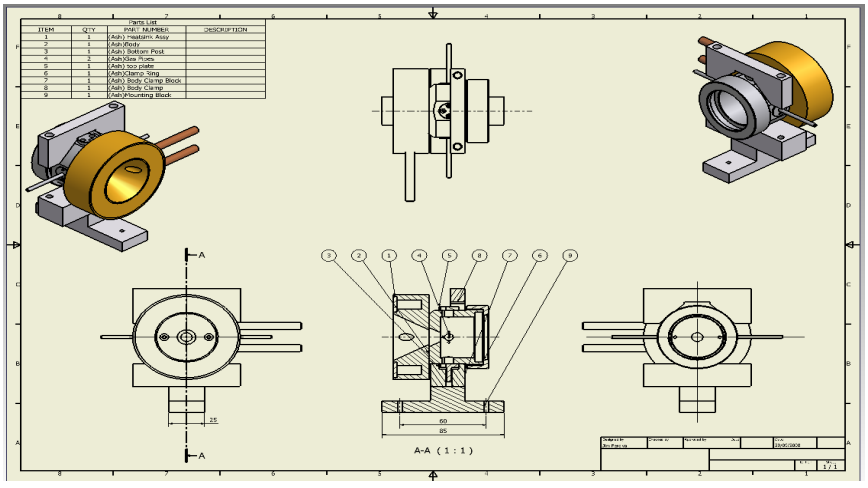

FIG. 11: A schematic of a copper cooling jacket designed and made at UCL, for attaching to both a membrane DAC for laser heating and also to the M7G cell for resistive heating.

2.1.8.2 Resistive Heating and the M7G Cell

A second common heating technique for inside the diamond anvil cell is the use of resistive heating. The range of temperature attainable with this technique is wide, from just above room temperature to 3000 K, as reported by Zha and Bassett [113]. An advantage of using resistive heating over the use of lasers is that heating is generally more homogeneous and temperatures can be held constant with greater stability [114]. In addition, a much simpler laboratory set up is required compared to laser heating.

The resistive heating cell available at UCL is the M7G (Diacell®HeliosDAC), which is a stainless steel membrane DAC with an internal ceramic heater capable of achieving up to 800 K at pressure. Initial resistive heating cells consisted of wires wound around the backing plates through which a current was passed, generating heat [115, 116]. The set up of the M7G consists of a ceramic heater in which the metal gasket sits in and it is through this contact that the heat is transferred to the sample chamber. The gasket performs a two-fold role, initially holding the sample in place between the opposing anvils and acting as an ohmic heating element [117]. The compact internal resistive heater is connected to a power supply with which the amount of current allowed to pass through the heater is controlled. The cell is purged during the heating procedure with a reducing mixture of gas of 98-2 % Ar-H respectively, to minimise oxidation of the internal components of the cell. The pressure of the DAC is adjusted using a gas-driven membrane.

During part of my PhD the M7G cell was used for HPHT studies in conjunction with synchrotron radiation techniques (FIG. 12). This technique was carried out to study the PT phase diagram of bismuth stanate (Sn) and hafnium (Hf) pyrochlores and was carried out in collaboration with Andrew Hector from Southampton University. The X-ray diffraction patterns were collected at I15 (Diamond) with the temperature fixed at 500 K and the pressure range of 0 to 40 GPa was scanned. Although the design of this cell consists of an internal heater, the heat generated can dissipate throughout the cell and the external part of DAC can equal that of the heater. As a result, the DAC had to be mounted on a specially-designed mount that consisted of a ceramic stage and cooling jacket to minimise heat transferal to the diffractometer. This jacket was designed by the design engineer James Percival (UCL) and myself and was built

at UCL (FIG. 11). It is attachable to all the membrane cells at UCL and provided an excellent method to minimize the heating up of the various DACs during LH. However the temperatures of the outside of the DAC still reached above 70 °C making the cell too hot to handle. As a result the membrane used for the DAC was calibrated previously in the laboratory using the same samples and at both ambient temperature and 500 K (FIG. 13). This method of calibrating the membrane pressure with the internal DAC pressure has been shown to be reliable for examining amorphous systems [16, 118] as well as at synchrotron stations where removing the cell from the diffractometer and checking the pressure can be too time consuming.

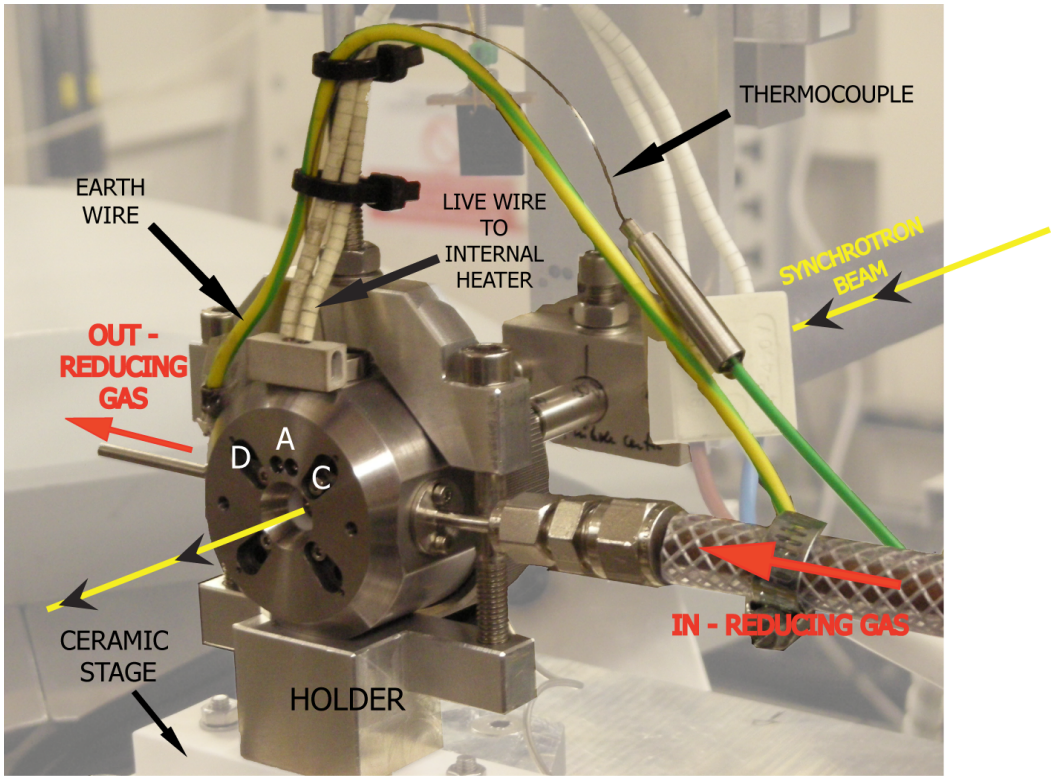

FIG. 12: A M7G resistive heating cell, fully assembled and mounted on the diffractometer at I15, Diamond.

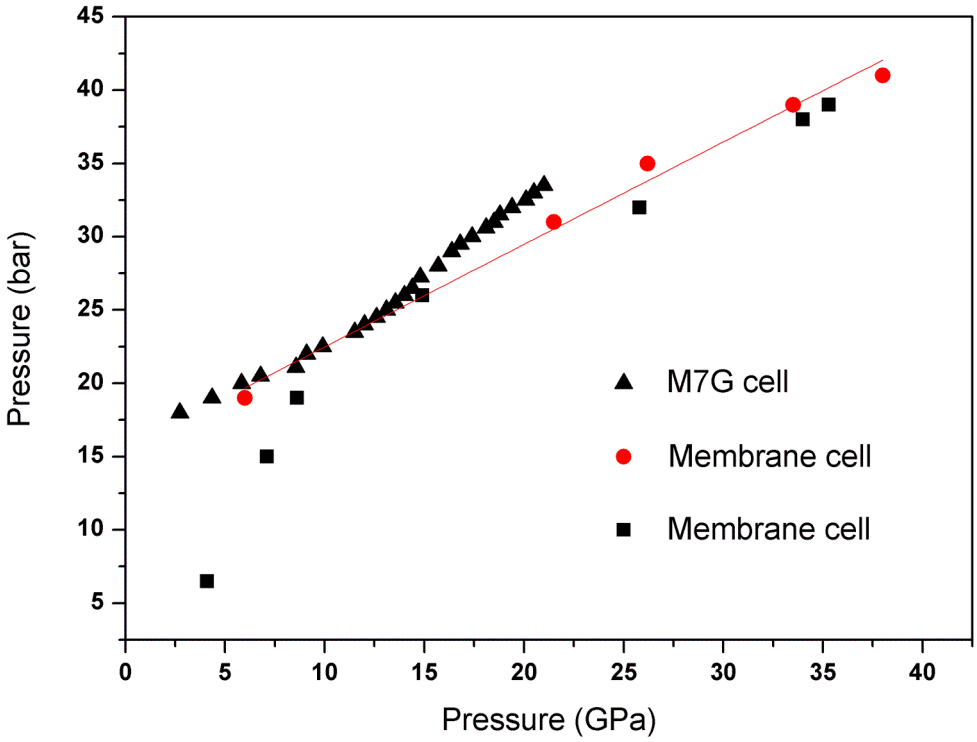

FIG. 13: A plot of the internal pressure of different membranes (bar) versus the pressure in side the sample chamber (GPa). This data represents measurements at ambient conditions. The red circles represent a Diacell®RamanDAC, whilst the black squares represent a Diacell®X-raydiffractionDAC. The difference in their calibration at lower pressures is due to varying stiffness in the action of their piston-cylinder fitting.

2.2 Raman Spectroscopy

The use of vibrational spectroscopy allows the probing of samples inside the DAC and provides valuable information about the bonding and structure of the systems under observation. The vibrational techniques available at UCL are Infrared and Raman spectroscopy. Although these techniques are complementary to one another they differ in mechanism. The Raman effect, which is observed when shining light on a molecule, arises from a scattering phenomenon, whilst the IR method results from an absorption effect. The focus of this section will be solely on the Raman effect and optical set-up for high-pressure studies at UCL [119].

The Raman effect is named after, and honours, the work carried out by C. V. Raman [120-122]. It describes the inelastic scattering of an incident

photon by a sample, which results in a frequency shift of the scattered photon. When using monochromatic light on a clear sample, whether gas, liquid or solid, most of the incident light will pass through the sample or be elastically scattered (Rayleigh scattering). A small number of photons will, however, be scattered inelastically, resulting in a shift in frequency to that of the incident light. Therefore, when a monochromatic light is shone on a sample, the spectrum collected will consist of the Rayleigh scattered laser line at 0 cm^{-1}, and of shifted frequencies equally distanced either side. Those shifted towards positive frequencies are nominally weaker in intensity than those towards the negative. The shifts observed in the spectrum are referred to as Raman frequencies and are usually very weak and have an intensity10^{-6} or less of that of the incident beam. They are independent of the wavelength of the incident photon and unique to the scattering sample [123].

Using classical mechanics, the Raman effect can be described as the interaction of the electric field of an incident photon with the electron cloud of an atom resulting in a temporary dipole moment. This induced polarisation **P** of the sample by the electric field **E** of the photon is related by a polarisability tensor, α and can be rewritten as:

$$\mathbf{P} = \alpha \bullet \mathbf{E}$$

The same phenomenon can be described using a quantum mechanical argument. The model now is of the perturbation of the wave-functions of the scattering molecule by the electric field of the incident light. The induced transition moment is expressed as the induced electric moment matrix element P_{mn}, describing a transition between the initial state (n) and a final state (m). This is given as:

$$P_{mn} = \int \psi_m^* P \psi_n \, d\tau$$

where P is the induced dipole moment and the ψ_m and ψ_n are the time independent wave-functions of the initial and final vibrational states. All components are integrated over the full range of coordinates. It is $(P_{mn})^2$ that determines the intensity of the scattering light which is involved in causing a transition between an initial and final state (n $\rightarrow$ m). The scattering radiation can also be defined as the incident radiation $\nu_0 + \nu_{nm}$. When m = n and $\nu_{nm} = 0$ then the state of the scattering atom remains unchanged and the incident radiation has been elastically scattered. When m $\neq$ n and $\nu_{nm} \neq 0$ then there has

been a change of state regarding the scattering molecule and therefore a Raman frequency (FIG. 14). The energy difference between vibrational eigenstates is given as:

$$\nu_{nm} = (E_n - E_m) / h$$

where h is Planck's constant. When the transition is to a lower energy state (m → n) then ν_{nm} is positive and is called an anti-Stokes Raman line. When the transition is from a lower state to a higher one (n → m) then the ν_{nm} is negative and this is a Stokes Raman line. The transition process is described by the presence of a virtual state, virtual as no energy change occurs and the photon is not absorbed. The Stokes Raman line has a lower frequency and therefore a longer wavelength. This also explains the reason that the Stokes Raman line is more dominant than the counterpart anti-Stokes line at room temperature, as its ground state will be more populated than any of the excited states.

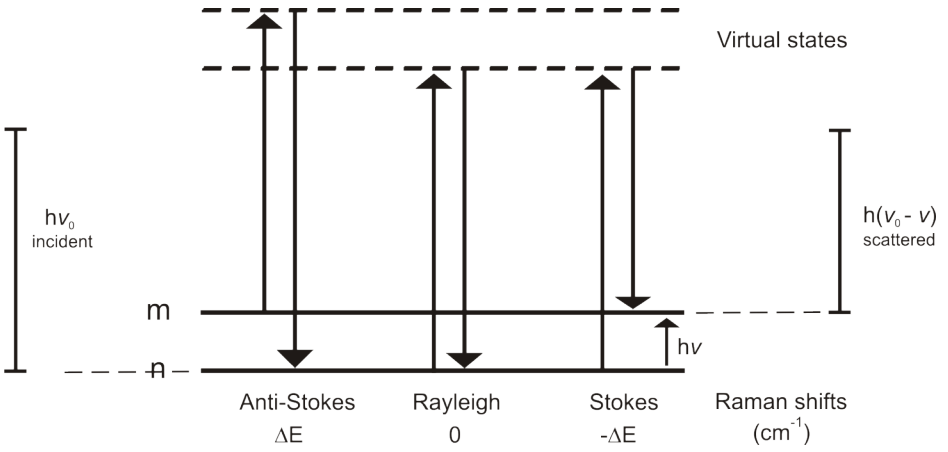

FIG. 14: Schematic of elastic light scattering (Rayleigh) and the excitation of a Stokes and Anti-Stokes Raman line from inelastic scattering.

2.2.1 The High-Pressure Optical Bench at University College London.

The Raman effect occurs during inelastic scattering of light by molecular systems. At UCL we have a home-built Raman system designed and built by Emmanuel Soignard and Paul F. McMillan. It uses laser excitation sources and is based on a supernotch filter system which is specifically designed for weakly scattering systems and DAC work [124]. The advantage of an excitation source is that it generates only a single exciting line which is highly monochromatic. There are two lasers, each operating at different excitations, allowing alternative lines to be used to avoid fluorescence in the sample. The two laser lines we select are the 514.5 nm line of the Ar ion laser and the 633 nm line of a HeNe laser. The Ar ion laser is a 50 mW Laser Physics® Reliant 150M and the HeNe is by Melles Griot®, providing 35 mW at 633 nm. The Ar ion laser has an adjustable power output and is normally set at a low value to minimise luminescence. The HeNe laser has a fixed power source and its intensity is adjusted using neutral density filters along the optical path. The light produced by both lasers is plane polarised.

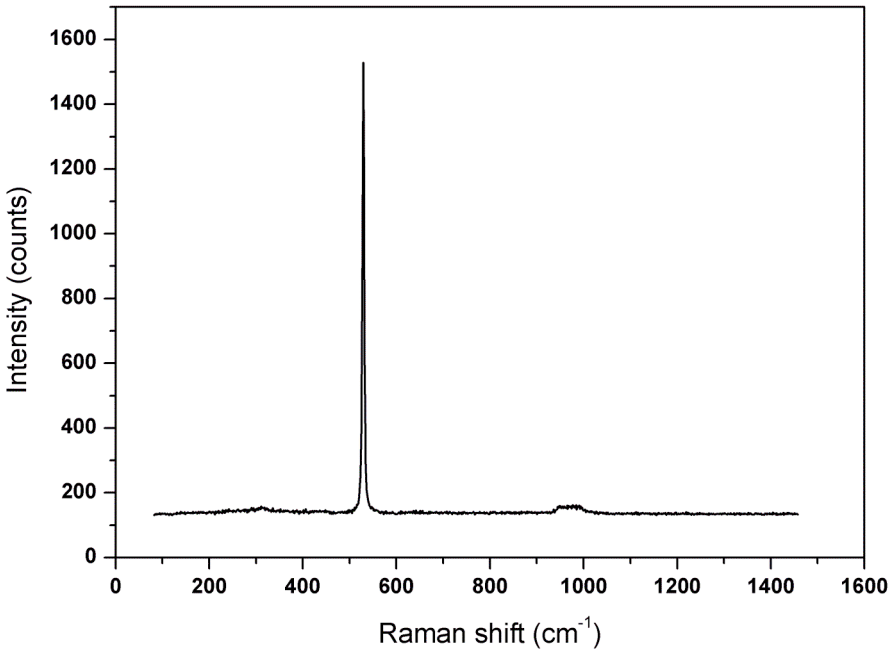

FIG. 15: A Raman spectrum of silicon is shown with the first order peak at 520.5 cm^{-1} and the second order peak at 980 cm^{-1}. A 1200 cm^{-1} grating was used and the cut off point at 80 cm^{-1} is as low as the notch filters system permits.

The Ar ion laser emits a number of laser lines at different wavelengths, of which we select one of the more intense lines, the 514.5 nm. This is done using a Kaiser® transmission grating which is made up of a holographic grating mounted between two prisms. The required laser line is reflected off at right angles to the source and the remaining lines are discontinued using a beam dump or a shield. The height of the shutter for the Ar ion laser is used as a reference plane at which the DAC and the optics are leveled. The HeNe laser produces only one laser line (633 nm) and has no need for a Kaiser® grating but does have a two mirror tower to allow the laser line to be bought parallel with the rest of the optical path. Both lasers rely on a series of Si coated mirrors to travel around the optical table. However, both lasers cannot be used simultaneously on the table as each one requires its own specific notch filter. A notch filter (Kaiser® SuperNotch-Plus™ holographic filter) consists of near parallel fringes which reflect incident light of a narrow bandwidth and allows all other wavelengths of light to pass through [125, 126]. This enables the first notch on the optical path to act as a mirror to the desired laser line, reflecting the incident radiation into the objective (Mitutoyo®, SL10-20-50, all with numerical aperature of 0.48). The collimated radiation is focused by the objective onto the sample and the scattered light is collected by the same objective, re-collimated and sent back down the optical path towards the notch filter (a back-scattering geometry). The notch filter reflects the laser line and permits only Raman scattered light through, preventing the laser line saturating the spectrometer. A second notch filter further down the optical path minimises any remaining Rayleigh scattering, which is particularly important when observing weakly scattering samples [127].

Each notch filter is unique and has an optimum angle of incidence to the incoming light, which is specified by the manufacture. This angle is usually between 4 – 8 degrees and must be positioned correctly in the optical path to have maximum efficiency. An effective method of identifying the best position for the notch filter is to place it into the path of the beam and then shine white light down the optical path through the filter whilst rotating the filter [128]. At the optimum angle, the filter will maximise the reflection of the laser line, minimising the amount of Rayleigh scattering entering the spectrometer (FIG. 16).

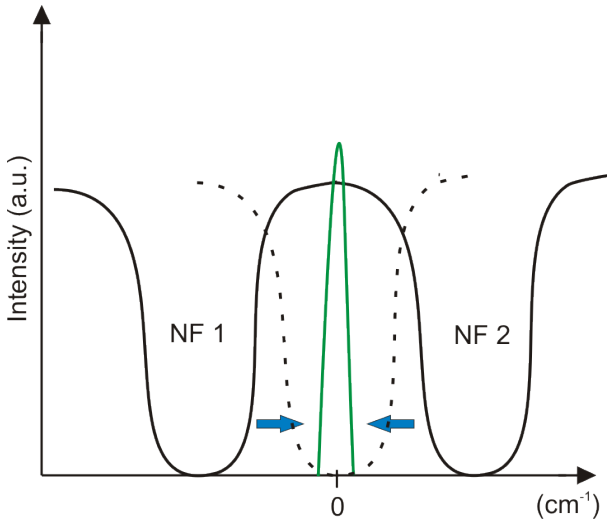

FIG. 16: A schematic of the laser line and the regions of interest regarding the use of two notch filters. The laser line is positioned at zero wavenumbers whilst the notch filters are positioned either side. By rotating the notch filters they can be placed on top of the laser line, removing any Rayleigh scattering from entering the spectrometer.

Prior to the availability of notch filters the main approach was to design and use complex multi-element spectrometers and spectrographs which consist of a series of double of triple diffraction gratings. This method allows the excitation wavelength to be rejected and the spectrally shifted Raman-scattered light to pass. An advantage of this system over the notch filter set-up is that although the latter provides a more intense Raman scattered signal, it is not possible to record spectra below ~100 cm^{-1}. A double or triple subtractive system allows Raman scattering intensities to be recorded to ~2-3 cm^{-1} either side of the laser line at zero. Although the overall signal recorded is weaker (30 %) than using a notch filter approach, it does allow low Raman frequencies to be observed, crucial for studying amorphous systems.

A number of additional procedures are carried out to clean up the Raman signal and minimise any loss in intensities [129]. The desired laser line prior, to reaching the notch filter, is passed through a plasma filter, which eliminates discrete plasma lines present in the Raman spectra. Once the Raman signal has passed through the first notch filter it is passed through a confocal spatial filter which consists of a lens and a variable aperture. The data window is defined by the aperture and can be adjusted to limit the amount of light around the region of interest, thus reducing background contributions from the diamond anvils. A second lens brings the signal back to parallel and on the optical path. After this,

the signal passes through the second notch filter before being focused by an achromatic doublet lens onto the diffraction grating inside the spectrometer. The spectrometer (Acton Research SpectraPro® 500i spectrometer) has a turret of three diffraction gratings on a rotatable stage. These are 600, 1200 and 2400 lines/cm giving a spectral range of 2500, 1400 and 800 cm^{-1} respectively. Each grating is calibrated using a mercury source and is selected according to desired spectral resolution (3, 1 and 0.5 cm^{-1}) and frequency range. The spectrometer is attached to a liquid nitrogen cooled silicon CCD detector (Princeton Instruments Spec10:100B).

In addition to the Raman spectroscopy set-up on the optical table (FIG. 17) there are also two larger lasers available. These are the CO_2 gas and the solid-state Nd:YAG lasers which are used for heating. Each is aligned using a visible diode (635 nm) that is matched with the optical path of the laser. The diode of the CO_2 laser can be used to align both of the excitation sources. The 514.5 nm notch filter allows the diode from the CO_2 laser to follow the length of the optical path to the spectrometer and on to the CCD detector slits. Having aligned this visible source, irises are placed to define the optical path before the first notch filter. The excitation sources are then moved to match the positions of the irises. This provides a cursory method of alignment but does allow the Raman signal to be observed using the detector, from which a much finer alignment of the optical set-up can be carried out. For the solid-state laser, a prism is positioned by its shutter, splitting the near-IR beam as well as its visible diode. This provides a double-sided focusing onto the DAC and is positioned using Mitutoyo objectives either side.

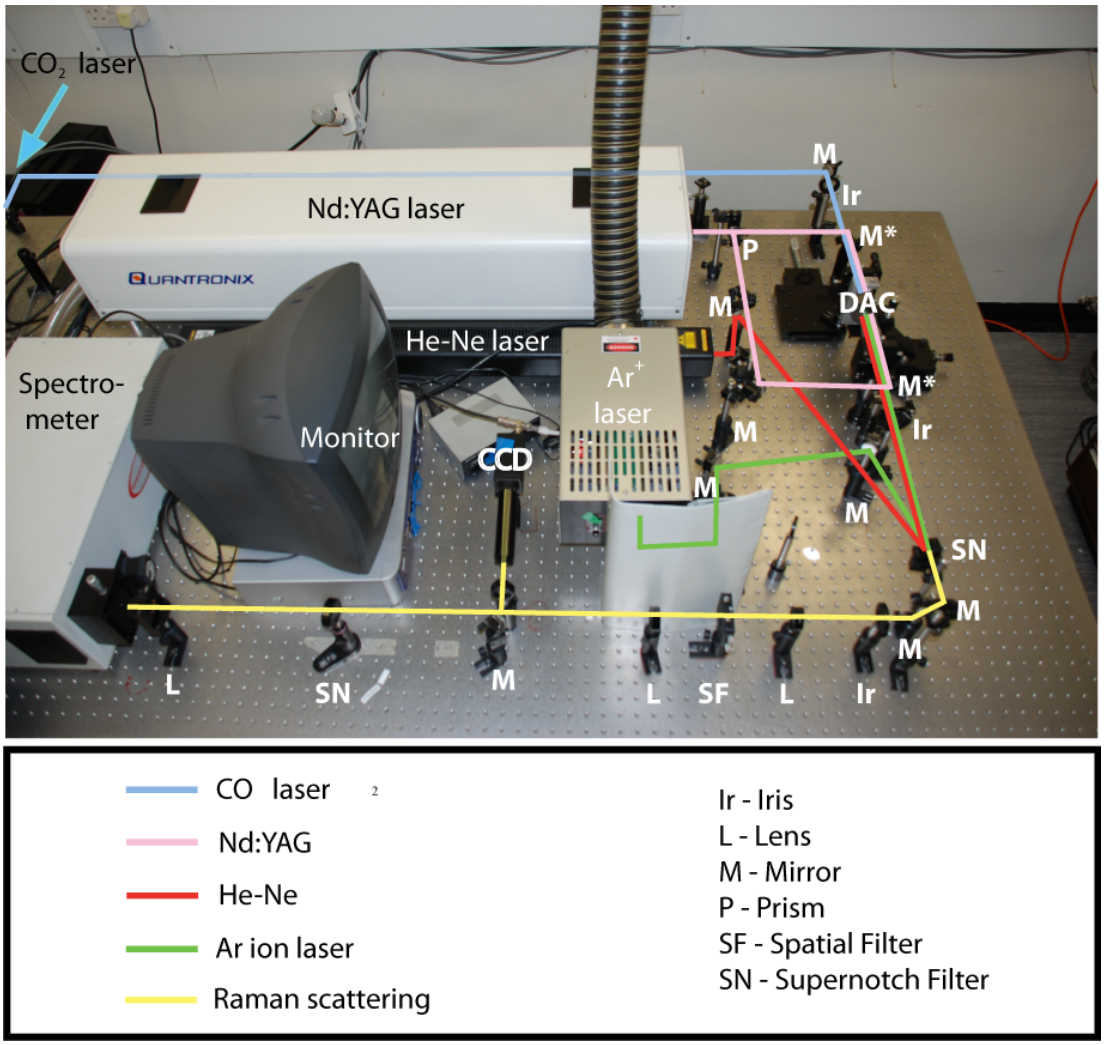

FIG. 17: A photograph of the optical bench used for Raman spectroscopy at UCL. The overlaid schematic highlights the optical paths of the various laser available on the system. The CO_2 and Nd:YAG lasers are positioned at the top half of the table. Both the excitiation lasers, the Ar ion and HeNe are set-up with a back scattering geometry using a notch filter which also discriminates against any Rayleigh scattering travel to the spectrometer.

2.3 X-ray Diffraction

X-ray diffraction is a well-understood analytical technique that has its origins in the work of M. von Laue and W. and L. Bragg in the early part of the 20th century [130-133]. It is based on the interaction of X-rays with the ordered array of atoms in a crystal, resulting in a characteristic diffraction pattern and enabling the calculation of crystallographic data such as the size and shape of the unit cell and the arrangement of the atoms within it [134-136]. This may then be used to identify phases and phase transitions and to recognise new materials in order to characterise systems on an atomic level. For the research presented here, it allows this information to be gathered from a sample within the DAC in situ at pressure. This chapter outlines the principles of this analytical method as it is relevant to this research, but it is thoroughly described elsewhere, such as the seminal papers by Rietveld [137], Le Bail *et al.* [138] and Pawley [139, 140].

2.3.1 Basic Theory

When an X-ray travels through a substance, it may interact with the atoms within it by being either absorbed or scattered. Scattering is a phenomenon whereby the path of the incident photon is deflected from its initial path; two types of this occur: coherent and incoherent scattering. Elastic scattering is when the photon from the incident beam has the same energy as the photon from the scattered beam. There is no change in energy during the scattering process and hence it is considered as an elastic process. The second process is incoherent scattering, also known as Compton scattering. This is an inelastic process where the scattered photon has a different energy and hence wavelength to that of the incident photon because of an energy loss during the collision with an electron core [141].

When the wavelength of the X-rays is similar in magnitude to the distance between the atoms against which they are incident, diffraction is possible. This occurs when there is constructive interference of the scattered incident radiation. Collection of these scattered photons produces a diffraction pattern which may be analysed by different methods to give information about the scattering atom. The explanation of diffraction given in this work is focused

on coherent scattering, as it is the main contributor to diffraction; it will be placed in the context of the investigation of solid sate systems using powder diffraction.

2.3.2 Diffraction by Crystals

The definition of a crystal can be given as a solid with a periodic repetition of atoms, ions or molecules in a three-dimensional arrangement. This periodicity of the crystal is better understood as a lattice and the repeating motif of the crystals is referred to as a unit cell. In theory the lattice is regarded as infinite. The distances and the bond angles between the constituent parts are fixed and there is long range order through the lattice. The dimensions of the unit cell are defined by vectors **a, b, c** and by the inter-vectors **α, β, γ.** Having defined the crystallographic dimensions of the unit cell, the atoms can be described as sitting in parametral planes. These crystallographic planes are described by the scalar terms *h, k, l* which are referred to as Miller indices. FIG. 18 illustrates how X-rays when exposed at a crystal can undergo constructive coherent scattering from the atoms on these parametral planes, giving rise to diffraction. This is in accordance to the Bragg expression [142] for diffraction and describes the relationship between the diffraction angle (Braggs angle), the wavelength of the incident beam and the interlayer spacing between the different planes (Eq. 2).

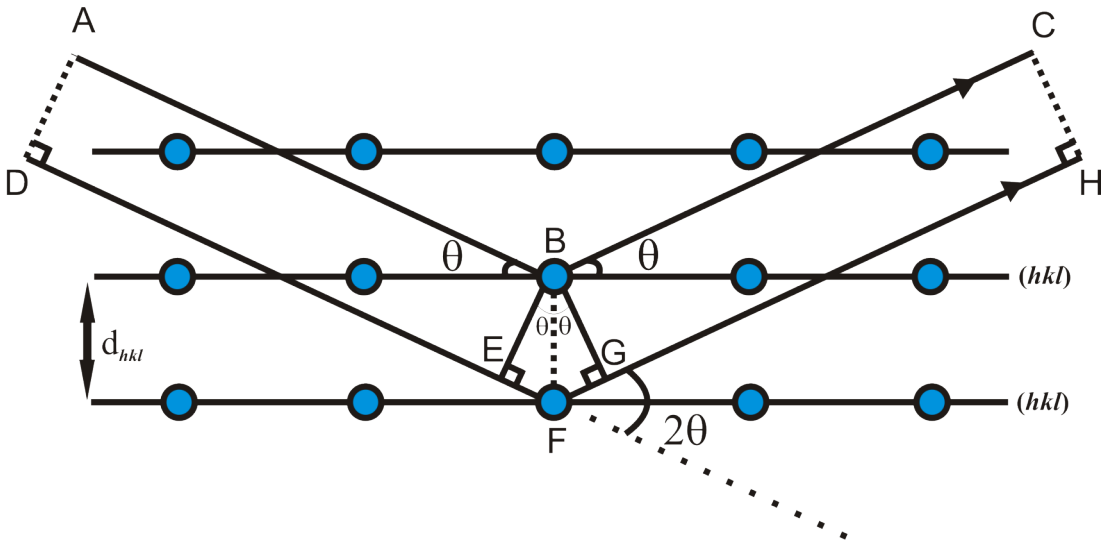

FIG. 18: A geometrical representation of Bragg's law.

The incident wavefront of the X-ray begins at point AD on FIG. 18 and travels towards the parametral planes. Once the X-ray has been scattered by the atoms in the different planes it now travels at a different trajectory, defined by θ, and becomes a reflected wavefront. Now the incident path of AB and DF which are reflected to the paths BC and GH respectively by an angle θ have travelled different distances as a result. This path difference (δ) explains the interference effects between reflected wavefronts and is described as:

Eq. 1:

$$\delta = EF + FG = d\sin\theta + d\sin\theta = 2d\sin\theta$$

Constructive interference is at its maximum when the path difference between the reflected wavefronts is at an integer of the wavelength of radiation. This is known as Bragg's law:

Eq. 2:

$$n\lambda = 2d_{hkl}\sin\theta_{hkl}$$

where λ is the wavelength of the X-ray, d_{hkl} is the spacing of the planes and θ_{hkl} is half the total scattering angle, 2θ. The constructive interference of the scattered wavefronts lead to a diffraction pattern by the sample. This is in the form of diffraction rings, which are concentric with the primary beam and at specific values of 2θ satisfying Bragg's law. This can then be analysed to determine the structure of the crystal.

2.3.3 Crystallographic Data Collection and Analysis of Powdered Samples

The preparation process for XRD experiments using the DAC must be carried out with vigilance and great care to ensure the highest quality data possible. As mentioned earlier the selection of an appropriate PTM is vital to permit the observation of the diffraction peaks belonging to the sample. It is also essential to ensure no contaminants are introduced to the DAC as this may affect the analysis of the XRD data collected. There are several factors to be taken into account when preparing samples. Powdered samples should be finely ground and homogeneous in size to minimise graininess and avoid unwanted

diffraction spots which are difficult to correct after exposure. Sample thickness must also be considered when looking at light elemental systems as this affects the relative intensities of the pattern.

Before collecting XRD data on a synchrotron beamline, it is important to select the correct sample to detector distance suitable for the experiment and to the 2θ scale as dictated by the conical aperture of the backing plates (FIG. 19). The distance chosen is required to allow the full scattering range to be observed. For the separation of diffraction rings at higher d-spacings it is possible to shorten the sample to detector distance allowing a more detailed examination of small angle scattering. The sample to detector distance is accurately determined using normally a silicon standard with which a data analysis program is used to calculate the various parameters of the instrumentation. Fit2D was used for this purpose in all the data collection and analysis in this report.

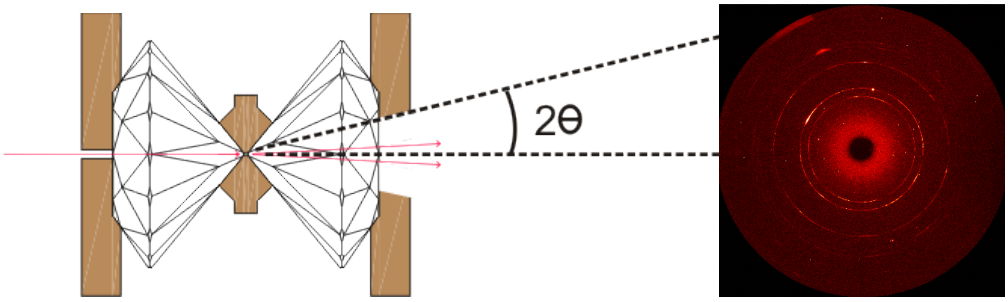

FIG. 19: A schematic of the DAC and the total scattering angle (2θ) range permitted by the conical aperture of the exiting backing plate. The collected image by detector is of Debye-Scherrer diffraction rings for the sample under observation.

The use of a crystalline standard such as silicon also serves an important purpose for during the refinement process. HP crystallographic data can be relatively low in quality and which contributes to additional difficulties during the refinement process and refining various parameters. Therefore the silicon standard can be used to determine all the instrumental variables which then act as the default values during refinement.

The use of powdered samples can lead to preferred orientation of the crystallite material which can cause systematic distortions of the reflection intensities. To minimise preferred orientation, the stage on which the DAC is mounted on can be rotated +/- a few degrees (the maximum amount without

clipping the gasket) around the centre of rotation during data collection to improve the statistics. However, any distortions that might arise can be mathematically modelled and corrected by applying 'preferred orientation functions' [143] using various refinement packages.

Scattering is dependent on atomic number and so exposure times must be assessed for each sample, for example weakly scattering samples obviously require longer exposure times. However, exposures that run for too long may saturate the detector, produce overexposed diffraction spots and be an inefficient use of synchrotron time. This latter problem is now minimised due to the extremely high flux and CCD detectors available as standard in third generation synchrotron sources such as the ESRF. In addition, it is better to accumulate a number of XRD patterns over a shorter range of time then to have one long exposure as it provides a better noise to signal ratio.

Once the XRD patterns have been assimilated the software Fit2D is used to convert the two-dimensional Debye-Scherrer diffraction rings into a one-dimensional projection. This is the format in which powder diffraction data are analysed in and describes the position of the Bragg peaks as a function of intensity.

2.3.4 Background

In the case of the weakly scattering systems such as those presented in this work, the background or baseline of the XRD pattern is often curved or hump-like (FIG. 20). This is due to the ~4 mm of diamond the beam must travel through to reach the detector. Nearly all the scattering actually comes from the exiting diamond anvil as any contribution from the top diamond anvil is blocked by the cell and the exiting backing plate. The presence of the background becomes more dominant the weaker the scattering of the system under observation. It may also be noted that the presence of the broad background increases with pressure. This is due to the sample thinning out during compression and contributing less to the scattered X-ray pattern. The background from the diamond anvils may be subtracted by taking the XRD

pattern of an empty cell, closed with a gasket in place and exposing it for the same time as that for the sample. The diamond can also cause the X-rays to undergo Compton scattering as well as single crystal diffraction that may result in large diffraction spots on the XRD pattern, and these must be masked out if visible. The subtracted background is included in the refinement process and it is considered a standard procedure to refine the background intensities.

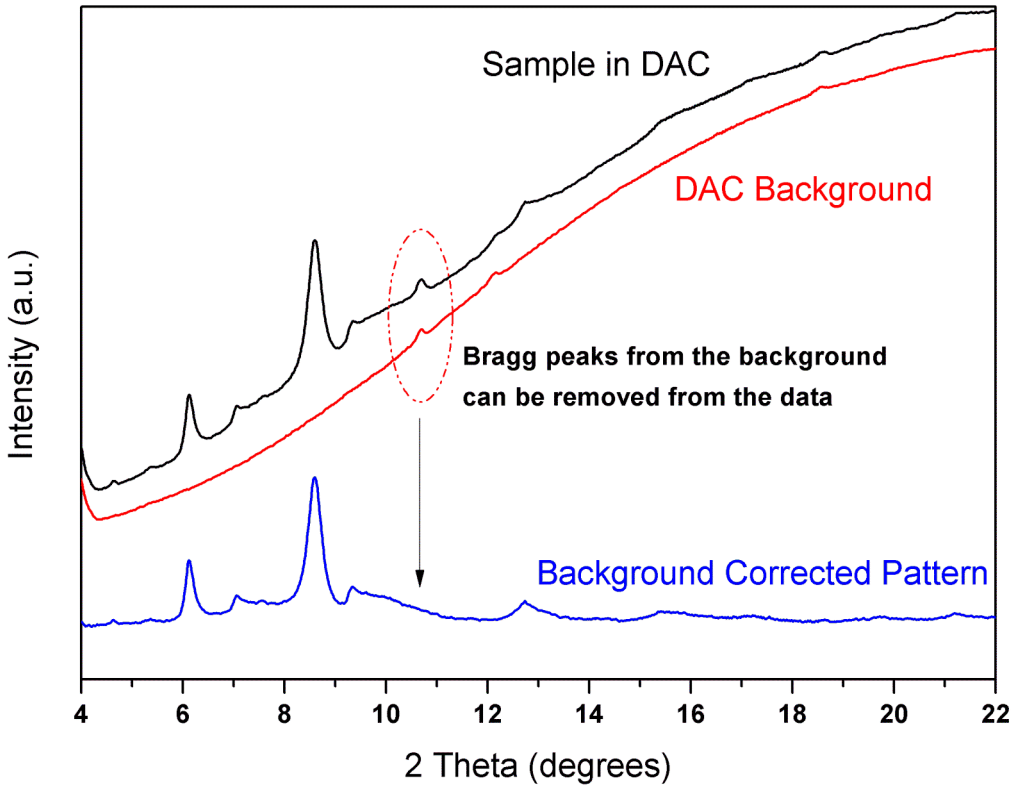

FIG. 20: This figure highlights the ability to remove the background contribution in from a DAC in HP XRD data, giving a flat baseline. The plot shows an experimental XRD pattern of a sample in a DAC at pressure, a XRD of the same empty DAC (the cell closed with the same gasket, cleaned, as that used for the experimental data) and a pattern after the pressure data has had the DAC background removed. Any contribution from the diamond anvils that are present in the background diffraction pattern can be accounted for and removed.

2.3.5 Indexing

Once the diffraction results are collected the next step is determining the unit cell by indexing the diffraction pattern. Indexing powder diffraction patterns can be very challenging, more so than single-crystal diffraction data. In single-crystal diffraction data a full 3D array of reflection positions are available, whereas the data from powder-diffraction patterns is reduced to a 1D projection after integrating the Debye-Scherrer diffraction rings. This means that the only data available for indexing is the d-spacings of the peak positions; this is further complicated by the likelihood of the peaks overlapping one another.

A number of programs are available for indexing the peak positions and are available from the website www.ccp14.ac.uk which maintains a large selection of crystallographic software. The indexing software used for the work presented here are TREOR [144, 145], DICVOL [146, 147] and CRYSFIRE [148]. These programs can successfully index powder diffraction patterns and are relatively simple to use. The input files generally require only the peak positions of the observed reflections and the wavelength of the source. However, indexing a pattern, especially a novel material or *in situ* at HP can be extremely challenging.

The success of indexing relies primarily on the quality of the XRD pattern and the absence or minimal presence of systematic errors. Furthermore, the peak positions must be determined as accurately as possible. This highlights the difficulties involved with high-pressure crystallographic analysis as the quality of data is lowered due to the stresses and strains acting upon the sample [149].

The programs will generally suggest a number of possible solutions for the input data from which those with the highest reliability values would be selected for further investigation. The following methodology was used to find a successful solution:

- 8 peaks are initially selected for indexing and the program provides a number of suggested solutions. Data containing impurities may be indexed as the program is able to ignore a number of Bragg reflections. However, it is very important not to accept any un-indexed peaks from the software unless the absences can be explained.

- The most stable suggestions are investigated further using lattice parameter refinement to evaluate the merit of the space group.
- During lattice parameter refinement process, all of the calculated reflections must be accounted for in the observed diffraction pattern. This is especially applicable in the low Bragg angle region where the peaks are well resolved.
- Any unobserved reflections must be accounted for. Once the unit cell is selected distinctive absences are essential in selecting a correct space group.

An extra factor to take into consideration is that when synthesising novel materials, the difficulty that arises from *ab initio* indexing is that the space group selection only is proven correct once the crystal structure has been solved and refined. This means that without taking the crystallographic analysis to completion there still could be a level of uncertainty regarding the indexing solution.

2.3.6 Rietveld Method

The Rietveld method is a least-squares refinement process for the experimental data [137, 143]. The data is processed digitally and consists of a collection of numerical values intensity values, y_i, at each of several thousand equal increments of data points, i, in the pattern. In every case, the aim is to find the best least-squares fit to all the thousands of y_i's simultaneously. The purpose of the Rietveld method is to match as closely as possible a diffraction pattern simulated from a structural model to that of the observed experimental data set. There are a number of parameters available for refining simultaneously and they can be classified as either specific to each phase present or a global contribution (resulting from instrumentation etc.). The refinement process can be assumed to be optimised when the square of the differences between the intensities calculated from the structural model, $y_i(calc)$, and the observed intensities of the diffraction data, $y_i(obs)$, are minimised. This can be expressed as follows:

$$S_y = \sum_i w_i \left(y_i(obs) - y_i(calc) \right)^2$$

where:

- S_y = the least squares residual that is minimised;
- $w_i = 1/y_i$.
- $y_i(obs)$ = intensity of the observed diffraction pattern at the i^{th} step;
- $y_i(calc)$ = intensity of the calculated pattern at the point $2\theta_i$ and is given by the following formula:
-

$$y_i(calc) = s \sum_k L_k |F_k|^2 \phi(2\theta_i - 2\theta_k) P_k A + y_i(bg)$$

where:

- s is the scale factor.
- K represents the Miller indices, h k l, for a Bragg reflection.
- L_k is the Lorentz factor and also contains the polarisation and multiplicity factors.
- F_{hkl} is the structure factor of the k^{th} Bragg reflection.
- ϕ is the reflection profile function.
- P_k is the preferred orientation function.
- A is an absorption factor.
- y_i(bg) is the background function at the ith step.

With Rietveld refinement there are many parameters that can be refined and are included in the structural model. These include atomic positions, thermal and site-occupancy but there are additional parameters that arise from the instrumentation optics. The parameters that result from the instrumentation are considered global, as they are the same for that specific piece of equipment and affect mainly the peak position of the Bragg reflections and their shape. This is very useful when observing weakly scattering systems as most of these

parameters can be defined using a standard such as silicon. The parameters that are specific for each phase, present in the sample, nominally affect the intensity of the Bragg reflections and have a direct effect on the structure factor.

During refinement it is vital that the global minimum is found at the end of the procedure and to avoid any false minima. For the refinement to be successful, it is essential that the number of observations $y_i(obs)$ exceeds the number of parameters in the model that will be refined so that the model will be not be over-fitted. This can be achieved by using constraints and restraints in the crystallographic model using different software, which enables the number of parameters to be kept to a minimum. The main refinement program used in this work has been WinPLOTR which is part of the FullProf suite package.

2.3.7 R-factors

The process of Rietveld refinement is to ensure the adjustment of refinable parameters to acquire a 'best fit' between the calculated and observed patterns. It is vital that the refinement process converges to a global minimum rather than a false local minimum and that there is nothing more to gain by repeating the refinement cycles. When carrying out structural refinement it is important to monitor the quality of the fit, which can be done visually and also with the use of reliability factors, *R*-factors. There are several *R*-factors that have been taken from single-crystal crystallography and adapted for the Rietveld method.

The most significant *R*-factor with which to follow the progress of the refinement process is the weighted profile *R*-factor, R_{wp}. This is given by the following equation:

Eq. 3:

$$R_{wp} = \sqrt{\frac{\sum_i w_i \left(y_i(obs) - y_i(calc) \right)^2}{\sum_i w_i \left(y_i(obs) \right)^2}}$$

With this, the R_{wp} is the most meaningful of the *R*-factors available as the Rietveld residual is the numerator that is being minimized. This provides the most valuable method for following the progress of the refinement.

Another *R*-factor value to consider during refinement is the expected *R*-factor, R_e. This is defined as:

Eq. 4:

$$R_e = \sqrt{\frac{N-P}{\sum_i^N w_i\left(y_i(obs)\right)^2}}$$

where *N* is the number of observations, *P* is the number of parameters. This is a measure of the quality of the data collected. Variations in the value of the R_e are normally caused by the different collection times for the sample. Values for R_e can turn out to be small if the data is over collected, whilst the opposite applies when the collection time is insufficient and this leads to a large value for R_e. During the progress of the refinement R_{wp} should approach the R_e. This comparison can be used to judge the quality of a refinement that has gone to completion. This is can be interpreted as the 'goodness of fit' or χ^2 statistical value. It is defined as follows:

Eq. 5:

$$\chi^2 = \frac{R_{wp}}{R_e}$$

Ideally, this statistic should approach 1 for the best possible fit. However, a value less than 1 is regarded as being over-fitted and incorrect. In practice, a χ^2 value of 1.5 is considered very satisfactory for Rietveld refinements.

A final *R*-value to consider is the structure factor *R*-value. This is defined as:

Eq. 6:

$$R_F = \frac{\sum_{hkl}\left|F_{hkl}(obs) - F_{hkl}(calc)\right|}{\sum_{hkl}\left|F_{hkl}(obs)\right|}$$

where F_{hkl} denotes the structure factor of the *hkl* reflection. In addition to using the *R*-value it is important to observe visually how well the experimental and observed fits compare and to assess both the progression of the refinement and the final refined model structure.

2.3.8 Le Bail Method

Work carried out by Le Bail *et al.* described a method that was an iterative adaptation of the original Rietveld code [137, 138]. This incorporated an extension to obtaining estimates for observed structure-factor magnitudes to the situation where no structural model is required for refinement. What made the Le Bail method more attractive than previous refinement methods such as that described by Pawley [139], was that it was easy to code into the existing Rietveld programs. In addition, compared to the previous method described by Pawley where peak intensities are treated as least-squares parameters, the Le Bail method does not take this into account and therefore the each cycle of least-squares is carried out handling smaller matrices. The advantage of this is a fast and reliable method for converging the refinement fit. Since the assumption is taken that the structure of the system under observation is unknown and therefore no calculated structure factors exist, then the refinement code makes the assumption that all the integrated intensities are initially equal. Therefore, the Le Bail method permits the estimate of the best possible fit when there are irregularities in the profiles of a diffraction pattern. As no structural model is required it allows additional phases to be fitted where structure is not known or where texture is a problem.

2.3.9 Synchrotron Radiation

Synchrotron sources provide intense, highly collimated, high brilliance beams of light [141]. They emit an extremely high flux of photons, which is ideal for the rapid probing of light elemental systems, as reported here. The use of a monochromator on the synchrotron radiation allows the tuning and selection of the required incident photon energy. The incident beam can then be micro-focused, ideal for the microscopic size of samples involved in DAC work [51].

The range of spectroscopic analysis from synchrotron radiation is large and it has dominated as a multidisciplinary analytical tool in X-ray spectroscopy

for crystallography and structural analysis [150]. Bond lengths, sizes and atomic positioning of a system are determined by exposure to X-ray radiation from an intense electromagnetic source which covers a broad range of energies.

High-pressure DAC X-ray experiments were carried out at two different synchrotron sources: station I15 of Diamond Light Source (Didcot, UK) and station ID27 of the ESRF (Grenoble, France). An overview of both stations is provided. Interpreting the powder diffraction results from both HP and recovered ambient data is discussed in the second section of this chapter.

Synchrotron radiation refers to electromagnetic radiation which is produced by the acceleration of ultra-relativistic elementary particles (mainly electrons and positrons) along a curved trajectory [141]. The change in velocity of the particle along the curved path results in the loss of energy, which for these purposes is the emission of energy. To achieve this, charged particles are injected by a linear particle accelerator into a storage ring and are accelerated around a planar orbit, which is maintained by superconducting magnets under high vacuum (10^{-8} torr). The charged particles are introduced at very high energies and are further accelerated in the ring to energies ranging from 1–9 GeV. Storage rings are not truly circular in shape but consist of small curved sections of non-magnetic tubes connected by straight sections. Magnets are located on the curved path, where the synchrotron radiation is emitted tangential to these curved sections. Energy loss is inevitable in the storage ring as a result of particle-particle and particle-gas molecule interactions and the electrons have a finite lifetime ranging for 2–24 hours for maintaining these high energies.

The incident X-ray beam produced hitting the sample has the energy:

Eq. 7:

$$E = h\upsilon = hc/\lambda$$

where h is Planck's constant, υ is the frequency, c is the velocity of light and λ is the wavelength.

As mentioned, synchrotron radiation is characterised by a high intensity that covers a broad and continuous range. The light emitted from the acceleration of the electrons (or positrons) along a curved path is given by the relativistic approximation [151]:

Eq. 8:

$$\Delta E = [4\pi e^2/3R]\,[E/mc^2]^4$$

where e, E and m are the particle charge, energy and mass respectively and R is the curvature radius of the particle trajectory [150]. The total intensity emitted is proportional to ΔE and the current of the particle beam in the storage ring. The equation above implies that the energy emitted is inversely proportional to the mass and therefore greater for particles of smaller size.

2.3.10 Insertion Devices

Diamond anvil cell experiments have very small sample volumes and so for high energy dispersion scattering on beam lines a very high brilliance is required for high spatial resolution [51]. Here brilliance is defined as flux emitted per unit of source area and per unit of solid angle. Experiments carried out in this field are often concerned with a narrow bandwidth of radiation and also a high flux and small geometrical divergence which result in exceptional brilliance [141] . The size of the geometrical divergence comes from the high collimation from the synchrotron radiation which is a natural phenomenon caused by relativistic effects. In order to achieve the orders of brilliance required (10^{17}, 10^{18} photons/s/mm^2/mrad^2/0.1%bw) [152], conventional bending magnets are bolstered with wigglers [153] or undulator magnets [154]. These are placed in the straight section of the storage ring between the bending magnets and shift the synchrotron radiation to higher photon energy. Undulators have two rows of magnets set up to create fields of alternating polarity perpendicular of the electron beam. This leads to the electrons following a sinusoidal trajectory, resulting in overall flux enhancement from the increased oscillations of the electrons [141]. The radiation produced in an undulator is very intense and concentrated in narrow energy bands in the spectrum (FIG. 22). A monochromatic beam can be selected using a silicon (111) monochromator and focused using crystals or mirrors.

Wiggler magnets often have a broader spectrum (FIG. 22) of radiation then those of undulator magnets and are based on a Halbach array arrangement. This specific arrangement of permanent magnets allows the magnetic flux to

reinforce itself on one side of the plane of the device while cancelling the field to near zero on the other side. This is a result of having the magnetized components $\pi/2$ out of phase with each other and it occurs for any magnetized system [155]. The obvious advantage of this set up is the ability to double the field in the preferred side of a device and to assist greatly with field confinement in giant structures such as synchrotron rings.

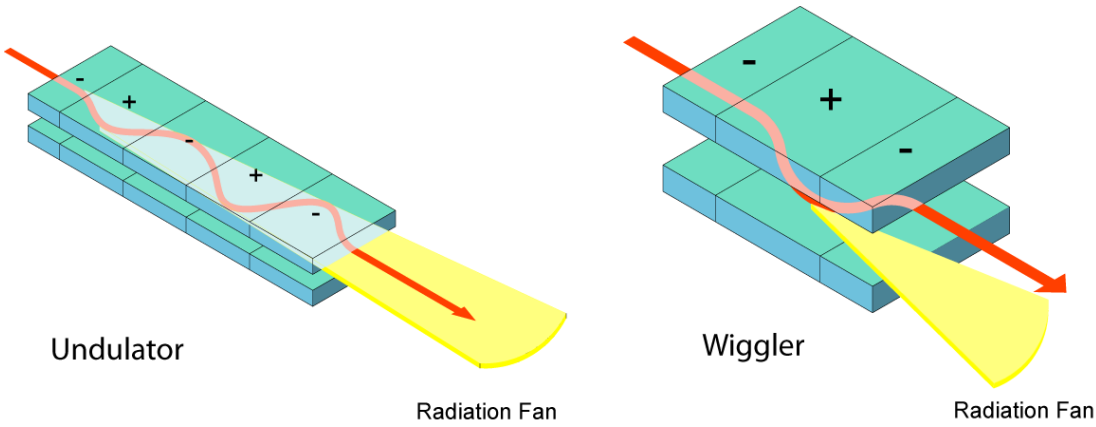

FIG. 21: Schematic representation of two insertion devices. The undulator consists of an array of 20 to 30 magnets with alternating low field magnetic poles. This leads to an alternating series of inward and outward electron accelerations that can be described as "undulations". This arrangement of alternating magnets leads to the individual radiation emission from each pole. A simple description of a wiggler is one of three magnets arranged with the outer two magnets having opposing magnetic fields to that of the central magnet. The arrangement of magnets bends the electron path out and back into the original path that could be described as a "wiggle". This device incorporates the use of a very powerful magnet, usually a super-conducting magnet, with the HP station at station I15 having a 3.5 T wiggler device.

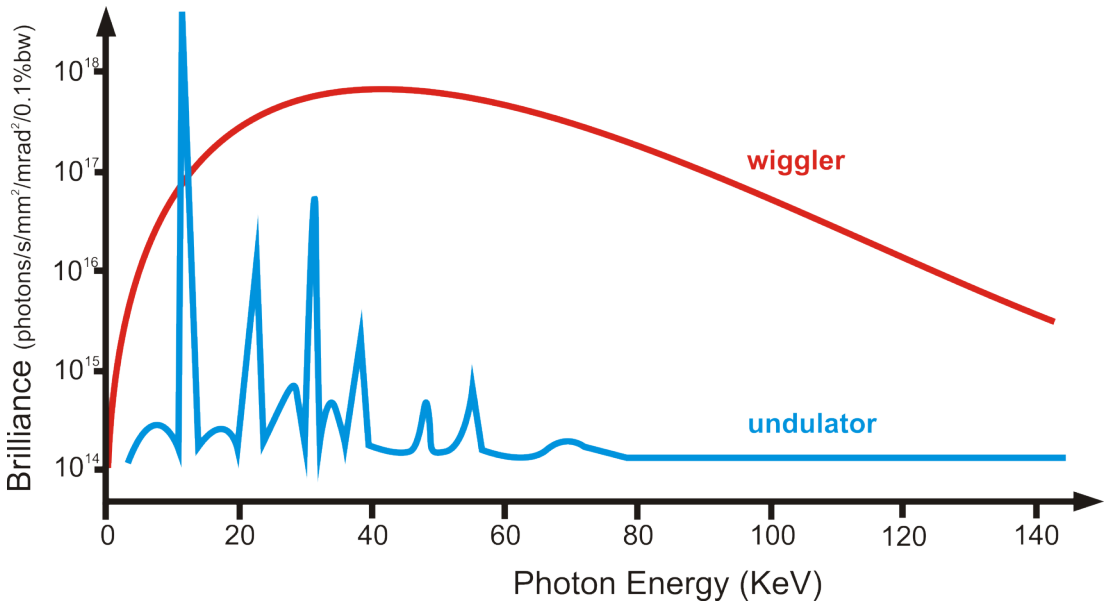

FIG. 22: A comparison of the energy spectra produced by an undulator insertion device and that of a wiggler insertion device.

2.3.11 ID27 - ESRF

The demand for a new beamline dedicated to high-pressure research [154, 156] at the ESRF lead to the design and instalment of a new instrument, station ID27. The previous station ID30 which although optimised for high-pressure research was initially established for polychromatic XRD [157]. Station ID30 had 3 insertion devices providing a X-ray source, two undulator magnets which provided a high photon flux in the low energy domain (<30 KeV) and a wiggler magnet which provided a flat white-beam energy spectrum up to 100 KeV. The need for a high-energy monochromatic beamline lead to an upgrade to a specialised station designed and built specifically for research based on the extreme conditions field. The new instrument was installed with two small-gap in-vacuum undulator magnets which provide a high-energy monochromatic X-ray source (FIG. 22). The monochromatic beam is tuned by a Si (111) monochromator and is focused using multilayer mirrors. The set-up at ID27 allows the incident X-ray beam to be focused to 2 x 3 μm which is ideal for examining the sample area inside the DAC. This also allows the sample chamber to be mapped, treating the area under observation as a mesh and scanning points on a virtual grid.

The detection of X-rays at the beamline is carried out either a MAR CCD detector or a MAR345 image plate. The introduction of the CCD detector onto the beamline along with the high flux of photons has allowed for the rapid collection of data at a rate of nearly one second a data point. This has been very important in the analysis of the weakly scattering samples presented in this work. With respect to the $C_6N_9H_3$.HCl sample, data collection previously at station 9.5 of the SRS would take up to five hours of exposure time to collect one good diffraction pattern at pressure, whilst at ID27 this would take only a maximum of five minutes.

The set-up of ID27 has also incorporated laser heating on the beamline [109] along with XRD data collection [158, 159]. The instalment of two high-power diode pumped Nd:YAG IR lasers on the optical bench provides a crystallographic probe for monitoring H-P H-T experiments (FIG. 23). The station also provides a method of measuring temperatures inside the DAC during LH, providing a state-of-the-art instrument for extreme conditions research.

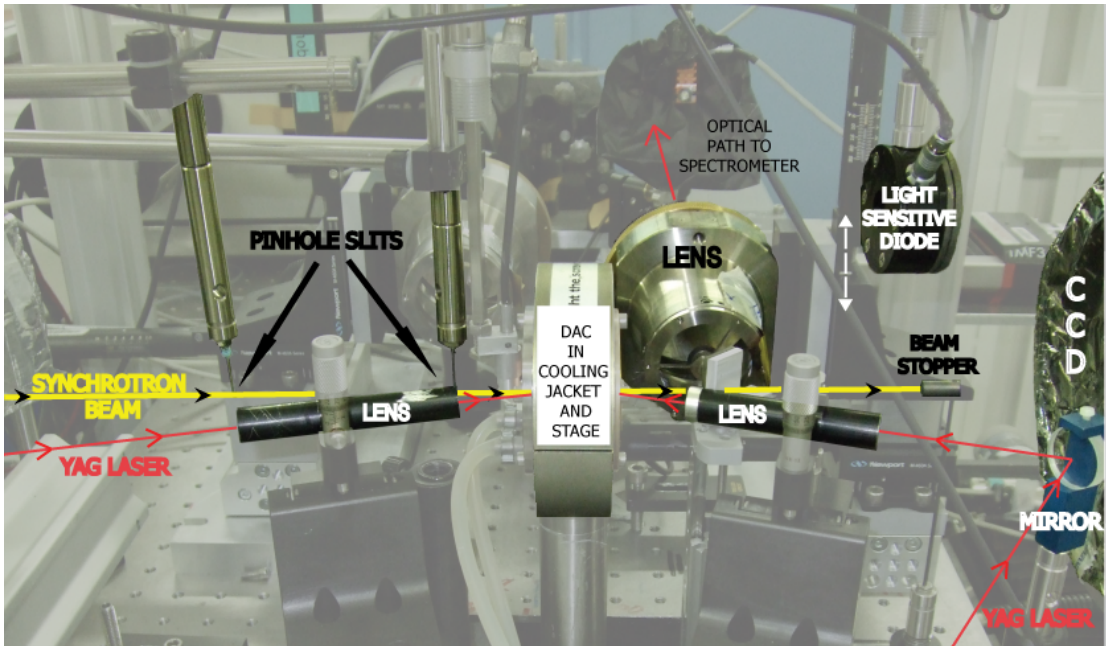

FIG. 23: An image of the optical bench of the high-pressure beamline ID27 of the ESRF.

2.3.12 I15 – DLS

Diamond Light Source is the new UK Synchrotron Source. It is a third generation facility which was designed and built to replace the 'first' second generation synchrotron source, Synchrotron Radiation Source, at the Daresbury Laboratory [160]. It has a dedicated extreme conditions beamline, I15, which provides a high-energy, micro-focused beam ideal for high-pressure experiments. Diamond was opened to users in January 2007 and so is a relatively new facility, which is currently working hard to become a world leading large-scale facility. The high-pressure beamline I15 has a wiggler magnet as its insertion device that provides a wide energy range of 20–80 keV (FIG. 22). The use of the wiggler magnet allows for the option of carrying out white beam experiments at the beamline, however a silicon (111) double crystal monochromator is used to provide a monochromatic beam for the HP experiments. Currently they have Kirkpatrick-Baez Mirrors (vertical and horizontal focusing) in place to focus the radiation beam down to a spot size of ~70 μm after which a collimator is used to further reduce it to a 30 μm size. Currently, using beam energy greater than 30 keV requires a non-collimated beam as the X-rays become transparent to the collimating tube at these high energies. The use of the wiggler insertion device provides a flux at 50 keV of 10^9 ph/s. At a time at which these experiments were carried out, only a MAR345 image plate was available to users, although the option of using an Oxford Diffraction CCD detector should be available soon.

3 Results and Discussion

3.1 Tetrahedrally Bonded Dense C_2N_3H

3.1.1 Introduction

The first of the two C-N-H systems presented in this thesis is C_2N_3H, a new carbon nitride imide material, synthesised at H-P H-T from the molecular precursor, dicyandiamide (DCDA: $C_2N_4H_4$). Work in systems with a high carbon to nitrogen ratio extends from theoretical predictions that the sp^3-bonded forms of carbon nitride with stoichiometry C_3N_4 might be superhard [20, 21]. Since then there has been intense interest in developing novel high-density materials within the C-N-H system. The proposed properties of these types of materials extend to applications for energy storage because of their potential photocatalytic properties [18]. Analogous compounds with X_3N_4 stoichiometry include refractory ceramics based on Si_3N_4 [161] and Ga, Ge containing nitrides that provide wide bandgap materials for optoelectronics and blue UV laser applications [162]. H-P H-T synthesis experiments have resulted in novel cubic spinel-structured forms of Si_3N_4 by using a nitrogen PTM which acts as a reactant, coupling with the silicon sample [119]. Also Ga_3O_3N [163, 164] has been synthesised using H-P H-T and both systems exhibit low compressibility, high hardness and are wide bandgaps. A range of synthesis routes in the DAC is possible, either by direct synthesis from the elements or using molecular precursors treated under H-P H-T conditions. Various dense C_xN_y and $C_xN_yH_z$ materials up to date have been produced using physical or chemical vapour deposition methods but their structure, properties and chemical composition have not yet been fully determined [165-167].

Horvath-Bordon *et al.* [168] recently reported synthesis of a new solid state compound C_2N_3H prepared from the molecular precursor dicyandiamide in a laser-heated diamond anvil cell (LH-DAC) at P >27 GPa and T~1800 K. The new material could be recovered to ambient conditions. Several grains were studied by electron energy loss spectroscopy in the TEM along with nano-SIMS to determine the chemical composition and show that C and N were tetrahedrally

bonded with sp^3 hybridisation. The structure was investigated using electron diffraction. The results combined with density functional theory (DFT) predictions indicated the structure was of a defective wurtzite (dwur) type as found in Si_2N_2O, $Si_2N_2(NH)$ (i.e., Si_2N_3H). The structure of dwur-C_2N_3H is related to a tripled $\sqrt{3}x\sqrt{3}$ cell of hexagonal C-lonsdaleite. N atoms occupy one set of tetrahedral sites and tetrahedral C atoms fill 2/3 of the other sublattice. The remaining positions are filled with H atoms bound to N (FIG. 24). In the present work we have obtained new X-ray diffraction data in the DAC at high-pressure and during decompression that confirm the structural model. The dwur-C_2N_3H synthesized at pressure is fully recoverable to ambient conditions. The carbon nitride imide is synthesised from dicyandiamide ($C_2N_4H_4$) by laser heating in a diamond anvil cell at 45 GPa. Through synchrotron X-ray scattering experiments it is confirmed that C_2N_3H ($Cmc2_1$) is synthesised above pressures of 30 GPa and has a bulk modulus of 258±21 GPa. Metastable phases identified during intermediate stages of the synthesis and subsequent decompression suggests the existence of further new dense compounds within the C-N-H system. The successful synthesis of C_2N_3H also implies a possible formation route to the predicted superhard material C_3N_4, which is discussed in detail.

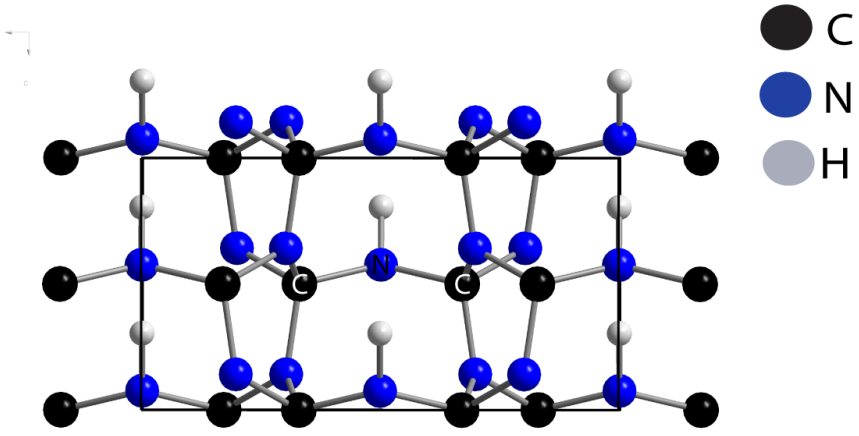

FIG. 24: Defective wurtzite structure of C_2N_3H

3.1.2 Experimental Techniques

Dicyandiamide ($C_2N_4H_4$: Aldrich**,** 99%) was loaded under O_2/H_2O-free conditions into cylindrical DACs using either sodium chloride (NaCl) or lithium fluoride (LiF) as a pressure-transmitting medium (PTM) and to provide thermal insulation to the diamond windows during laser heating experiments. We found no evidence for reactions occurring between the C-N-H phases and the PTM during synthesis experiments. Rhenium gaskets were pre-indented to 30 μm with 100 μm holes drilled by electro-erosion and used to contain the samples. Pressures were determined by ruby fluorescence [85].

The pressure was raised initially to 30-45 GPa and samples were heated to T~2500-2800 K using either a 150 W CO_2 laser (10.6 μm) at UCL or a Nd:YAG laser (1.064 nm) at ESRF. Tests using Nd:YAG laser heating were also conducted at UCL prior to the synchrotron runs. For Nd:YAG LH-DAC experiments Re powder was mixed with the sample (1:100 ratio) to couple with the near-IR laser beam. XRD experiments were carried out at beamline I15 of Diamond Light Source (Didcot, UK: λ = 0.350714 Å) and at ID27 of the ESRF (Grenoble, France: λ = 0.26473 Å). Some preliminary studies were also carried out at station 9.5 of the SRS (Daresbury, UK: λ = 0.443970 Å) [160]. Diffraction patterns were recorded as 2-D angle-dispersive data sets using MAR image plate or CCD detectors: the data were transformed to intensity *vs* wavelength/energy/d-value spectra and analysed using Fit2D [169] and FullProf [170] software packages. Raman spectra were obtained at UCL with 514.5 nm Ar^+ laser excitation using a home-built high-throughput optical system based on Kaiser supernotch filters, an Acton spectrograph and LN_2 cooled back-thinned CCD detector [164]. Bulk moduli and their first derivatives were obtained from the E(V) results using a third-order Birch-Murnaghan equation of state. Simulated XRD patterns were created using PowderCell [171].

3.1.3 Results

3.1.3.1 X-ray Diffraction

The initial challenge facing this project was to determine whether Hovarth *et al.* had reported the correct structural model of a defective wurtzite structure for C_2N_3H and whether the material being synthesised at HP was the same as the recovered sample. A range of different loadings were attempted in the glove box using NaCl and LiF PTMs as well as attempting indirect LH using Re powder mixed with the DCDA precursor with Nd:YAG double sided heating. The procedure was fine tuned in the laboratory and found to be more successful at pressures and temperatures higher than those reported previously of 27 GPa and 1800 K. In fact the synthesis procedure was very harsh and consecutive 15 mins periods of LH were required for a successful transformation. Early on in the synthesis setup it was noted that the previous work by Hovarth *et al.* had actually reported a mixed phase at pressure of which they had recovered the stable phase to ambient conditions.

The preliminary studies thus indicated that several C-N-H phases might coexist metastably within the sample following initial heating and that either prolonged heating (>15 mins) or several consecutive laser heating runs were necessary to fully convert the material to a single phase, FIG. 25 patterns (2) and (1) respectively. Those preliminary findings are confirmed in this study and the results are discussed in more detailed by using Raman spectroscopy.

Another major challenge was that Horvath *et al.* had reported the recovery of C_2N_3H single crystals measuring one micron in length. The set up for these experiments was for HPHT synthesis and the backing plates selected were with a tight aperture (55°) and so the data window was too small for single crystal XRD: furthermore, it was important to not only be able to convert the DCDA into the fully transformed dwur-structure but also to be able to collect good, reliable powder diffraction data by synthesising a number of crystals in a small region and specifically in the case of data collection at ID27, using the 2x3 um beams to collect powder diffraction data (FIG. 26). To improve the statistical quality of data collected and minimise any preferred orientation of the crystallite material the stage was rocked in the kphi axis by 2 degrees in both directions at a rate of 2 degrees a second throughout the data collection.

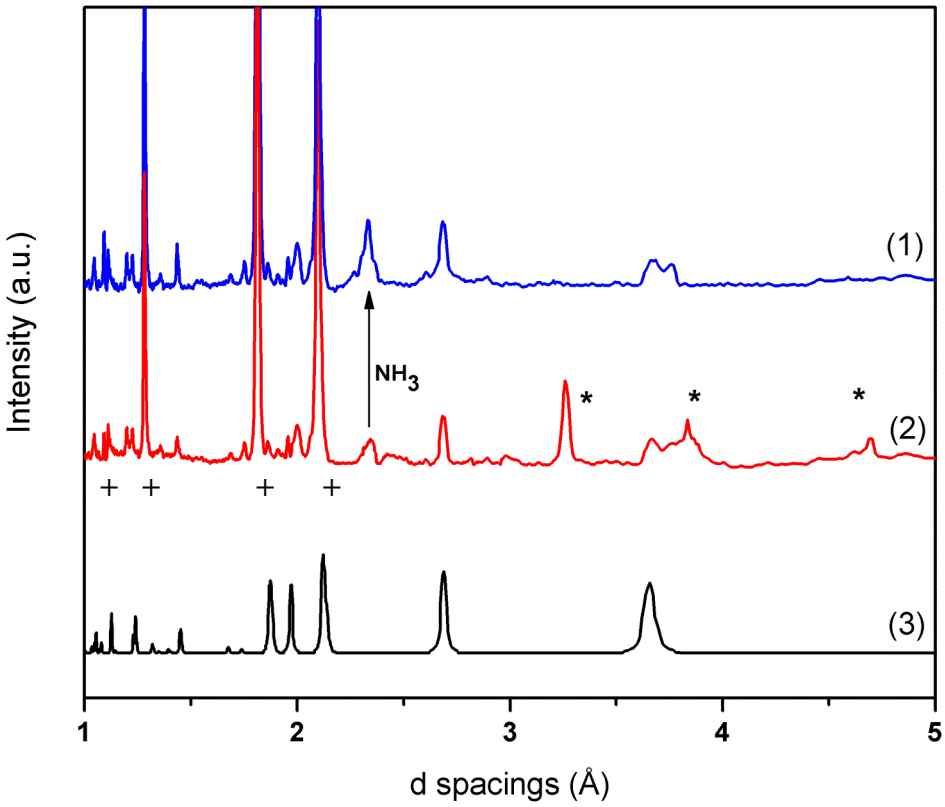

FIG. 25: XRD patterns obtained at 45 GPa following LH-DAC synthesis of dwur-C_2N_3H from DCDA. Pattern (1) obtained after extended heating and pattern (2) is captured beforehand during the initial heating period. Additional peaks (*) correspond to an unidentified new C-N-H metastable phase formed during the initial synthesis reaction. The main peak of NH_3-III is identified in both experimental patterns and is a by-product of the synthesis reaction; $C_2N_4H_4 = C_2N_3H + NH_3$. (3) Corresponding calculated pattern (DFT) at 45 GPa. [(+) indicate Bragg peaks from LiF, used as PTM].

We were able to obtain X-ray diffraction patterns for samples synthesised from the DCDA precursor in the DAC at pressures ranging from 30-45 GPa following laser heating at UCL (Diamond) and also *in situ* during laser heating experiments combined with synchrotron XRD at ESRF. Following prolonged heating in the DAC, an X-ray diffraction pattern was obtained that could be fully assigned to dwur-C_2N_3H (FIG. 25 (1)) in agreement with the structure suggested previously from electron diffraction and DFT calculations (FIG. 25 (3)) [168].

Identification of nearly the full set of predicted diffraction peaks was made possible by combining data from several runs carried out using both NaCl

and LiF PTM, as well as measurements carried out in the DAC during decompression (FIG. 27a) and at ambient pressure following recovery (FIG. 27b, TABLE 3).

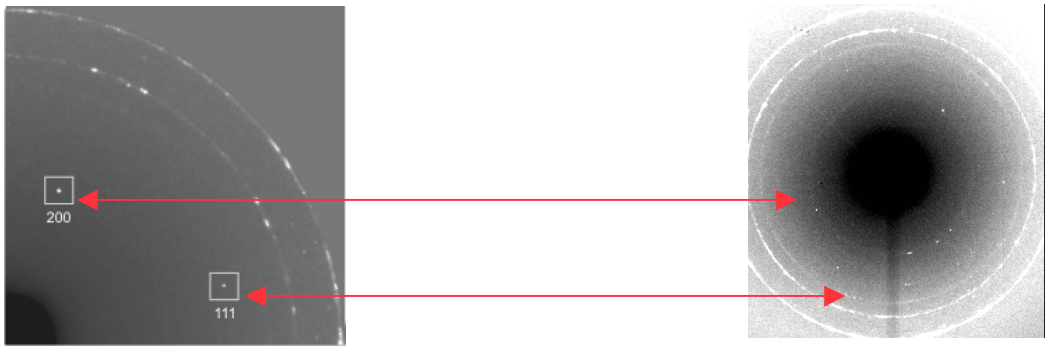

(a) Single crystal diffraction of C_2N_3H (b) Powder diffraction of C_2N_3H

FIG. 26: Debye-Scherrer diffraction patterns taken in situ at 45 GPa during LH at ID27 (a) This pattern is taken during the end of a 10 minute heating session. The single crystal diffraction spots are identified as belonging to the (200) and (111) reflections of the dwur-C_2N_3H. (b) This pattern is taken after four 10 minute LH sessions. By moving the LH spots around a small region it is possible to attain a powder diffraction pattern. This extended heating was potentially very dangerous for the diamond anvils in use and a very careful loading is required. [The two distinct outer Debeye rings in both patterns are of the LiF PTM].

Following LH-DAC synthesis of the sample at 45 GPa X-ray diffraction patterns were recorded during decompression to ambient conditions. Approximately twenty of the predicted reflections could be followed throughout the decompression process (FIG. 27). That result confirms that the dwur-C_2N_3H phase produced by laser-heating in the DAC from DCDA precursor is fully recoverable to ambient conditions, that no decomposition or phase transitions occur during decompression, and thus that it has the chemical composition and structure deduced from electron diffraction, EELS and nano-SIMS experiments on recovered materials combined with DFT predictions [168]. This then constitutes a new high-density tetrahedrally-bonded material produced in the C-N-H system that might have interesting and useful properties in its own right, as well as providing a potential precursor to dense carbon nitride phases.

The choice of PTM was an important issue for the X-ray diffraction experiments. NaCl has been well tested for LH-DAC experiments but it has strong diffraction lines that mask some of the key reflections of the C_2N_3H phase. The situation is further complicated by the B1-B2 transition that occurs at P ~27 GPa but with considerable hysteresis during decompression [78]. LiF is less well established as a PTM for LH-DAC synthesis studies: however, we found it performed well during these experiments and its use enabled us to complete the set of diffraction data observed for C_2N_3H. In addition, the choice of NaCl as a PTM made collecting refinement quality data very difficult. The main (111) reflection is obscured by the hkl peaks of the NaCl and the shoulder of (200) hkl is not seen. Not only are the three main peaks not seen or poorly defined but the remaining peaks are of too low intensity when compared to the dominating peaks generated by the NaCl.

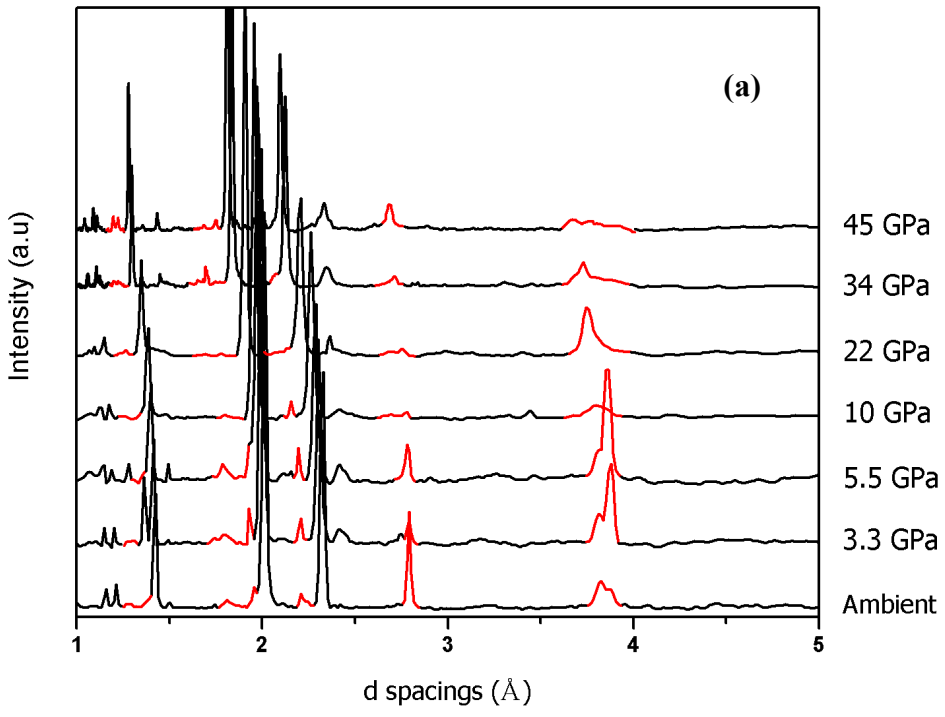

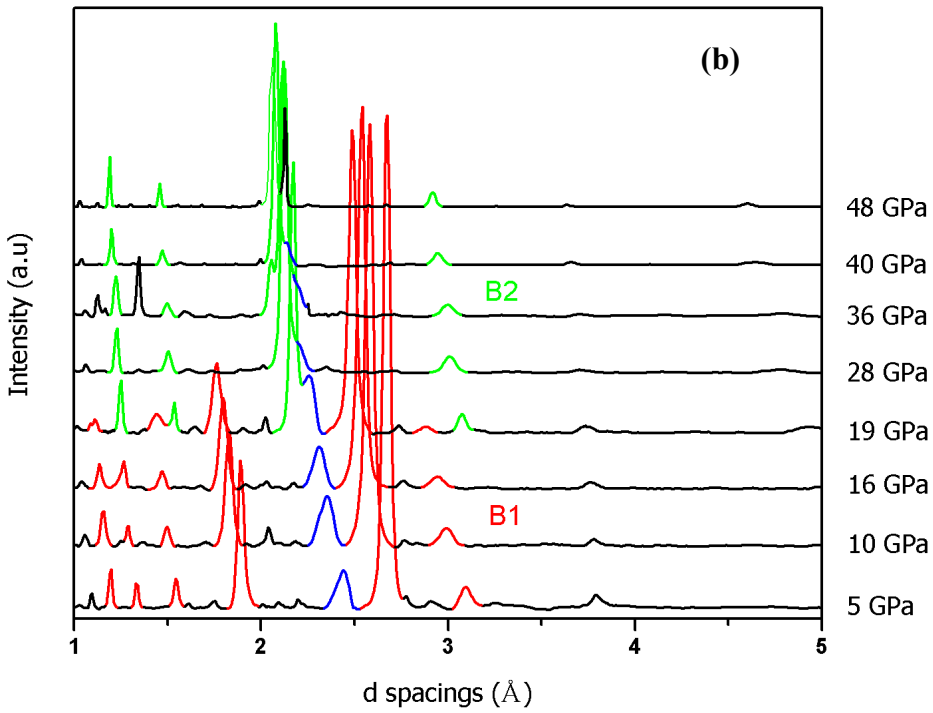

FIG. 27: XRD pattern obtained during decompression following LH synthesis of DCDA in the DAC at pressure to ambient P,T conditions using either LiF or NaCl as PTM. (a) Pattern collected at ID27 using LiF as PTM. The regions and peaks highlighted in red have been assigned to dwur-C_2N_3H. (b) This Pattern was collected at I15 using NaCl as the PTM. The peaks dominating the pattern belongs to the presence of the NaCl and both the B1 and B2 phase are highlighted, in red and green respectively. The presence of ammonia is also highlighted in blue and its principal broad peak at 2.3 Å could be followed during decompression down to ~5 GPa.

3.1.3.2 Ambient Conditions

In recovering the dwur-C_2N_3H material to ambient conditions the initial question to be answered was whether the recovered ambient sample of the C_2N_3H was in agreement with theoretical structural model and refinement could be carried out successfully. The carbon nitride imide material was recovered using both choices of PTM, NaCl and LiF, and just as in the decompression data analysis the results with NaCl present were not as useful as those containing LiF PTM. The relative intensities of the NaCl are dominating and covers most of the Bragg peaks owing to the sample. Interestingly, the synthesis experiments with NaCl as PTM also appeared to result in crystalline dwur-C_2N_3H with highly

preferred orientation, resulting in the apparent disappearance of certain peaks from the pattern, e.g., the (110) reflection near 3.8 Å (FIG. 28).

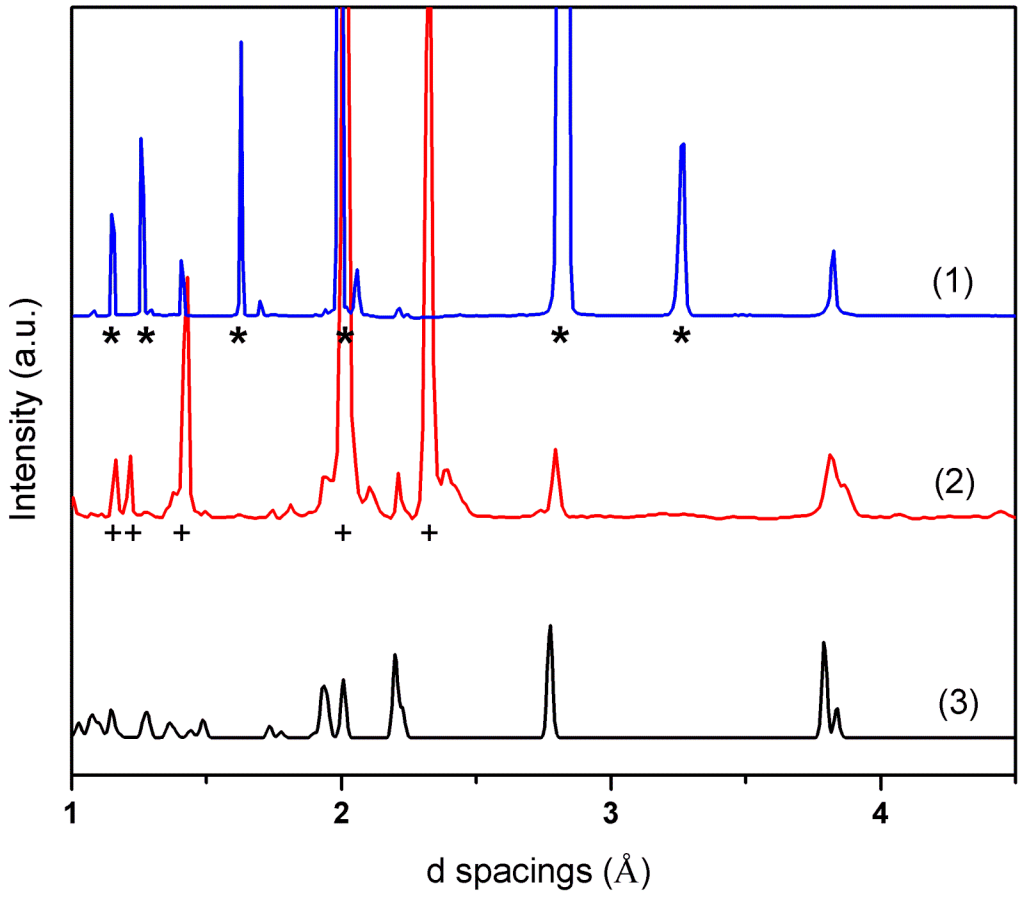

FIG. 28: Experimental and theoretically predicted XRD patterns for dwur- C_2N_3H at ambient conditions. (1) Ambient-pressure XRD pattern of C_2N_3H recorded at I15 (Diamond) following LH-DAC synthesis. (*) indicate Braggs peaks from NaCl as PTM. (2) Ambient-pressure XRD pattern of C_2N_3H recorded at ID27 (ESRF) following LH-DAC synthesis. (+) indicate Bragg peaks from LiF used as PTM (3) Predicted pattern for dwur-C_2N_3H at ambient P,T conditions from DFT calculations.

Attention was therefore focused on the recovered sample with LiF as PTM which (FIG. 28 (2)) shows to be overall a much better XRD pattern with nearly all reflections observable and the relative intensities of sample to PTM comparable. The reflection of the (110) plane is observed as a shoulder and the dominant (111) reflection is not obscured. The refinement procedure here started off by simulating an ambient pattern of LiF using PowderCell and identifying all the peaks in the pattern resulting from the PTM. Having identified the peaks, the positions were then indexed to confirm the space group

(*Fm*3*m*) and the cation and anion were inputted to the special positions as required by the space group (TABLE 2).

Lattice Parameters	*a* (Å)	*b* (Å)	*c* (Å)
	4.049 (1)	4.049 (1)	4.049 (1)
Fractional Coordinates	*x*	*y*	*z*
Li	0	0	0
F	0.5	0.5	0.5

TABLE 2: Lattice parameters and refined fractional coordinates of LiF (*Fm*3*m*)

Rietveld refinement was carried out for the LiF and from this also the zero shift error of the pattern was determined and then fixed. Having fitted the LiF with a R_{wp} value of 1.98 which is very respectable the peaks associated with the recovered sample were then indexed. Using the simulated pattern as predicted with DFT it was possible to assign and exclude broad peaks that were believed to belong to unconverted DCDA precursor. An orthorhombic unit cell was identified with the highest merit of figure using the program CRYSFIRE, which agreed with the DFT predictions. Following this the lattice parameters of the ambient structure were determined by Le Bail refinement: a = 7.618 (5) Å, b = 4.483 (2) Å, c = 4.038 (1) Å (V_o= 137.904 (8) Å^3) within space group $Cmc2_1$ which were in excellent agreement with DFT predictions (TABLE 4) and with a R_{wp} value of 3.45.

Having determined the unit cell parameters of the dwur-C_2N_3H the next step was to carryout a structural refinement of the ambient XRD pattern. The structural model provided by both the initial DFT calculations [168] and the most recent calculations done by our group [172] confirm the carbon and nitrogen atoms in the special positions as determined by the space group. With this piece of information the atomic positions of the carbon atom and one of the nitrogen were both inputted with a multiplicity and a Wyckoff letter of 8b respectively and starting positions of 0.3 for each of the three coordinates. The second nitrogen was inputted with a multiplicity and a Wyckoff letter of 4a and starting positions for y and z coordinates also at 0.3. The R_{wp} value of 5.72 and χ^2 of 25.1 was given for the Rietveld refinement which is very good for a sample synthesised at pressure and recovered with the presence of PTM and

unconverted precursor. For determining the R_{wp} value the areas with unaccounted broad peaks were excluded from the regions of interest as to improve of the fit between observed and calculated.

hkl	$d_{\_theor}$ (A)	$I_{\_theor}$	$d_{\_obs}$ (A)	$I_{\_obs}$
110	3.8318	25	3.869	49
200	3.7864	81	3.808	91
111	2.7682	100	2.780	100
020	2.2213	27	2.246	28
310	2.1947	78	2.210	65
002	2.0018	57	2.008	48
021	1.9423	34	1.960	54
311	1.9245	44	1.936	59
211	1.7282	12	1.743	12
022	1.4870	8	1.497	11
312	1.4790	13	1.487	6
330	1.2773	24	1.290	18
600	1.2621	10	1.269	9

TABLE 3: The crystal structure of dwur-C_2N_3H at ambient conditions. The thirteen most intense reflections, that are possible to follow throughout decompression, are noted.

Lattice Parameters	a (Å)	b (Å)	c (Å)
	7.618 (5)	4.483 (2)	4.038 (1)
Fractional Coordinates	*x*	*y*	*z*
C	0.325 (3)	0.328 (3)	0
N1	0.310 (1)	0.364 (4)	0.358 (2)
N2	0	0.285 (3)	0.422 (4)
Lattice Parameters	a (Å)	b (Å)	c (Å)
	7.573	4.443	4.004
Fractional Coordinates	*X*	*y*	*z*
C	0.330	0.340	0
N1	0.302	0.365	0.358
N2	0	0.285	0.424

TABLE 4. Lattice parameters and refined fractional coordinates of dwur-C_2N_3H ($Cmc2_1$) at ambient conditions. (top) Experimental and (bottom) theoretical values.

The atomic positions as determined by the Rietveld refinement are shown below and are in excellent agreement with that of the calculated DFT values. This confirms that the recovered sample of the new material does have a defective wurtzite structure and combined with the decompression data, which confirms that this is the structure that is formed at pressure and is recoverable as the same phase to ambient.

	Angle [°]			Distance [Å]	
	Experimental	DFT		Experimental	DFT
N1-C-N1	107.74 (2)	107.32	C-N1	1.46 (1)	1.45
	109.84 (2)	108.11		1.50 (1)	1.46
	110.74 (1)	109.84			
			C-N2	1.46 (2)	1.43
N1-C-N2	108.88 (3)	113.15			
C-N1-C	112.31 (1)	115.7			
	116.54 (1)	116.19			
	118.31 (1)	120.37			
C-N2-C	131.79 (2)	127.78			

TABLE 5: Selected interatomic distances and angles of dwur-C_2N_3H from the Rietveld analysis of the structural solution from the experimental results and values from the theoretical models calculated at UCL.

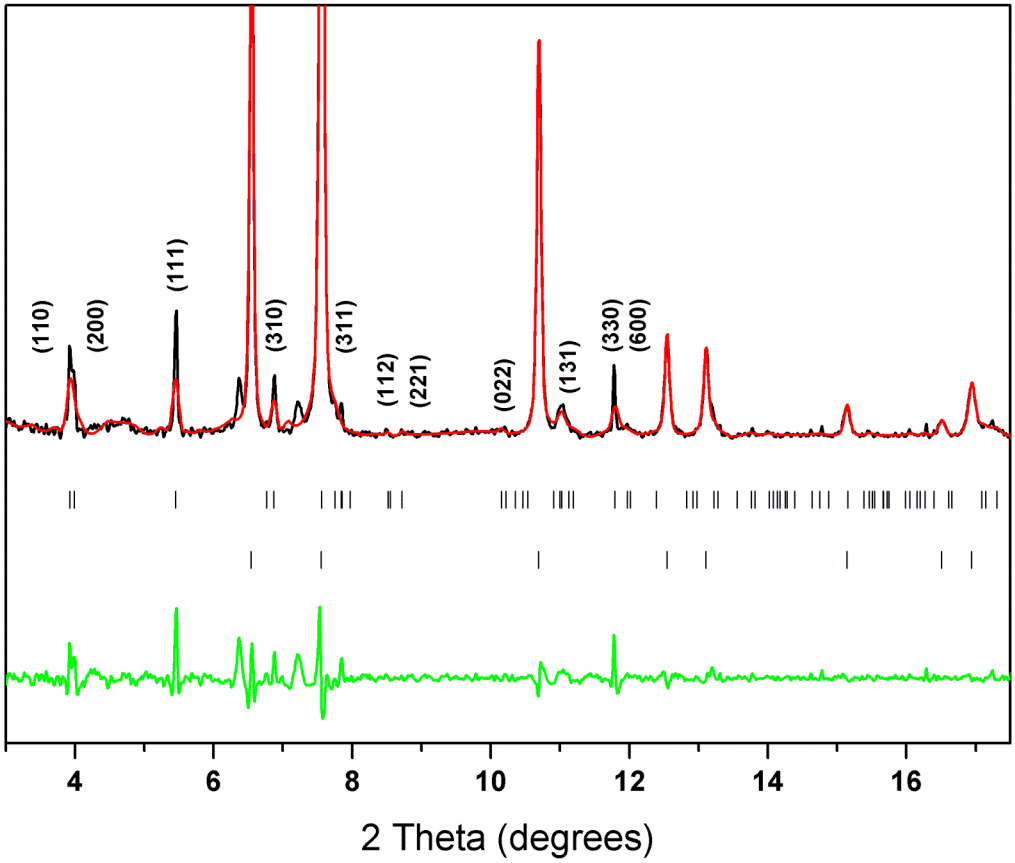

FIG. 29: A Rietveld refined X-ray diffraction profile of dwur-C_2N_3H at ambient conditions. The Rietveld fit is shown in red and the experimental data in black. The top set of markers identify the positions of the reflections belonging to the dwur-C_2N_3H phase and the bottom set of markers identify the reflection of the LiF, present as the PTM. The difference between the observed powder pattern and that calculated using the crystal structure is given by the green fit. The unaccounted peaks with 2θ values at 6.3 and 7.2 were not accounted for and are assigned to remnants of an intermediate phase present during the intermediate stage of synthesis.

3.1.3.3 Compressibility Measurements

The synchrotron X-ray diffraction data was used to construct a P(V) plot and evaluate the molar volume and compressibility parameters of the dwur-C_2N_3H phase. The initial attempts at extracting the volumes for given pressures lead to a P(V) plot that was describing a HP phase being synthesized at pressure and upon decompression under going a phase transition at ~20 GPa into the already accounted for dwur-structure . The Le Bail refinement was convincing

enough to assume that there was a phase transition being observed. However, this did not describe the decompression Raman work carried out on the same system by Katherine Woodhead at UCL. The spectroscopy analysis had observed a single phase being formed at high pressure and could be followed throughout the subsequent decompression to ambient conditions. This problem highlighted that the synthesis run for the XRD analysis had intermediate phases present whose reflections could not be assigned and accounted for and were affecting the refinement process.

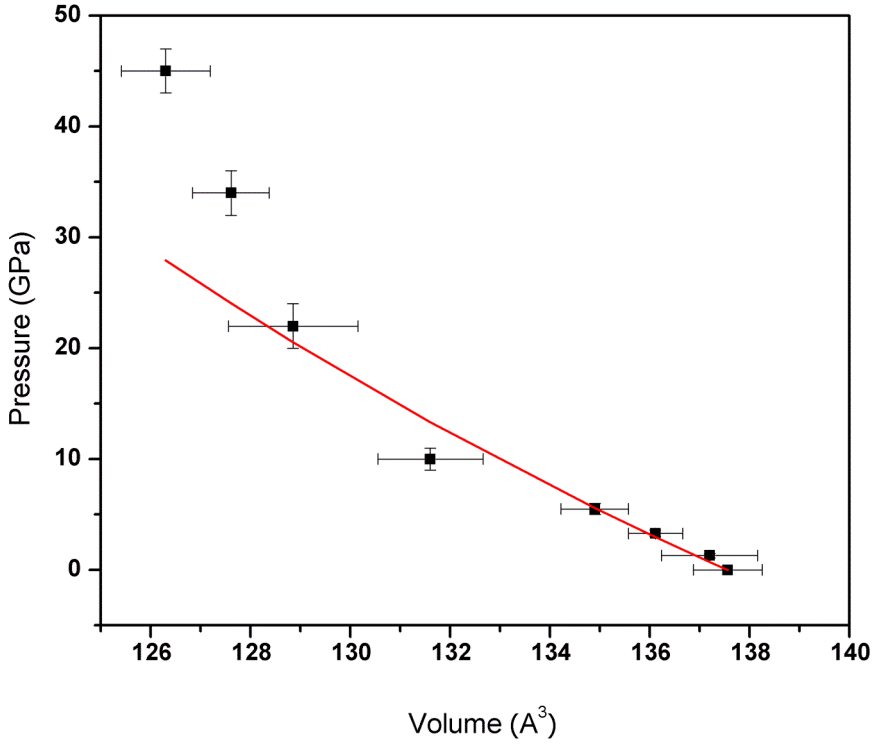

FIG. 30: The initial P(V) calculated from the XRD results. This was prior to any DFT support and the plot describes a phase transition occurring at ~20 GPa. The DFT results suggested that the ambient structure would remain as a single phase beyond the pressure ranges experimentally examined. The high-pressure data was re-indexed and re-analysed to produce the P(V) plot in FIG. 31.

Therefore additional supported was required for further understanding the formation process of the C_2N_3H structure at pressure and an understanding of its energy volume landscape. This was provided by computational work carried out by Aishia Rahman and Furio Corà at UCL. They carried out DFT calculations that showed the stability of the dwur-C_2N_3H and described a single phase formed at pressure and recoverable to ambient conditions. They did their

calculations under periodic boundary conditions using CRYSTAL06 [173] and they employed two different hybrid-exchange functionals, namely B3LYP [174] and PBE0 [175]. The advantage of doing the calculation like this means that unlike LDA, which is reliant solely on electronic density, here the hybrid functional takes a source like LDA and incorporates an exact exchange from a Hartree-Fock contribution. Therefore these hybrid functionals are expressed in terms of the Kohn-Sham orbitals and not electronic density. The *ab initio* calculations confirmed the presence of a single phase describing that of the defective wurtzite structure of the C_2N_3H at HP and its recoverability to ambient conditions. With calculated unit cell parameters and atomic positions various XRD patterns were simulated allowing for peak matching with the experimental XRD decompression data. This method allowed for any anomalous peaks to be identified and removed from the area of interest during the Le Bail refinement procedure. By doing so the decompression was re-analyzed and produced a P(V) plot confirming a single phase being formed at pressure and fully recoverable to ambient conditions (FIG. 31).

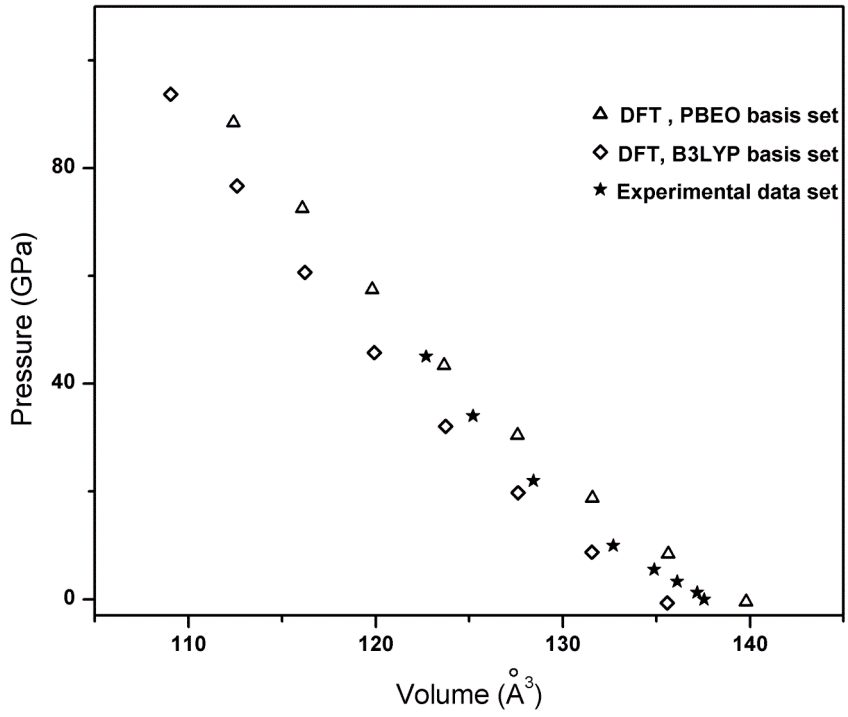

FIG. 31: P(V) plot of structure from DFT, PBEO (K_0 = 288 GPa) and B3LYP (K_0 = 270 GPa) against the experimental data (K_0 = 258 GPa).

FIG. 32 illustrates the positions of the reflections owing to the dwur-C_2N_3H throughout the decompression. The positions of the peaks are identified visually as to be independent from the refinement software. Additionally, the values are reported in d spacings as to be wavelength independent. This plot also confirms a continuity in the phase between the structure synthesized at HP and that at ambient conditions. The major difficulty with all of the compression data had been the lack of the reliable data points available though out the whole pressure range. This made following reflections closely as a function of pressure difficult, especially between 10 and 21 GPa where previously some structural change had thought to be occurring.

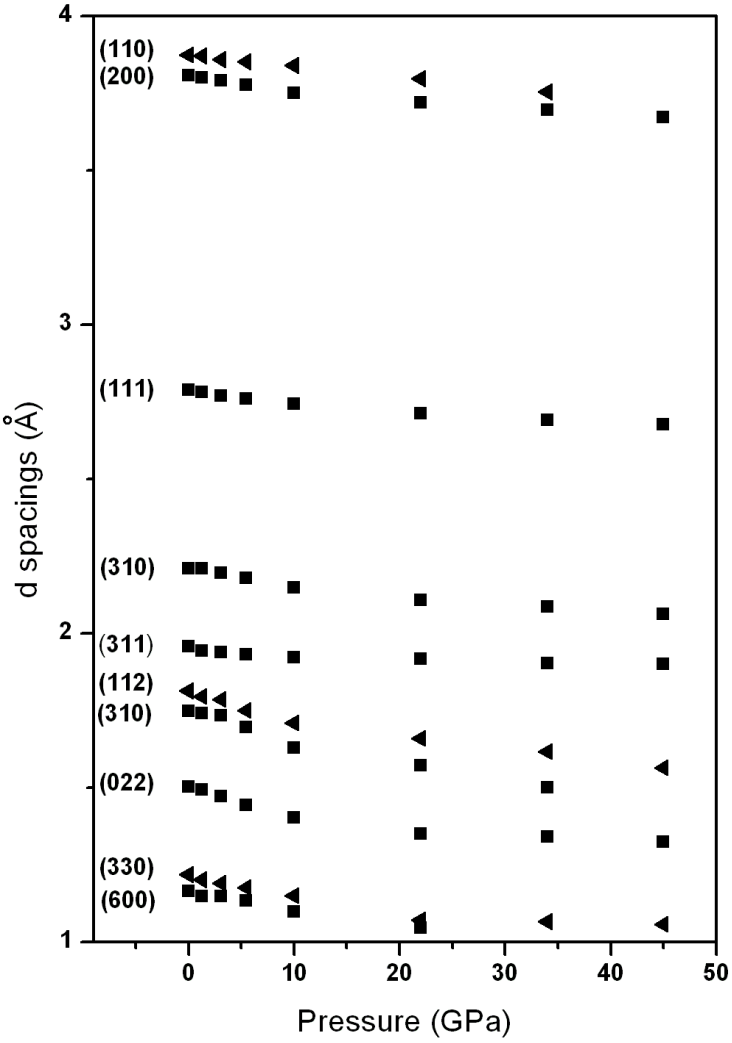

FIG. 32: d spacings versus pressure plot having identified the dwur-structure being formed at HP and recoverable as a single to ambient pressure.

Having confirmed the presence of a single phase throughout the decompression the data were analysed using a finite strain Birch-Murnaghan equation of state (EOS) expression expanded to third order [176]:

Eq. 9:

$$P(V) = 3K_0 f(1+2f)^{5/2}\left(1+\frac{3}{2}(K_0'-4)f\right)$$

Here K_0 is the zero pressure bulk modulus and K_0' its pressure derivative. Transforming the volume strain into the reduced variable:

Eq. 10:

$$f = \frac{1}{2}\left[\left(\frac{V_0}{V}\right)^{2/3} - 1\right]$$

and using a normalized pressure F defined by:

Eq. 11:

$$F = P(3f(1+2f)^{5/2})^{-1}$$

provides a linearised version of the $P(V)$ equation for useful determination of K_0 and K_0' values [177]. The data indicate a bulk modulus value K_0 = 258±21 GPa with K_0' = 6.3±0.8 in good agreement with theoretical calculations (K_0 = 271 GPa, K_0' = 3.97: B3LYP; K_0 = 288 GPa, K_0' = 3.94: PBE0). The bulk modulus for dwur-C_2N_3H is comparable with that determined for the refractory high-hardness ceramic Si_3N_4 (K_0 = 256 GPa) [161].

In using the F-f plot (FIG. 33) it is possible to observe a linear relationship, which is well adapted to least-squares fitting and error analysis of the results. The intercept as F→0 defines K_0 and the gradient of the slope determines K_0'. Within the Birch-Murnaghan third-order equation of state formulation the gradient is equal to zero K_0' is defined as 4. In fact many different classes of material have K_0' defined as 4 which conveniently cancels out the last term of the Birch- Murnaghan in Eq. 9: [177, 178]. The error analysis for the F-f plot was carried by first evaluating the error given for the volume of the unit cell at V_0 and V at various pressures using the WinPLOTR

and carrying these through a mathematical workup. The other variable present in F is that of Pressure (P) and for this a number of ruby grains where placed around the sample chamber for which three or four spots would be measured and an average as well as an estimated error would be determined.

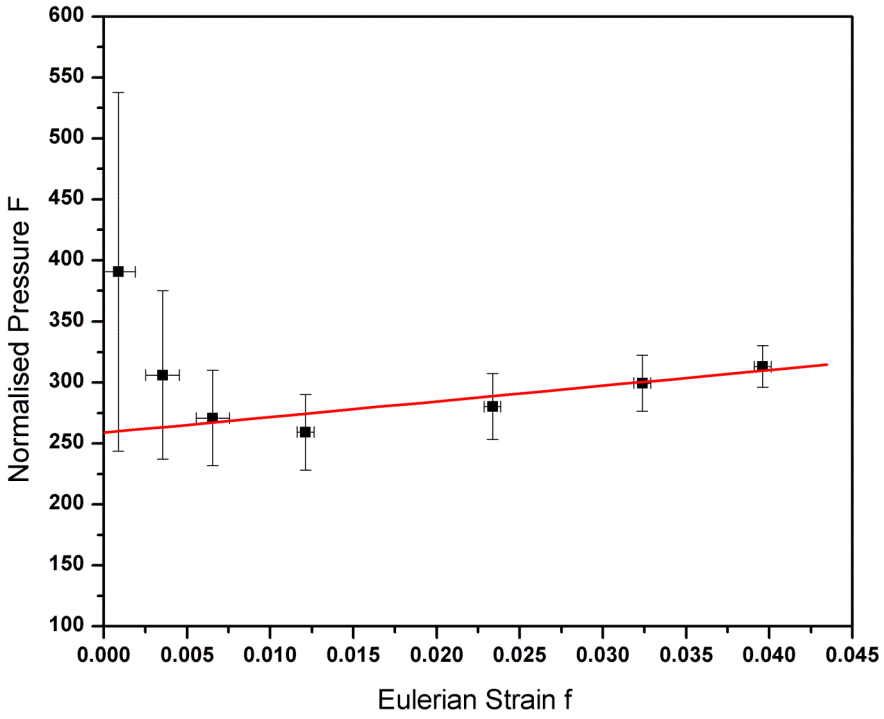

FIG. 33 Normalised pressure *vs*. Eulerian strain for the data corresponding to the final experimental P(V) data.

3.1.3.4 The High-Pressure, High-Temperature Reaction

$C_2N_4H_4 = C_2N_3H + NH_3$

Since the first report of synthesis of dwur-C_2N_3H from DCDA ($C_2N_4H_4$) by LH-DAC methods at P>27 GPa and T>1800 K it has been assumed that the reaction proceeds by elimination of NH_3 to produce the new solid-state compound. That reaction has now been confirmed by our new synchrotron X-ray results that show the appearance of solid NH_3 (phase III: $P2_12_12_1$) [179, 180] identified in the diffraction patterns at high-pressure and during decompression (FIG. 25 and FIG. 27b). During the final stages of decompression the ammonia

solid phase becomes liquid and escapes from the cell (FIG. 34). The principal broad peak of solid NH_3 at 2.3 Å could be followed during decompression down to ~5 GPa. At room temperature ammonia crystallises at 1 GPa in a rotationally disordered, face-centred-cubic phase (phase III, space group *Fm*3*m*), although we did not have decompression data to this low a pressure [181]. A first order phase transition occurs for ammonia at 4 GPa to solid IV which was first described as hexagonal close packed (hcp) by XRD experiments and later shown to actually be orthorhombic by Loveday *et al.* using neutron experiments on ND_3 [179]. It is noted that initially we had spectroscopically assigned a broad peak at 300 cm^{-1} to the formation of hydrogen as we had not been able to observe any evidence of ammonia in the Raman work, as the expected bands at 3050 and 3130 cm^{-1} were not observed during the synthesis.

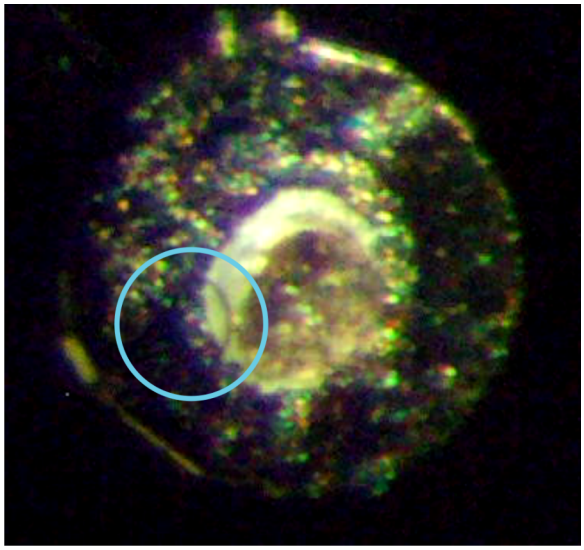

FIG. 34: An optical micrograph of the sample chamber defined by the Re gasket in the DAC following decompression to ambient conditions and as the top diamond has just been lifted to open the cell. The ring highlights a drop of liquid NH_3, formed during decompression below 1 GPa, exiting the chamber. This was produced by the dwur-C_2N_3H synthesis reaction and remained within the cell as a solid phase at high-pressure until full decompression.

3.1.4 Discussion

Observed Data by Liu		Observed Data of C_2N_3H by Salamat			Phase X
d (Å)	I/Io	d (Å)	I/Io	(hkl)	d (Å)
4.878	14				4.878
4.669	11				4.669
4.139	7	Could be the 110 relection			
3.857	20	3.808	91	200	
2.943	41				2.943
2.901	24				2.901
2.885	11				2.885
2.776	100	2.78	100	111	
2.623	80				2.623
2.526	10				2.526
2.421	33	2.246	28	020	
2.336	2				2.336
2.231	19	2.21	65	310	
2.218	15	2.008	48	002	
1.948	6	1.96	54	021	
1.815	5	1.906	16	400	
1.716	3	1.743	12	211	
1.702	2				1.702
1.665	17				1.665
1.624	22				1.624
1.541	4				1.541
1.472	17	1.4684	11	130	
0.142	3	1.4438	11	510	
0.139	2	1.3941		222	
0.131	4				0.131
0.130	6	1.29	18	330	
0.118	2	1.186	4	132	
0.110	3	1.1019	3	223	
0.109	3	1.081	8	041	

TABLE 6: A table showing the position of the diffraction peaks in d spacings and relative intensities as reported by Liu *et al.* In the original paper the proposed position of the β-C_3N_4 diffractions are compared to the experimental diffraction data accumulated from the shock experiments. Here, the position of diffraction peaks of the dwur-C_2N_3H by Salamat *et al.* are compared to the diffraction results by Liu *et al.* The remaining unaccounted peaks from the shock experiment are identified as Phase X as described by the Liu paper.

The majority of the XRD peaks observed in the dwur-C_2N_3H may be matched to those produced by Liu *et al.* [182], who claim that they have identified β-C_3N_4 during their shock experiments using DCDA. They assign the

most intense peak of their XRD data at 2.77 Å to the (200) reflection of β-C_3N_4 but do not observe the associated (100) and (110) reflections at higher d spacings. We postulate that dwur-C_2N_3H is the stable HP phase when using DCDA for the described HPHT conditions and thus it is possible that the peak they observe at 2.77 Å may be due to the (111) reflections of the dwur-C_2N_3H (TABLE 6). Additionally, many of the peaks that are assigned by Liu *et al.* as phase X may result from intermediate phases observed in this work at pressure and recovered to ambient conditions. Hence the successful synthesis and identification of a C_3N_4 polymorph still remains elusive.

A comment is made on the structural relaxation of the dwur system upon decompression. In following the peak positions in d spacings as a function of pressure (FIG. 32) between n the 21–9 GPa pressure region some slight structural relaxation must be occurring which leads to the peak positions following a different trend, from 10 GPa to ambient, then that observed for the higher pressure data sets. This is not observed in the P(V) data.

The identification of NH_3 as a major product confirms the reaction suggested above. The fact that NH_3 can be removed from the cell under ambient conditions indicates that the predicted superhard C_3N_4 phases might be accessed by the subsequent reaction:

$$3\ C_2N_3H = 2\ C_3N_4 + NH_3$$

Using the C_2N_3H as a precursor to C_3N_4 polymorphs or other C-N / C-N-H systems highlights the importance of its recovery to ambient conditions fundamental for the further synthesis of new materials using the H-P H-T procedure explained in this work. As described, the formation of ammonia is the driving kinetic force in the synthesis of C_2N_3H at pressure and any further production of the new material is limited by the amount of ammonia able to be formed. Several attempts in this work have been made in the pursuit of synthesis of C_3N_4 polymorphs using the recovered C_2N_3H material.

One method of attempting to synthesis C_3N_4 polymorphs was making C_2N_3H at elevated pressures and temperature and its recovery to ambient condition, at which point the DAC is opened and the ammonia is allowed to evaporate (this was carried out in a number of different ways from having the

cell in a oven or under vacuum or under a strong light source for a long period of time, in all cases this was done to encourage the removal of ammonia). With the ammonia removed, the cell was closed again and very slowly taken up to pressures of ~50 GPa, this was done assuming that the PTM was still isolating the sample from the diamond and LH could be carried out again on the sample. The major problems with this approach have been that the PTM does not retain its initial packing and so LH cannot be maintained for the lengths of time to observe any change. When LH had been successful the ability to identify a region where there might be new material present to be able to collect reliable data then became very challenging. Even in the case of using 2 x 3 μm synchrotron radiation beam (ID27) to identify new material, interpreting the results is very difficult; in the sample chamber there can be a number of different materials that have to be accounted for before attempting to identify any evidence of a stable new material. For refining the XRD data for such a synthesis run, all the contributions made by unconverted DCDA, intermediate phases, reaction between any remaining ammonia and any possible ammonia salts have to all be accounted for to be able to make a positive identification of the new material.

3.1.4.1 Conclusion

Using synchrotron XRD it can be concluded that heating DCDA ($C_2N_4H_4$) as a molecular precursor at high pressure produces the high-density dwur-structured compound C_2N_3H. This new C_2N_3H phase is recoverable to ambient conditions and it has a large bulk modulus comparable with high hardness silicon nitride ceramics. An unidentified new metastable C-N-H phase is also produced during the initial synthesis reaction for which further investigation would be required to identify. The synthesis process could lead to new routes to preparing bulk samples of theoretically predicted superhard C_3N_4 materials. Recently Liu *et al.* identified XRD lines that they assigned to the theoretically predicted phase β-C_3N_4 among the products of their shock synthesis experiments using DCDA as a precursor. Our results indicate that the XRD pattern obtained by Liu *et al.* likely corresponds mainly to dwur- C_2N_3H along with some intermediate phases produced by high-P, T shock synthesis.

3.2 Potential Other Phases in the C-N-H Systems: Results from Laser Heating Experiments I

3.2.1 Evidence of a New Metastable Phase Formed During the Synthesis of C_2N_3H

During the initial LH procedure an intermediate phase was observed by both synchrotron radiation work and Raman spectroscopy, revealing more of the C-N-H HPHT landscape for which further studies are required. The diffraction peaks of the intermediate phases could not be assigned to any of the predicted C_3N_4 polymorphs and could not be indexed or matched to any existing C-N-H predicted structures. In both analytical methods the intermediate phase is clearly distinguishable from the dwur structure and undergoes a change to form the dwur structure upon further heating. XRD patterns were collected during laser heating at ID27, providing a crystallographic method of monitoring the reaction. Here, we observed a mixture of the intermediate phase and the dwur-C_2N_3H phase. LH was continued until the peaks (FIG. 25 (2) and FIG. 36) were no longer observable and the two most intense reflections (200, 111) of the dwur structure transformed from single crystal diffraction spots into concentric diffraction rings. Raman work carried out at UCL was also able to single out the intermediate phase during the initial LH stages.

In the initial studies of synthesis of C_2N_3H from the DCDA precursor Horvath *et al.* [168] reported a Raman spectrum taken *in situ* at high-pressure in the DAC that contained sharp peaks at 577 and 874 cm^{-1} and a broader asymmetric band at 770 cm^{-1}. In the present study we have now determined that the 577 and 874 cm^{-1} peaks correspond to different phases. After initial laser heating in the DAC at 30-45 GPa a spectrum is obtained that is dominated by the 874 cm^{-1} peak and there is no evidence for the 577 cm^{-1} feature: after prolonged heating, the 874 cm^{-1} peak disappears and the 577 cm^{-1} band dominated the spectrum at high-pressure (FIG. 35). That material (FIG. 35 (1)) is assigned from our *in situ* X-ray diffraction results to the dwur-C_2N_3H structure [172].

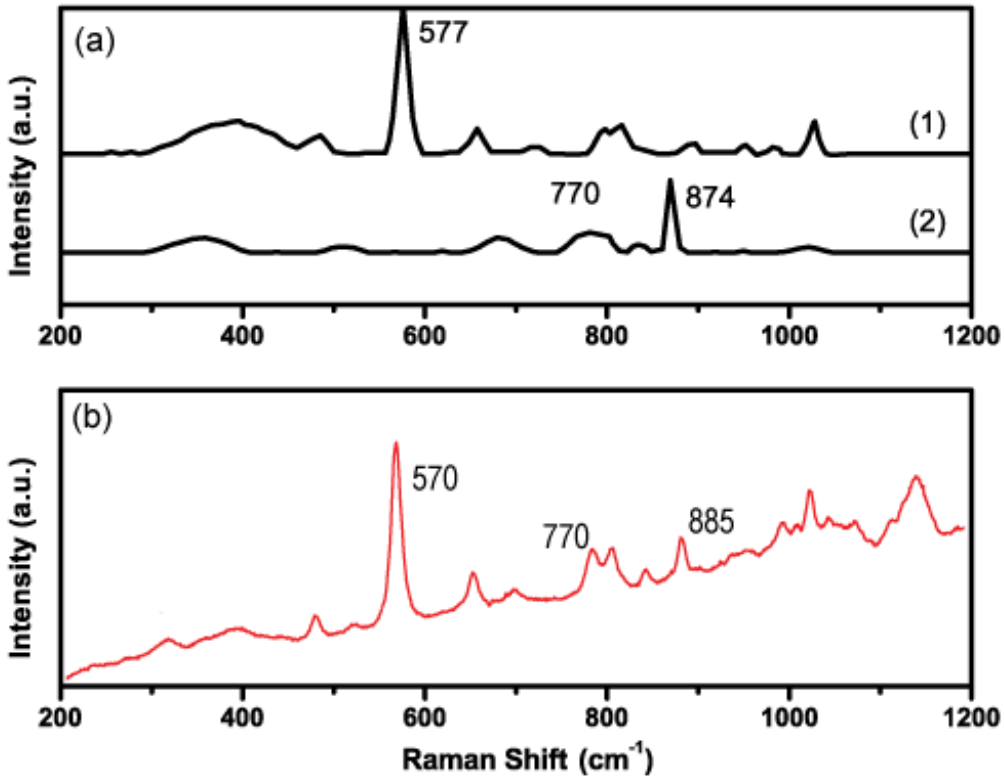

FIG. 35: Raman spectra obtained during decompression of C_2N_3H following LH synthesis from DCDA in the DAC at 45 GPa. (a) (1) Spectrum taken after extended LH is that of the dwur- C_2N_3H structure. The 577 cm^{-1} peak is a distinctive feature of this HP phase. (2) The spectrum was collected during the initial LH stages of the experiment where the 874 cm^{-1} peak is a distinctive feature and the emergence of the 577 cm^{-1} peak has not started. (b) Spectra taken before full transformation to the HP phase. Both phases are observed.

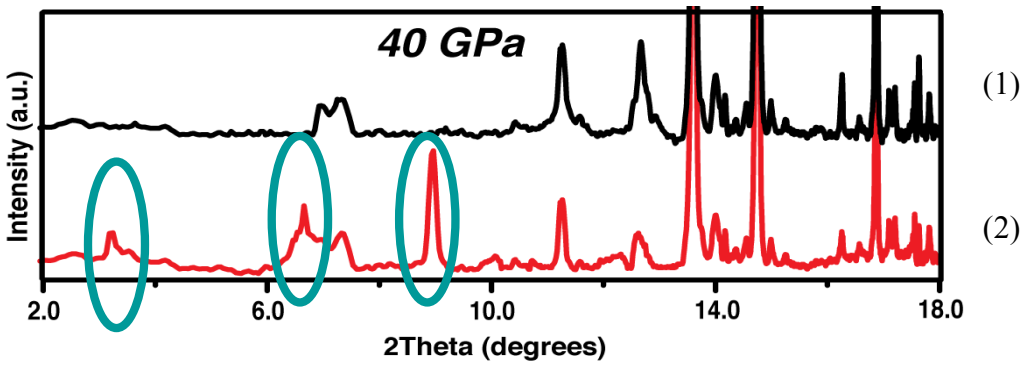

FIG. 36 : XRD data collected at 40 GPa following the LH synthesis from DCDA in the DAC. (1) Pattern collected after extensive LH shows the presence of only the dwur-C_2N_3H phase present. (2) The pattern was collected after only the initial LH period. The peaks identified by the coloured rings highlight the presence of an intermediate phase which we believe is also identified by the Raman work illustrated above.

3.3 Pressure-Induced Hybridisation in Layered $C_6N_9H_3$·HCl and Formation of A New Pillared Graphitic Carbon Nitride Phase

3.3.1 Introduction

Carbon nitrides with C_xN_y stoichiometry have been predicted to exist in several polymorphs of which the graphitic phase is predicted to be the most stable at ambient conditions [21] and potentially the first to be synthesised. Initially, studies into carbon nitride materials were conducted by reactions between or decomposition of (C,N)-containing compounds and highlighted the strong interaction between inorganic and organic solid state and molecular chemistry. Berzelius *et al*. had originally described an amorphous solid with a composition approximately $C_6N_9H_3$ which was later named by Liebig *et al*. as "melon" [183]. In fact polymeric carbon nitrides such as melon are noted as being the first reported polymers [184] and so there is a rich history in this field of chemistry [185-187]. Of the C_xN_y compounds the C_3N_4 polymorphs have been predicted to have the most unique and useful properties. These constitute potential high energy materials such energy storage or for explosives [188]. They have also recently been suggest as a new family of photocatalysts for splitting water [18].

There have been reports of sp^2-bonded graphitic layered carbon nitride compounds obtained both by vapour deposition and by high-pressure synthesis from precursors including heterocyclic aromatic molecules [189, 190]. A C_3N_4 graphitic solid was first produced by chemical vapour deposition and characterised using electron diffraction and energy loss spectroscopy techniques, as well as FTIR [22]. Several related C,N graphitic or single layer graphene structures have been studied by first principles calculations [191-194].

The graphitic starting material reported here is based on condensation of triazine (C_3N_3) rings linked by -(NH)- units. Using high-pressure high temperature synthesis techniques in the 0.5-4 GPa range at T~400-500^{o}C, Demazeau *et al.* [195] in Bordeaux and McMillan *et al.* [189] in Arizona carried out condensation reactions between melamine and cyanuric acid to form graphitic solids. Nominally the reactions proceed *via* elimination of HCl during formation of -(NH)- bridges between the triazine ring units, however studies

have shown that some chloride is retained within the product, with Cl^- species occupying voids within the C,N layers giving rise to a composition best expressed as $C_6N_9H_3 \cdot HCl$ [189, 190, 196, 197]. During a recent theoretical investigation it was predicted that compression of such layered graphitic C,N materials should result in formation of sp^2/sp^3-bonded structures containing C-N linkages between the layers [197] [198]. In the present work the g-$C_6N_9H_3 \cdot HCl$ was compressed at room temperature in a diamond anvil cell, and a structural study of the solid and its high-pressure behaviour was examined using synchrotron X-ray diffraction. Also some preliminary work by V. Lees during her PhD at UCL had taken the g-$C_6N_9H_3 \cdot HCl$ to 30 GPa and had reported the sample undergoing amorphisation. Some of those findings are contested in this work. The study of pressure-induced modifications and the effect of annealing the sample are also discussed. To this goal, the sample was annealed at ~1500 K at a pressure of around 30 GPa. The appearance of a new series of diffraction peaks signalled the formation of a new carbon nitride phase. The structural model for this new-pillared phase is compared to the results of first principles calculations.

3.3.2 Experimental Techniques

Samples of graphitic $C_6N_9H_3 \cdot HCl$ were prepared by Victoria Lees and Edward Bailey at UCL [196, 199]. The sample is made by loading 1:2 mixtures of melamine ($C_3N_6H_6$) and cyanuric chloride ($C_3N_3Cl_3$) in a piston cylinder device at pressures between 0.5-1.5 GPa and T = 500-550^oC [189, 196]. All manipulations were carried out in an Ar-filled dry box. The structure and chemical composition of the material were established using powder X-ray diffraction and bulk chemical analysis [189, 196].

The g-$C_6N_9H_3 \cdot HCl$ was loaded into a mechanically driven cylindrical 4-post cell and gas-driven membrane cells. Diamonds with 300 μm culets were used in most cases except for when collecting data between 60-70 GPa, in which 200 μm culets were opted for. Rhenium gaskets were pre-indented to ~30μm and gasket holes ~80 μm in diameter were drilled by electro-erosion. The samples were packed into the cell chamber in the glove box using no pressure-transmitting medium. The ruby fluorescence data indicated that the sample itself

being a soft solid provided a reasonably "hydrostatic" medium for the compression experiments; no obvious large pressure gradients were detected across the cell during the experiments.

XRD experiments were carried out at beamline I15 (Diamond Light Source, UK: λ = 0.444051 Å) and at ESRF ID27 (Grenoble, France: λ= 0.3738 Å) using angle dispersive techniques. Diffraction patterns were recorded as 2-D angle-dispersive data sets using a MAR image plate or a CCD detector: the data were analyzed using Fit2D [169] and FullProf software [170].

During the XRD experiments at Diamond the compression data were collected using a membrane driven cell, where we had previously calibrated the membrane pressure with that of the DAC pressure. We have found this approach reliable for observing amorphous systems [16] and reconfirmed our calibration using LiF diffraction peaks as pressure markers. This approach allowed the sample to remain completely fixed for the duration of the data collection, which is vital for a reliable background subtraction, which becomes fundamental when observing weakly scattering or disordered systems. More precisely, once the data has been collected, the DAC must be able to be removed attached to its holder/mount/stage. At I15 (Diamond) the DAC is held using a kinematic stage and the stage is removed with the DAC still firmly held, as to not alter the orientation or position of the cell. The piston is gently removed from the cell along with the gasket, both the culets are cleaned and the sample removed from the gasket and the gasket cleaned. It is very important that the part of the cell attached to the stage has not moved. To get the best possible background pattern it is vital to place the gasket back into its origin position, cleaned, and place the piston half of the DAC back into its original position. With the empty DAC still held firmly the whole unit is placed back onto the diffractometer and the centre of rotation is located and a background pattern taken with the same exposure times as the experiment.

When carrying out the laser heating (LH) experiments, the sample was pressed into a pellet and loaded inside a glove box into the DAC. NaCl and LiF plates were used to provide thermal insulation from the diamonds. Samples were heated to a range of different temperatures from 1000–2000 K. The temperatures were determined by measuring the thermal radiation and fitting it as a grey body to a Plank function [200, 201]. Direct LH was performed using a 150 W CO_2 (10.6 μm) laser and using NaCl as the thermal insulator. When

using LiF, the salt partially absorbs the CO_2 laser and we carried out LH at station ID27 (ESRF) using two 50W Nd:YAG (1.064 nm) lasers and having Re powder mixed with the sample to couple with the near-IR beam.

3.3.3 Results and Discussion

3.3.3.1 Ambient Conditions

The original structural model proposed by Zhang *et al.* [189] described the graphitic $C_6N_9H_3{\cdot}HCl$ as a layered hexagonal ($P6_3/m$) structure. They assumed a two-dimensional $C_6N_9H_3$ framework that is structurally related to the hypothetical $P6m2$ graphitic phase of C_3N_4, but with an ordered arrangement of C_3N_3 voids. Their attempts at synthesising C_3N_4 were unsuccessful as the synthesis process using cyanuric chloride ($C_3N_3Cl_3$) meant that the presence of chlorine was incorporated into the graphitic layer. The chloride ions occupied the large voids present in the graphene sheets and the authors had to assumed an equivalent number of nitrogen atoms on the framework protonated for charge balance. They confirmed their structural model using FTIR spectroscopy and ^{13}C NMR which allowed them to suggest the location of the additional H atoms associated with the incorporation of the HCl into the structure. They postulated that the H atoms are attached to the N(1) nitrogen atom involved in the triazine rings, rather than to the bridging N(2)H groups between triazine units, thus forming the $C_{12}N_{12}$ voids within the structure. This was recently confirmed by Deifallah *et al*. [197, 198] using *ab initio* calculations.

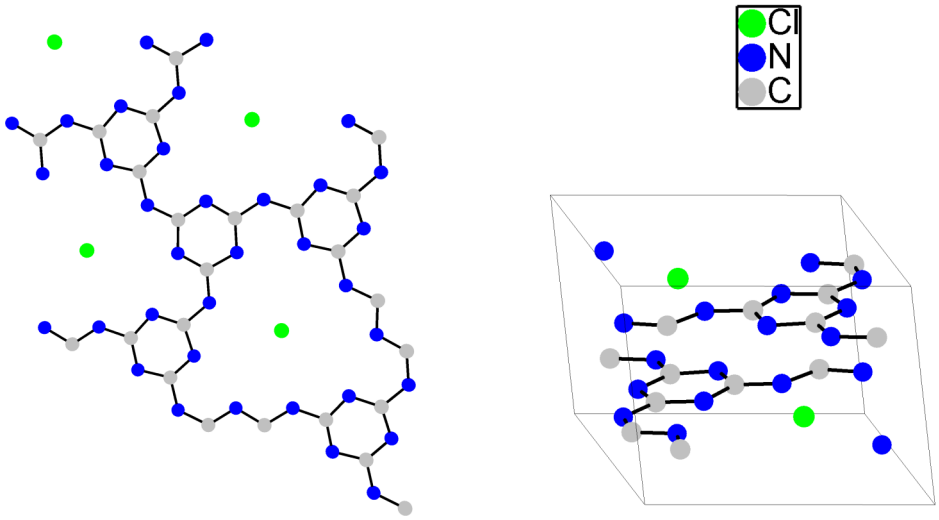

FIG. 37: The planar structure of the graphitic- $C_6N_9H_3 \cdot HCl$. The image on the left is a top view of the planar framework and the image on the right is of the unit cell of the system.

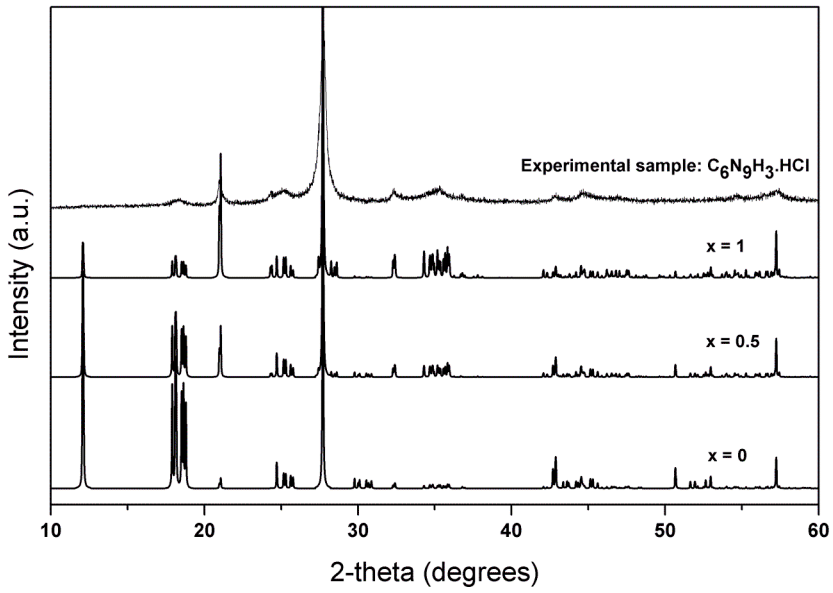

FIG. 38: The complete plot of a comparison of the experimental and theoretical patterns with varying composition of HCl. The top pattern is of the experimental XRD pattern of the graphitic $C_6N_9H_3 \cdot xHCl$. The rest of the patterns are simulated with different occupancies for the Cl^- ion predicted from DFT calculations. The space group for the DFT patterns is assumed to be *P*1 [197], which is discussed, and the best match to the experimental pattern is when x is defined as 1. These findings were carried out by V. Lees and M. Deifallah during their PhD thesis at UCL. The plots were constructed by myself for the publication [196].

Further examination of the ambient model highlights some additional problems. Zhang *et al.* identified that with the composition it is possible that the formulation of the sample could be $C_6N_9H_3 \cdot xHCl$ with $0 \leq x \leq 1$ as not all of the chlorines would occupy the void sites within the structure. Work by V. Lees during her PhD at UCL suggested that the best structural solution would have all the voids occupied with x = 1 and this was confirmed by Deifallah *et al*. using a computational approach (FIG. 38) [197, 199].

3.3.3.2 Determination of the Space Group for g-$C_6N_9H_3 \cdot xHCl$

Zhang *et al.* had identified the $P6_3/m$ space group as the best matched to their experimental data using Le Bail extraction and Rietveld refinement techniques. However, the quality of XRD pattern generated from this sample only allows for a limited refinement of the structure and DFT calculations [196, 197] have shown that the structural model of this system is more complicated than assumed by Zhang *et al*.

The difficulty with this system is that the XRD patterns collected have broad features not characteristic of a well-ordered crystalline sample. This makes indexing the diffraction pattern very unreliable. Indexing of the peak positions using the software CRYSFIRE and DICVOL generates a number of possible space groups, the most stable being $P6_3/mmc$ and $P6_3/m$. However, the reliability of the suggested space groups was not sufficient to be able to identify the correct one using this method. In addition, once the sample was under any compression, the shearing of the unit cell, as well as deviatoric stress, made indexing impossible. The challenge was to identify a space group that would best describe the structure at ambient and throughout compression [202].

When comparing a simulated XRD pattern using the structural model information provided by Zhang *et al.* with that of the experimental pattern the two do not match well. The frequency of reflections of the simulated pattern and their relative heights and peak shapes do not fit the experimental XRD. The experimental XRD pattern consists of a mixture of broad and narrow peaks for which the $P6_3/m$ space group does not match. Deifallah *et al.* [196] have suggested that the $P6_3/m$ does not provide a full description of the unit cell and

therefore does not account for the these peaks. They go on to suggest further that the experimental peak shapes are due to disorder-induced broadening and the presence of nanocrystallanity within the sample. They describe the origin of this disorder due to slight off-centre shifts in the Cl^- positions occupying the large voids in the graphitic sheets. Also additional disordering is assigned to the attachment of H atoms to N around the heptazine rings. During their structural modelling they recommend that a *P*1 unit cell best describes the disordering which is present in the material. They calculate that the NH bonding pattern causes distortions within the planar lattice causes a buckling of the C-N framework. This combined with the displacements of the Cl^- ions within the voids acts upon lowering the overall symmetry of the unit cell.

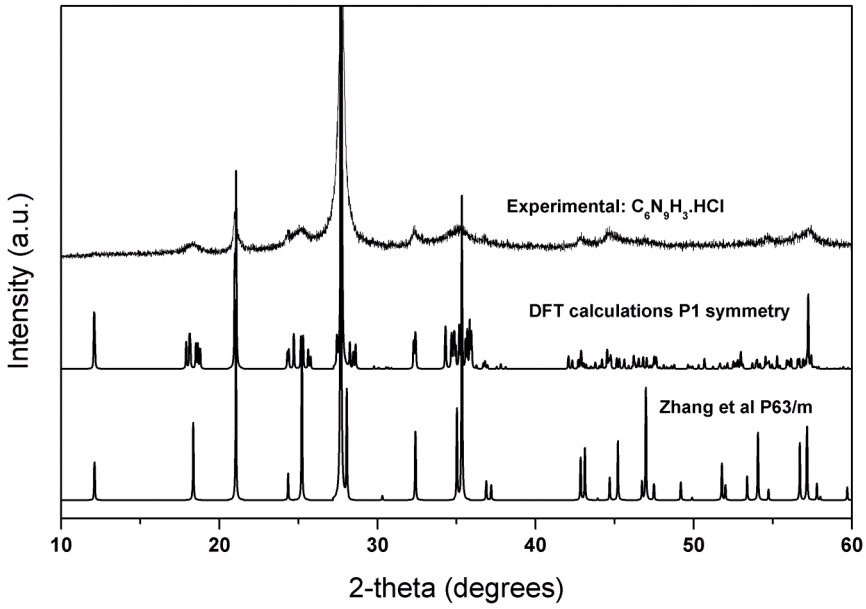

FIG. 39: Experimental XRD pattern of graphitic $C_6N_9H_3{\cdot}HCl$ compared with the $P6_3/m$ structure proposed by Zhang *et al*. [17] (top) and the lower diagram indicates the diffraction peaks calculated for a structural model with *P*1 symmetry that assumes an ordered H–N attachment arrangement to the N1 nitrogens and with Cl atoms moved slightly off centre with in their sites accordingly [30]. In the true overall structure it is likely that the N1–H attachment and Cl displacements occur in a disordered manner within each layer.

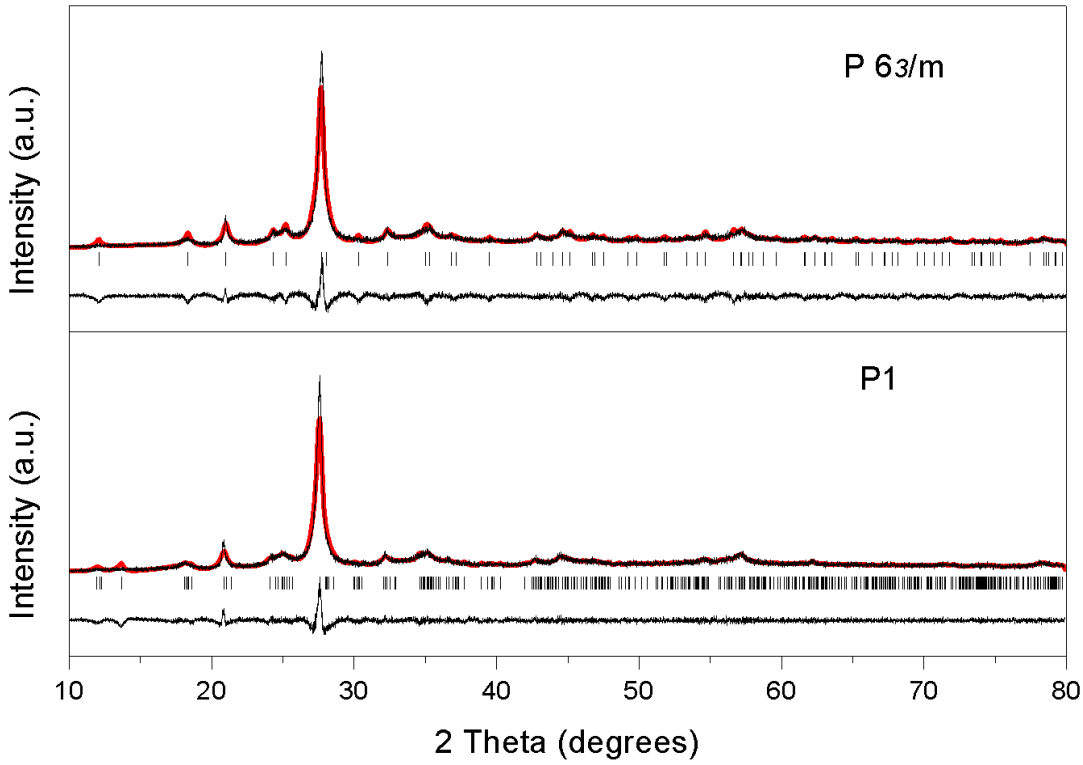

FIG. 40: $P6_3/m$ vs $P1$ Le Bail refinement

Although the DFT calculations have used a $P1$ model to attempt to describe the unit cell of the g-$C_6N_9H_3$·xHCl this space group has no constraints ($\chi^2 < 1$) when used in structural refinement. The calculated model describes disordering throughout the supercell and its assignment of a $P1$ space group is attempting to describe the lack of possible long range symmetry. Although this disordering can be modelled as $P1$ symmetry there still must be some symmetry throughout the unit cell, especially short order, for the sample to have produced a number of defined narrow peaks. This short correlation range was attempted to be model as best it can. An attempt to assign the space group through understanding the chemistry of the graphitic system was carried out. The reported structure by Zhang *et al.* is acknowledged in this work as the most suitable description of the unit cell at ambient conditions, data permitting. Starting with this $P6_3/m$ space group Le Bail refinement was carried out and the symmetry of the space group reduced to attempt to improve the structural fit. As the graphitic system undergoes compression the *ab initio* calculations by Deifallah *et al.* suggest that the layered system undergoes shearing, as observed by the asymmetric peak broadening in experimental data. To test this the first symmetry parameter removed was the mirror plane. This was examined by

reducing symmetry to $P6_3$. Next investigated was the loss of the six-fold and 3 turn symmetries. Finally a $P1$ model was attempted. The various fits with potential space groups are illustrated in FIG. 41.

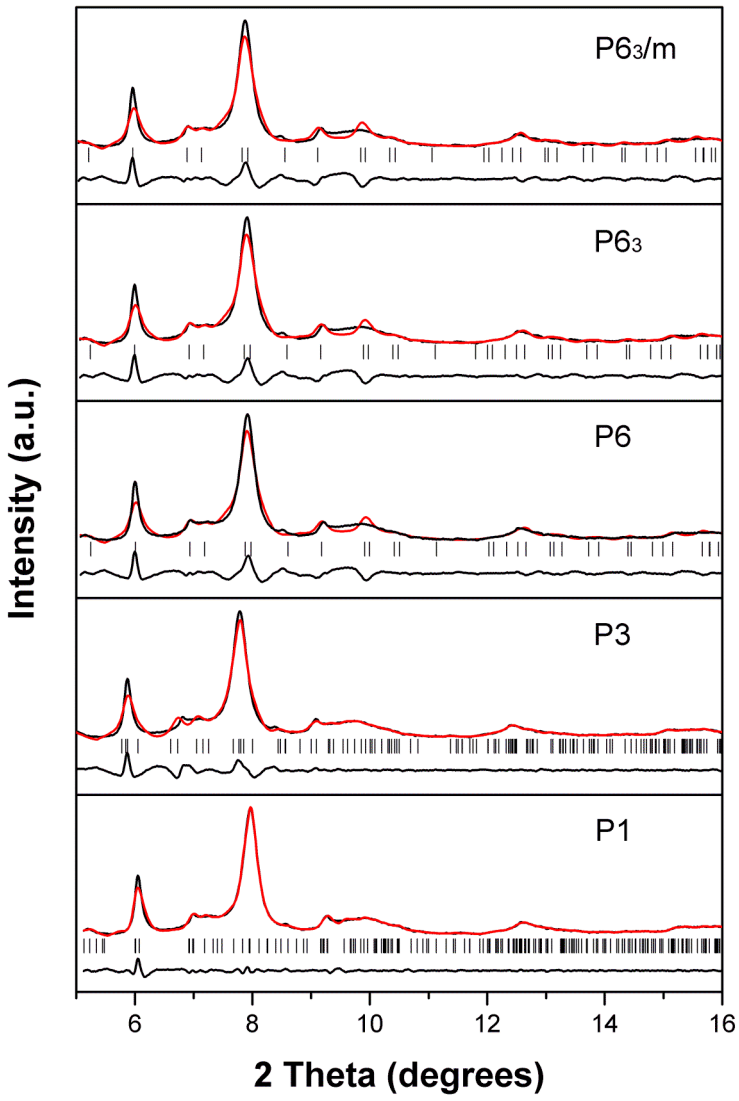

FIG. 41: The stack of patterns present the experimental XRD pattern of the graphitic $C_6N_9H_3$·HCl collected at 5 GPa and fitted using Le Bail refinement with different space groups.

The broad XRD data even at ambient conditions made any attempts at improving the refinement fits through the lowering of symmetry difficult. The $P6_3/m$, $P6_3$ and $P6$ models all gave roughly the same R_{wp} and χ^2 values of ~7 and ~30 respectively. What was made apparent was that improving on the structural model proposed by Zhang *et al.* could not be improved on using powder diffraction techniques. The Le Bail refinements were carried out assuming two different space groups for the solid: first the $P6_3/m$ structure

suggested in the first synthesis of $C_6N_9H_3$·HCl by Zhang *et al.*; and second reducing the symmetry to $P6_3$, with loss of the horizontal plane of symmetry.

The latter choice ensues from the computational results discussed earlier, that showed layers in the $C_6N_9H_3$·HCl solid to be buckled and thus incompatible with the Zhang *et al.* assignment. Although more accurate structure analysis can be derived from the computational work [194], the presence of structural constraints is very useful in this initial stage of structure refinement using XRD patters with broad peaks, and even the $P6_3/m$ model provides a useful choice.

	Experimental		Zhang	DFT
	$P6_3/m$	P1	$P6_3/m$	P1
a	8.452 (3)	8.508 (2)	8.4379	8.33
b	8.452 (2)	8.312 (1)	8.4379	8.37
c	6.440 (3)	6.463 (3)	6.4296	6.23
alpha	90	90.837 (5)	90	89.68
beta	90	90.384 (4)	90	92.56
gamma	120	119.685 (4)	120	121.2
volume	398.538 (9)	397.018 (6)		

TABLE 7: The unit cell parameters of the experimental graphitic-$C_6N_9H_3$·HCl compared to the Zhang *et al.* model and the theoretical model calculated by DFT.

3.3.3.3 New Refinement of the Ambient Pressure Structure of g-$C_6N_9H_3$·HCl

The initial Rietveld refinement reported by Zhang *et al.* using the $P6_3/m$ space group assumed that the C-N framework was planar and rigid. All the *z* fractional coordinates for the atomic positions of the atoms in the unit are fixed at 0.25, describing the planar structure. FIG. 42 illustrates the Rietveld refinement carried out using the atomic coordinates already reported. The fit is not that well matched to the observed pattern especially when accounting for the peak heights as determined by the atomic positions. However, the structural model it is based on does describe a C-N framework and accounts for the $C_{12}N_{12}$ voids within the structure. It also positions the chloride ions within these voids, planar to the framework. Attempts were made to relax the atomic positions of the planar unit cell using FullProf as a refinement package. Keeping the unit cell

parameters fixed, the atomic positions were refined initially one at a time as well as a full overall refinement. Although this produced overall better fits to the experimental data, the structural models outputted were not accurate in describing a C-N framework (FIG. 43).

The refinement package when allowed to refine the atomic positions would not contain the atoms within the initial proposed framework, characteristic of a graphitic system. In all cases the structural models simulated from the new atomic positions were not regarded as reliable or realistic. This lead to the conclusion and confirmation of work previously reported that any Rietveld refinement carried out the compression data would be invalid and the only real data to be extracted would be through Le Bail refinement with which to evaluate the volumes of the unit cell at given pressures.

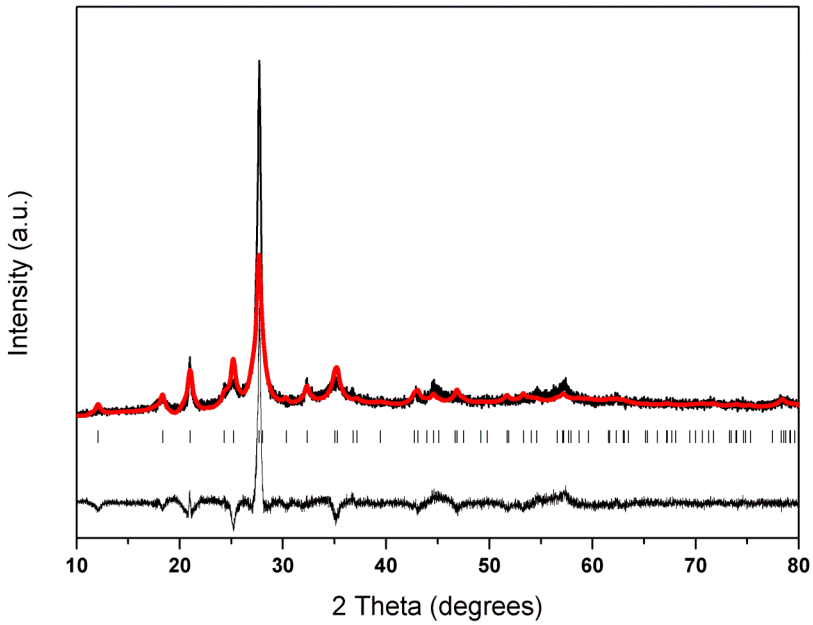

FIG. 42: Rietveld refinement of $C_6N_9H_3{\cdot}HCl$ using the fractional coordinates as determined by the structural model of Zhang *et al.* [189] ($P6_3/m$). The fit is only moderate and highlights the poor match with the suggested structural model. The pattern was collected on Bruker D4 diffractometer using CuK_α radiation (λ = 1.5418 Å). R_p: 43.1, R_{wp}: 44.2, R_{exp}: 23.13, χ^2: 3.66.

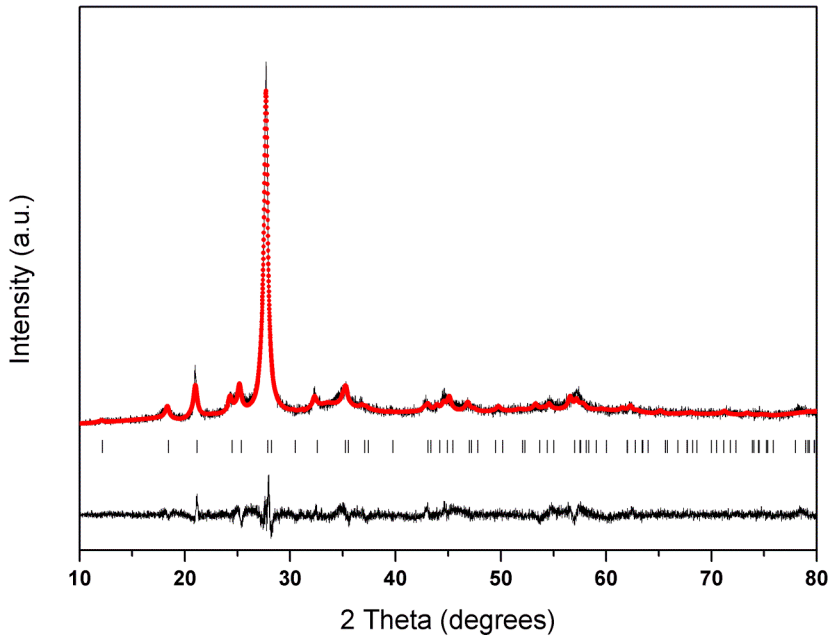

FIG. 43: Rietveld refinement of $C_6N_9H_3 \cdot HCl$ allowing for the atomic positions to be refined as determined by the structural model of Zhang *et al.* [189] (*P*1). The pattern was collected on Bruker D4 diffractometer using CuK_α radiation (λ = 1.5418 Å). R_p: 40.0, R_{wp}: 34.0, R_{exp}: 27.83, χ^2: 1.49.

3.3.3.4 Structural Changes During Pressurisation at Ambient Temperature

The experimental results are now discussed, starting with an initial compression of the synthesised material at ambient temperature. Compression runs were carried up to 70 GPa and investigated using synchrotron radiation at I15 (Diamond). The XRD pattern of the sample has defined peaks up to a pressure of ~15 GPa, at which point shearing of the graphic layers contributes to peak broadening and asymmetrical peak shapes. Similar shear distortions have also been observed computationally. It was possible to carry out Le Bail refinement for data sets up to 40 GPa, after which it was decided that the diffraction peaks were too broad and weak for reliable refinement. Angle dispersive XRD data in this pressure range are reported in FIG. 44 and FIG. 45.

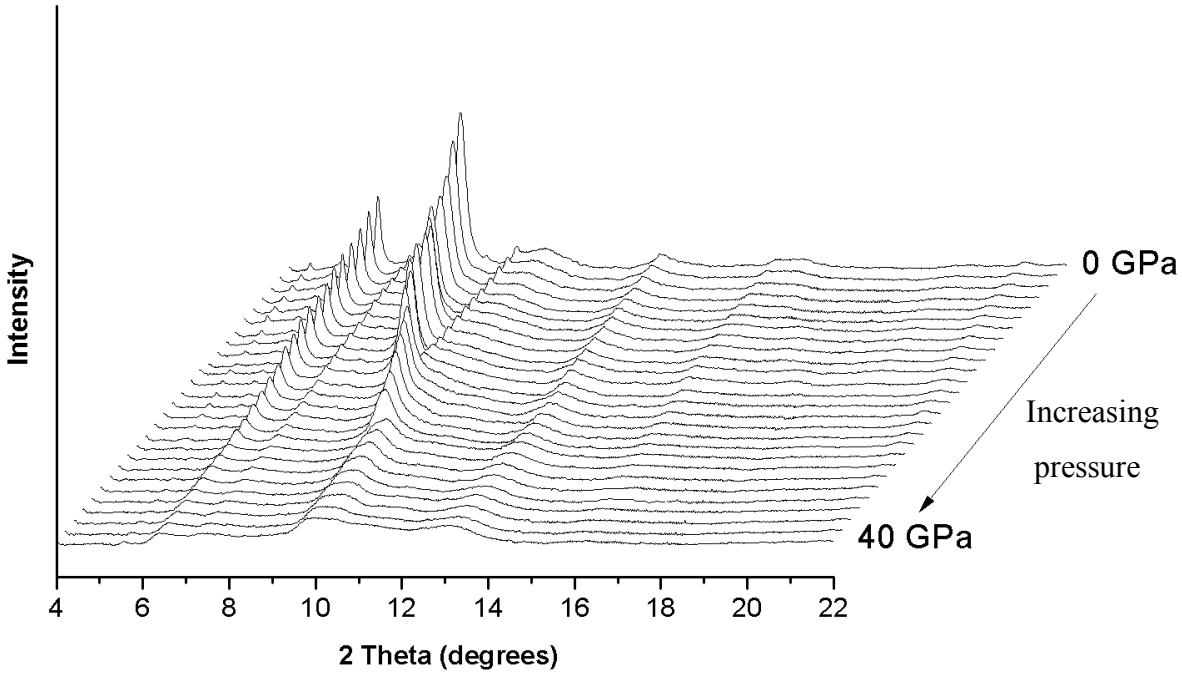

FIG. 44: Angle dispersive synchrotron X-ray diffraction data for graphitic $C_6N_9H_3$·HCl. The waterfall plot illustrates the compression data starting from ambient conditions up to 40 GPa.

The Le Bail refinement was carried out by fixing the position of the (002) reflections to that of the most dominant peak of the diffraction, as described by simulated patterns using PowderCell and DFT calculations. For the data sets above 40 GPa the XRD patterns collected were directly compared to calculated patterns; this is discussed later. Using the experimental compression data the observed lattice spacings (FIG. 46) unit cell volume (FIG. 48) and lattice parameters (FIG. 50) as a function of pressure are reported.

Using PowderCell we simulated XRD patterns of the $C_6N_9H_3$·HCl at various pressures (unit cell volume) and predetermined that the (002) reflections is defined by the position of the most dominant peak. With this as a starting point the LeBail refinement was carried out with the (002) reflections always fixed relative to the most intense peak. The value of the (002) was determined by applying a Lorentzian fit to the peak profile and extracting the mid point value of the peak. This determines the c – axis, the distance between the layers of the graphitic system.

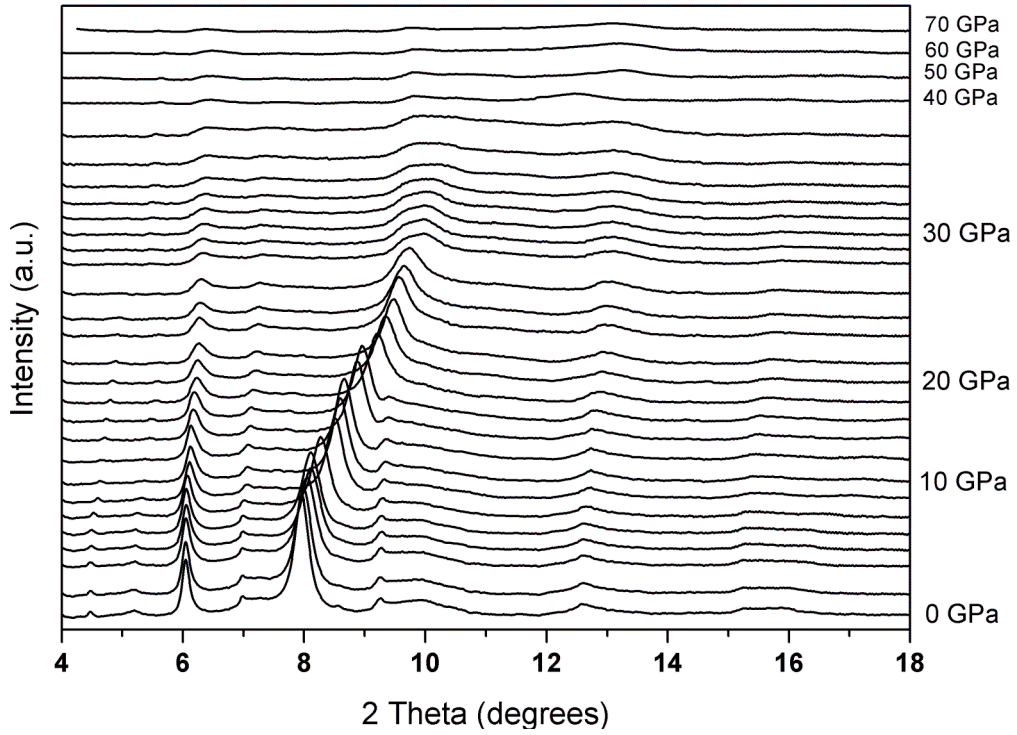

FIG. 45: Angle dispersive synchrotron X-ray diffraction data for graphitic $C_6N_9H_3{\cdot}HCl$. The stacking plot illustrates the compression data starting from ambient conditions up to 70 GPa.

Within our data sets, it was decided that the visual assignment of reflections would not be accurate due to the broad weak features of the XRD data, especially at higher pressures (FIG. 46). Therefore, all reflections were followed using a Le Bail fit using FullProf. Using this method, in conjunction with calculated simulated patterns, it was possible to follow all the reflections up to 40 GPa unlike the observations made by Wolf *et al.* [190], who reported on a similar sample of graphitic $C_6N_9H_3{\cdot}HCl$ using energy dispersive synchrotron X-ray techniques. They reported observation of the (002), (200) and (110) reflections up to P = 34 GPa, but (210) could only be recorded up to 28 GPa, (111) to 12 GPa and the (011) reflection was no longer visible after 4 GPa. However, our results are generally consistent with those obtained by Wolf *et al.* as both reports observe a crossover occurring between the (210) and (002) reflections at P ~15 GPa (FIG. 47). In fact, we observe an additional crossover of the (012) reflection with that of the (210) at ~5 GPa, as well as a crossover of the (002) and (021) reflections (~2 GPa). The original work by V. Lees [199] had not managed to identify any of the observations reported by Wolf *et al.* [190] and provided a different description of the system under pressure. Having the opportunity to reanalyse her original data, I was able to identify the presence

of graphite peaks in her XRD diffraction data, probably belonging to a graphitised layer on the culet, emerging as the signal from the sample became weaker with an increase in pressure. The undetected presence of this impurity effected all of the analysis and was a major reason for why we decided to re-examine this system using HP techniques.

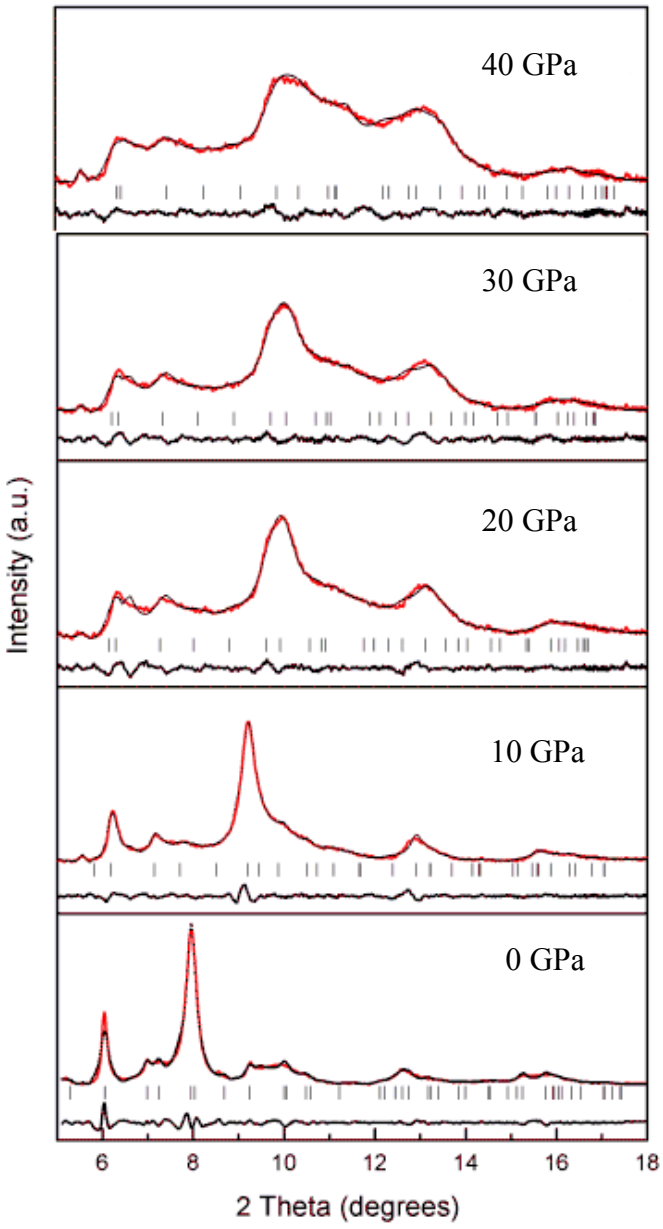

FIG. 46: Angle dispersive synchrotron X-ray diffraction data for graphitic $C_6N_9H_3{\cdot}HCl$ shown at 10 GPa intervals up to 40 GPa. The Le Bail refinement fit is shown in red and the experimental data in black. The markers identify the positions of the reflections belonging to the $C_6N_9H_3{\cdot}HCl$. The difference between the observed powder pattern and that calculated using the crystal structure is given by the bottom fit in black.

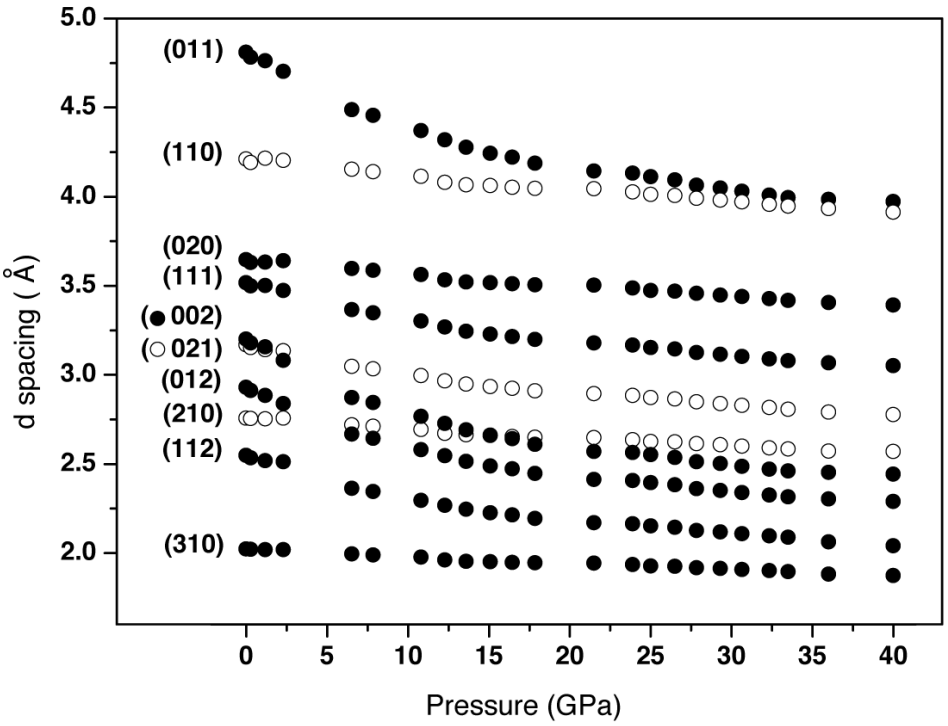

FIG. 47: Variation of d spacings with pressure of reflections distinguished as a function of pressure. Reflections were assigned using Le Bail refinement.

The d(P) plot (FIG. 47) illustrates that the reflections describing a non-zero *l* value (c axis) undergo a much more rapid compression than those of (*h k 0*) type. This is confirmed by comparing the a, b axis to that of the c axis as a function of pressure (FIG. 50). FIG. 47 and FIG. 50 describe a rapid compression (collapse) of the c axis. When examining the V(P) plot of the compression data (FIG. 48) there seems to be a change in the gradient of the data points at around 20 GPa; fits of these data points to a third-order Birch Murnhagan equation of state show that there is a subtle but obvious discontinuity starting from ~22 GPa. The change is less evident in the evolution with pressure of the individual a, b and c lattice parameters FIG. 50. When nearing the compression data around the 15-20 GPa region the X-ray diffraction pattern of the layered g-$C_6N_9H_3$·HCl phase loses its definition. As mentioned earlier, the peaks become broadened, often in an asymmetric manner, in the angle dispersive synchrotron X-ray diffraction spectra.

Deifallah *et al*. [198] reported that a discontinuity in a pressure versus volume plot associated with the formation of the ILB1 structure would also have to show a collapse in the c spacing. The discontinuity seen in the experimental data at ~22 GPa is not matched with a collapse in the c axis (FIG. 53) and

therefore is not describing the formation of the ILB1 structure as these pressures. The DFT work had identified the buckling of the C-N frameworks and this change in the V(P) slope could be due to a change from flat to buckled layers and a change in symmetry from $P6_3/m$ space group to $P6_3$. This loss in the mirror plane could arise from a buckling effect however the low quality of the XRD data makes it very difficult to confirm. Above 40 GPa several characteristic reflections of the graphitic structure can no longer be distinguished. Above this pressure range it is difficult to assign a crystalline structure to the observed diffraction pattern. These data indicate that several structural disordering processes occur within the $C_6N_9H_3{\cdot}HCl$ compound at pressures above 15-20 GPa. Insight into the nature of possible structural changes that occur within such layered graphitic carbon nitride phases can be gained by making reference to results from the DFT calculations by Deifallah *et al*.

Having carried out a Le Bail refinement using the higher symmetry space group of $P6_3/m$, the symmetry was reduced to $P1$ as suggested by DFT calculations and a less constrained unit cell was evaluated (FIG. 49). The first few attempts of using a $P1$ symmetry provided a random P(V) plot with no definable trend. With no symmetry constrains the refinement package was assigning reflections randomly and with no consistency. Therefore some parameters were attempted to be constrained by using predetermined values for the zero shift as determined from the silicon standard and *a* and *c* lattice parameters from the more constrained $P6_3/m$ model. The $P1$ model was only allowed to refine the b axis, alpha, beta and gamma variables. With a more constrained unit cell somewhat of a trend can be observed, however, the $P1$ model cannot be applied for a refinement procedure as already mentioned.

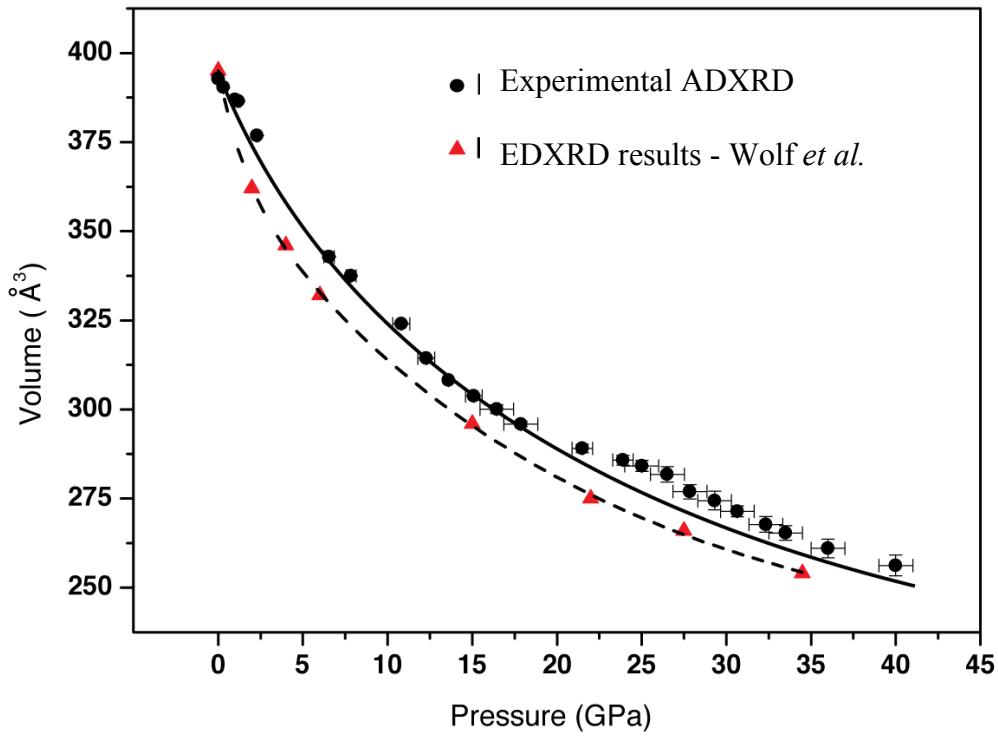

FIG. 48: V(P) plot of the experimental angle dispersive XRD and the previously reported energy dispersive XRD work [190]. A discontinuity is observed in the experimental work after the 20 GPa range not previously reported.

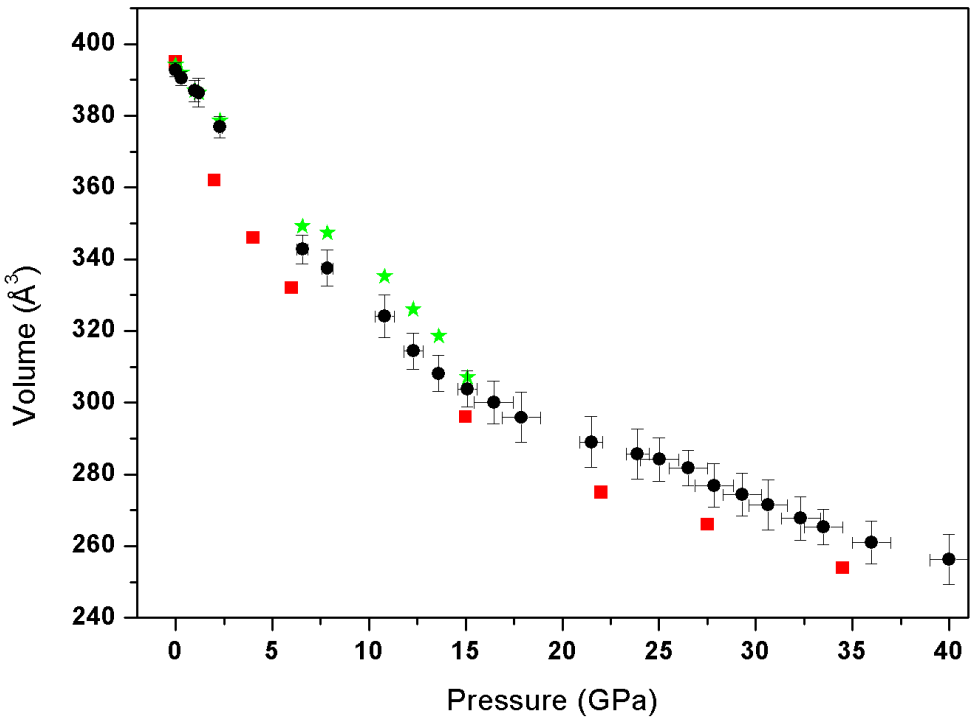

FIG. 49: V(P) plot of the experimental angle dispersive XRD. The black data points are of the experimental data using $P6_3/m$, green stars $P1$ symmetry and the red represent the previously reported work as referred to in the previous figure.

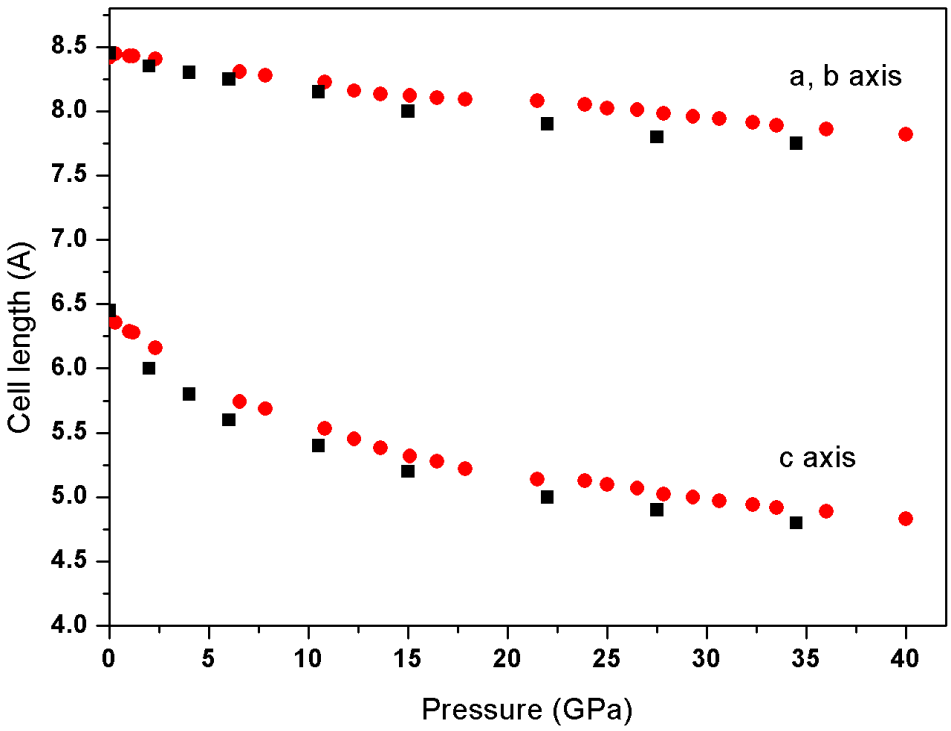

FIG. 50: The unit cell parameters are described as a function of pressure. The current work reported here (red circles) is compared to those of the cell parameters derived by previously reported energy dispersive work (black squares) [190].

The high-pressure compressibility studies highlights characteristics associated with graphitic structures, specifically one with a continuous planar network. This is described in FIG. 50, which examines and compares the compressibility's of the *a*, *b* and *c* axis. The reader is reminded that within a hexagonal unit cell the both the *a* and *b* axis are of equal value. A large compression is observed in the *c* parameter characteristic of a graphitic system. By 40 GPa, the *c* parameter has reached a value of 4.830 Å, representing a 24.5% reduction with respect to value of 6.339 Å at ambient conditions. This means that the interlayer separation between the graphitic layers by 40 GPa is at 2.415 Å. The corresponding change in *a* is only 7.1%, from 8.418 Å to 7.820 Å. It is this low compressibility in the *a* axis that makes the system highly anisotropic, characteristic of a graphitic system that contains a continuous network, much like the incompressibility of the basal plane of graphite. If the graphitic carbon nitride system did not have a continuous framework structure then it would be expected to possess a large compressibility in all directions. In describing the unit cell of the sample the compressibility of the *a* axis is

considered as being constant throughout the 40 GPa pressure range, with a near linear decrease. When compared to the values reported by Wolf *et al.* there is a good correlation at the lower pressure points. After ~15 GPa the experimental data begins to deviate from the previously reported data and there is a slight increase in the *a* axis which is accommodated with a minimal decrease in the *c* axis. It is this increase which contributes to the discontinuity observed in the V(P) data plots (FIG. 48 and FIG. 49).

3.3.3.5 Pressure-Induced Hybridisation: Experimental Results *vs.* Theoretical models

Before discussing the high-pressure (above 40 GPa) results of this work the reader is informed about the decision to stop the refinement of the experimental XRD data above the 40 GPa mark. The broad non-distinct peak shapes made the continuation of refinement unreliable and a different approach was adopted. Theoretical work carried out by Malek Deifallah and Furio Corà at UCL [194, 197] on the same system, g-$C_6N_9H_3$·HCl, as reported here provided an excellent and detailed template with which to compare the experimental work.

Initially the X-ray diffraction pattern of the starting graphitic $C_6N_9H_3$·HCl sample taken inside the DAC at ambient conditions was compared to a DFT simulated XRD pattern after geometry optimisations and full relaxation. The experimental data was collected using synchrotron radiation (λ = 0.444 Å) at I15 at DLS and the theoretical pattern was calculated with the same wavelength in order to generate XRD patterns with the x-axis in the 2θ range. The two XRD patterns can be considered as nearly identical in terms of relative peak intensities and absolute width. The slight offset of the dominant peak in the experimental data is most likely due a small amount of strain being applied with the closure of the DAC. Both patterns exhibit the distinct broadening in the principal peaks as observed with this material. This provides strong evidence of the presence of intrinsic structural disordering within the material, rather than to experimental conditions or instrument parameters.

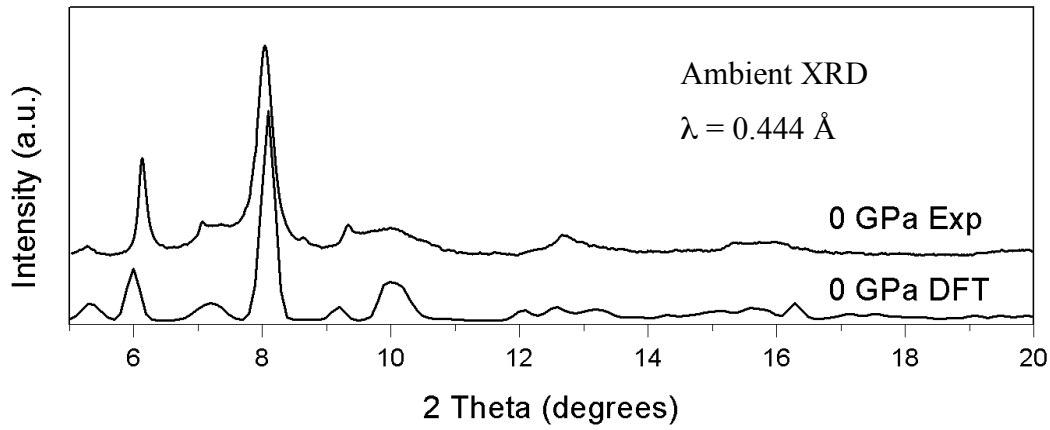

FIG. 51: A comparison of the experimental and DFT simulated XRD patterns of the g-$C_6N_9H_3$·HCl at ambient conditions. The experimental XRD data was collected at I15 of Diamond Light Source.

The theoretical calculations carried out by the Deifallah *et al.* at UCL examined the structural response during pressurisation of an "ideal" graphitic layered $C_6N_9H_3$ material and $C_6N_9H_3$·HCl [194]. They reported that both compounds exhibited similar structural changes occurring during compression although at different pressures ranges. For the purpose of the discussion here the $C_6N_9H_3$·HCl model will be examined in detail.

The behaviour of theoretical g-$C_6N_9H_3$·HCl model displayed two discontinuities in the curves representing the pressure variation of lattice parameters and enthalpy. These were estimated to be at ~70 and ~90 GPa, respectively, higher than the values provided by the "ideal" $C_6N_9H_3$ and the first experimental discontinuity mentioned above at 20 GPa. Similar to the experimental results however, the theoretical g-$C_6N_9H_3$·HCl model displayed a more pronounced decrease in *c* parameter then that of the *a* and *b* parameters. These values were smaller than those of the $C_6N_9H_3$ model, suggesting that the incorporation of Cl^- ions within the heptazine rings of the graphitic layers renders the material less compressible.

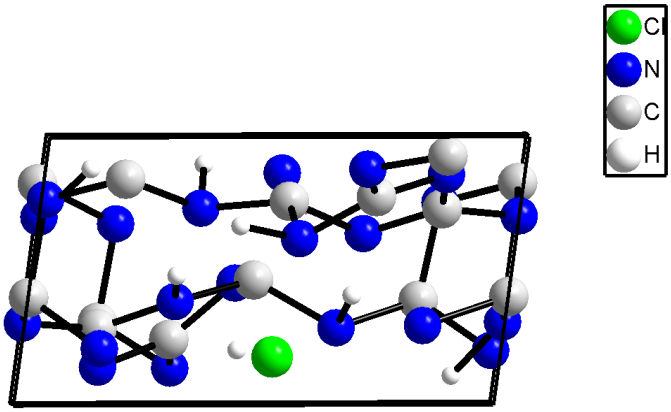

FIG. 52: A unit cell of the proposed high-pressure pillared structure of the sp^3 bonded $C_6N_9H_3 \cdot HCl$ by DFT calculations.

The first principles results of Deifallah *et al.* indicate that interlayer bonding should occur within graphitic carbon nitride phases above approximately 40-70 GPa following a reduction in the *c* parameter (FIG. 52). This has been described as a sp^2 to sp^3 rehybridisation process and shown to occur abruptly in both of the theory models. Initially the intralayer stress was shown to be absorbed by compressing the C-N intralayer bonds rather than by buckling the layers that remain atomically flat. However, as the pressure is increased this formation becomes energetically unfavourable and a buckling of the C-N framework occurs. The C-N bonds between adjacent layers can occur in a non-systematic fashion between layers above and below the central plane, and this likely results in the highly disordered nature of the $C_6N_9H_3 \cdot HCl$ sample observed above P = 25-30 GPa in the experimental study. The presence of the Cl^- atoms located in the $C_{12}N_{12}$ interstices also contribute to strong short-range repulsion resulting in the NH bonds becoming bent out-of-plane and increasing the disorder observed in the system. This has been shown by Deifallah *et al.* to be done so at the expense of π electron delocalisation.

The theoretical model follows this by prescribing that the continuation of an increase in pressure to ~70 GPa leads to the sp^3 hybridisation of a C_3N_3 ring and the creation of new bonds between the C and N on adjacent layers. C_3N_3 rings that are directly above each other therefore recombine to form interlayer bonds. The simultaneous bond formation that follows is described as non-uniform and can lead to structural disordering such as that observed in our

experimental study. In attempting to confirm the existence of this new sp^2-sp^3 bonded carbon nitride phase, containing three-dimensional pillars, a direct comparison was made between the simulated XRD patterns of the DFT models and the collected experimental work (FIG. 53). The two models used from theory consisted of a non-pillared structure, named ILB0, in which the planar network was keep rigid and not allowed to undergo interlayer bonding. The second model was named ILB1, here the system was allowed full structural optimisation and it described a pillared system with interlayer bonding.

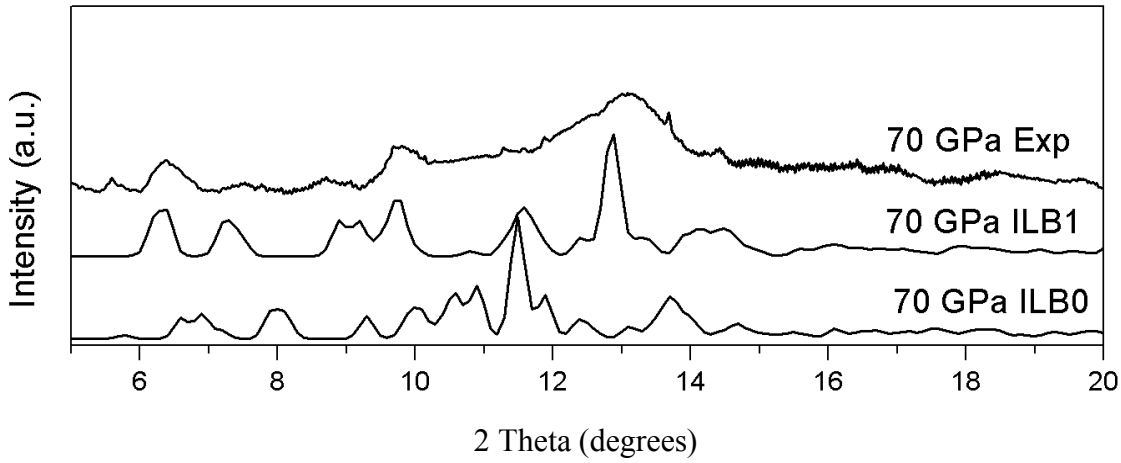

FIG. 53: A comparison of the experimental XRD pattern generated at 70 GPa versus two simulated patterns from *ab initio* calculations. The ILB1 pattern is from a pillared graphitic $C_6N_9H_3{\cdot}HCl$ structure that is shown to be the most stable phase at these elevated pressures. The ILB0 pattern is when the graphitic $C_6N_9H_3{\cdot}HCl$ structure is when there is no interlayer bonding.

There is a direct correlation between the collected experimental XRD pattern and that of the ILB1 model is observed in FIG. 53. The experimental pattern is very broad, describing a highly stressed and disordered system. This makes it very difficult for direct peak assignment. However, the dominant broad peak of the (002) reflection in the experimental pattern is described by the ILB1 pattern whose main peak has a similar 2θ value. The comparison is further confirmed when the ILB0 model is referred to as this fails to simulate a XRD pattern any resembling features with that of the experimental pattern. This similarity between the experimental and the ILB1 pattern confirms that the graphitic $C_6N_9H_3{\cdot}HCl$ system is undergoing structural changes as described by the pillared model.

3.3.3.6 Conclusion

Here we conducted a study of graphitic $C_6N_9H_3$·HCl using HP techniques and angle-dispersive synchrotron methods. An initial study of this materials was carried out by V. Lees *et al.* who had identified the Cl content in the sample but had described an amorphisation of the sample above ~20 GPa. This was not in agreement with the report by Wolf *et al.* who had described a crystalline phase up to 40 GPa. Theoretical calculations carried out by M. Deifallah *et al.* in conjunction with the work done by V. Lees suggested the formation of a new pillared structure forming at ~70 GPa. With these new findings and uncertainty regarding the high pressure behaviour of the graphitic $C_6N_9H_3$·HCl, the system was re-examined.

The graphitic layered compound $C_6N_9H_3$·HCl was subjected to pressures of up to 70 GPa in a diamond anvil cell and its structural behaviour was examined using synchrotron X-ray diffraction. The initial structural model proposed by the work by Zhang *et al*. of a layered hexagonal ($P6_3/m$) structure was compared to a theoretical model of a disordered ($P1$) structure, which described the graphitic unit cell as disordered and triclinic. The work here has highlighted the difficulties in using $P1$ symmetry to carrying out Le Bail and Reitveld refinement and how unrealistic the refinement results become during the refinement of high pressure data. The layered hexagonal ($P6_3/m$) model was shown to be a realistic description of the material at least up to a pressure range of 40 GPa.

Closer examination of the resulting V(P) plot (FIG. 48) indicates a slight maximum occurring near 20 GPa that is not normally physically reasonable for the compression of a single phase. This anomaly indicates a structural change occurring within the material that significantly affects the mechanical properties, that is normally associated with a second order or subtle first order transition between low- and higher-density forms of the material. Our third-order Birch Murnhagan analysis of the equation of state data indicate discontinuity at ~22 GPa. Upon approaching the 15-20 GPa region the X-ray diffraction peaks of g-$C_6N_9H_3$·HCl phase become broadened and asymmetric.

The compressibility's of the cell parameters describe a large compression in the *c* parameter characteristic of a graphitic system. This axis represents a 24.5 % reduction with respect to value of 6.339 Å at ambient conditions by a

pressure of 40 GPa. This means that the interlayer separation between the graphitic layers by 40 GPa is at 2.415 Å. The corresponding change in *a* is only 7.1%, from 8.418 Å to 7.820 Å. It is this low compressibility in the *a* axis that makes the system highly anisotropic, characteristic of a graphitic system that contains a continuous network, much like the incompressibility of the basal plane of graphite.

Attempts at structural refinement were limited to experimental data up to a pressure of 40 GPa as it was felt that the quality of the collected data was too statistically poor for a reliable assessment. Data at these pressures (> 40 GPa) was compared to the theoretical calculations carried out by Deifallah *et al.* The *ab initio* calculations had identified the formation of a new pillared structure formed at pressure greater than 70 GPa. The experimental XRD data were compared to the theoretical XRD data and confirmed that the predicted pillared structure referred to as ILB1 was the most convincing match to the observed work. The formation of the pillared structure was shown to be due to the sp^2 hybridised C in a layered framework undergoing a pressure induced change to sp^3 bonding with the formation of C-N bonds between adjacent layers in the graphitic structure. The close match between the experimental data and that of the ILB1 structure suggests that the graphitic system is undergoing the change in hybridisation as shown by the *ab initio* calculations.

3.4 Potential Other Phases in the C-N-H Systems: Results from Laser Heating Experiments II

3.4.1 Synthesis of a New C_xN_y Phase After Laser Heating g-$C_6N_9H_3$·HCl

During the experimental study, 30 GPa of pressure was applied in a DAC to a sample of $C_6N_9H_3$·HCl, which was then gently laser heated with a ~30 W power output using NaCl as the thermal insulator. The sample was monitored in situ with Raman spectroscopy; the ambient structure fluoresces heavily throughout compression as well as at ambient conditions and does not provide a Raman spectrum. However, after short periods of LH the fluorescence stopped and a Raman pattern was observed; this identified a mechanical or electronic change in the overall structural of the system. Once this phase change had occurred, the LH sample in the DAC was transported to the ESRF and analysed with XRD at the synchrotron source. A new series of crystalline X-ray diffraction peaks were observed on the sample and which could be followed as the sample was returned to ambient conditions. In order to confirm the reproducibility of the experiment, the sample was also LH in situ at the ESRF which produced the same diffraction pattern. The diffraction patterns before and after laser heating are illustrated in FIG. 54. The diffraction pattern after LH clearly shows the presence of a new crystalline material which is formed. The emergence of the dominant peak at 2.2 Å does not match the (002) reflection of the ambient structure at 30 GPa and neither does the presence of the Bragg peaks at 4.2 and 4.8 Å. The experimental diffraction was then compared to simulated XRD patterns generated using the DFT calculations conducted by Furio Corà and Aishia Raman.

The ILB1 which was described earlier, as a pillared graphitic structure, was chosen for comparison. Although there is no real decipherable match at higher pressures (FIG. 55a), upon decompression a similarity develops. FIG. 55b shows a comparison of the recovered LH sample at ambient conditions compared to the ILB1 structure at 7 GPa. The purpose of this is the ILB1 structure has been calculated to collapse into the non-pillared below 3 GPa and so the lowest pressure calculated model is at 7 GPa. The comparison of the two XRD patterns does however highlight some similarities between the two

structures although the DFT model is translated along the x axis. Both patterns contain the double Bragg peaks at higher d spacings situated around ~4.5 Å and some other potential peak matching, although as mentioned the DFT pattern does not match the x-axis of the experimental work.

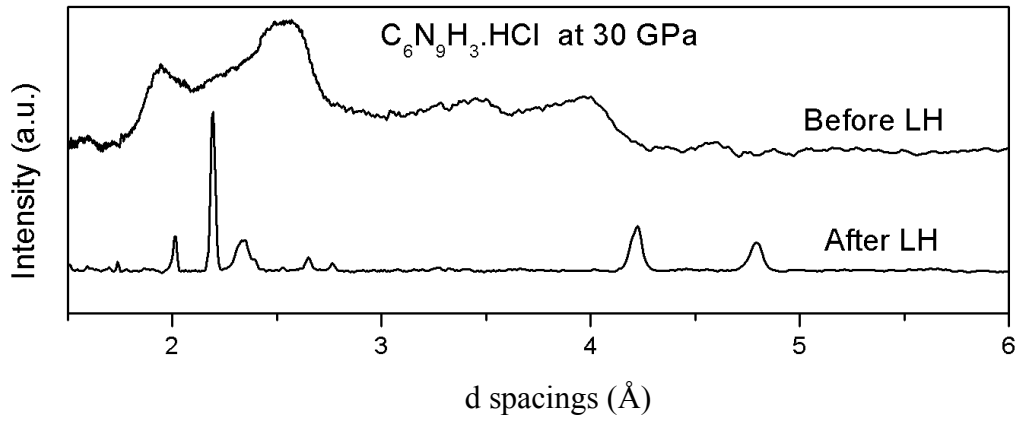

FIG. 54: A comparison of before and after laser heating of the g-$C_6N_9H_3$·HCl at 30 GPa. The PTM peaks have been masked out.

The fully recovered sample after LH was then attempted to structurally refinement and a structural model was attempted to be established. First, the sodium chloride peaks were indexed and identified correctly as having a *Fm*3*m* space group. After modelling the NaCl, the position of the seven strongest peaks were indexed in Dicvol which proposed a few tetragonal, hexagonal and orthorhombic cells. Since the starting material was hexagonal and also the indexing software had given this type of primitive cell the greatest relative stability, the hexagonal cell seemed the best choice. Following this, the diffraction peaks belonging to the sample were re-indexed and a number of possible options were given using CRYSFIRE with relative stabilities. The best match with using Le Bail refinement was with the $P6_3$ and $P6$ space groups, although a systematic absence of the (003) reflection using $P6_3/m$ might indicate the $P6$ group as a more accurate description of the unit cell (FIG. 56). Although the space groups, as high as $P6_3/mmc$ and $P6_3/mc$ were suggested.

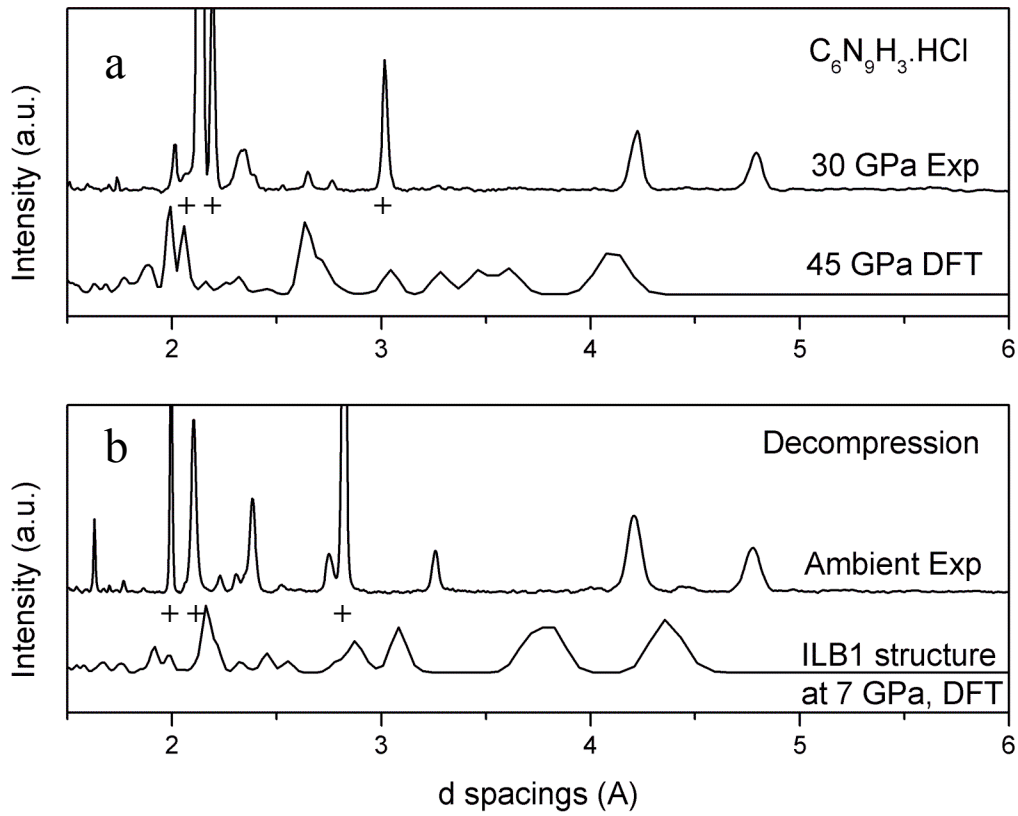

FIG. 55: A comparison of the XRD pattern of the experimental data after laser heating and the simulated patterns of the ILB1 structure from the DFT calculations. In both plots the position of the NaCl diffraction peaks are identified by +. (a) The plot illustrates the experimental data immediately after laser heating compared to a DFT generated pattern of the closest pressure point. (b) The plot is of the experimental structure at ambient conditions following the subsequent decompression compared to lowest calculated ILB1 structure available.

An initial attempt was made at Rietveld refinement of the XRD pattern using the atomic positions from the DFT calculation of the ILB1 structure at 7 GPa although this was calculated at a different pressure to that of the ambient XRD. The unit cell parameters from the Le Bail refinement were used along with the calculated atomic positions from the DFT calculations. This approach did not work as the DFT model was calculated to have a *P*1 symmetry and the positions of the atoms were not possible to fit into the special positions de ermined by the assigned space group. Several attempts were made by just filling in the general positions using the theoretical values. No real fit to the XRD pattern was ever generated and the structural model after refinement seemed implausible.

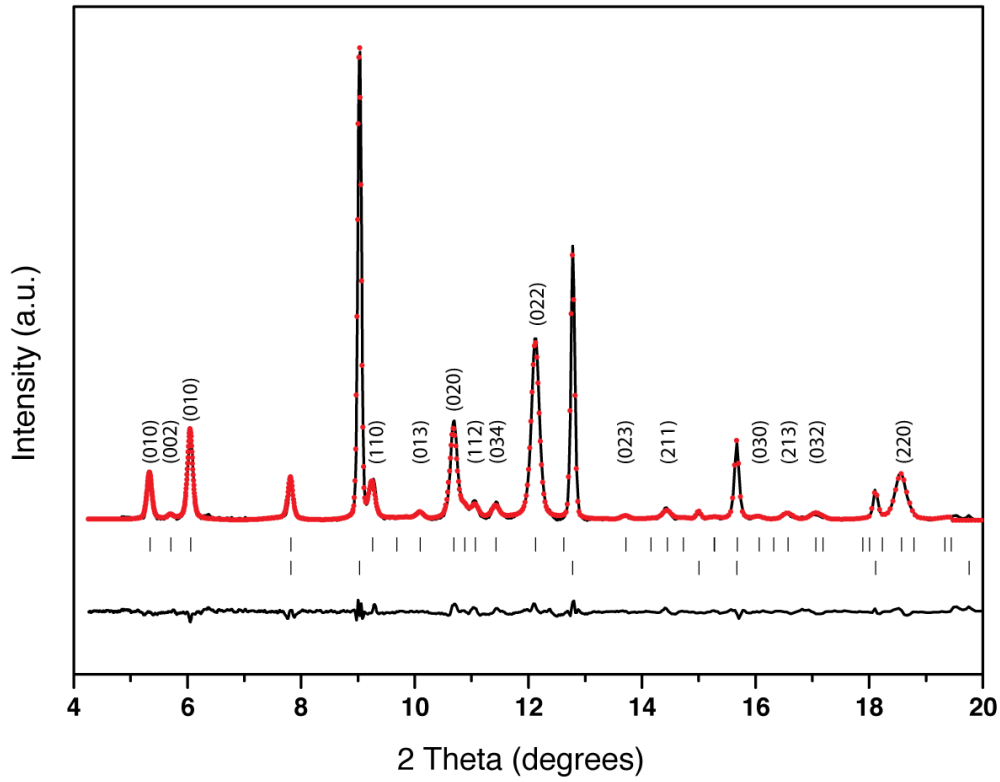

FIG. 56: The Le Bail refinement of the recovered laser heated sample at ambient conditions using the *P*6 space group. Diffraction peaks with intensity greater than 3% belonging to the recovered sample are indexed. The Rietveld method was used to fit the presence of the NaCl PTM. (The R values for the PTM phase are R_p: 1.38 R_{wp}: 1.81 R_{exp}: 1.20. The R values for the new recovered phase are R_p: 11.6 R_{wp}: 7.86 R_{exp}: 5.21. χ^2: 2.27 for the overall fit).

An attempt was made at trying to develop a structural solution for the XRD pattern to assist with the structural refinement. It was assumed that the LH procedure had not change the composition of the starting material and that a similar starting point with the same rigid planar C_3N_3 ring and a rigid framework proposed by Zhang *et al.* would be attempted. A rigid planar C_3N_6 fragment was defined and converted in a Z-matrix by iBabel. This consists of taking the Cartesian coordinates of the atomic position within the unit cell and transforming them into internal coordinates. The atoms are defined in this way as by their atomic number, bond length, bond angle and dihedral angle. By describing the atoms within the unit cell in this manner the information was then imported into the program FOX which is a *ab initio* crystal structural solution

software. With this software the Cl atoms were inputted with some anti-bump constraints to prevent the atoms from approaching each other too closely. The Cl atoms were relaxed in a number of positions, first trying to keep the planar rings parallel to the ab plane and then optimising their positions. This approach did not provide a structural model that matched the diffraction pattern well. Although some peaks were fitted within a reasonable degree of error, the overall model was not sufficient. Therefore, a correct structural model and the resulting structural refinement were not acquired.

3.4.1.1 Conclusion

The g-$C_6N_9H_3$·HCl system was laser heated at a pressure of 30 GPa after the system was identified to be going under some sort of structural changes as by the discontinuity of the V(P) plot at a pressure of around 25 GPa. The broad featureless XRD pattern of the g-$C_6N_9H_3$·HCl sample revealed to have formed a crystalline material after being laser heated. The new crystalline XRD patterns seem to have a close match to the predicted pillared structure as calculated by the *ab initio* work at 30 GPa and near ambient conditions. Although the predicted pillared structure has been suggested to collapse below a pressure of 7 GPa, the new crystalline material is recoverable to ambient conditions as a single phase from the point of synthesis. The new recovered crystalline phase was successfully indexed as hexagonal and fitted to a *P*6 space group. The Le Bail refinement was very convincing however, a structural model was not possible to be elucidated and this is something that is on going.

3.5 High-Pressure High-Temperature Synthesis and the Solid State Chemistry of Ti-O-N Systems

3.5.1 High-Pressure High-Temperature Transformations of Amorphous-Nanocrystalline Ti_xN_y Materials Obtained from Organometallic Precursors

3.5.1.1 Introduction

Many of the materials within the transition metal nitride and carbide compounds have a number of desirable physical properties [203] including high hardness and high melting points [129, 204]. In addition to being metallically conductive, some of the semi-metallic compounds can achieve relatively high values of the superconducting T_c (e.g. 12-17 K for cubic ε-NbN and hexagonal δ-MoN) [205, 206]. In contrast to non-transition metal superconducting materials which generally show a decrease in their T_c with high-pressure, the transition metal compounds and alloys seem to show a increase in T_c [207, 208]. Both the nitride and carbide analogous compounds often have hexagonal or cubic structures that are based on close-packed metal sublattices with N or C atoms occupying interstitial sites [203, 209]. The focus of this work has been to investigate the existence of titanium nitride polymorphs. To date only the rocksalt-structured phase "TiN" has been reported which is usually non-stoichiometric, forming compounds TiN_x with x ranging between = 0.6-1.2 and that can contain vacancies present on anion or cation sites [210, 211]. A similar compositional range is encountered for cubic B1-structured titanium carbide materials [209].

A new family of nitrides for the group XIV elements with composition M_3N_4 (M = Si, Sn, Zr) was discovered, using HP and carrying out synthesis by coupling the element with a nitrogen rich environment. Zerr *et al.* showed that this is also possible for group IV, having synthesized Zr and Hf nitrides using high-pressure techniques [80, 212]. First-principles calculations indicated that Ti_3N_4 spinel would be stable at high-pressure [213] and calculations by P. Kroll [31] go further to suggest that a number of Ti nitride polymorphs would be

accessible with the application of HP. Attempts have been made by to synthesise this matter by direct reaction between the elements, and from the lower nitride. However, all attempts have been unsuccessful and it is unlikely that such a material could be prepared using such a direct route because of the very high density and refractory nature of TiN. However, an alternative method we have set out to investigate is whether its synthesis could be achieved by a metastable route, starting with a chemically-produced precursor.

Instead of this HP route, Baxter *et al*. used a classical chemistry approach and originally reported the synthesis of what they identified as an amorphous solid titanium nitrides with a bulk composition near Ti_3N_4 [214, 215]. They had carried out reactions between organometallic species ($Ti(NMe_2)_4$, $Ti(NEt_2)_4$) and ammonia, followed by heat treatment in NH_3 or N_2 atmospheres at 450-1000^oC. This work was re-investigated recently by Hector *et al*. with a collaboration between Southampton University and UCL [216]. They found that reaction between $Ti(NMe_2)_4$ and NH_3 yielded a precipitate with composition $TiC_{0.5}N_{1.1}H_{2.3}$, which did not have a stoichiometry of $TiN_{1.33}$, which is required for Ti_3N_4. This indicates that whilst Baxter *et al.* did not produce Ti_3N_4, they did identify a synthesis route for the manufacture of materials with a high Ti:N ratio which could be used as precursors for DAC work.

It is expected that nitrogen and carbon in these materials behave similarly. Thermogravimetric analysis by Jackson *et al.* [216] had shown that a plateau between ~300-500^oC occurs in the weight loss curves of these compounds during their transformation into Ti(N,C) compounds. Heating to above 700°C in NH_3 had given rise to nearly stoichiometric TiN, with a particle size ~8-9 nm as measured by TEM. However, heating in N_2 atmosphere had led to 4-12 nm particles of a carbonitride phase, close to $TiC_{0.2}N_{0.8}$ in composition. Heating to ~450°C in N_2 gave rise to an X-ray amorphous black powder with metallic conductivity, with typical composition $TiC_{0.22}N_{1.01}H_{0.07}$ [216]. Analogous materials prepared by heating in NH_3 had lowered carbon contents and it was these materials that were used as precursors for the HPHT studies reported here.

The work by Jackson *et al.* had used X-ray absorption spectroscopy at the Ti K edge and EXAFS analysis to determine the T-(N,C) and Ti...Ti distances and coordination numbers. The bond lengths were consistent with octahedral sites such as those found in the rocksalt structure, but the

coordination number analysis indicated that ~50% vacancies were present on the Ti sites, and ~40% vacancies on the non-metal sites. These observations could be accounted for by a highly disordered structural model generally based on the local bonding present within the rocksalt structure, that could be formed from oligomers produced by addition of NH_3 groups to the tetrahedral $Ti(NMe_2)_4$ molecules, followed by condensation into corner- and edge-sharing $Ti(N,C)_x$ clusters with an octahedral geometry around the metal cation [216]. Although the powder X-ray diffraction pattern from an in-house diffractometer had indicated an "amorphous" structure, TEM analysis as well using synchrotron radiation had shown that the materials prepared at 450 ^oC actually contained rocksalt-structured $Ti(N,C)_x$ nanoparticles with a size range ~2-4 nm, embedded in an amorphous matrix.

In the present study, the precursor that had been prepared at 350 ^oC was selected to produce an amorphous structure or at least smaller nanoparticles then previously reported. The high-pressure and high-P,T behaviour of this material was examined with synchrotron X-ray diffraction and Raman spectroscopy, in a laser-heated diamond anvil cell (DAC).

3.5.1.2 Precursor Synthesis and Diamond Anvil Cell Loading Techniques

The precursors for the H-P H-T experiments were provided by Andrew Hector at Southampton University as part of a collaboration with UCL. The samples were prepared by reaction between $Ti(NMe_2)_4$ and NH_3, with slight variations in procedure to investigate whether an amorphous precursor could be synthesized [216]. In addition to being amorphous, it was required that the precursor should have a Ti:N stoichiometry as close as possible to 1:1.33 and that it should contain minimal organic impurities. Previous attempts at producing a truly amorphous material resulted only in nanocrystalline or composite materials.

The precursor materials were transported from Southampton to UCL inside sealed ampoules, and all manipulations with the sample as well as the preparation of the DACs were carried out inside a glove box. Before loading into the DAC, the solid precursor was pressed into pellets between two tungsten carbide blocks inside the glove box and loaded onto a tripod of specks of ruby

dust on the diamond culet. Diamonds with culets of 300 μm were selected. Re gaskets were pre-indented to ~30 μm thickness and electro-eroded with a 100 μm diameter hole. N_2 was selected as the PTM and it is loaded into the DAC cryogenically by submerging the DAC in a liquid nitrogen bath. The nitrogen seeps into the DAC through a very small opening between the top diamond and the gasket; the DAC is then closed after a period of 20 minutes.

Samples	Description of sample preparation
678a	$Ti(NEt_2)_4$ heated with liquid ammonia in an autoclave at ~50-60 °C overnight and the recovered powder heated under flowing dry ammonia at 350 °C
678b	Same as above but recovered at 450 °C
679a	$Ti(NEt_2)_4$ dissolved in a small amount THF and then a large excess of liquid ammonia condensed into the solution. Allowed to evaporate over several hours and the recovered powder heated under flowing dry ammonia at 350 °C
679b	Same as above but recovered at 450 °C

TABLE 8: A description of the different sample preparation available to high-pressure studies.

One sample, 679a, was selected for LH experiments as its synthesis method made it most likely to be amorphous (we were not able to determine whether the sample was truly amorphous as the in-house diffractometer cannot identify nanocrystals). The pressure of this sample was mechanically increased to 17 GPa and it was heated for several short consecutive heating periods using a 150 W CO_2 laser. Pressures inside the DAC were measured with the ruby fluorescence technique [85]. The sample was investigated using Raman spectroscopy and a change in spectrum was led to a stop of LH. Prior to this the 679a sample had been taken up to 30 GPa at ambient T and investigated using a Raman probe. A custom-built microbeam instrument was used to obtain Raman spectra [119]. The scattering was excited with the 514.5 nm line of an air-cooled 50 mW Ar^+ laser focused into the DAC using a Mitutoyo 50SL objective. The Raman scattered signal was collected in backscattered geometry

through the same objective. Kaiser® SuperNotch® filters were used to discriminate the incident laser from the Raman scattering. Spectroscopy was carried out using a 500 mm Acton® 300 spectrometer and a liquid N_2-cooled back-illuminated Si CCD detector. Following this, the pressure was increased to 28 GPa and then the sample was decompressed to ambient conditions.

Sample 679a was then analyzed using *in situ* high-pressure angle-dispersive synchrotron X-ray diffraction at the I15 beamline at the Diamond Light Source (Didcot, UK: $\lambda = 0.442110$ Å). Diffraction patterns were collected with an image plate detector (MAR345). The two-dimensional diffraction images were analysed using Fit2D software yielding one-dimensional intensity *vs.* diffraction angle 2θ patterns [169].

3.5.1.3 Results and Discussion

The initial XRD patterns taken at UCL using a Bruker diffractometer ($\lambda = 1.540$ Å) showed all four precursors to be totally amorphous. However, having taken the sample to the DLS, the angle-dispersive synchrotron X-ray experiments revealed that the samples exhibited diffuse Debye-Scherrer rings. Integrating the diffraction patterns gave rise to a broad 1-D diffraction pattern similar for all of the samples. Having nominated sample 679a for a full investigations the maxima for the Bragg reflections occurred at 10.41, 12.05, 16.97, 20.59 2θ ($\lambda = 0.442110$ Å). The preparation procedure for sample 697a and the fact it was annealed at a lower temperature has intended to give an amorphous sample, however as the synchrotron data revealed, all the samples seem to have the same FWHM and therefore assumed to be of the same crystallite size.

Baxter *et al.* had originally used such patterns to indicate the "amorphous" nature of these materials [215]. However, the positions and relative intensities correspond to a pattern calculated for nanostructured B1-structured Ti_xN_y materials, consisting of nanoparticles ~4 nm in dimension (FIG. 57). This observation is consistent with the detection of 2-3 nm sized nanoparticles embedded within an amorphous "matrix", determined from the TEM, XAS and EXAFS analysis by Jackson *et al.* [216]. The dimension of these

nanoparticles correspond to approximately 4-5 times the cubic unit cell edge length of rocksalt-structured TiN/TiC compounds (i.e., a_o~4.2 Å).

Sample 679a was then taken to a pressure of 17 GPa in a DAC and laser heated in short consecutive burst at a temperature of 1400 K. Following this the system was characterised *in situ* at HP and upon recovery to ambient conditions following the high-P, T experiments by a combination of synchrotron X-ray powder diffraction and laboratory Raman spectroscopy in the DAC [217]. Both the diffraction and spectroscopy data revealed the formation of a new set of peaks and bands uncharacteristic of the thermodynamically stable TiN rocksalt phase.

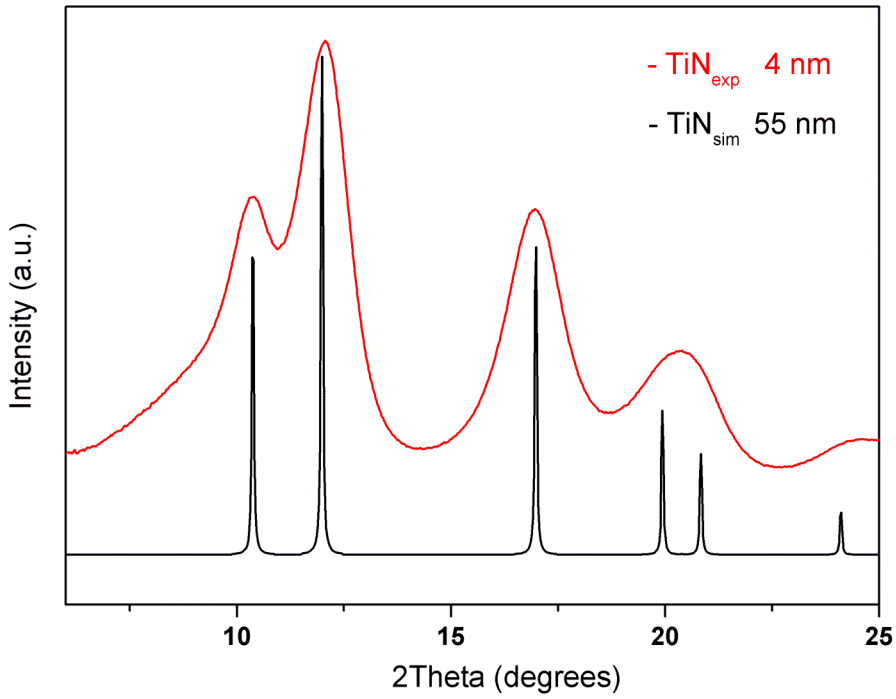

FIG. 57: The experimental XRD pattern of sample 679a shown against the simulated XRD pattern of the TiN. The crystallite size of the grains in sample 679a were analysed to be ~ 4nm by using the Scherrer equation and are compared to an ideal TiN pattern.

3.5.1.3.1 Raman Spectroscopy

Raman spectroscopy of the nanocrystalline-amorphous precursor was possible due to a particular phenomenon which occurs in such materials with a rocksalt structure. This phenomenon relates to the defects or vacancies which may be present on cation or anion sites and are observed in TiNx materials. There are usually no Raman active vibrations at the Brillouin zone centre in the *Fm*3*m* B1 structure, but vacancies or defects within the cubic rocksalt structure remove the translational symmetry and thus the definition of vibrational propagation within reciprocal space [218]. This alters the normal selection rules and produces a vibrational density of states in the Raman spectrum that is normally only observed by inelastic neutron or X-ray scattering experiments [219-221].

In the Raman spectra at ambient conditions, all the TixNy samples exhibit the same broad, featureless bands at ~250 and ~630 cm^{-1} (FIG. 58). Sample 679a was selected for HP investigation using a DAC. At P > 12GPa, three well-defined bands emerge which are similar to the acoustic modes seen in the vibrational density of states (VDOS) spectrum of $Ti(N,C)_x$ compounds with a rocksalt structure [220, 221] (FIG. 58). Thus, the amorphous presence in the sample may be undergoing densification, enabling the material to support acoustic mode vibrations with a dispersion over an appreciable correlation length similar to that encountered in the crystalline structure. However, there are only two peaks in the 200-340 cm^{-1} region of the VDOS spectrum of TiN and these correspond to the transverse and longitudinal acoustic mode branches. The triple peaked structure of the Ti_xN_y spectrum may correspond to a separation of the TA1 and TA2 branches as a result of anisotropy among the transverse acoustic mode propagation. Alternatively, the features in the low frequency region of the spectrum of the amorphous solid correspond to localised vibrations involving Ti translation modes.

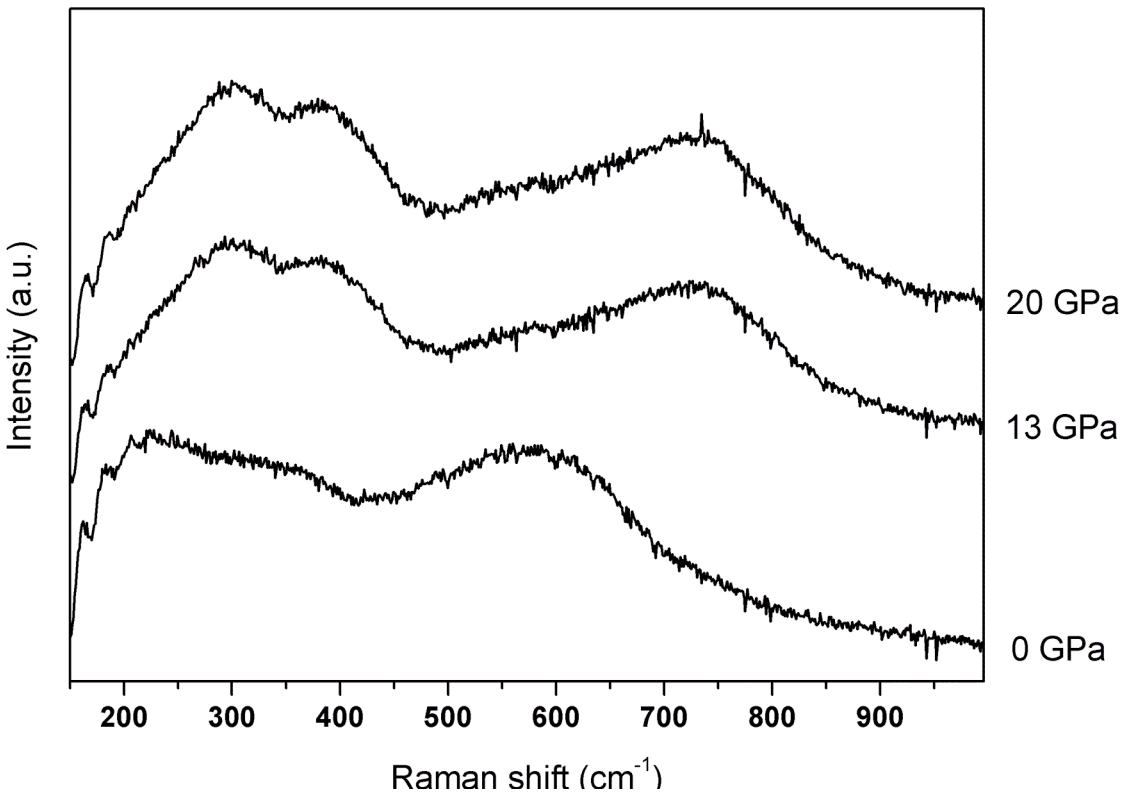

FIG. 58: Raman spectra of the 679a sample. This figure shows three Raman spectrum at different pressures and highlights the development of the two bands in the 300-400 cm^{-1} region.

On decompression, the triplet of well-defined bands disappears below 18-20 GPa and is replaced by the broad, low frequency feature observable before compression. The high frequency modes in the 500-800 cm^{-1} region remain broad during compression and decompression. They are likely to be associated with the local disorder caused by the anion and cation vacancies, resulting in local bonding environments within partially completed $Ti(N,C)_6$ octahedra and thus a broad distribution of Ti-N and Ti-C stretching frequencies. This work corroborates that of Jackson et al who have used X-ray absorption and EXAFS techniques to characterise the structure of $Ti_x(N,C)_y$ nanocrystalline-amorphous materials. They showed that the local structure was based on the rocksalt structured compounds TiN or TiC and that it contained ~40-50 % vacancies on both the cation and anion sites [222].

Further to the work on the Ti_xN_y system under pressure at ambient T, the HP behaviour of material prepared from the same precursor was investigated using Raman spectroscopy following LH at 17 GPa in the DAC (FIG. 59). On LH, new Raman bands appear at ~500 cm^{-1} and at ~420 cm^{-1}, both not associated

with the rocksalt structure of Ti_xN_y (FIG. 59). These may indicate that LH has caused the synthesis of a new material. The high frequency modes at 500-800 cm^{-1} remain broad up to a pressure of 65 GPa; this may confirm the local disorder associated with anion/cation vacancies, or it may be caused by the presence of untransformed precursor remaining in the sample chamber.

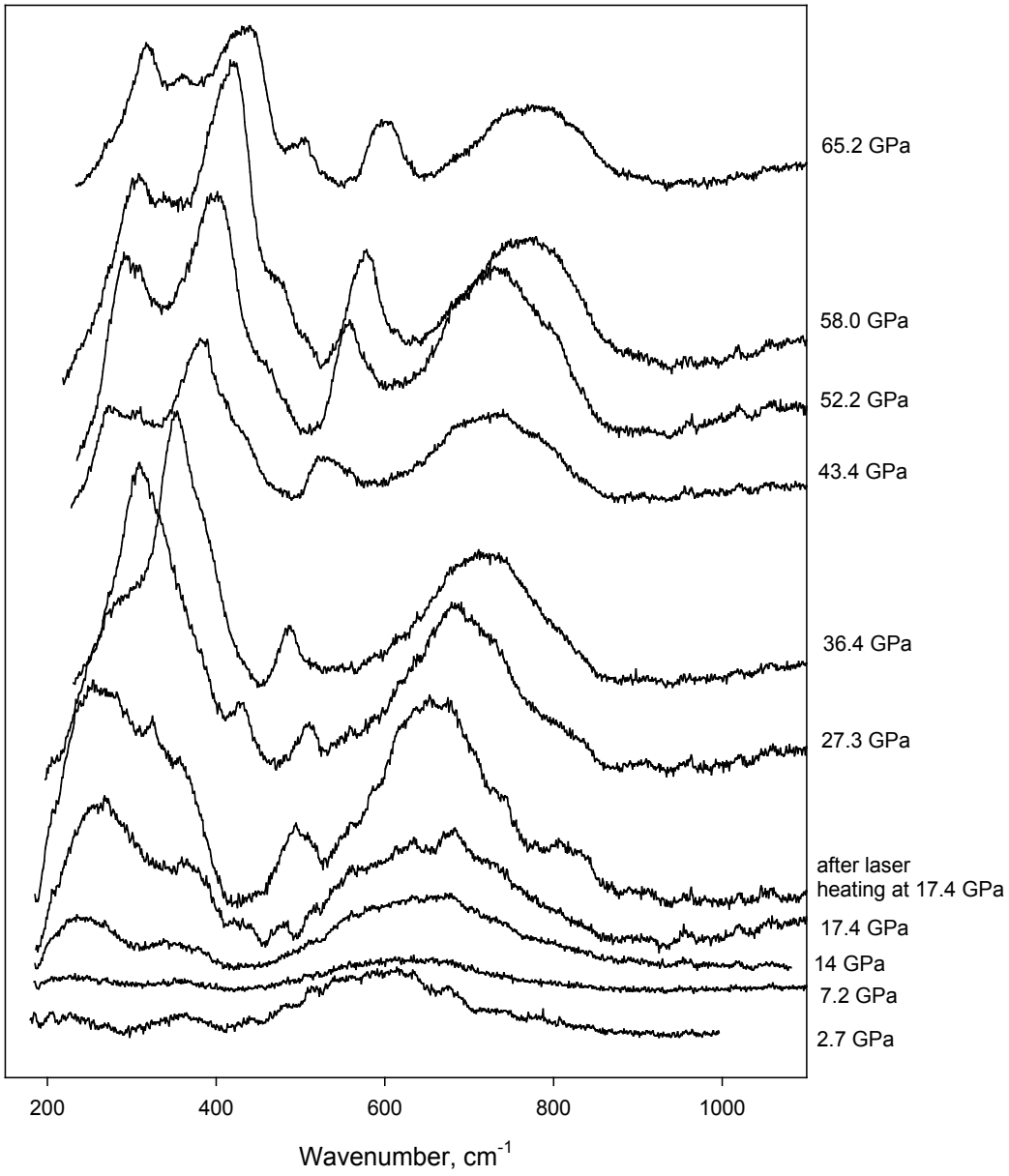

FIG. 59: Raman spectra of the Ti_xN_y nanocrystalline-amorphous material compression up to 65 GPa. At a pressure of 17 GPa the sample was laser heated before commencing with the compression run. Spectrum was obtained at UCL and is provided by Dr. Olga Shebanova who is currently working at APS.

3.5.1.3.2 Synchrotron XRD of Ti_xN_y Sample

The sample was initially taken up in pressure, using a membrane driven DAC, to a membrane pressure of 50 bar (around 45 GPa, refer to FIG. 13 for calibration curve) without the presence of a PTM (FIG. 60). This was to confirm the presence of the expected single phase of the rocksalt structured Ti_xN_y up to and beyond the desired pressure for laser heating. The sample preparation and loading were then carried out to imitate that of the Raman spectroscopy experiment and to reproduce the same synthesized material and analyse using synchrotron X-ray powder diffraction.

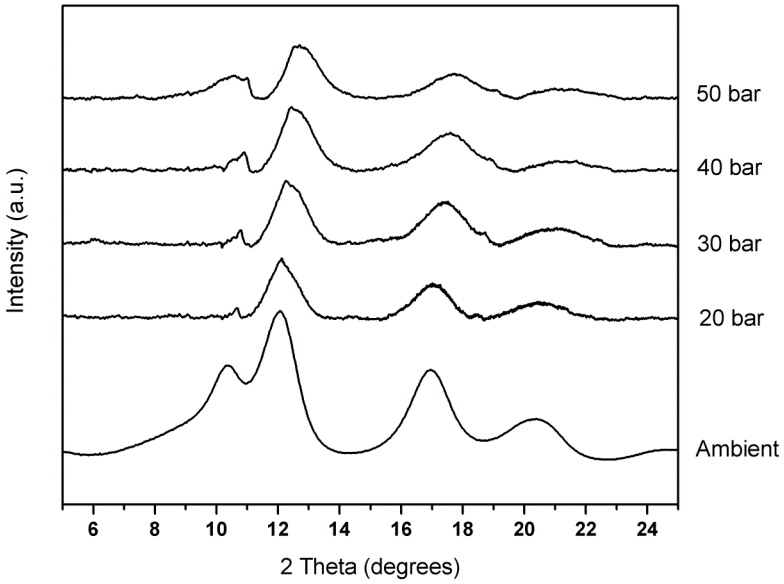

FIG. 60: A XRD pattern of the 679a sample upon compression with no PTM

Following this the sample was loaded in a DAC along with nitrogen as the PTM and taken up to 17 GPa in pressure. The sample was then gently laser heated with a ~50 W CO_2 and monitored *in situ* with Raman spectroscopy in the laboratory. Once the emergence of the new Raman band at ~500 cm^{-1} was observed, the LH was stopped and the sample, inside the DAC, was transported to the DLS and analysed with angle-dispersive XRD. A new series of crystalline X-ray diffraction peaks were observed with the sample and which could be followed as the sample was returned to ambient conditions. The diffraction patterns before and after laser heating are illustrated in FIG. 61. The diffraction pattern after LH clearly shows the presence of a new crystalline material formed.

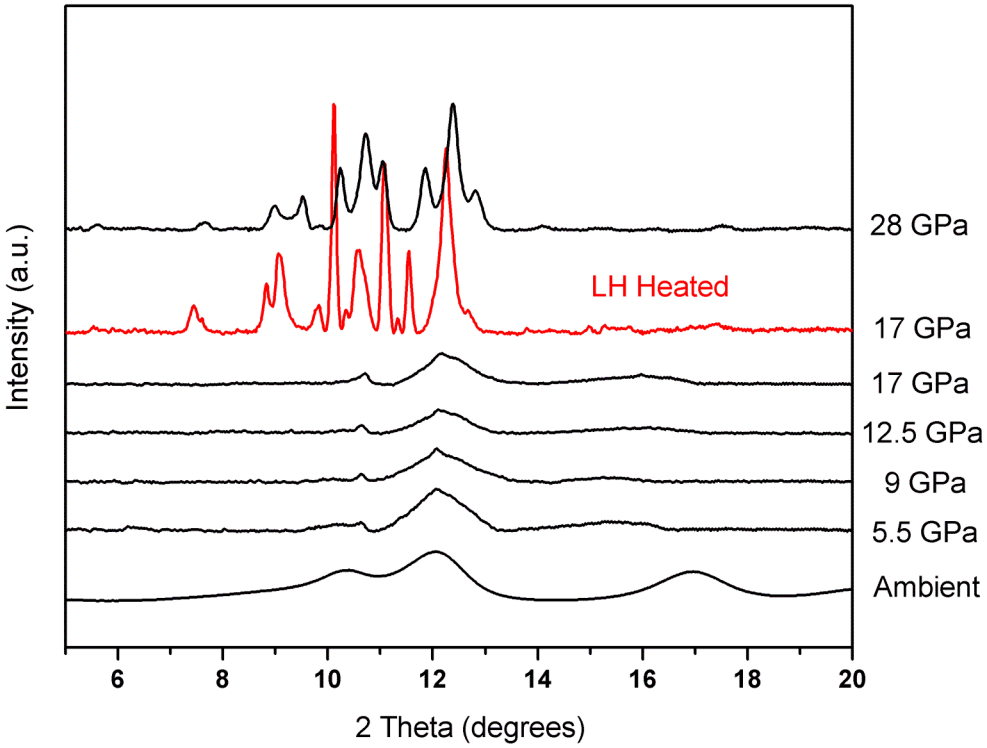

FIG. 61: The hydrostatic compression of sample 679a is shown up to 17 GPa. Following this, the data set highlighted in red is after the sample was laser heated for a period of 5 mins using a 50 W CO_2 gas laser. The compression was then continued with the laser heated sample to 28 GPa.

An attempt was made to characterise the new crystalline material by indexing the new HP structure. The 13 peaks observed at 17 GPa could not be indexed satisfactorily *ab initio* as a single phase in any reasonable space group, even one with a low symmetry. The sample was therefore taken up in pressure to 28 GPa to determine whether the XRD pattern at this higher pressure could be indexed. This was also unsuccessful and the sample recovery to ambient conditions was then attempted to determine whether a single phase could be isolated and indexed. At 3 GPa four peaks can be observed which are identified as belonging to the HP phase, at d-spacings of 2.115, 2.446, 2.546 and 3.511 Å. This structure can be followed from 17 GPa although the difficulty has been confirming the presence of other phases as the initial XRD pattern at 17 GPa could not be indexed successfully, suggesting a mixed-phase pattern. The 3 GPa pattern has two of the peaks with shoulders, suggesting possibly a mixed phase (FIG. 63). These were not included in the indexing solution. The sample could be recovered to ambient conditions and was removed from the DAC and analysed using synchrotron radiation techniques.

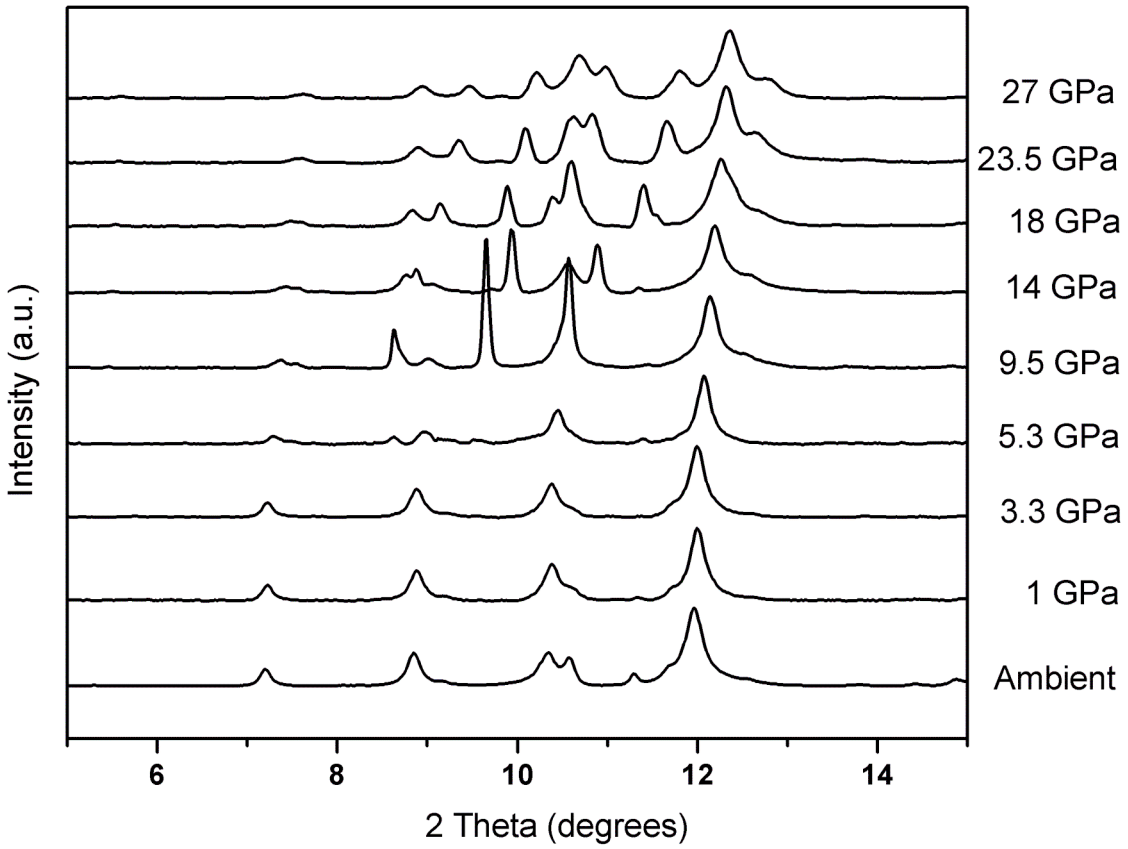

FIG. 62: A XRD pattern obtained during decompression of sample 679a after LH from 26 GPa. The sample was LH at 17 GPa and was taken to 28 GPa before decompression commenced.

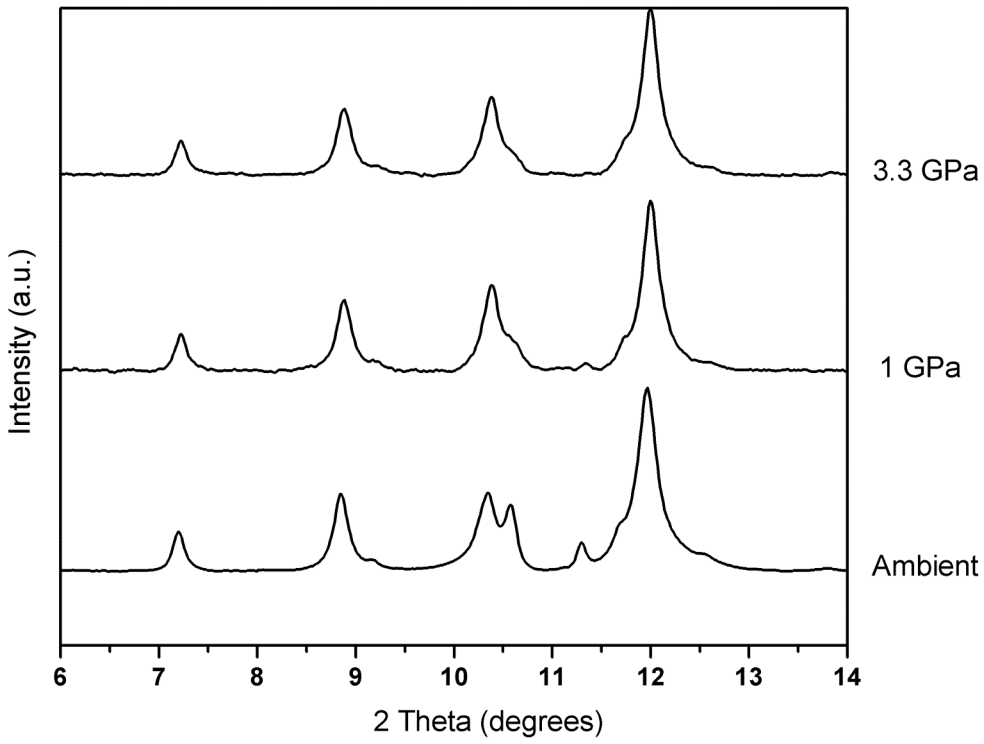

FIG. 63: A close up of the decompression XRD data from FIG. 62

Attempts were made to index the HP phase. The 4 peaks observed of the HP structure could be indexed satisfactorily *ab initio* as a single phase in an orthorhombic space group. A number of different indexing packages were used and four solutions were identified, all as being orthorhombic and with merits of figure ranging from 228.60 to 157.25. The XRD data was refined using a Le Bail method and is shown in FIG. 64. Although the overall refinement suggests a possible fit there are concerns that having such a limited number of reflections observable introduces too much uncertainty with matching four reflections to three orders of freedom within the orthorhombic unit cell.

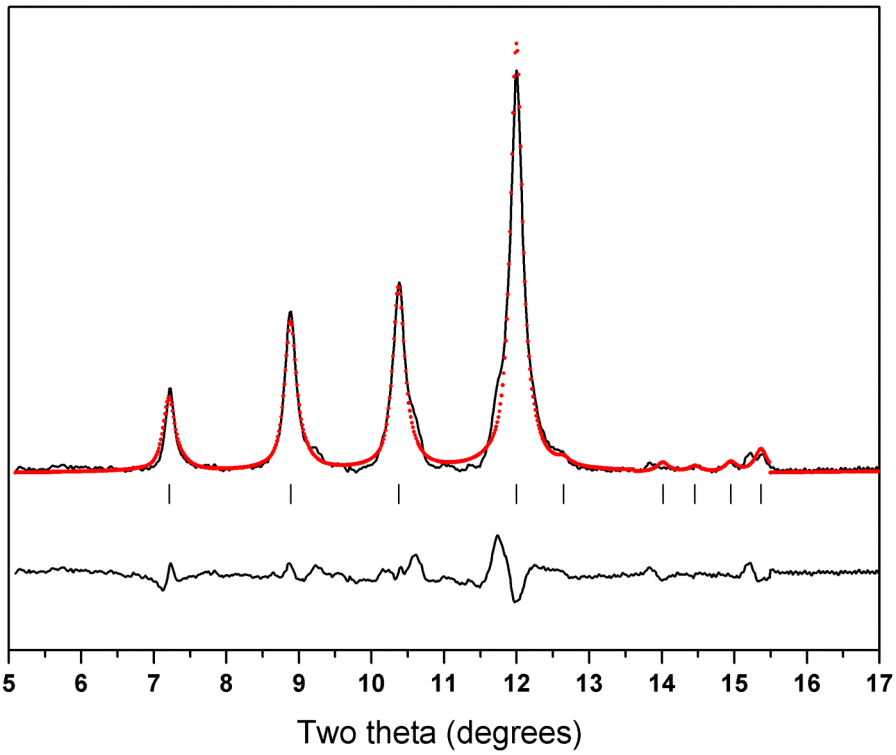

FIG. 64: The hydrostatic decompression of Ti_xN_y at 3 GPa. The Le Bail refined X-ray diffraction pattern is of the recovered high pressure phase of the system and was carried out following indexing.

The lattice parameters of the structure as determined by Le Bail refinement were given as a = 4.012 (3) Å, b = 3.513 (6) Å, c = 4.888 (3) Å (V_o= 68.873 (9) Å^3) within space group $Pmc2_1$ R_{wp} value of 6.21. These values are comparably smaller than those reported for the orthorhombic phase of Zr_3N_4 by Lerch *et al*. [223, 224] (TABLE 9). With this factor considered it is reasonable

to assume that either the assigning of an orthorhombic unit cell is not describing the material correctly since there is such a large discrepancy between the experimental work and its group 14 analogous counterpart or that the new orthorhombic system is considerably smaller.

Lattice Parameters	*a* (Å)	*b* (Å)	*c* (Å)
	9.7294 (5)	10.8175 (6)	3.2810 (1)
	Fractional Coordinates		
Atom/Site/Oxi. state			
Zr1 / 4c / 4	0.3922(4)	0.0934(4)	0.25
Zr2/ 4c / 4	0.2671(4)	0.3519(4)	0.25
Zr3/ 4c / 4	0.238(3)	0.710(3)	0.25
N1 / 4c / -3	0.138(3)	0.984(3)	0.25
N2 / 4c / -3	0.999(3)	0.227(2)	0.25
N3 / 4c / -3	0.606(3)	0.024(2)	0.25
N4 / 4c / -3	0.4316(4)	0.6241(4)	0.25

TABLE 9: Lattice parameters of orthorhombic-Zr_3N_4 ($Pna2_1$) as reported by Lerch *et al*. Volume of unit cell is given as 345.318 (8) $Å^3$.

Before continuing with further attempts at refinement the sample was removed from the DAC and examined using micro-probe analysis with a SEM. The major obstacle with using micro-probe analysis on a system like this is that the titanium L-edge and the nitrogen K-edge overlap and it is very difficult to use this method for identifying relative ratios of these elements present in a sample. However, this method did confirm that the sample only contained Ti and N and no other elements were identified in the sample. A photograph of the recovered sample is shown taken using SEM (FIG. 65).

Having confirmed only the presence of the starting elements, it was suggested that the initially identified orthorhombic unit cell could be describing a distorted form of the predicted spinel phase of Ti_3N_4. Therefore, attempts at indexing a cubic unit cell to the experimental data were carried out. However, no reliable solution was given by the indexing software relating to a cubic unit cell and so attempts were made at trying to match the experimental data to a number of different observed polymorphs of group IV X_3N_4 systems of hafnium and zirconium with titanium substituted into the metal sites.

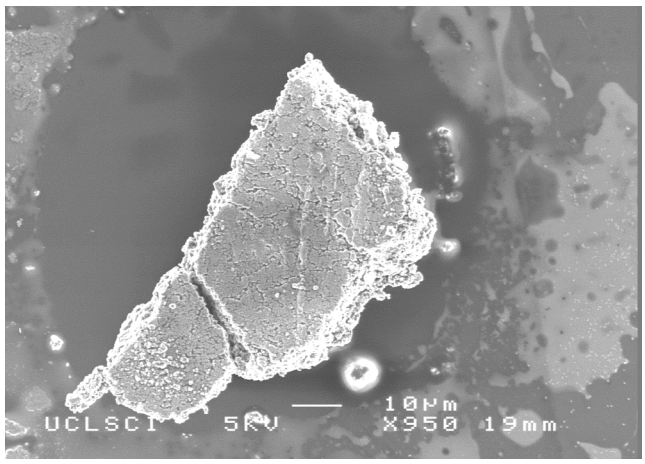

FIG. 65: A SEM image of the recovered sample after LH.

The first comparison analysed was taking the orthorhombic Zr_3N_4 structure and substituting in titanium into the metal sites in place of zirconium. An attempted at comparing the possibility of the titanium polymorph of the already reported zirconium analogous was carried out. The pattern generated did not match that of the experimental work observed, confirming that the material synthesised in HPHT does not match that of orthorhombic-Zr_3N_4 (FIG. 66 (a)). A similar treatment was given using the cubic-Hf_3N_4 phase and entering titanium for the hafnium cations (FIG. 66 (b)). The unit cell information of both the cubic phases of hafnium and zirconium nitride are given in TABLE 10. Once again the plot simulated did not match that of the experimental data collected. Obviously, the major difference observed with the replacement of the cation sites with titanium in both plots described was the change in the overall intensity of the reflections due to the weaker scattering contribution from the lighter metal, titanium.

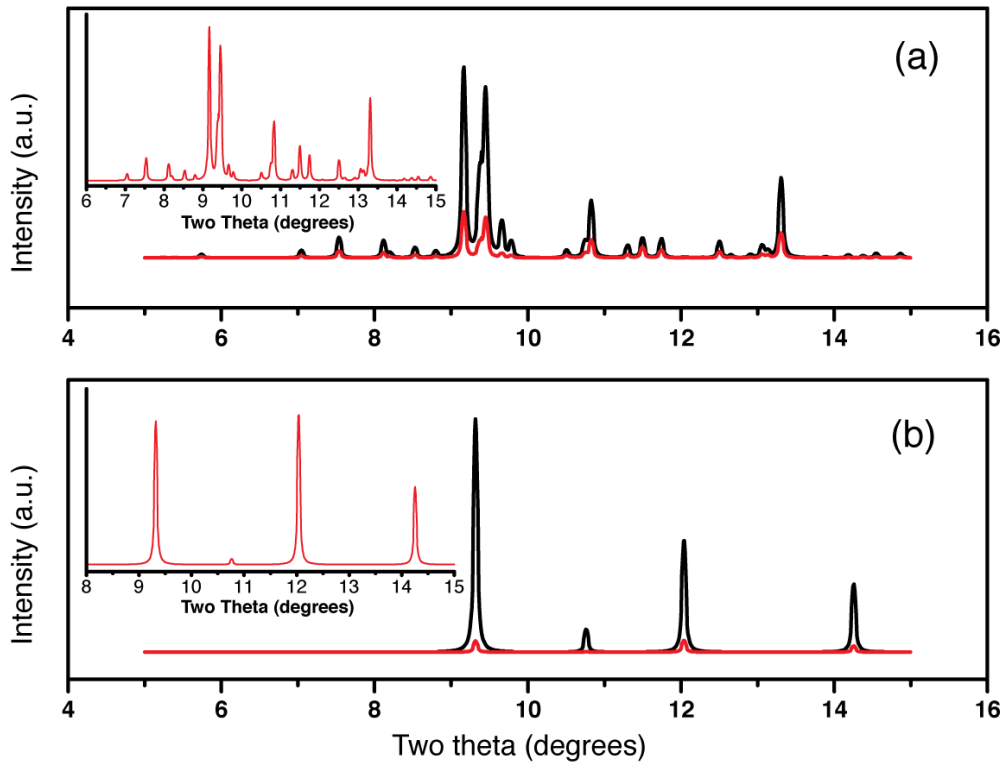

FIG. 66 (a) (Black) Zr_3N_4-ortho, (Red) Zr_3N_4-ortho with Ti substituted in metal sites. The unit cell parameters are given in TABLE 9. (b) (Black) Hf_3N_4-cubic, (Red) Hf_3N_4-cubic with Ti substituted in metal sites. The unit cell parameters are given in TABLE 10. In both plots the XRD pattern shown in the top right corner is of the titanium substituted unit cell.

Lattice Parameters	*a* (Å)	*b* (Å)	*c* (Å)
	6.701 (6)	6.701 (6)	6.701 (6)
	Fractional Coordinates		
Atom/Site/Oxi. state	*x*	*y*	*z*
Hf / 12a / 4	0.375	0	0.25
N / 16c / -3	0.063 (3)	0.063 (3)	0.063 (3)

Lattice Parameters	*a* (Å)	*b* (Å)	*c* (Å)
	6.740 (6)	6.740 (6)	6.740(6)
	Fractional Coordinates		
Atom/Site/Oxi. state	*x*	*y*	*z*
Zr / 12a / 4	0.375	0	0.25
N / 16c / -3	0.063 (3)	0.063 (3)	0.063 (3)

TABLE 10: (top) Lattice parameters of cubic-Hf_3N_4 (*I*4-3*m*). (bottom) Lattice parameters of cubic-Zr_3N_4 (*I*4-3*m*). Both systems are reported by Zerr *et al*. [225].

The simulated patterns described above do not give the correct relative intensity for the reflections as determined by the atomic position within the unit cell. Ignoring this factor the unit cell of the cubic titanium substituted nitride was modified to establish whether it was possible to achieve a reasonable fit with that of the experimental data in terms of the positions of the reflections nd hence describing a similar unit cell shape and size. The unit cell of the predicted structure had to be expanded to achieve a diffraction pattern to match that of the experiment which seems to be unreasonable since it would be expected that the titanium nitride would have a smaller unit cell than that of its larger hafnium and zirconium nitride counterpart. This details some of the difficulties involved in elucidating a reasonable structure for this new crystalline material since there such limited number of peaks are observed. The ability to extracted information is hindered and any further progress in terms of crystallographic analysis must involve the use of either an attempt at bulk synthesis since the pressure and temperature conditions are within the capabilities of a large volume press or the DAC experiment must be repeated using a wider backing plate aperture.

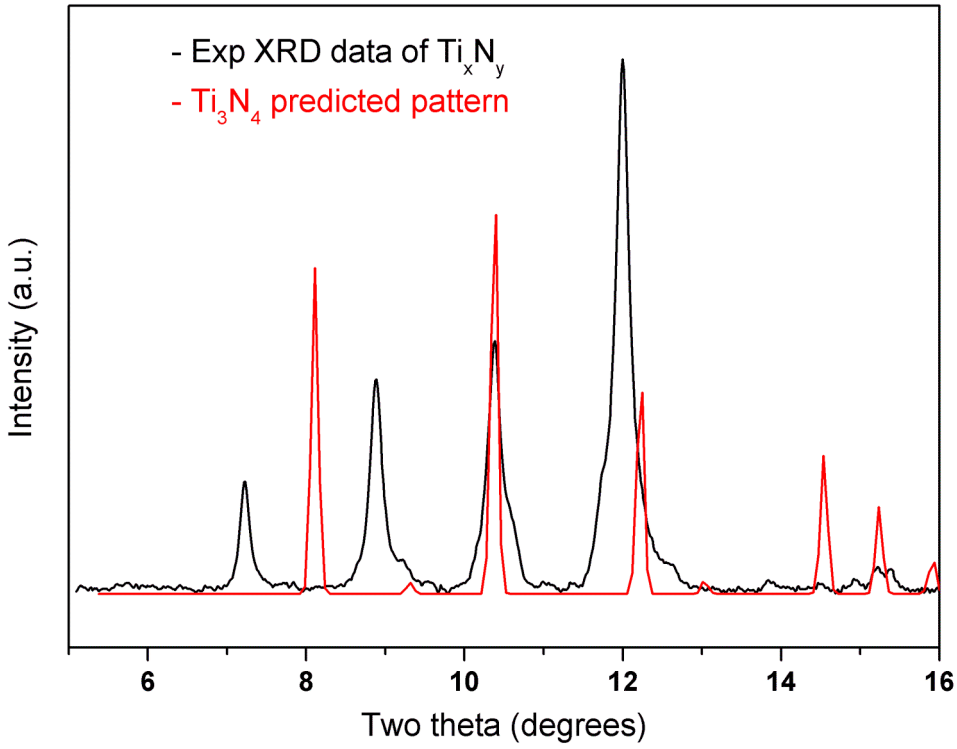

FIG. 67: A plot of the experimental XRD at 3 GPa of the TixNy sample after laser heating compared to the simulated XRD pattern of cubic-Ti_3N_4 using the atomic position given for cubic-Hf_3N_4. The unit cell size has been expanded in attempting to fit the two patterns.

3.5.1.4 Conclusion

As part of the second class of system investigate we conducted a study of " Ti_3N_4" materials prepared from organometallic precursors (i.e., reactions between NH_3 and $Ti(NMe_2)_4$), followed by heating at T=700-1000 K in N_2 or NH_3 atmospheres, that had been shown to be "amorphous" from X-ray diffraction experiments. Here, our initial goal was to explore the potential formation of a new spinel-structured " Ti_3N_4" material by treating the amorphous precursors under high-P,T conditions. However, during our initial characterisation of these precursor-synthesised materials, we made the following observations. First, the amorphous powders treated at high-T in NH_3 atmospheres contained substantial amounts of C and H as well as N, depending upon the synthesis/processing conditions; however, the overall $Ti_x(N,C,H)_y$ composition was close to x:y = 3:4. Next, all the compounds formed had a structure based on the B1 rocksalt pattern formed by TiN and TiC. A specific precursor was chosen and taken to 17 GPa and laser heated. Both Raman spectroscopy and XRD experiments identified the appearance of a new set of peaks and the emergence of a new material.

Attempts at indexing the high pressure XRD after laser heating were hindered with the presence of broad features. Following on from the subsequent decompression the data collected at lower pressures were successfully indexed and described the possibility of an orthorhombic unit cell. The large difference in the volume determined from refinement compared to values in the literature for the orthorhombic-Zr_3N_4 material give rise to the possibility that either the unit cell solutions is not realistic or that the orthorhombic material synthesised has a much smaller unit cell then that of its counterpart. A comparison to a cubic structure of the group IV nitrides also did not provide a reasonable match. Although the possibility of having synthesised and observed an orthorhombic unit cell is considered the possibility that the system could be a distorted form of the predicted spinel phase is not ruled out. In summary, the emergence of a new crystalline material after the treatment of HPHT is clearly evident and is recoverable to ambient conditions. The identity of the system has not been completed, however, the formation and recovery of a new crystalline material composing purely of titanium and nitrogen is a very exciting and encouraging result.

3.5.2 High Pressure Behaviour and Polymorphism of Titanium Oxynitride Phase, $Ti_{2.85}O_4N$.

3.5.2.1 Introduction

A new titanium oxynitride phase, $Ti_{2.85}O_4N$, has recently been discovered by the synthetic route of atmospheric pressure chemical vapour deposition [37, 226]. Only a small number of titanium oxynitride polymorphs are known to have been synthesised at present. There are two major groups of these that have been investigated: firstly, the TiO_xN_y phases, which exist as a solid solution between the two rock-salt structured end members TiN and TiO (where $x + y \sim 1$), and also the nitrogen doped TiO_2N_x phases, where the nitrogen doping is less than 5% and often less than 1%. The latter of these has been identified as a potential visible light photocatalyst, as has $Ti_{2.85}O_4N$. This, with the relative scarcity of known titanium oxynitride phases, makes it a strong candidate for further study [227, 228].

Ti_3O_5 is considered as a n=3 member of the titania Magneli phases and is found at room temperature as an insulator with a monoclinic crystal structure (β). A first phase transition is observed in this material at 450 K with the system transforming to a second monoclinic structure (β') with a sharp 6% increase in the unit cell volume. Extended heating to 500 K leads to a second phase transition to the orthorhombic α crystal structure [229]. The phase transition and volume increase at 450 K are associated with an insulator to metal transition. The β phase which is formed at low temperature has the titanium d-electrons localised in a metal-metal bond which above the transition temperature become delocalised - it the breaking of the metal-metal bond which results in a relaxation of the structure and unit cell expansion. Previous work has found that reduction of the Fermi level by substituting titanium ions for cations of lower charge causes a lower temperature of transition to be observed as the number of electrons available for metal-metal bonding is reduced [230-232]. Hyett *et al.* have recently demonstrated that a similar effect can be observed using higher charge anionic substitution in the compound $Ti_{2.85}O_4N$ which at room temperature is found to crystallise with the α crystal structure, associated in Ti_3O_5 with temperatures above 500 K [233].

The application of extreme compression has been shown to be a powerful tool in materials chemistry for synthesis and phase discovery, where systems undergo a forced volume change that correlates to phase and structural transformations [11]. When applied to solid state compounds [234], these techniques can bring fundamental changes to structural, thermal, optical or mechanical properties of matter. The use of high pressure can therefore lead to the formation of new dense crystalline materials [168, 235] which are not accessible through other techniques. A high-pressure study by Åsbrink *et al.* [236] on β-Ti_3O_5 (*C*2/*m*) up to pressures of 40 GPa was unable to identify the presence of any of the proposed phases as observed by varying the temperature of synthesis. In this report we present the first high-pressure X-ray diffraction studies on the novel compound $Ti_{2.85}O_4N$. Using a diamond anvil cell we have carried out compression studies and observed two high-pressure phases. Compressibility measurements are reported for the ambient structure and the high pressure phases are indexed. This work had been carried out in collaboration with Dr Geoff Hyett and Professor Ivan Parkin.

3.5.2.2 Experimental Techniques

A sample of $Ti_{2.85}O_4N$ was prepared as described by Hyett *et al.* [37] *via* atmospheric pressure chemical vapour deposition from the reaction of gaseous $TiCl_4$ (Aldrich, 99.9%), ethyl-acetate (Fisher, Reagent grade) and ammonia onto a glass surface. The thin film was then delaminated and ground into a powder sample and its purity confirmed by X-ray diffraction. The $Ti_{2.85}O_4N$ was pre-compressed between tungsten carbide cubes before being loaded into a cylindrical DAC. For the hydrostatic compression runs nitrogen was used as the pressure-transmitting medium (PTM). Two diamond culet sizes were opted for: 300 μm for data collection up to 50 GPa and 200 μm for pressures recorded up to 68 GPa. Rhenium gaskets were pre-indented to a thickness of 30 μm and drilled using electro-erosion with holes with a diameter of 80 μm. Pressure was determined using ruby fluorescence [85]. X-ray diffraction experiments in the DAC were carried out at beamline I15 at Diamond Light Source (Didcot, λ_0 = 0.4441 Å) and station ID27 of the European Synchrotron Radiation Facility (Grenoble, λ_0 = 0.3738 Å). For the ambient $Ti_{2.85}O_4N$ XRD patterns were

recorded on an in-house Bruker diffractometer (λ_0 = 1.54 Å). All compression and decompression data were collected at I15. The data collected at ID27 were of the recovered material out of the DAC after compression; the micro-focused beam available at the high-pressure station was used to map the sample. The two-dimensional diffraction rings were recorded on either a CCD detector or a MAR 345 image plate and integrated with Fit2D [169] and analyzed using WinPLOTR, GSAS [237, 238], FullProf [170] and PowderCell [171].

3.5.2.3 Results

3.5.2.3.1 X-Ray Diffraction

Confirming the purity of the starting sample $Ti_{2.85}O_4N$ following chemical vapour deposition synthesis was vital for the high-pressure study. The choice of a pure starting sample enabled high quality powder diffraction patterns to be recorded of the material inside the diamond anvil cell up to ~20 GPa. The identity of the starting sample was confirmed by powder X-ray diffraction conducted under ambient conditions, producing a pattern that could be indexed in the *Cmcm* space group with lattice parameters, a = 3.80(1) Å, b = 9.62(1) Å and c = 9.88(1) Å, matching, within error, the previously published values [37]. An impurity peak at 2.52 Å was identified corresponding to TiC, however refinement of the phase fraction found that this impurity represented less than 0.5% of the sample by mass.

The complete X-ray diffraction data from all patterns collected under pressure were initially analyzed prior to any refinement methods (FIG. 69). This permitted the identification of any impurity present and the ordered cubic phase of the pressure transmitting medium. Using nitrogen as the pressure transmitting medium, 17 diffraction patterns were recorded between pressures of 2 to 30 GPa, at approximately 1 GPa intervals (FIG. 68). The unit lattice parameters at these pressures of the ambient phase are provided in TABLE 11. Le Bail refined x-ray results at 2, 8.3, 11.6, 14.2, 18.4 GPa are shown in FIG. 70.

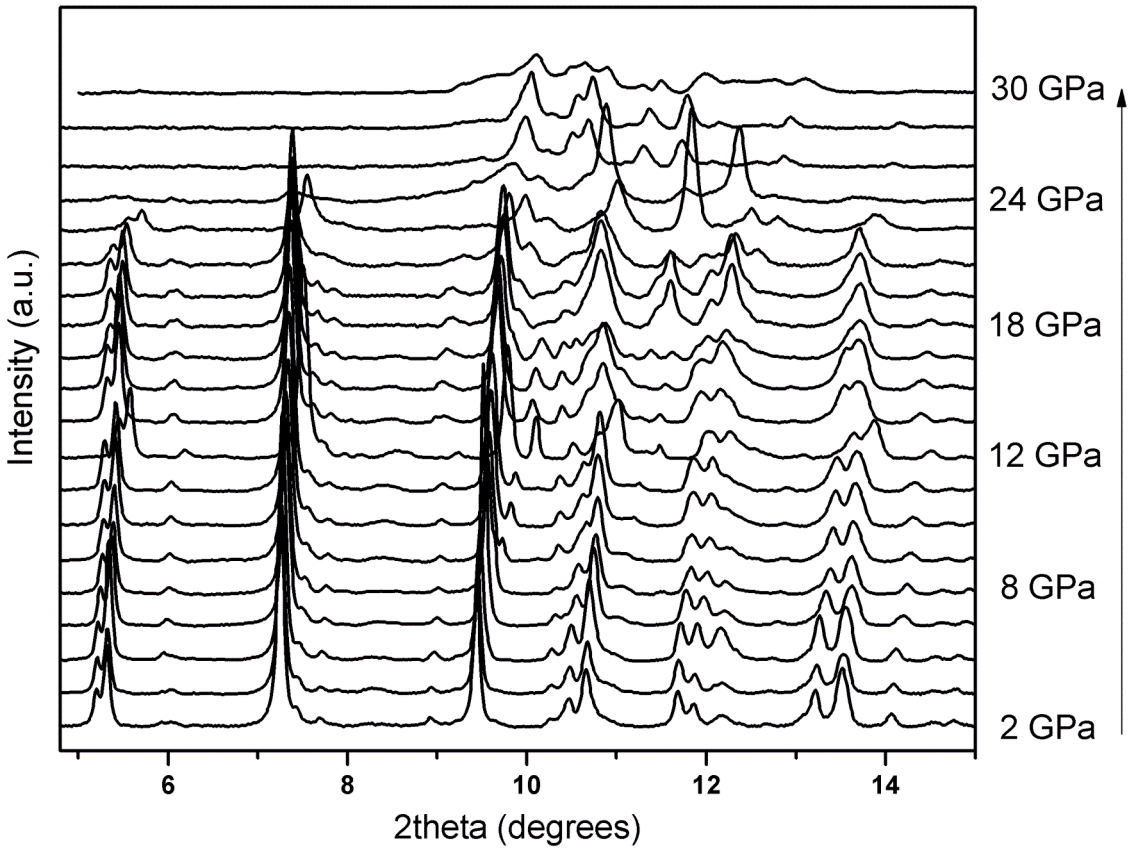

FIG. 68: Figure shows the compression of $Ti_{2.85}O_4N$ from a pressure 2 to 30 GPa. In total 17 diffraction peaks were collected at ~1.5 GPa intervals.

An earlier attempt at collecting synchrotron XRD data without the use of a PTM had led to poor-quality data and highlighted the importance of a good hydrostatic loading. A number of cryogenic loadings were carried out at station I15 and checked for crystallographic quality before commencing with the HP run. The initial few pressure steps were collected a number of times using different exposure times and different levels of rocking with the rotational stage on the diffractometer. Once the optimum conditions were confirmed and a suitable loading identified, the compression data was collected over a period of 18 hours as the earlier run had shown that rapid compression of the sample led to the transformation of an amorphous phase. Dr Geoff Hyett used GSAS and the EXPGUI suite of software packages and I myself used both GSAS and WinPLOTR to carry out a Le Bail refinement process to extract the lattice parameters of the ambient phase (*CmCm*) for each pressure data set recorded.

Pressure (GPa)	*a* (Å)	*b* (Å)	*c* (Å)	Volume (Å^3)
2	3.7751(2)	9.577(1)	9.8053(8)	354.51(3)
3	3.7710(2)	9.5644(9)	9.7906(8)	353.12(3)
4	3.7636(3)	9.540(1)	9.767(1)	350.68(6)
5.3	3.7583(2)	9.520(1)	9.742(1)	348.53(5)
6.8	3.7474(3)	9.481(1)	9.730(1)	345.69(4)
8.3	3.7456(2)	9.455(1)	9.674(1)	342.58(4)
9.5	3.7364(3)	9.428(1)	9.665(1)	340.49(5)
10.2	3.7321(2)	9.409(1)	9.650(1)	338.84(5)
11.6	3.7272(2)	9.397(1)	7.638(1)	337.59(4)
12.4	3.7211(3)	9.373(2)	9.604(2)	334.95(7)
14.2	3.7207(3)	9.337(1)	9.585(1)	332.99(5)
15.6	3.7221(3)	9.325(1)	9.576(1)	332.39(5)
17.2	3.7156(4)	9.294(2)	9.530(2)	329.10(7)
18.4	3.7159(4)	9.268(2)	9.513(2)	327.63(7)
19.7	3.7149(5)	9.264(2)	9.499(2)	326.91(9)
21.4	3.7197(5)	9.190(2)	9.449(2)	323.0(1)
23.1	3.7245(5)	9.194(2)	9.442(2)	323.3(1)

TABLE 11: Cell constants and unit cell volume for $Ti_{2.85}O_4N$ (*CmCm*) as determined by Le Bail refinement. These values were determined by Dr G. Hyett and myself.

A selection of the experimental diffraction patterns is shown in FIG. 70. The first two patterns at 2 and 11.6 GPa highlight the compression of the ambient structure as a single phase as the raw data and the Le Bail refined model pattern are well matched. The diffraction pattern at 18.4 GPa begins to clearly show the presence of a second phase emerging along side the still present ambient structure. In fact, the ambient orthorhombic (*CmCm)* phase of $Ti_{2.85}O_4N$ remains stable up to 15.6 GPa from which point the onset of a new phase begins. The full transformation of the ambient phase to the HP phase is complete at 25 GPa. The pattern at 23.1 GPa shows that the peaks associated with this new HP phase dominate the pattern and although the ambient pressure phase peaks are reduced in intensity they can still be observed.

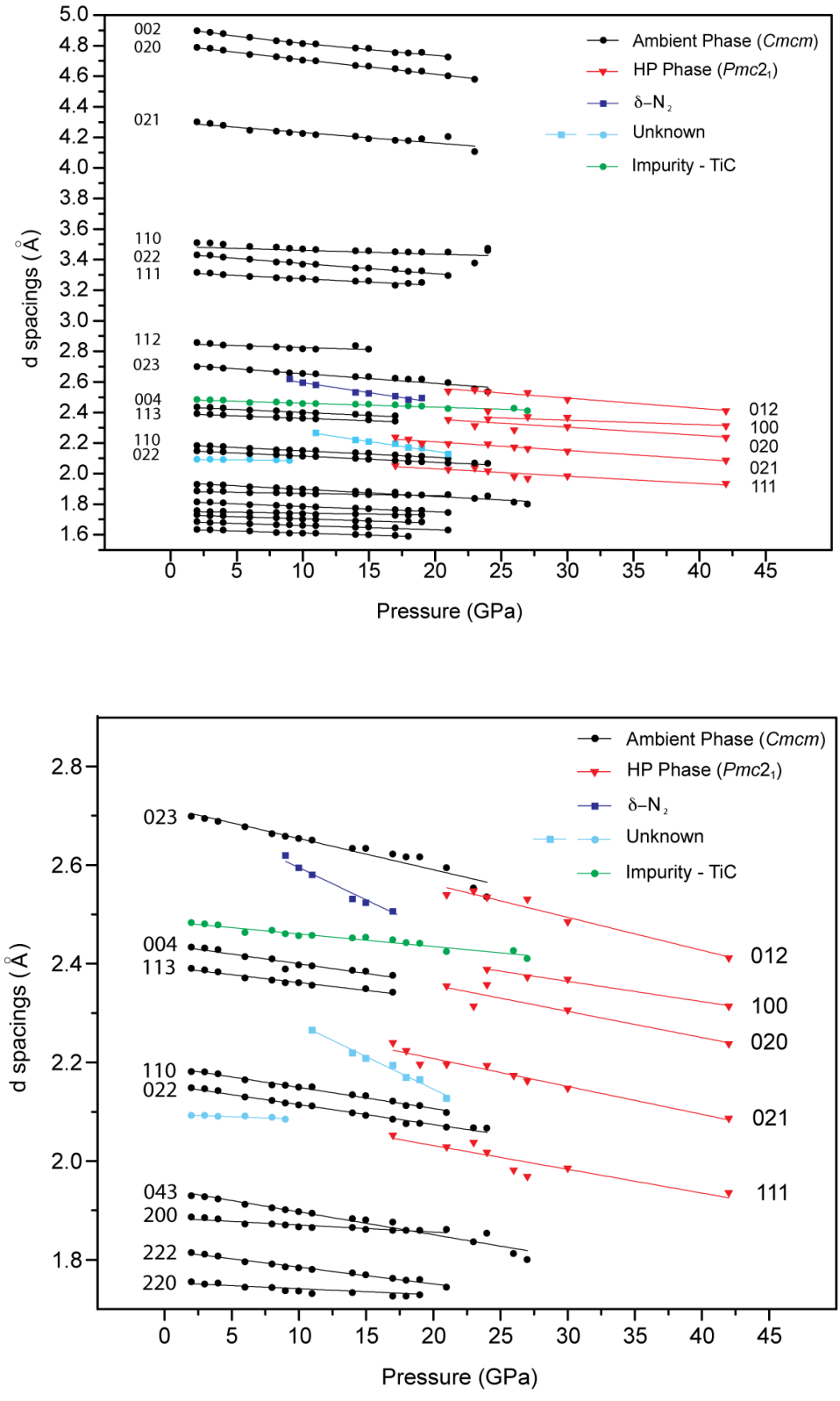

FIG. 69: The position of the diffraction peaks present in the XRD data in d spacings (Å) as a function of pressure (GPa) over two different d spacings scales. The selected region of interest in this plot is from 1.75 to 2.8 Å and highlights the presence of the ambient phase (*Cmcm*) beyond the onset of the transition to the high pressure phase ($Pmc2_1$). The impurity TiC from the starting material is identified along with the

presence of the pressure transmitting medium, the ordered cubic (δ) phase of N_2. Two sets of diffraction peaks in the XRD data with relatively low intensity could not been identified or assigned to any of the phases present throughout. Some of the peak positions of the high pressure phase (labelled as HP phase in the figure) were inputted from the non-hydrostatic data and are in confirmation with the trends described when having a pressure transmitting medium present.

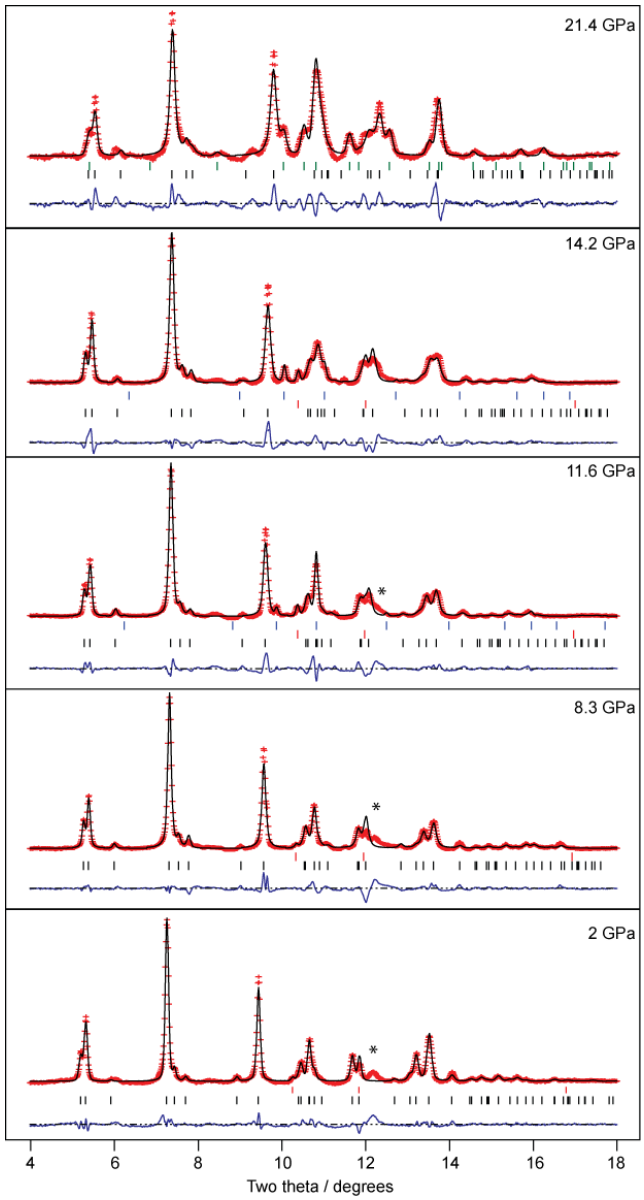

FIG. 70: Diffraction data for the sample collected at 5 different pressures. Data is shown in red, refined Le-Bail in black and difference plot in blue throughout the data sets. The tick-marks below the data indicate the peaks for each phase. Black tick-marks for ambient structure of $Ti_{2.85}O_4N$, red for TiC impurity, blue for δ-N_2 pressure medium at 11.6 and 21.4 GPa and green for high pressure structure of titanium oxynitrides at 21.4 GPa. * The broad peak labelled in the lower pressure data sets was not identified successfully and is shown in FIG. 69 as an unknown. This plot was provided by Dr G. Hyett.

A second series of compressions runs were carried out up to 70 GPa but this time as a non-hydrostatic experiment with no PTM. Although an earlier non-hydrostatic compression turn had revealed that the XRD data collected was not refinement quality this attempt did allow the phase transition from the ambient structure to the HP phase to be observed much more clearly than the hydrostatic experiment. The phase transition in the hydrostatic run had been noted from 18 GPa but not yet complete at 23 GPa. In FIG. 71 the diffraction pattern at 24 GPa has shown the phase transition to the HP phase to have gone to completion.

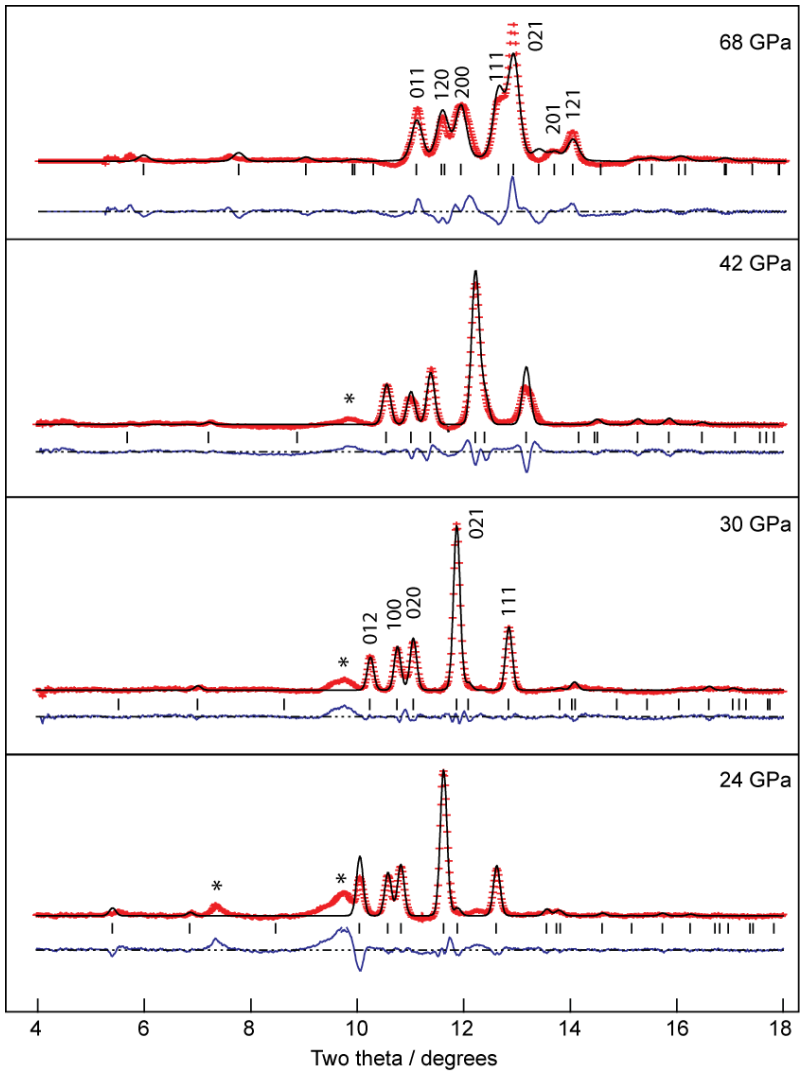

FIG. 71: The non-hydrostatic compression data of the $Ti_{2.85}O_4N$ system at 24, 30 and 42 GPa. The Le Bail refined X-ray diffraction patterns are of the high pressure phase of the system and the reflections highlighted were used for indexing to identify the unit cell parameters. * The broad peaks labelled are identified as the remaining ambient phase in the sample. This plot was provided by Dr G. Hyett.

Pressure (GPa)	*a* (Å)	*b* (Å)	*c* (Å)	Volume (Å^3)
19	2.446(1)	4.799(1)	6.107(1)	71.686(3)
21.4	2.422(1)	4.714(1)	6.022(1)	68.755(3)
23.1	2.410(1)	4.692(1)	6.023(1)	68.106(3)
24	2.401(1)	4.712(1)	6.019(1)	68.096(3)
30	2.371(1)	4.612(1)	5.906(1)	64.582(3)
42	2.315(1)	4.481(1)	5.735(1)	59.492(3)

TABLE 12: Cell constants and unit cell volume for the high pressure phase of $Ti_{2.85}O_4N$ ($Pmc2_1$) as determined by Le Bail refinement.

The presence of a new phase at high pressure was observed in both the hydrostatic and non-hydrostatic X-ray diffraction data. However, unexpectedly the diffraction data from the non-hydrostatic work provided clearer patterns of the high pressure phase then that of the loadings using a pressure transmitting medium. Reasoning for this is discussed later in this report.

At 24 GPa five peaks can be observed in the non-hydrostatic data belonging to the high pressure phase, at d-spacings of 2.019, 2.191, 2.355, 2.409 and 2.535 Å. This phase is stable beyond 42 GPa. The unit lattice parameters for the first high pressure phase are given in TABLE 12. The 5 peaks observed between 24 GPa and 42 GPa of the HP structure could be indexed satisfactorily *ab initio* as a single phase in an orthorhombic unit cell with lattice parameters at 24 GPa of a=2.401 Å, b=4.712 Å, c=6.019 Å (V = 68.10 Å^3). Systematic absences within the orthorhombic unit cell identified $Pmc2_1$ as the appropriate space group. At 68 GPa two of the peaks develop shoulders, suggesting a potential further phase change (FIG. 72).

At 68 GPa a second high pressure is apparent, seemingly related to the phase observed from 18 to 42 GPa but with two additional peaks. This phase has been indexed as monoclinic and identified with a $P2_1/c$ space group, describing a distortion of the orthorhombic cell of the first high pressure phase with an increase of the β bond angles to 99.7(1)°. A Le Bail refinement was carried out in this space (FIG. 71 (top)) with lattice parameters at 68 GPa of a = 4.3456(5) Å, b = 5.177(3) Å, c = 2.872(1) Å.

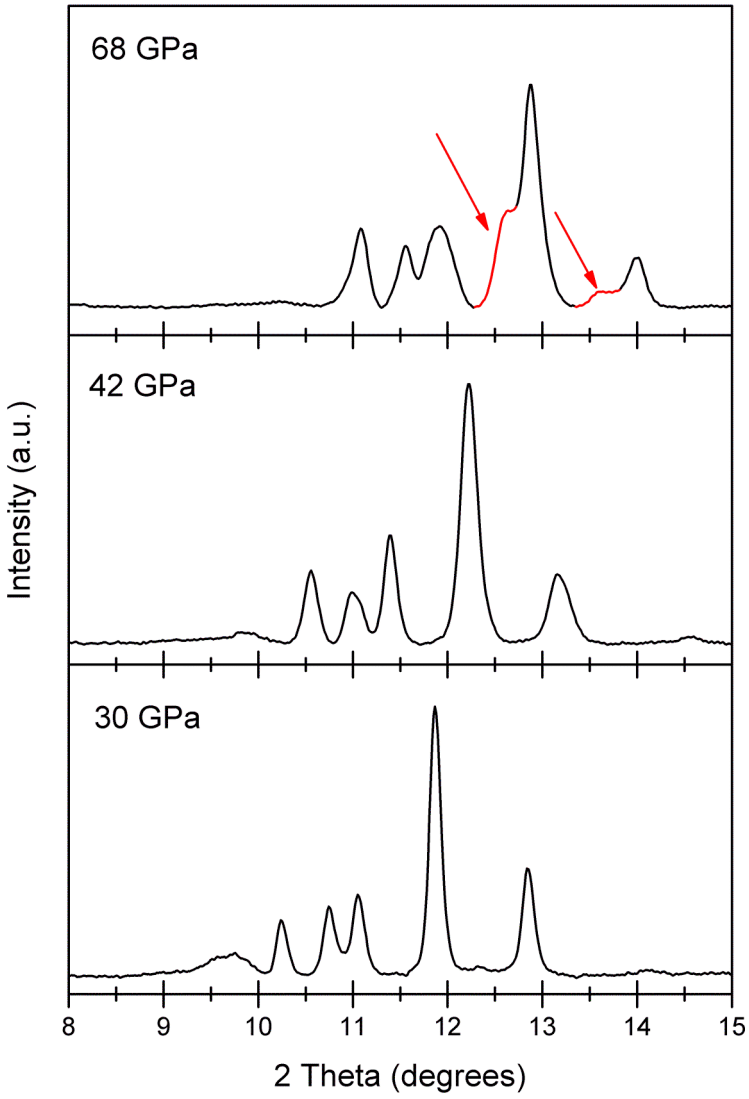

FIG. 72: The non-hydrostatic compression data of the $Ti_{2.85}O_4N$ system. The appearance of two new peaks at 68 GPa, highlighted in red, could be due to the emergence of a new phase.

3.5.2.3.2 Compressibility Measurements

The synchrotron X-ray diffraction data was used to construct a P(V) plot and evaluate the molar volume and compressibility parameters of the ambient $Ti_{2.85}O_4N$ phase. Rietveld refinement was used to identify the presence of the ambient phase up to 7 GPa. However, it was assumed that Le Bail refinement would be accurate enough to identify the presence of the ambient throughout the

compression data and was used to determine the volume of the unit cell. The presence of the nitrogen PTM was assumed to be negligible and was not accounted for during the refinement process. Having confirmed the presence of a single phase throughout the decompression the data were analysed using a finite strain Birch-Murnaghan equation of state (EOS) expression expanded to third order as given in Eq. 9 and shown in FIG. 73. The data matches the EOS fit very well and this confirms the existence of the ambient phase up to a pressure of 23 GPa. The data was then re-analysed by fitting it to a linearised version of the *P(V)* equation which is more useful determination of K_0 and K_0' values [177]. These expressions have already been given in Eq. 10 and Eq. 11 and are used to give a F-f plot (FIG. 74). This permits a linear relationship to be observed, which is well adapted to a least-squares fitting and error analysis of the results. The data indicate a bulk modulus value K_0 = 154±22 GPa with K_0' = 5.2±0.5 for the *Cmcm* phase of $Ti_{2.85}O_4N$. This value is similar to that for β-Ti_3O_5 (K_0 =173 GPa) which is described with a highly anisotropic compression along the [010] direction [236]. However, the bulk modulus is comparably less then what is determined for the high-hardness ceramic TiN (K_0 = 251 GPa) and TiO_2 (K_0 = 215.5 GPa) [239]. The intercept as F→0 defines K_0 and the gradient of the slope determines K_0'. Within the Birch-Murnaghan third-order equation of state formulation when the gradient is equal to zero, K_0' is defined as 4. The value of V_0 was determined by extrapolating it from the V(P) plot. The error analysis for the F-f plot was carried by first evaluating the error given for the volume of the unit cell at V_0 and V at various pressures using the GSAS which were provided by Dr Geoff Hyett and were worked through a standard error analysis. The other variable present in F is that of Pressure (P), the error for this was estimated on the work carried out on the C_2N_3H project.

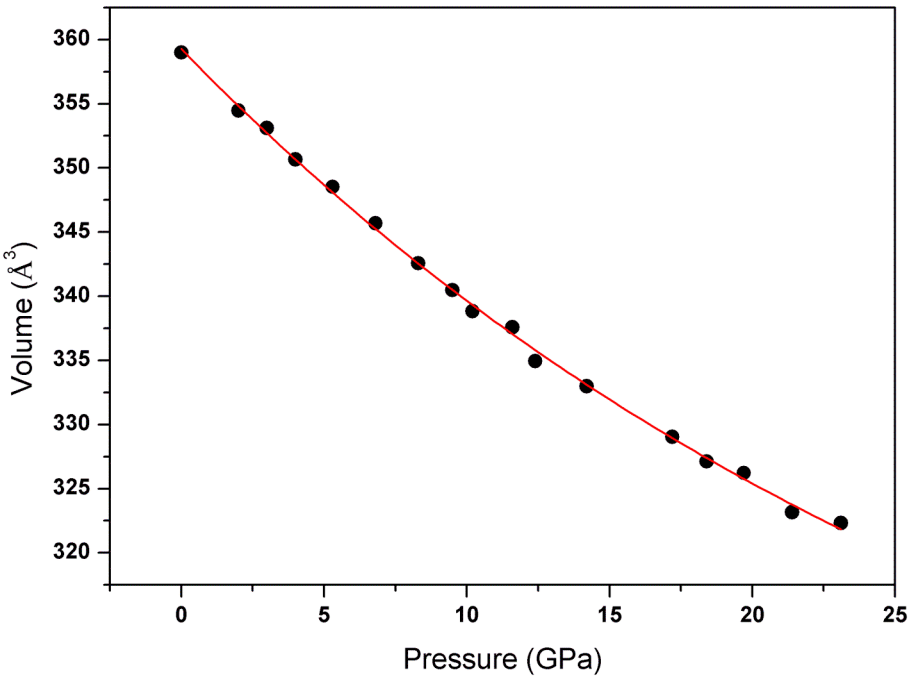

FIG. 73: A V(P) plot of compression data for the *CmCm* phase of $Ti_{2.85}O_4N$. A Birch-Murnaghan equation of state reduced to the third order is fitted to the single phase.

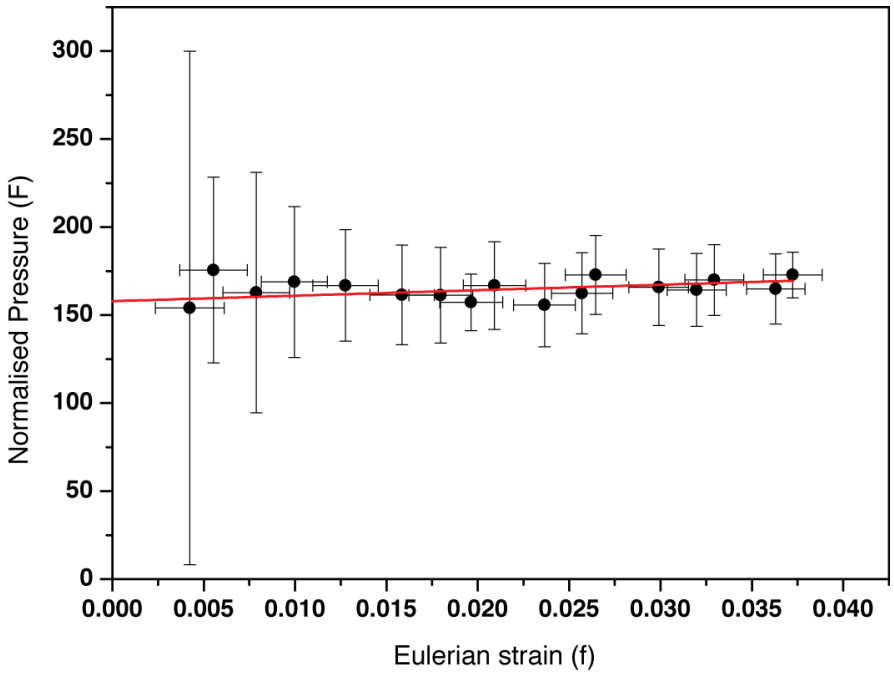

FIG. 74: Normalised pressure (F) vs Eulerian strain (f)

3.5.2.4 Discussion

In attempting to index the hydrostatic data it was apparent that the X-ray diffraction patterns were of lower quality then that of the non-hydrostatic data at the phase transition pressure range. The hydrostatic data, loaded with a nitrogen pressure transmitting medium had provided high refinement quality diffraction patterns up to 18 GPa. A sudden reduction in quality of the diffraction peaks and profiles occurs during the same pressure range as the phase transition seen by the $Ti_{2.85}O_4N$ as described before. In addition to this there is also a phase transition that occurs for the nitrogen pressure transmitting medium at 16.5 GPa. This transition is from the δ-N_2 phase which has disc-like and spherical molecules orientated, within a disordered cubic (*Pm*3*n*) unit cell [240, 241] to the ordered rhombohedral ε- N_2 ($R\ \bar{3}$) structure [242, 243]. Both the sample and the pressure transmitting medium are undergoing a phase transition within a similar pressure range. This contributed to a heterogeneous environment within the sample chamber and a drastic effect on the X-ray diffraction patterns during this pressure range.

The start of the phase transition into the high-pressure phase begins at around 18 GPa and is from orthorhombic *Cmcm* to $Pmc2_1$. The ambient structure is still present up to 42 GPa confirming a mixture of both the ambient and high pressure phases present during compression. There is a presence of a second high pressure phase by 68 GPa and was successfully indexed as monoclinic ($P2_1/c$). Our experiments had also shown that a rapid compression of the sample led to an amorphous system, highlighting the fact that the transformation from the ambient to the first high pressure phase is in fact a first order phase transition. The high pressure phase was attempted to be recovered following the subsequent decompression. This was carried out once the presence of the ambient sample was minimised at above 30 GPa. The recovery of a crystalline material was not achieved and decomposition led to the formation of an amorphous system. Previous experiments had shown that a rapid compression of the sample led to an amorphous phase and this highlights the fact that the transformation from the ambient to HP phase could be a first order phase transition. It was considered that if the transition was truly first order then the

HP phase could in fact be recoverable to lower pressures if not ambient conditions.

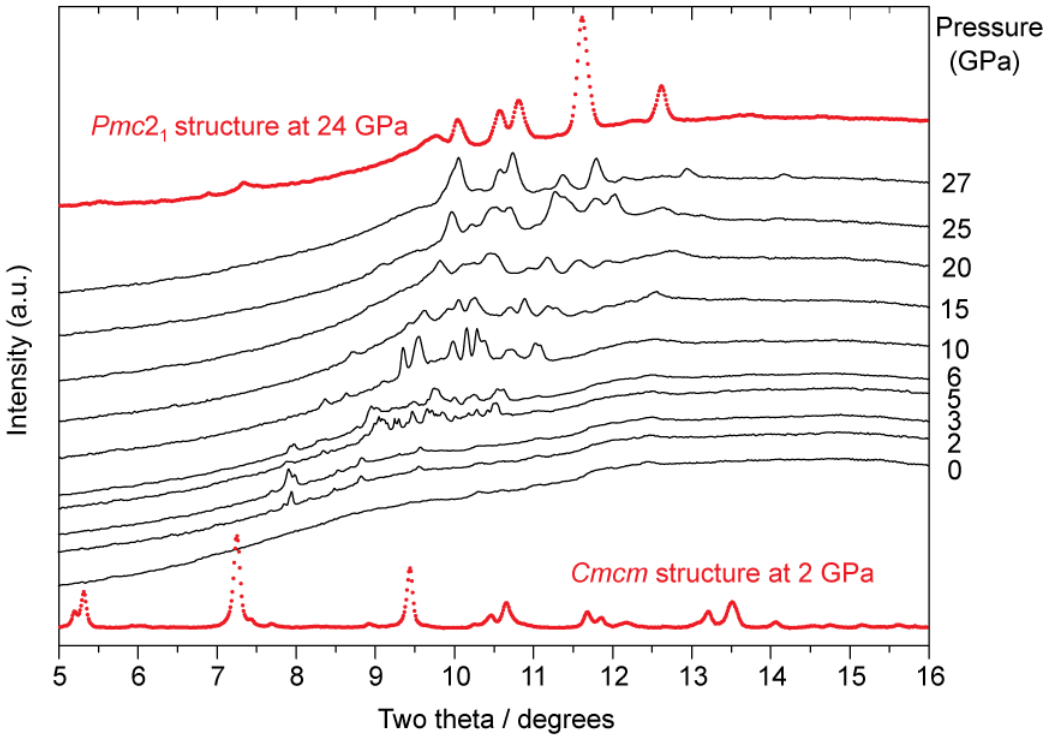

FIG. 75: X-ray diffraction patterns of the decompression of the high-pressure phase of $Ti_{2.85}O_4N$ from 27 GPa to 0 GPa. Patterns shown in red are for reference and from the compression data sets at 2GPa and 24GPa showing the patterns of the ambient structure and high pressure structure respectively.

The recovery of the high pressure phase was studied following the subsequent decompression to ambient conditions. This was conducted above 30 GPa as to minimise the presence of the ambient phase in the X-ray diffraction data. Following the decompression data the diffraction pattern of the high-pressure phase ($Pmc2_1$) was clearly visible during the first two pressure steps down to 25 GPa (FIG. 75). However, the relative intensities of the XRD data became distorted and the general overall quality of the XRD data was reduced. Any changes between the relative intensities observed between two pressure

points are likely due to changes in crystallite orientation occurring relative to the incident beam.

Continuing with the decompression the main diffraction peaks by 20 GPa became further broadened and a series of additional peaks began to become apparent. Below the pressure range of the transition during the compression study to the first high pressure phase, the pattern at 15 GPa stills showed remains of the high pressure phase but also revealed a number of additional sharper peaks that became further defined by 10 GPa. Although more diffraction peaks appeared between the 5-6 GPa region, these features disappeared by 2 GPa and the pattern was replaced by a simple peak pattern superimposed on a broad amorphous background. The various known polymorphs of $Ti_xO_yN_z$ were unsuccessfully attempted to be matched to the decompression data. These patterns are likely to correspond to metastable phases occurring as the highly metastable high density $Ti_{2.85}O_4N$ structure is decompressed beyond its low pressure stability limit. The full decompression to ambient conditions revealed a XRD pattern of only weak broad bands indicating an amorphous or high disordered nanocrystalline material remain in the pattern. *Pmc*2_1 phase was not recoverable to ambient conditions, and decompression in the diamond anvil cell at room temperature resulted in recovery of amorphous material.

The compressibility measurements of the ambient *Cmcm* phase gave the values of K_0 = 154±22 GPa with K_0' 5.2±0.5. The first of the high-pressure phases was not recoverable to ambient conditions and only possible to follow on the subsequent decompression to 15 GPa. Therefore, no attempt to extrapolate a theoretical value for the volume at ambient pressure was carried out, as calculating a value for K_0 would have no physical relevance. FIG. 76(a) shows how the lattice parameters of the ambient structure of $Ti_{2.85}O_4N$ behave under compression, with values taken from the Le Bail refinement (TABLE 11) at different pressures and plotted. These results show that in the *b* and *c* directions an approximately linear decrease in cell dimension occurs with increasing pressure. However, in the *a* direction the unit cell responds in a different manner and the compression seems to cease at around 12 GPa, with the cell constant settling at 3.72(1) Å regardless of increasing pressure up to 23.1 GPa. This effect can be seen more starkly in FIG. 76(b) where the cell dimensions are

plotted as percentages of the initial value at 2 GPa. In this figure it can be seen that initially all three lattice parameters decrease at approximately the same extent (approximately 0.2% per GPa), and the *b* and *c* parameters continue to decrease up to 24.3 GPa, where they are 96% of their initial values. The *a* lattice parameter, however, reduces to 98.5% of its initial value by 12 GPa, but does not decrease with further compression. The compressibility behaviour exhibited by the high pressure phase of $Ti_{2.64}O_4N$ ($Pmc2_1$) is considered more isotropic (FIG. 76(c)). All of the lattice parameters of this phase follow a near linear relationship throughout compression up onto the onset of the second high pressure phase ($P2_1/c$).

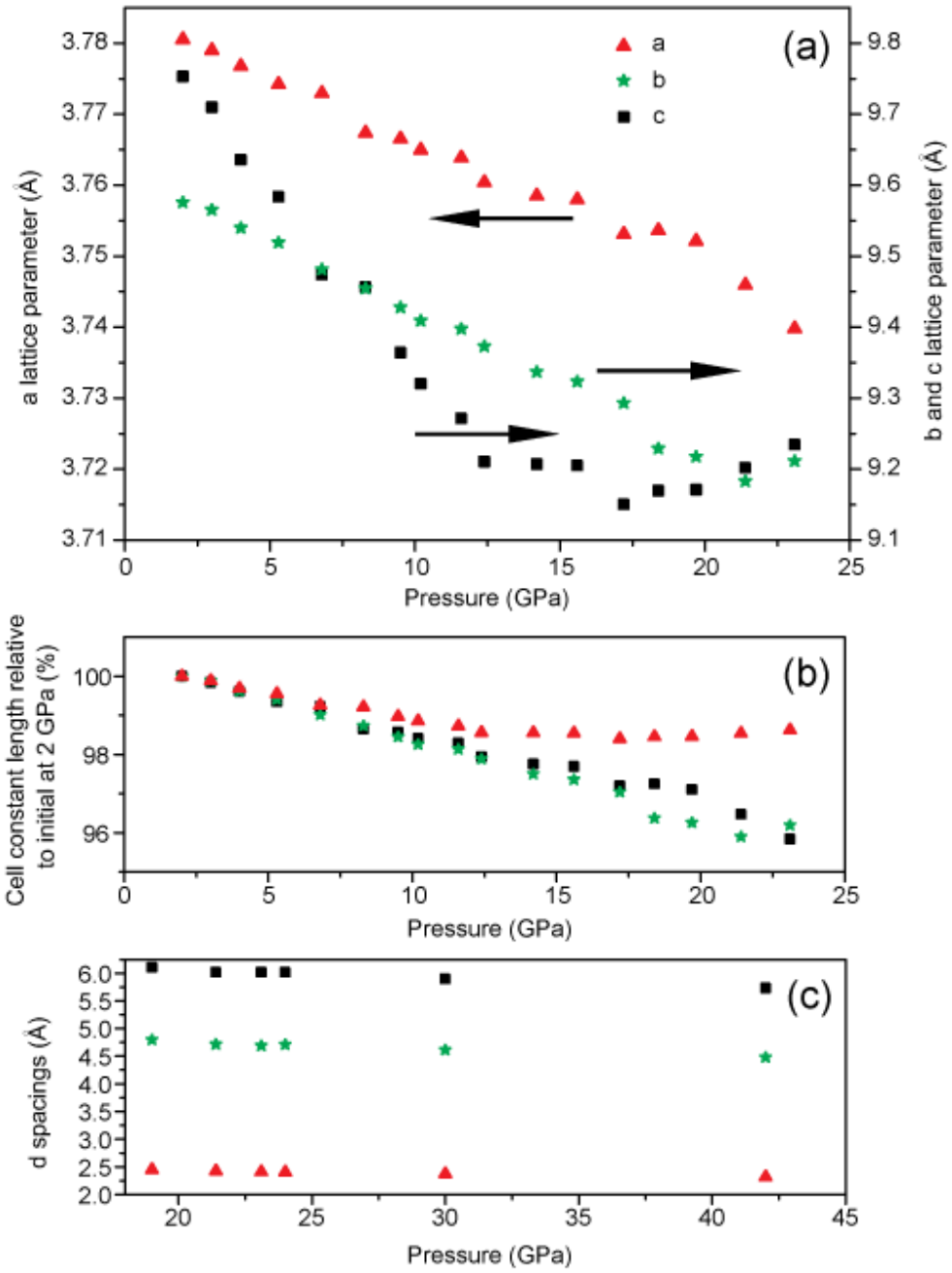

FIG. 76: (a) Plot of the *a, b* and *c* lattice parameters (Å) for the ambient phase of $Ti_{2.85}O_4N$ (*Cmcm*) against pressure (GPa). The lattice parameters were determined using Le Bail refinement and are plotted with their corresponding *y*-axis. (b) Plot of the lattice parameters of $Ti_{2.85}O_4N$ (*Cmcm*) at different pressures, shown as a percentage of the their initial values at 2 GPa. (c) Plot of the *a, b* and *c* lattice parameters (Å) for the first high pressure phase of $Ti_{2.85}O_4N$ ($Pmc2_1$) against pressure (GPa).

3.5.2.5 Conclusion

An investigation of the high-pressure behaviour of $Ti_{2.85}O_4N$ was carried out using the application of the diamond anvil cell combined with synchrotron X-ray techniques. The ambient *Cmcm* phase of the ambient structure was observed as a single stable phase up to 18 GPa. Compressibility measurements were carried out on the ambient structure using a Birch-Murnaghan equation of state to describe a relatively soft material (K_0 = 154 GPa) compared to its constituent component TiN and TiO_2 but similar to β-Ti_3O_5 (K_0 =173 GPa). The compressional behaviour showed that the *b*- and *c*-axis parameters decreased in a near-linear relationship throughout the pressure range. The *a*-axis parameter exhibits different characteristics and showed a much smaller compressibility and stopped above 12 GPa. The first of the high pressure phase transitions was observed at 18 GPa, the transformation of the ambient structure to an orthorhombic $Pmc2_1$ system. An examination of diffraction data revealed the ambient phase remained persistent in the diffraction data up to a pressure of 42 GPa, this combined with the discontinuity between the volume of the ambient and high pressure phases confirmed a first order phase transition.

The second high pressure phase above at 65 GPa was also successfully indexed, a monoclinic unit cell with $P2_1/c$ symmetry was identified. The recovery of this first high pressure phase ($Pmc2_1$) was attempted to be recovered following the subsequent decompression study. During decompression experiments the $Pmc2_1$ phase was not recoverable to 1 atm. A number of metastable crystalline phases were observed to be present during decompression and these have not yet been identified. The material recovered to ambient conditions was amorphous.

4 General Conclusion and Future Works

The work conducted and presented throughout this thesis is primarily focused on the use of molecular precursors for the synthesis of materials through the application of extreme conditions. The application of the diamond anvil cell coupled with laser heating techniques have provided the synthesis tools to access solid state systems that are not accessible at ambient conditions or through other techniques. The unique properties of diamond and the advancements in cell design, optical spectroscopy and synchrotron facilities have enabled *in situ* measurements of samples at high pressure and high temperature to be conducted: using Raman spectroscopy and synchrotron radiation. These two analytical techniques have been used to assist in describing the compressional behaviour of materials within two solid-state systems, C-N-H and Ti-N-O.

The major challenges facing the systems examined were involved in the identification of new unreported materials and having to work within the limitations of the diamond anvil cell; as discussed in this work. The micron sized samples and the requirement of high-energy synchrotron radiation amounted to collecting XRD data with relatively low resolution as compared to the use of an in-house diffractometer. This combined with the limited two theta range permitted by the backing plates of the diamond anvil cell provided the single most challenging aspect of this work. The limited information provided by this source of collecting XRD data meant that for most of the systems investigated the opportunity to carryout full Rietveld refinement and the determination of a structural model were not statistically reasonable. This was relevant with the new materials synthesised using laser heating within both of the C-N-H and Ti-N-O systems.

This problem is first encountered with the C_2N_3H system. Although the dwur-C_2N_3H was fully recovered and fully structurally refined in agreement with DFT calculations carried out, the metastable phase identified during the intermediate laser heating stages only gave three distinct reflections relative to the dominant dwur-C_2N_3H. This limited amount of crystallographic information prevented attempts at indexing and obviously any further crystallographic analysis. This problem was been addressed by collaboration within UCL and using DFT to conduct structure prediction calculations. Already a number of

energetically favourable new systems have been identified to which there is a match to the experimental XRD data. This has now become an ongoing project and is intended to be taken to completion. Although there also is accompanying Raman spectroscopy data identifying the presence of the metastable phase, a similar problem arises, as vibrational calculations are required to assist in identifying any symmetry aspects of this system.

Continuing within the C-N-H systems, the recovered laser heated g-$C_6N_9H_3$.HCl material provided similar problems. Although the new recovered material was successfully indexed and convincingly refined using a Le Bail approach no further information regarding a structural model could be interpreted. Difficulties arise with the permitted range of the two theta angle accessible using the diamond anvil cell. This problem is being attempted to be resolved by repeating the experiment using a new generation of Boehler-Almax backing plates that enables a range of a 45 degrees two theta to be accessed. The larger two theta range would allow a greater number of reflections to be observed and possibly provide the additional information that will allow a sound structural model to be elucidated.

With the Ti-O-N systems determining a structural model for the phases observed at high pressure were also not possible. The $Ti_{2.85}O_4N$ system was identified undergoing two phase transitions during compression. Both were successfully indexed and Le Bail refinement allowed the unit cell information to be determined. However, any attempts at carrying out a full Rietveld refinement were hindered by the limited number of observable reflections. This problem was again encountered when attempting to identify the system synthesised using the Ti_xN_y molecular precursor. The XRD data was successfully indexed and refined using the Le Bail method but again the analysis could not be taken any further.

The work conducted here highlights some of the major problems facing high pressure chemistry and the compulsory analysis that follows it. The preparations of samples, loadings and the challenges facing the analysis process involved have been discussed in depth. The general approach adapted in this work when dealing with light elemental systems specifically within the high pressure field has been to use a multidisciplinary undertaking to allow as much information to be extracted from either the experimental results or to ensue a theoretical route to assist and guide in the analytical process.

5 References

[1] P. F. McMillan, Nature Materials **4**, 715 (2005).
[2] D. M. Newitt, Biographical Memoirs of Fellows of the Royal Society **8**, 26 (1962).
[3] C. E. Weir, E. R. Lippincott, A. Vanvalkenburg, and E. N. Bunting, Journal of Research of the National Bureau of Standards Section a-Physics and Chemistry **63**, 55 (1959).
[4] G. J. Piermarini, and S. Block, Review of Scientific Instruments **46**, 973 (1975).
[5] R. M. Hazen, The Diamond Makers, Cambridge Press (1999).
[6] H. K. Mao, and R. J. Hemley, Rev. Min. **37**, 1 (1998).
[7] R. J. Hemley, and H. K. Mao, Mineralogical Magazine **66**, 791 (2002).
[8] P. F. McMillan, Nature Materials **1**, 19 (2002).
[9] P. F. McMillan, Chem.Commun. 919 (2003).
[10] R. Jeanloz, Annu. Rev. Phys. Chem. **40**, 237 (1989).
[11] V. Schettino, and R. Bini, Chem. Soc. Rev **36**, 869 (2007).
[12] R. J. Hemley, Annual Review of Physical Chemistry **51**, 763 (2000).
[13] M. I. McMahon, T. Bovornratanaraks, D. R. Allan, S. A. Belmonte, and R. J. Nelmes, Phys. Rev. B **61**, 3135 (2000).
[14] V. Schettino, and R. Bini, Phys. Chem. Chem. Phys. **5**, 1951 (2003).
[15] M. Citroni, M. Ceppatelli, R. Bini, and V. Schettino, J. Phys. Chem. B **111**, 3910 (2007).
[16] P. F. McMillan, M. Wilson, D. Daisenberger, and D. Machon, Nature Materials **4**, 680 (2005).
[17] J. V. Badding, Annual Review of Materials Science **28**, 631 (1998).
[18] X. C. Wang, K. Maeda, A. Thomas, K. Takanabe, G. Xin, J. M. Carlsson, K. Domen, and M. Antonietti, Nature Materials **8**, 76 (2009).
[19] E. Horvath-Bordon, R. Riedel, A. Zerr, P. F. McMillan, G. Auffermann, Y. Prots, W. Bronger, R. Kniep, and P. Kroll, Chem. Soc. Rev **35**, 987 (2006).
[20] A. Y. Liu, and M. L. Cohen, Science **245**, 841 (1989).
[21] D. M. Teter, and R. J. Hemley, Science **271**, 53 (1996).
[22] J. Kouvetakis, A. Bandari, M. Todd, B. Wilkens, and N. Cave, Chemistry of Materials **6**, 811 (1994).
[23] J. V. Badding, Advanced Materials **9**, 877 (1997).
[24] Z.-M. Ren, Y.-C. Du, Y. Qiu, J.-D. Wu, Z.-F. Ying, X.-X. Xiong, and F.-M. Li, Phys. Rev. B **51**, 5274 (1995).
[25] T. Komatsu, Phys. Chem. Chem. Phys. **6**, 878 (2004).
[26] C. Niu, Y. Z. Lu, and C. M. Lieber, Science **261**, 334 (1993).
[27] K. M. Yu, M. L. Cohen, E. E. Haller, W. L. Hansen, A. Y. Liu, and I. C. Wu, Phys. Rev. B **49**, 5034 (1994).
[28] T. Malkow, Materials Science and Engineering **292**, 112 (2000).
[29] J. H. Nguyen, and R. Jeanloz, Materials Science and Engineering a-Structural Materials Properties Microstructure and Processing **209**, 23 (1996).
[30] D. C. Nesting, J. Kouvetakis, and J. V. Badding, (1998).
[31] P. Kroll, Phys. Rev. Lett. **20**, 125501 (2003).
[32] H. C. Chen, B. H. Tseng, M. P. Houng, and W. H. Wang, Thin Solid Films **445**, 112 (2003).
[33] D. J. Blackwood, and J. Corros, Rev. Min. **21**, 97 (2003).

[34] G. B. Smith, A. Ben-David, and P. D. Swift, Renew. Energy **22**, 79 (2001).
[35] W. Lengauer, Transition Metal Carbides, Nitrides and Carbonitrides in Handbook of Ceramic Hard Materials, 1 ed. R. Riedel, Wiley-VCH, Weinheim pp. 202-252 (200).
[36] S. T. Oyoma, The Chemistry of Transition Metal Carbides and Nitrides. Blackie Academic & Professional, Glasgow (1996).
[37] G. Hyett, M. A. Green, and I. P. Parkin, J. Am. Chem. Soc **50**, 15541 (2007).
[38] K. L. Choy, J. Solid State Chem. **136**, 67 (2003).
[39] H. K. Mao, and P. M. Bell, Science **191**, 851 (1976).
[40] H. K. Mao, P. M. Bell, J. W. Shaner, and D. J. Steinberg, J. Appl. Phys. **49**, 3276 (1978).
[41] A. L. Ruoff, H. Xia, and Q. Xia, Review of Scientific Instruments **63**, 4342 (1992).
[42] D. K. Bradley, J. H. Eggert, R. F. Smith, S. T. Prisbrey, D. G. Hicks, D. G. Braun, J. Biener, A. V. Hamza, R. E. Rudd, and G. W. Collins, Phys. Rev. Lett. **102**, 075503 (2009).
[43] S. T. Wier, J. Akella, C. Aracne-Ruddle, Y. K. Vohra, and S. A. Catledge, Appl. Phys. Lett. **77**, 3400 (2000).
[44] A. L. Ruoff, L. Sun, S. Natarajan, C.-S. Zha, and G. Stupian, Review of Scientific Instruments **76**, 036102 (2005).
[45] A. Jayaraman, Review of Scientific Instruments **57**, 1013 (1986).
[46] A. Jayaraman, Rev. Mod. Phys. **55**, 65 (1983).
[47] D. J. Dunstan, and I. L. Spain, J. Phys. E: Sci. Instrum. **22**, 913 (1989).
[48] I. L. Spain, and D. J. Dunstan, J. Phys. E. Sci. Instrum. **22**, 923 (1989).
[49] B. A. Weinstein, and G. J. Piermarini, Phys. Rev. B **12**, 1172 (1975).
[50] G. J. Piermarini, and C. E. Weir, J. Res. Natl. Bur. Stand. **66A**, 325 (1962).
[51] K. E. Brister, Y. K. Vohra, and A. L. Ruoff, Review of Scientific Instruments **57**, 2560 (1986).
[52] S. Block, C. E. Weir, and G. J. Piermarini, Science **148**, 947 (1965).
[53] L. Merrill, and W. A. Bassett, Review of Scientific Instruments **45**, 290 (1973).
[54] A. V. Valkenburg, Review of Scientific Instruments **33**, 1462 (1962).
[55] R. A. Forman, G. J. Piermarini, J. D. Barnett, and S. Block, Science **176**, 284 (1972).
[56] G. J. Piermarini, S. Block, J. D. Barnett, and R. A. Forman, J. Appl. Phys. **46**, 2774 (1975).
[57] W. B. Daniels, and M. G. Ryschkewitsch, Review of Scientific Instruments **54**, 115 (1983).
[58] R. Letoullec, J. P. Pinceaux, and P. Loubeyre, High Pressure Research **5**, 871 (1990).
[59] R. Letoullec, J. P. Pinaceaux, and P. Loubeyre, High Pressure Research **1**, 77 (1988).
[60] V. V. Brazhkin, A. G. Lyapiny, and R. J. Hemley, Philosophical magazine A **82**, 231 (2002).
[61] J. Walker, Rep. Prog. Phys. **42**, 1605 (1979).
[62] R. Boehler, Review of Scientific Instruments **77**, 115103 (2006).
[63] S. Merkel, A. K. McNamara, A. Kubo, S. Speziale, L. Miyagi, Y. Meng, T. S. Duffy, and H. R. Wenk, Science **316**, 1729 (2007).

[64] G. Zou, Y. Ma, H. K. Mao, R. J. Hemley, and S. A. Gramsch, Argonne, Illinois (USA): AIP (2001).
[65] M. Ishizuka, Review of Scientific Instruments **76**, 123902 (2005).
[66] J. Akella, S. T. Weir, Y. K. Vohra, H. Prokop, S. A. Catledge, and G. N. Chesnut, International Conference on High Pressure Science and Technology. (1999).
[67] D. Leong, H. Feyrit, A. D. Prins, V. A. Wilkinson, K. P. Homewood, and D. J. Dunstan, Review of Scientific Instruments **63**, 5760 (1992).
[68] E. Pugh, H. E. Thompson, R. B. Balsod, and S. V. Brown, Review of Scientific Instruments **77**, 5 (2006).
[69] A. K. Singh, and G. C. Kennedy, J. Appl. Phys **47**, 3337 (1976).
[70] A. K. Singh, C. Balasingh, H. K. Mao, R. J. Hemley, and J. Shu, J. Appl. Phys **83**, 7567 (1998).
[71] G. Gatta, I. Kantor, T. B. Ballaran, L. Dubrovinsky, and C. McCammon, Physics and Chemistry of Minerals **9**, 627 (2007).
[72] K. R. Hirsch, and W. B. Holzapfel, Review of Scientific Instruments **52**, 52 (1981).
[73] J. C. Jamieson, Science **139**, 762 (1963).
[74] R. J. Angel, M. Bujak, J. Zhao, G. D. Gatta, and S. D. Jacobsen, J. Appl. Cryst. **40**, 26 (2006).
[75] S. Klotz, J.-C. Chervin, P. Munsch, and G. L. Marchand, J. Phys. D: Appl. Phys **42**, 75413 (2009).
[76] A. Merlen, P. Toulemonde, N. Bendiab, A. Aouizerat, J. L. Sauvajol, G. Montagnac, H. Cardon, P. Petit, and A. S. Miguel, Physica status solidi **3**, 690 (2006).
[77] L. Dubrovinsky, N. Dubrovinskaia, S. Saxena, and T. LiBehan, Materials Science and Engineering, **288**, 187 (2000).
[78] X. Li, and R. Jeanloz, Phys. Rev. B **36**, 474 (1987).
[79] J. Liu, L. Dubrovinsky, T. B. Ballaran, and W. Crichton, High Pressure Research **27**, 483 (2007).
[80] A. Zerr, G. Miehe, G. Serghiou, M. Schwarz, E. Kroke, R. Riedel, H. Fueß, P. Kroll, and R. Boehler, Nature **400**, 340 (1999).
[81] V.Iota, C.S.Yoo, and H.Cynn, Science **283**, 1510 (1999).
[82] C. S. Yoo, H. Cynn, F. Gygi, G. Galli, V. Iota, M. Nicol, S. Carlson, D. Häusermann, and C. Mailhiot, Phys. Rev. Lett. **83**, 5527 (1999).
[83] M. Santoro, F. A. Gorelli, R. Bini, G. Ruocco, S. Scandolo, and W. A. Crichton, Nature **441**, 857 (2006).
[84] M. Santoro, and F. A. Gorelli, Chem. Soc. Rev **35**, 918 (2006).
[85] H.-K. Mao, J. Xu, and P. M. Bell, J. Geophys. Res **91**, 4673 (1986).
[86] J. D. Barnett, S. Block, and G. J. Piermarini, Review of Scientific Instruments **44**, 1 (1973).
[87] D. L. Decker, Journal of Applied Physics **42**, 3239 (1971).
[88] R. N. Jeffery, J. D. Barnett, H. B. Vanfleet, and H. T. Hall, J. Appl. Phys. **37**, 3172 (1966).
[89] J. H. Eggert, K. A. Goettel, and I. F. Silvera, Phys. Rev. B **40**, 5724 (1989).
[90] J. H. Eggert, K. A. Goettel, and I. F. Silvera, Phys. Rev. B **40**, 5733 (1989).
[91] H. K. Mao, and P. M. Bell, Science **191**, 4229 (1976).
[92] H. K. Mao, P. M. Bell, J. W. Shaner, and D. J. Steinberg, J. Appl. Phys **49**, 3276 (1978).
[93] D. L. Decker, J. Appl. Phys **13**, 5012 (1966).

[94] J. M. Brown, J. Appl. Phys **10**, 5801 (1999).
[95] D. L. Decker, J. Appl. Phys **1**, 157 (1965).
[96] J. C. Jamieson, J. N. Fritz, and M. H. Manghnani, Pressure measurement at high temperature in X-ray diffraction studies: gold as a primary standard, in High Pressure Research in Geophysics, S. Akimoto and M.H. Manghnani, Editors. 1982, Tokyo: Center for Academic Publications, 27 (1982).
[97] K. E. Brister, Y. K. Vohra, and A. L. Ruoff, Review of Scientific Instruments **59**, 316 (1988).
[98] D. D. Klug, and E. Whalley, Review of Scientific Instruments **54**, 1205 (1983).
[99] A. Grzechnik, P. Simon, P. Gillet, and P. McMillan, Physica B: Condensed Matter **262**, 67 (1999).
[100] P. T. T. Wong, and D. J. Moffat, Applied Spectroscopy **43**, 1279 (1989).
[101] S. K. Saxena, L. S. Dubrovinsky, P. Haggkvist, Y. Cerenius, G. Shen, and H. K. Mao, Science **269**, 1703 (1995).
[102] A. Zerr, A. Diegeler, and R. Boehler, Science **281**, 243 (1998).
[103] A. F. Goncharov, P. Beck, V. V. Struzhkin, R. J. Hemley, and J. C. Crowhurst, Journal of Physics and Chemistry of Solids **69**, 2217 (2008).
[104] L. Ming, and W. A. Bassett, Review of Scientific Instruments **45**, 1115 (1974).
[105] G. Shen, M. L. Rivers, Y. Wang, and S. R. Sutton, Review of Scientific Instruments **72**, 1273 (2001).
[106] M. Kunz, W. A. Caldwell, L. Miyagi, and H. R. Wenk, Review of Scientific Instruments **78**, 6907 (2007).
[107] T. Yagi, T. Kondo, T. Watanuki, O. Shimomura, and T. Kikegawa, Review of Scientific Instruments **72**, 1293 (2001).
[108] T. Watanuki, O. Shimomura, T. Yagi, T. Kondo, and M. Isshiki, Review of Scientific Instruments **72**, 1289 (2001).
[109] E. Schulz, M. Mezouar, W. A. Crichton, S. Bauchau, G. Blattmann, D. Andrault, G. Fiquet, R. Boehler, N. Rambert, B. Situad, and P. Loubeyre, High Pressure Research **25**, 71 (2005).
[110] N. Funamori, and T. Sato, Review of Scientific Instruments **77**, 93903 (2006).
[111] R. Boehler, and A. Chopelas, Geophys. Res. Lett. **18** (1991).
[112] G. Hearne, A. Bibik, and J. Zhao, J. Phys. Condens. Matter **14**, 11531 (2002).
[113] C. S. Zha, and W. A. Bassett, Review of Scientific Instruments **74**, 1255 (2003).
[114] K. Shinoda, and N.Noguchi, Review of Scientific Instruments **79**, 015101 (2008).
[115] W. A. Bassett, Nuclear Instruments and Methods in Physics Research Section B: Beam Interactions with Materials and Atoms **Part 1**, 309 (1985).
[116] W. A. Bassett, A. H. Shen, M. Bucknum, and I. M. Chou, Review of Scientific Instruments **64**, 2340 (1993).
[117] N. M. Balzaretti, E. J. Gonzalez, G. J. Piermarini, and T. P. Russel, Review of Scientific Instruments **70**, 4316 (1999).
[118] D. Daisenberger, M. Wilson, P. F. McMillan, R. Q. Cabrera, M. C. Wilding, and D. Machon, Phys. Rev. B **75**, 224118 (2007).
[119] E. Soignard, M. Somayazulu, J. Dong, O. F. Sankey, and P. F. McMillan, J. Phys. Condens. Matter **13**, 557 (2001).

[120] C. V. Raman, and K. S. Krishnan, Nature **121**, 501 (1928).
[121] C. V. Raman, and K. S. Krishnan, Nature **121**, 711 (1928).
[122] G. Landsberg, and L. Mandelstam, Naturwissenschaften **16**, 557 (1928).
[123] H. A. Szymanski, Raman Spectroscopy, Plenum Press (New York) (1967).
[124] E. Soignard, University College London: London, p. 176 (2003).
[125] B. Yang, M. D. Morris, and H. Owen, Applied Spectroscopy **45**, 1533 (1991).
[126] C. L. Schoen, S. K. Sharma, C. E. Helsley, and H. Owen, Applied Spectroscopy **47**, 305 (1993).
[127] D. Schiferi, S. K. Sharma, T. F. Cooney, S. Y. Wang, and K. Mohanan, Review of Scientific Instruments **64**, 2821 (1993).
[128] J. Barbillat, B. Roussel, and E. D. Silva, J. Raman Spectrosc. **30**, 745 (1999).
[129] E. Soignard, O. Shebanova, and P.F.McMillan, Phys. Rev. B **75** (2007).
[130] M. v. Laue, Ann. Physik **41**, 989 (1912).
[131] W. Friedrich, P. Knipping, and M. V. Laue, Sitzb. Kais. Akad. Wiss., Munchen (1912).
[132] W. Friedrich, P. Knipping, and M. V. Laue, Ann. Physik **41**, 971 (1912).
[133] W. L. Bragg, Proc. Cambridge Phil. Soc. **17**, 43 (1913).
[134] T. Hahn, International Tables for Crystallography: Volume A, Kluwer Academic Publishers, Dordrecht (2002).
[135] M. F. C. Ladd, and R. A. Palmer, Structure determination by X-ray crystallography, Plenum Press (New York) (1994).
[136] V. K. Pecharsky, and P. Y. Zavalij, Fundamentals of powder diffraction and structural characterisation of materials, Springer Science and Business Media (2009).
[137] H. M. Rietveld, J. Appl. Cryst. **2**, 65 (1969).
[138] A. L. Bail, H. Duroy, and J. L. Fourquet, Materials Research Bulletin **23**, 447 (1987).
[139] G. S. Pawley, J. Appl. Cryst. **13**, 630 (1980).
[140] G. S. Pawley, J. Appl. Cryst. **14**, 357 (1981).
[141] H. Winick, and A. Bienenstock, Ann. Rev. Nucl. Part. Sci. **28**, 33 (1978).
[142] W. H. Bragg, and W. L. Bragg, Proceedings of the Royal Society **88**, 428 (1913).
[143] R. A. Young, International Union of Crystallographyv (1993).
[144] P. E. Werner, L. Eriksson, and M. Westdahl, J. Appl. Cryst. **18**, 367 (1985).
[145] A. Altomare, C. Giacovazzo, A. Guagliardi, A. G. G. Moliterni, R. Rizzi, and P. E. Werner, J. Appl. Cryst. **33**, 1180 (2000).
[146] A. Boutlif, and D. Louaer, J. Appl. Cryst. **24**, 987 (1991).
[147] A. Boutlif, and D. Louaer, J. Appl. Cryst. **37**, 724 (2004).
[148] R. Shirley, The CRYSFIRE user's manual. available at http://www.ccp14.ac.uk/tutorial/crys/. (2000).
[149] A. Katrusiak, and P. F. McMillan, High-Pressure Crystallography 1-20, Kluwer Academic Publishers (2004).
[150] G. E. Brown, G. Calas, G. A. Waychunas, and J. Petiau, Rev. Min. **18**, 431 (1988).
[151] M. Alexanian, Phys. Rev. **165**, 253 (1968).
[152] C. Giacovazzo, H. L. Monaco, G. Artioli, D. Viterbo, G. Ferraris, G. Gilli, G. Zanotti, and M. Catti, Fundamentals of Crystallography (Oxford UniversityPress, 2002).

[153] D. E. Baynham, and B. E. Wyborn, IEEE Transactions on Magnetics **17**, 1595 (1981).
[154] M. K. e. al, J. Synchrotron Radiation **12**, 650 (2005).
[155] J. C. Mallinson, IEEE Transactions on Magnets **9**, 678 (1973).
[156] A. C. Thompson, H. A. Padmore, A. G. Oliver, S. J. Teat, R. S. Celestre, S. M. Clark, E. E. Domming, K. D. Franck, and G. Y. Morrison, Synchrotron Radiation Instrumentation: Eighth International Conference, 482 (2004).
[157] A. C. Dhaussy, M. Mezouar, and O. Mentre, Synchrotron Radiation Instrumentation **705**, 1217 (2004).
[158] R. Boehler, J. Geophys. Res B. **95**, 21731 (1990).
[159] H. K. Mao, G. Y. Shen, R. J. Hemley, and T. S. Duffy, Properties of earth and planetary materials at high pressure and temperature **101**, 27 (1998).
[160] G. N. Greaves, C. R. A. Catlow, G. E. Derbyshire, M. I. McMahon, R. J. Nelmes, and G. van der Laan, Nature Materials **7**, 827 (2008).
[161] R. Riedel, Wiley, John & Sons, Inc **1** (2008).
[162] F. A. Ponce, and D. P. Bour, Nature **386**, 351 (1997).
[163] I. Kinski, G. Miehe, G. Heymann, R. Theissmann, R. Riedel, and H. Huppertz, Z. Naturforsch., B: Chem. Sci **60**, 831 (2005).
[164] E. Soignard, D. Machon, P. F. McMillan, J. Dong, B. Xu, and K. Leinenweber, J. Chem. Mater. **17**, 5465 (2005).
[165] J. P. Riviere, D. Texier, J. Delafond, M. Jaouen, E. L. Mathe, and J. Chaumont, Materials Letters **61**, 2855 (2007).
[166] M. Lejeune, O. Durand-Drouhin, K. Zellama, and M. Benlahsen, Solid State Communications **120**, 337 (2001).
[167] S. Matsumoto, E. Q. Xie, and F. Izumi, Diamond and Related Materials **8**, 1175 (1999).
[168] E. Horvath-Bordon, R. Riedel, P. F. McMillan, P. Kroll, G. Miehe, P. A. v. Aken, A. Zerr, P. Hoppe, O. Shebanova, I. McLaren, S. Lauterbach, E. Kroke, and R. Boehler, Angew. Chem. Int. Ed. **46**, 1476 (2007).
[169] A. P. Hammersley, S. O. Svensson, M. Hanfland, A. N. Fitch, and D. Hausermann, High Pressure Research **14**, 235 (1996).
[170] J. Rodriguez-Carvajal, Physica B **55** (1993).
[171] W. Kraus, and G. Nolze, J. Appl. Cryst **29**, 301 (1996).
[172] A. Salamat, K. Woodhead, P. F. McMillan, R. Q. Cabrera, A. Rahman, D. Adriaens, and F. Cora, Phys. Rev. B **80**, 104106 (2009).
[173] R. Dovesi, V. Saunders, C. Roetti, R. Orlando, C. Zicovich-Wilson, F. Pascale, B. Civalleri, K. Doll, N. Harrison, I. Bush, P. D'Arco, and M. Llunell, CRYSTAL 2006 User's Manual; University of Torino: Torino, Italy (2006).
[174] A. Becke, J. Chem. Phys. **98**, 5648 (1998).
[175] K. Burke, M. Enzerhof, and J. Perdew, Chem. Phys. Lett. **265**, 115 (1997).
[176] F. Birch, Phys. Rev. **71**, 809 (1947).
[177] T. S. Duffy, and Y. Wang, Ultrahigh-Pressure Mineralogy **37**, 425 (1998).
[178] F. Birch, J. Geophys. Res **83**, 1257 (1978).
[179] J. S. Loveday, R. J. Nelmes, W. G. Marshall, J. M. Besson, S. Klotz, and G. Hamel, Phys. Rev. Lett. **76**, 74 (1996).
[180] J. S. Loveday, and R. J. Nelmes, Phys. Rev. Lett. **83**, 4329 (1999).

[181] F. Datchi, S. Ninet, M. Gauthier, A. M. Saitta, B. Canny, and F. Decremps, Phys. Rev. B **73**, 174111 (2006).
[182] J. Liu, T. Sekine, and T. Kobayashi, Solid State Communication **137**, 21 (2006).
[183] B. V. Lotsch, M. Doblinger, J. Sehnert, L. Seyfarth, J. SEnker, O. Oeckler, and W. Schnick, Chem. Eur. J. **20**, 111 (2007).
[184] J. Leibig, Ann. Pharm. **10**, 10 (1834).
[185] W. C. Kurgla, and A. J. Papa, Flame retardancy of Polymeric materials. Vols 1-5, Dekker, New York (1973-1979).
[186] M. Groenewolt, and M. Antonietti, Adv. Mater. **17**, 1789 (2005).
[187] F. Goettmann, A. Fischer, M. Antonietti, and A. Thomas, Angew. Chem. Int. Ed. **45**, 4467 (2006).
[188] D. R. Millar, D. C. Swenson, and E. G. Gillan, J. Am. Chem. Soc **126**, 5372 (2004).
[189] Z. Zhang, K. Leinenweber, M. Bauer, L. A. J. Garvie, P. F. McMillan, and G. H. Wolf, J. Am. Chem. Soc **32**, 7788 (2001).
[190] G. H. Wolf, M. Bauer, K. Leinenweber, L. A. J. Garvie, and Z. Zhang, in Frontiers of High Pressure Research II: Application of High Pressure to Low-Dimensional Novel Electronic Materials, edited by H. D. Hochheimer (Kluwer Academic, The Netherlands, 2001), p. 29.
[191] J. Ortega, and F. O. Sankey, Phys. Rev. B **4**, 2624 (1995).
[192] D. T. Vodak, K. Kim, L. Iordanidis, P. G. Rasmussen, A. J. Matzger, and O. M. Yaghi, Chemistry- A European J. **17**, 4197 (2003).
[193] J. Gracia, and P. Kroll, J. Mat. Chem. **19**, 3013 (2009).
[194] M. Deifallah, P. F. McMillan, and F. Cora, J. Phys. Chem. C **112**, 5447 (2008).
[195] G. Demazeau, H. Montigaud, B. Tanguy, M. Birot, and J. Dunogues, J. Rev. High Pressure Sci. Technol **7**, 1345 (1998).
[196] P. F. McMillan, V. Lees, E. Quirico, G. Montagnac, A. Sella, B. Reynard, P. Simon, E. Bailey, M. Deifallah, and F. Cora, J. Solid State Chem. **182**, 2670 (2009).
[197] M. Deifallah, V. Lees, P.F.McMillan, and F. Cora, in press (2009).
[198] M. Deifallah, PhD thesis (UCL) (2007).
[199] V. Lees, PhD thesis (UCL) (2009).
[200] M. Planck, Ann. Phys. **1**, 719 (1900).
[201] W. L. Wolfe, and G. J. Zissis, The Infrared Handbook, Environmental Research Institute of Michigan, Washington, DC (1985).
[202] M. I. McMahon, J. Synchrotron Radiation **12**, 549 (2005).
[203] S. Ramanathan, and S. T. Oyama, J. Physical Chemistry **99**, 16365 (1995).
[204] P. F. McMillan, O. Shebanova, D. Daisenberger, R. Q. Cabrera, E. Bailey, A. Hector, V. Lees, D. Machon, A. Sella, and M. Wilson, Phase Transitions **80**, 1003 (2007).
[205] B. Palanivel, G. Kalpana, and M. Rajagopalan, Physica status solidi B-basic research **176**, 195 (1993).
[206] J. M. Vandenbe, and B. T. Matthias, Materials Research Bulletin **9**, 1085 (1974).
[207] X. J. Chen, V. V. Struzhkin, S. Kung, H. K. Mao, and R. J. Hemley, Phys. Rev. B **70**, 014501 (2004).
[208] X. J. Chen, V. V. Struzhkin, Z. Wu, M. Somayazulu, J. Quan, S. Kung, A. N. Chritensen, Y. Zhao, R. E. Cohen, H. K. Mao, and R. J. Hemley, PNAS **102**, 398 (2005).

[209] L. E. Toth, Transition Metal Carbides and Nitride (Academic, New York) (1971).
[210] W. Spengler, R. Kaiser, A. N. Christensen, and G. M. Vogt, Phys. Rev. B **17**, 1095 (1978).
[211] N. J. Ashley, R. W. .Grimes, and K. J. McClellan, J. Material Science **42**, 1884 (2007).
[212] A. Zerr, R. Riedel, T. Sekine, J. E. Lowther, W. Y. Ching, and I. Tanaka, Advanced Materials **18**, 2933 (2006).
[213] W. Y. Ching, S. D. Mo, L. Ouyang, I. Tanaka, and M. Yoshiya, Phys. Rev. B **61**, 10609 (2000).
[214] M. H. Chisholm, G. J. Gama, I. P. Parkin, V. F. Distasi, and D. V. Baxter, Abstracts of papers of the American Chemical Society **206**, 160 (1993).
[215] D. V. Baxter, M. H. Chisholm, G. J. Gama, V. F. Distasi, A. L. Hector, and I. P. Parkin, Chemistry of Materials **8**, 1222 (1996).
[216] A. W. Jackson, O. Shebanova, A. L. Hector, and P. F. McMillan, J. Solid State Chem. **179**, 1383 (2006).
[217] O. Shebanova, D. Machon, P. F. McMillan, D. Daisenberger, and A. L. Hector, in prep (2010).
[218] W. Kress, P. Roedhammer, H. Bliz, W. D. Teuchert, and A. N. Christensen, Phys. Rev. B **17**, 111 (1978).
[219] X.-J. Chen, V. V. Struzhkin, S. Kung, H.-k. Mao, and R. J. Hemley, Phys. Rev. B **70**, 014501 (2004).
[220] O. Shebanova, E. Soignard, and P. F. McMillan, High Pressure Research **26**, 87 (2006).
[221] W. Spengler, R. Kaiser, A. N. Christensen, and G. Müller-Vogt, Phys. Rev. B **17**, 1095 (1978).
[222] A. L. Hector, A. W. jackson, P. F. McMillan, and O. Shebanova, J Solid State Chem. **179**, 1383 (2006).
[223] M. Lerch, E. Fuglein, and J. Wrba, Z. Anorg. Allg. Chem. **622**, 367 (1996).
[224] W. H. Baur, and M. Lerch, Z. Anorg. Allg. Chem. **622**, 1729 (1996).
[225] A. Zerr, G. Miehe, and R. Riedel, Nature Materials **2**, 185 (2003).
[226] G. Hyett, M. A. Green, and I. R. Parkin, J. Photochem. Photobiol. A-Chem. **203**, 199 (2009).
[227] J. E. Lowther, MRS Bull **28**, 189 (2003).
[228] L. S. Dubrovinsky, N. A. Dubrovinskaia, V. Swamy, J. Muscat, N. M. Harrison, R. Ahuja, B. Holm, and B. Johansson, Nature **410**, 653 (2001).
[229] M. Onoda, J. Solid State Chem. **136**, 67 (1998).
[230] I. E. Grey, C. Li, and I. C. Madsen, J. Solid State Chem. **113**, 62 (1994).
[231] I. E. Grey, and J. Ward, J. Solid State Chem. **7**, 300 (1973).
[232] D. G. Kellerman, V. A. Zhilyaev, V. A. Perelyaev, and G. P. Shveikin, Inorganic Materials **19**, 221 (1983).
[233] G. Hyett, M. A. Green, and I. P. Parkin, J. Am. Chem. Soc. **129**, 15541 (2007).
[234] R. J. Hemley, Ann. Rev. Phys. Chem **51** (2000).
[235] A. Salamat, K. Woodhead, P. F. McMillan, R. Q. Cabrera, A. Rahman, D. Adriaens, J.-P. Philippe, and F. Cora, Phys. Rev. B **80**, 104106 (2009).
[236] S. Asbrink, L. Gerward, and J. S. Olsen, J. Appl. Cryst. **22**, 119 (1989).
[237] A. C. Larson, and R. B. V. Dreele, Los Alamos National Laboratory Report LAUR 86-748 (2000).

[238] B. H. Toby, J. Appl. Cryst. **34**, 210 (2001).
[239] J. D. Bass, Mineral Physics and Crystallogrphy: A Handbook of Physical Constants. (1995).
[240] D. T. Cromer, R. L. Mills, D. Schiferi, and L. A. Schwalbe, Acta Cryst. **37**, 8 (1981).
[241] B. Olinger, J. Chem. Phys. **80**, 1309 (1984).
[242] H. D. H. Olijnyk, M. Rubly, H-J. Jodl, H.D. Hochheimer, J. Chem. Phys. **93**, 8968 (1990).
[243] R. Bini, L. Ulivi, J. Kreutz, and H. J. Jodl, J. Chem. Phys. **112**, 8522 (2000).

6 Appendix

Using a Density Functional Method to Assist with High-Pressure Structural Refinement.

The application of pressure may be described as forcing materials to a state of lower volume, resulting in higher densities and structural changes. It is necessary to consider how a material responds to this state of higher density and the effect of compression on the energetics of its electrons. One approach to this is using a density functional method to assess energetic stabilities of solid-state systems as a function of volume change. Combining this *ab initio* method with high pressure research can provide a strong technique for exploring potential new systems and assist in analysing diffraction patterns especially for powdered samples, in which crystallographic data can be poor quality. Throughout the projects I have been involved with during my PhD, theoretical computational work has been indispensable. Many of the problems facing the crystallographic contribution would not have been resolved without a better understanding of the chemistry as provided by the computational work. The collaborations throughout the works presented here are given in each respective chapter. Here, the reader is referred to appendix A where a paper is presented on the density functional calculations I carried out whilst working on a project regarding the high pressure study of sodium silicide. Although no description of the methodology or results are provided here (see appendix for the full journal) an explanation of the aim of the computational work is given.

My involvement, under the supervision of Dr. Dewi Lewis (UCL), was to provide structural models of the high-pressure phase of the NaSi using density functional theory calculations. The problem with the XRD data collected at high-pressure was that it was too poor in quality to allow a full refinement and structure solution. Although some reliable information could be extracted using Le Bail and Rietveld refinement it became obvious that to improve our understanding of the system and confirm the refinement data, computational calculations were needed. The aim of my computational work was therefore to obtain structural models of the high-pressure phase which could then be used as

starting points for full structural refinement of the experimental data. This method of supporting the crystallographic analysis proved to be important and successful and highlights the important interaction between the two disciplines.

Publications

Tetrahedrally bonded dense C_2N_3H with a defective wurtzite structure: X-ray diffraction and Raman scattering results at high pressure and ambient conditions

Ashkan Salamat, Katherine Woodhead, Paul F. McMillan,* Raul Quesada Cabrera, Aisha Rahman, Davy Adriaens, and Furio Corà
Department of Chemistry and Materials Chemistry Centre, University College London, 20 Gordon Street, London WC1H 0AJ, United Kingdom

Jean-Philippe Perrillat
European Synchrotron Radiation Facility, BP 220, 38043 Grenoble Cedex, France
(Received 18 May 2009; revised manuscript received 13 August 2009; published 17 September 2009)

Synchrotron x-ray diffraction and Raman scattering data supported by *ab initio* calculations are reported for the dense tetrahedrally bonded phase (C_2N_3H) with a defective wurtzite (dwur) structure synthesized by laser heating from dicyandiamide ($C_2N_4H_4$) at high pressure in a diamond anvil cell. This work confirms the structure deduced in previous work from electron diffraction experiments. The phase ($Cmc2_1$) is recoverable to ambient conditions. The ambient pressure volume (V_0=137.9 Å^3) and bulk modulus (K_0=258±21 GPa) are in excellent agreement with density functional calculations (V_0=134.7 Å^3; K_0=270 GPa). The calculated Raman frequencies and pressure shifts are also in good agreement with experiment. Ammonia ($P2_12_12_1$) was identified among the reaction products as expected from the synthesis reaction.

DOI: 10.1103/PhysRevB.80.104106 PACS number(s): 62.50.−p, 31.15.A−, 61.50.Ks

I. INTRODUCTION

Since the theoretical prediction that sp^3-bonded forms of carbon nitride (C_3N_4) might be superhard[1,2] there has been intense interest in developing high-density materials within the C-N-H system. Such compounds could also have applications for energy storage.[3] Analogous compounds include refractory ceramics based on Si_3N_4 (Ref. 4) and Ga, Ge containing nitrides that provide wide band-gap materials for optoelectronics applications.[5] High-pressure, high-temperature (HPHT) synthesis experiments have resulted in spinel-structured forms of Si_3N_4 (Ref. 6) and Ga_3O_3N (Refs. 7 and 8) with low compressibility, high hardness, and wide band gaps. These materials were prepared by direct synthesis from the elements or using molecular precursors treated under HPHT conditions. Various dense C_xN_y and $C_xN_yH_z$ materials have been produced using physical or chemical vapor deposition methods but their structure, properties, and chemical composition have not yet been fully determined.[9–11]

Horvath-Bordon *et al.*[12] recently reported the synthesis of a new solid state compound C_2N_3H prepared from the molecular precursor dicyandiamide (DCDA: C_2N_3H) in a laser-heated diamond anvil cell (LH-DAC) at P>27 GPa and T ~1800 K. The new material was recovered to ambient conditions. Several grains were studied by electron energy loss spectroscopy in the TEM along with nano-SIMS to determine the chemical composition and show that C and N were tetrahedrally bonded with sp^3 hybridization.[13] The structure was studied using electron diffraction. The results combined with density functional theory (DFT) predictions indicated the structure was of a defective wurtzite (dwur) type as found in Si_2N_2O, $Si_2N_2(NH)$ (i.e., Si_2N_3H). The structure of dwur C_2N_3H is related to a tripled 3×3 cell of hexagonal C-lonsdaleite. N atoms occupy one set of tetrahedral sites and tetrahedral C atoms fill 2/3 of the other sublattice. The remaining positions are filled with H atoms bound to N (Fig. 1). In the present work, we have obtained x-ray diffraction (XRD) data in the DAC at high pressure and during decompression that confirms the structural model and that no phase transitions occur upon release of pressure and recovery to ambient conditions. The results are also confirmed by Raman spectra obtained following synthesis in the DAC and during decompression.

II. EXPERIMENTAL TECHNIQUES

Dicyandiamide ($C_2N_4H_4$: Aldrich, 99%) was loaded under O_2/H_2O-free conditions into cylindrical DACs using either sodium chloride (NaCl) or lithium fluoride (LiF) as a pressure-transmitting medium (PTM) and to provide thermal insulation to the diamond windows during laser heating experiments. We found no evidence for reactions occurring between the C-N-H phases and the PTM during synthesis experiments. The choice of PTM was an important issue for the x-ray diffraction experiments. NaCl has been well tested for LH-DAC experiments but it has strong diffraction lines that mask some of the key reflections of the C_2N_3H phase. The situation is further complicated by the B1-B2 transition that occurs at P ~27 GPa and with considerable hysteresis during decompression.[14] LiF is less well established as a PTM for LH-DAC synthesis studies: however, we found it per-

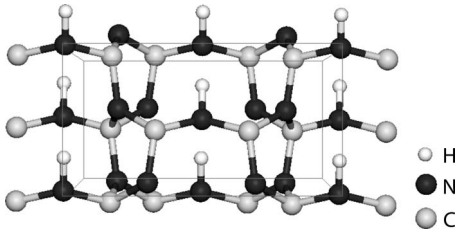

FIG. 1. C_2N_3H with a defective wurtzite (dwur) structure.

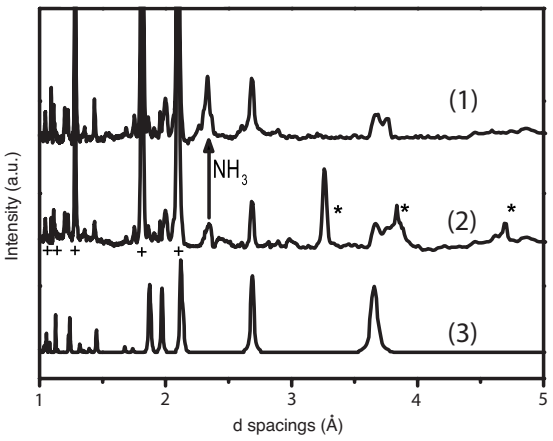

FIG. 2. XRD patterns obtained at 45 GPa following LH-DAC synthesis of dwur-C_2N_3H from DCDA. (1) Pattern obtained after extended heating and pattern (2) is captured beforehand during the initial heating period. Additional peaks (*) correspond to an unidentified C-N-H metastable phase formed during the initial synthesis reaction. The main peak of NH_3-III is identified in both experimental patterns. (3) Corresponding calculated pattern (DFT) at 45 GPa. [(+) indicate Bragg peaks from LiF, used as PTM].

formed well during these experiments and its use enabled us to complete the set of diffraction data observed for C_2N_3H.

Rhenium gaskets were preindented to 30 μm with 100 μm holes drilled by electro-erosion and used to contain the samples. Pressures were determined by ruby fluorescence.[15] The pressure was raised initially to 30–45 GPa and samples were heated to $T \sim 2500-2800$ K using either a 150 W CO_2 laser (10.6 μm) at UCL or a Nd^{3+}:YAG laser (1.064 nm) at ESRF. Tests using Nd^{3+}:YAG laser heating were also conducted at UCL prior to the synchrotron runs. For Nd^{3+}:YAG LH-DAC experiments Re powder was mixed with the sample (100:1 ratio) to couple with the near-IR laser beam. XRD experiments were carried out at beamline I15 of Diamond Light Source (Didcot, UK: $\lambda_0 = 0.350714$ Å) and at ID27 of the European Synchrotron Radiation Facility (Grenoble, France: $\lambda_0 = 0.26473$ Å). Some preliminary studies were also carried out at station 9.5 of the Synchrotron Radiation Source (Daresbury, UK: $\lambda_0 = 0.443970$ Å).[16] Diffraction patterns were recorded as two-dimensional (2D) angle-dispersive data sets using MAR image plate or charged couple device (CCD) detectors: the data were transformed to intensity vs wavelength/energy/d-value spectra and analyzed using FIT2D[17] and FULLPROF[18] software packages. Raman spectra were obtained at University College London with 514.5 nm Ar^+ laser excitation using a home-built high-throughput optical system based on Kaiser supernotch filters, an Acton spectrograph and LN_2 cooled back-thinned CCD detector or using an inVia Renishaw micro-Raman system using 785 nm excitation.

DFT calculations were carried out under periodic boundary conditions using CRYSTAL06.[19] We employed two different hybrid-exchange functionals, namely, B3LYP[20] and PBE0.[21] All atoms were described with an all electron 6–21G** basis set,[22] apart from the ambient pressure Raman mode calculation, which used Pople 6–21G* basis sets for C and N atoms and 8111G* for H atoms. Full geometry optimizations of the periodic systems were carried out to determine local minima on the potential energy surface (PES) using analytical gradients of the energy with respect to atomic positions and cell parameters. Symmetry was preserved throughout the optimizations. The SCF convergence threshold was set to 1×10^{-7} Hartree on the total energy. Calculations were performed using Pack-Monckhorst grids for integration in reciprocal space, with k-point nets of $4 \times 4 \times 4$. Geometry optimization was checked against root mean square (RMS) and absolute value of the largest component for both gradients and nuclear displacements, and considered complete when four conditions are simultaneously satisfied for both fractional coordinates and unit cell parameters, using the default values of 4.5×10^{-4} for the maximum gradient and 1.8×10^{-3} for the maximum displacement (all measured in a.u). Zone center phonons were calculated at the optimized structure for each pressure, using numerical differentiation of the analytical gradients of the energy with respect to atomic displacements using Cartesian displacements of 0.001 Å and a tighter convergence tolerance of 1×10^{-9} Ha in the total energy. The effects of pressure were simulated by performing a series of constant volume geometry optimizations for all structures, in which the volume varied between 109% and 80% of the ambient-pressure value. Following the constant-volume optimizations, a cubic fit to the internal energy (E) vs volume (V) curve was used to obtain pressure and enthalpy. Bulk moduli and their first derivatives were obtained from the E(V) results using a third-order Birch-Murnaghan equation of state. Simulated XRD patterns were created using PowderCell.[23]

TABLE I. Lattice parameters and refined fractional coordinates of dwur-C_2N_3H ($Cmc2_1$) at ambient conditions.

Lattice parameters	a (Å)	b (Å)	c (Å)
	7.618 (5)	4.483 (2)	4.038 (1)
Fractional coordinates	x	y	z
C	0.325 (3)	0.328 (3)	0
N1	0.310 (1)	0.364 (4)	0.358 (2)
N2	0	0.285 (3)	0.422 (4)

III. RESULTS AND DISCUSSION

A. X-ray Diffraction

We obtained x-ray diffraction patterns (Diamond) for samples synthesized from the DCDA precursor in the DAC at pressures ranging from 30–45 GPa following laser heating at UCL and also *in situ* during laser heating experiments combined with synchrotron XRD at the ESRF. Our preliminary studies indicated that several C-N-H phases might coexist metastably within the sample following initial heating and that either prolonged heating ($\sim$15 mins) or several consecutive laser heating runs were necessary to fully convert the material to a single phase (Fig. 2). Those preliminary findings are confirmed in this study and the results are discussed below. Following prolonged heating in the DAC, an x-ray diffraction pattern was obtained that could be fully

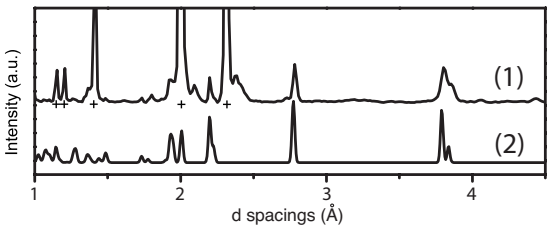

FIG. 3. XRD patterns for the dwur-C_2N_3H structure at ambient conditions: (4) Pattern of recovered sample after LH-DAC synthesis. (5) Predicted pattern from DFT calculations. [(+) indicates Bragg peaks from LiF, used as PTM].

assigned to dwur C_2N_3H, in agreement with the structure suggested previously from electron diffraction and DFT calculations.[12] Identification of nearly the full set of predicted diffraction peaks for each pressure recorded was made possible by combining data from several runs carried out using both NaCl and LiF PTM in the DAC during decompression. The lattice parameters of the structure recovered to ambient conditions were determined by LeBail refinement: a=7.618 Å, b=4.483 Å, c=4.038 Å (V_0=137.904 Å^3) within space group $Cmc2_1$ (Table I), in excellent agreement with DFT predictions (Fig. 3 and Table IV). Rietveld refinement was carried out on the ambient pressure sample following recovery, allowing the fractional coordinates of the atomic positions to be determined (Table I).

Following LH-DAC synthesis at 45 GPa x-ray diffraction patterns were recorded during decompression to ambient conditions. Approximately 20 of the predicted reflections could be followed throughout the decompression process when examining data from experiments using the 2 different PTMs. Table II shows the ten most intense peaks at ambient conditions that are possible to follow throughout decompression using LiF as the PTM. That result confirms that the dwur-C_2N_3H phase produced by laser heating in the DAC from the DCDA precursor is fully recoverable to ambient conditions, that no decomposition or phase transitions occur during decompression, and thus that it has the chemical composition and structure deduced from electron diffraction,

TABLE II. The crystal structure of dwur C_2N_3H at ambient conditions. The ten most intense reflections, that are possible to follow throughout decompression, are noted.

hkl	d (calc) (Å)	I (calc) (%)	d (exp) (Å)	I (exp) (%)
110	3.832	25	3.869	49
200	3.786	81	3.808	91
111	2.768	100	2.780	100
020	2.221	27	2.246	28
310	2.195	78	2.210	65
002	2.002	57	2.008	48
021	1.942	34	1.960	54
311	1.925	44	1.936	59
211	1.712	16	1.724	15
330	1.277	24	1.290	18

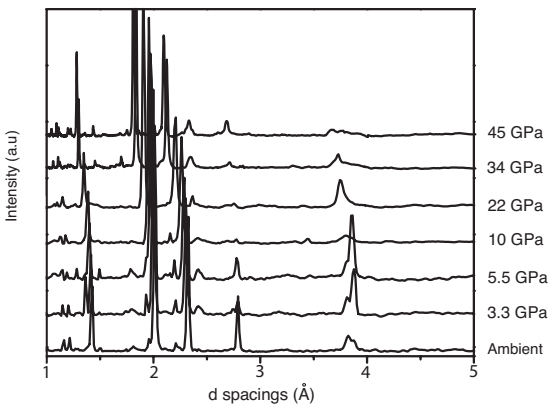

FIG. 4. XRD pattern obtained during decompression following LH synthesis of DCDA in the DAC at pressure to ambient P, T conditions using LiF PTM

EELS and nano-SIMS experiments on recovered materials combined with DFT predictions.[12] This then constitutes a high-density tetrahedrally bonded material produced in the C-N-H system that might have interesting and useful properties in its own right, as well as providing a potential precursor to dense carbon nitride phases.

We used the synchrotron x-ray diffraction data to construct a P(V) plot and evaluate the molar volume and compressibility parameters of the dwur-C_2N_3H phase (Figs. 4 and 5). The data were analyzed using a finite strain Birch-Murnaghan equation of state (EOS) expression expanded to third order:[24]

$$P(V) = 3K_0 f(1+2f)^{5/2}\left[1+\frac{3}{2}(K_0'-4)f\right] \quad (1)$$

Here K_0 is the zero pressure bulk modulus and K_0' its pressure derivative. Transforming the volume strain into the reduced variable

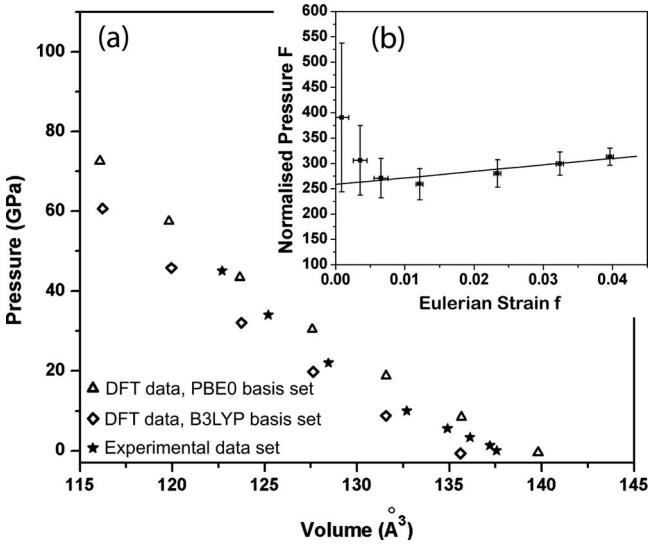

FIG. 5. (a) P(V) plot of structure A from DFT, PBEO (K_0 =288 GPa), and B3LYP (K_0=270 GPa) against the experimental data (K_0=258 GPa) (b) Normalized pressure (F) vs Eulerian strain (f)

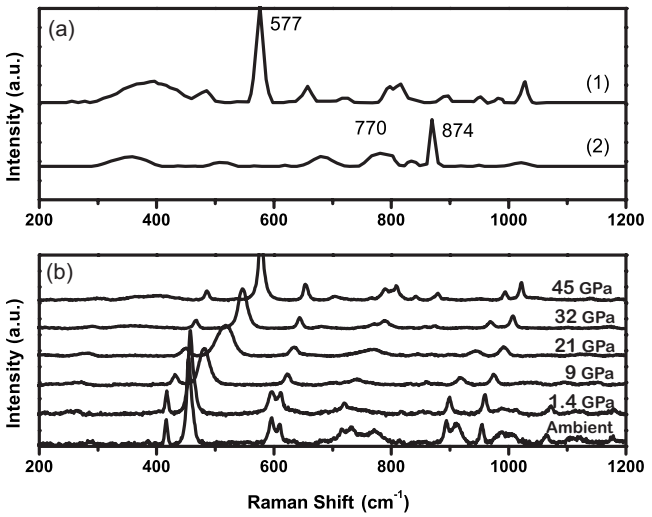

FIG. 6. (a) Raman spectra obtained following initial and extended laser heating of DCDA in a DAC at 45 GPa. (1) Spectrum of the dwur-C_2N_3H structure after extended LH. (2) Spectrum of an intermediate metastable phase formed during the initial stages of the heating reaction. (b) Raman spectra obtained following the decompression of dwur C_2N_3H from 45 GPa to ambient conditions.

$$f = \frac{1}{2}\left[\left(\frac{V_0}{V}\right)^{2/3} - 1\right] \tag{2}$$

and using a normalized pressure F defined by:

$$F = P[3f(1+2f)^{5/2}]^{-1} \tag{3}$$

provides a linearized version of the P(V) equation for useful determination of K_0 and K_0' values[21] [Fig. 5(b)]. The data indicate a bulk modulus value $K_0 = 258 \pm 21$ GPa with $K_0' = 6.3 \pm 0.8$ in good agreement with theoretical calculations ($K_0 = 271$ GPa, $K_0' = 3.97$: B3LYP; $K_0 = 288$ GPa, $K_0' = 3.94$: PBE0: Table IV). The bulk modulus for dwur C_2N_3H is comparable with that determined for the refractory high-hardness ceramic Si_3N_4 ($K_0 = 256$ GPa).[4]

B. Raman Spectroscopy

In our initial studies of synthesis of C_2N_3H from the DCDA precursor we reported a Raman spectrum taken in situ at high pressure in the DAC that contained sharp peaks at 577 and 874 cm^{-1} and a broader asymmetric band at 770 cm^{-1}. The 770 cm^{-1} band varied in relative intensity between syntheses carried out at MPI Mainz (Germany) and at UCL. During the present runs a doublet remains in this region but with greatly reduced intensity. We conclude that the strong broad 770 cm^{-1} feature observed in the initial runs is mainly due to a metastable C-N-H phase formed during the LH-DAC synthesis. In the present study, we have now determined that the 577 and 874 cm^{-1} peaks correspond to different phases. After initial laser heating in the DAC at 30–45 GPa a spectrum is obtained that is dominated by the 874 cm^{-1} peak and there is no evidence for the 577 cm^{-1} feature: after prolonged heating, the 874 cm^{-1} peak disappears and the 577 cm^{-1} band dominated the spectrum at high pressure [Fig. 6(a)]. That material is assigned from our in situ x-ray diffraction results to the dwur-C_2N_3H structure. During decompression this feature remained as the dominant peak in the 440–600 cm^{-1} region. It is assigned to the dwur-C_2N_3H from our DFT calculations (Table III).

TABLE III. Frequencies and symmetries of experimental and theoretical predicted active modes for C_2N_3H at ambient pressure. All the bands are Raman active although the A_2 are expected to be weak. In addition, with the exception of the A_2 bands the rest are also IR active. The corresponding experimentally determined Grüneisen parameters are also given.

(Calc) Peak position (cm^{-1})	(Exp) Peak position (cm^{-1})	Symmetry	(Exp) I (%)	(Exp) Grüneisen parameter
394	410	A_1	22	1.003
442	460	B_1	14	-
444	449	A_1	100	1.620
458		A_2		
583	592	B_1	13	-0.380
613	605	A_1	19	0.432
654		A_2		
663		B_2		
715	714	A_1	28	0.752
716	728	A_1	17	
769	773	B_1	46	0.509
780		A_2		
809		B_2		
850		A_2		
903	891	B_2	21	0.639
907	908	A_1	48	-
938	953	A_1	22	0.395
983	988	B_1	32	0.505
1033		A_2		
1034	1004	A_1	12	0.806
1056	1065	B_2	11	0.733
1067		B_2		
1070		A_2		
1099	1091	B_1	28	0.622
1104	1114	B_2	19	0.679
1120		A_2		
1124	1147	B_1	36	0.678
1180	1170	A_1	18	0.766

For the $Cmc2_1(C_{2v}^{12})$ structure we expect 33 Raman active vibrations:

$$\Gamma_{Raman} = 9A_1 + 8A_2 + 7B_1 + 9B_2 \tag{4}$$

We observe 16 peaks occurring between 200–1300 cm^{-1} that can be assigned to vibrational modes of dwur-C_2N_3H with symmetry species defined by the DFT calculations (Table III). All of the modes observed in the DAC at high pressure following the complete laser-heating synthesis could be followed to ambient conditions (Fig. 6(b)).

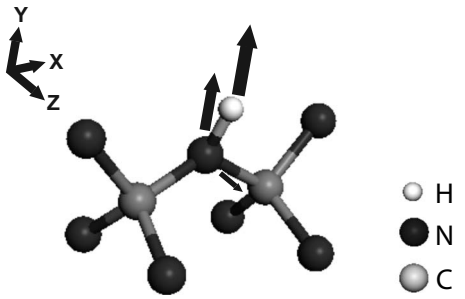

FIG. 7. The N and H displacements for the dominant A_1 Raman-active mode of dwur-C_2N_3H at 450–600 cm^{-1} are illustrated from DFT calculation results.

In addition the experimental mode Grüneisen parameters were defined by:

$$\gamma_i = \left(\frac{\partial \ln \omega}{\partial \ln V}\right)_{(T)} = \frac{K_0}{\omega_0}\left(\frac{\partial \omega}{\partial P}\right)_{(T)} \quad (5)$$

During decompression the dominant Raman peak at 440–600 cm^{-1} range exhibits significant broadening at ~21 GPa [Fig. 6(b)]. From examination of the calculated mode eigenvector we identify this as an A_1 symmetry mode due to a deformation vibration of the C-N-C linkage coupled with a large displacement of the H atoms (Fig. 7). That result indicates that some change might occur in the N-H ordering pattern within the dwur-C_2N_3H structure during decompression. That possibility is examined below using DFT calculations. We did not observe the N-H stretching modes predicted to occur at 3046 and 3131 cm^{-1}, and the N-H bending mode at 1594 cm^{-1} is only observed weakly in the high-pressure spectra.

C. Density Functional Theorem

In addition to providing support and interpretation for the x-ray diffraction and Raman spectroscopy results DFT calculations were used to investigate N-H bond rearrangements that might occur within the unit cell during decompression by considering different proton-ordered phases of the dwur-C_2N_3H structure. This part of the study was motivated by the observation that the dominant Raman peak in the 450–600 cm^{-1} region exhibited noticeable broadening during decompression at P ~ 21 GPa [Fig. 6(b)]. A full geometry optimization using both DFT methods was carried out for three C_2N_3H systems with different N-H ordering patterns within space groups $Cmc2_1$ or $Pmc2_1$) (Table IV). In Structure A the dwur unit cell has H atoms in identical sites with the N-H vectors aligned in the same direction. In Structure B, the H atoms occupy opposing axial positions, and Structure C contains a mixture of A and B structural units (Fig. 9). Energy optimizations within the three structures all converged and suggested that they might each occupy a subsidiary minimum within the potential energy surface. However, the energies are indistinguishable indicating that the structure formed experimentally might correspond to any one of the possibilities, or to an average among the structures with different N-H bonding patterns. The different structures examined by DFT methods have indistinguishable structural and compressibility parameters (Table IV).

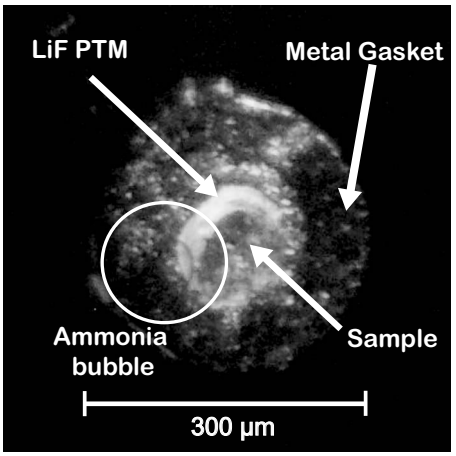

FIG. 8. A photograph looking through the top anvil of the DAC into the sample chamber upon opening. The ring shows a bubble of ammonia effervescing through the sample chamber. Available as a video sequence from the authors on request

TABLE IV. A comparison of ambient-P lattice parameters and bulk modulus values calculated (DFT) for different N-H ordered phases of dwur C_2N_3H and that of the experimental data.

	PBE0			B3LYP			
Structure	A	B	C	A	B	C	Experimental
Space Group	$Cmc2_1$	$Cmc2_1$	$Pmc2_1$	$Cmc2_1$	$Cmc2_1$	$Pmc2_1$	$Cmc2_1$
a (Å)	7.580	7.583	7.581	7.656	7.663	7.659	7.618
b (Å)	4.447	4.393	4.421	4.500	4.447	4.475	4.483
c (Å)	4.023	4.065	4.043	4.058	4.102	4.079	4.038
K_0 (GPa)	288	281	285	271	264	267	258 (21)
K_0'	3.94	4.18	4.04	3.97	4.01	3.94	6.3(0.8)
Vol ($Å^3$)	135.596	135.399	135.510	139.803	139.786	139.824	137.904(0.126)

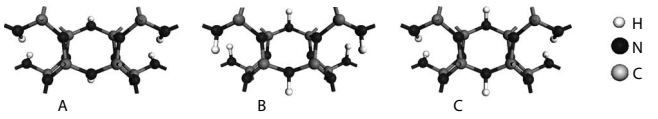

FIG. 9. The figure illustrates the three N-H phases investigated by DFT.

IV. DISCUSSION

Since the first report of synthesis of dwur-C_2N_3H from DCDA ($C_2N_4H_4$) by LH-DAC methods at $P > 27$ GPa and $T \sim 1800$ K it has been assumed that the reaction proceeds by elimination of NH_3 to produce the solid-state compound. That reaction has now been confirmed by our synchrotron x-ray results that show the appearance of solid NH_3 (phase III: $P2_12_12_1$)[25,26] identified in the diffraction patterns at high pressure and during decompression (Fig. 2). During the final stages of decompression the ammonia solid phase becomes liquid and escapes from the cell (Fig. 8). The principal broad peak of solid NH_3 at 2.3 Å could be followed during decompression down to 5 GPa.

V. CONCLUSION

Using a combination of synchrotron XRD and Raman spectroscopy supported with DFT calculations we conclude that the high-density dwur-structured compound C_2N_3H is produced by heating DCDA ($C_2N_4H_4$) as a molecular precursor at high pressure. This C_2N_3H phase is recoverable to ambient conditions and it has a large bulk modulus comparable with high hardness silicon nitride ceramics. An unidentified metastable C-N-H phase is also produced during the initial synthesis reaction. Recently Liu *et al.*[27] identified XRD lines that they assigned to the theoretically predicted phase β-C_3N_4 among the products of their shock synthesis experiments using DCDA as a precursor. Our results indicate that the XRD pattern obtained by Liu *et al.* likely corresponds mainly to dwur C_2N_3H along with some intermediate phases produced by high-P, T shock synthesis.

ACKNOWLEDGMENTS

This work was supported by EPSRC Portfolio Grant No. EP/D504782 and an EPSRC (Grant No. EP/D07357X) to PFM. During early experiments at the SRS we thank Alistair Lennie for his support and we thank Domink Daisenberger for discussion. We also acknowledge the assistance of Monica Amboage at Diamond Light for help with experiments at I15 and Mohamed Mezouar for access and help with facilities at ESRF.

*p.f.mcmillan@ucl.ac.uk

[1] A. Y. Liu and M. L. Cohen, Science **245**, 841 (1989).
[2] D. M. Teter and R. J. Hemley, Science **271**, 53 (1996).
[3] X. C. Wang, K. Maeda, A. Thomas, K. Takanabe, G. Xin, J. M. Carlsson, K. Domen, and M. Antonietti, Nature Mater. **8**, 76 (2009).
[4] R. Riedel, *Handbook of Ceramic Hard Materials* (Wiley, New York, 2008), Vol. 1.
[5] F. A. Ponce and D. P. Bour, Nature (London) **386**, 351 (1997).
[6] E. Soignard, M. Somayazulu, J. Dong, O. F. Sankey, and P. F. McMillan, J. Phys.: Condens Matter **13**, 557 (2001).
[7] I. Kinski, G. Miehe, G. Heymann, R. Theissmann, R. Riedel, and H. Huppertz, Z. Naturforsch., B: Chem. Sci **60**, 831 (2005).
[8] E. Soignard, D. Machon, P. F. McMillan, J. Dong, B. Xu, and K. Leinenweber, J. Mater. Chem. **17**, 5465 (2005).
[9] J. P. Riviere, D. Texier, J. Delafond, M. Jaouen, E. L. Mathe, and J. Chaumont, Mater. Lett. **61**, 2855 (2007).
[10] M. Lejeune, O. Durand-Drouhin, K. Zellama, and M. Benlahsen, Solid State Commun. **120**, 337 (2001).
[11] S. Matsumoto, E. Q. Xie, and F. Izumi, Diamond Related Materials **8**, 1175 (1999).
[12] E. Horvath-Bordon *et al.*, Angew. Chem. Int. Ed. **46**, 1476 (2007).
[13] J. Sjoberg, G. Helgesson, and I. Idrestedt, Acta Crystallogr., Sect. C: Cryst. Struct. Commun. **47**, 2438 (1991).
[14] X. Li and R. Jeanloz, Phys. Rev. B **36**, 474 (1987).
[15] H. K. Mao, J. Xu, and P. M. Bell, J. Geophys. Res. **91**, 4673 (1986).
[16] G. N. Greaves, C. R. A. Catlow, G. E. Derbyshire, M. I. McMahon, R. J. Nelmes, and G. van der Laan, Nature Mater. **7**, 827 (2008).
[17] A. P. Hammersley, S. O. Svensson, M. Hanfland, A. N. Fitch, and D. Hausermann, High Press. Res. **14**, 235 (1996).
[18] J. Rodriguez-Carvajal, Physica B **55**, 192 (1993).
[19] R. Dovesi *et al.*, *CRYSTAL 2006 User's Manual* (University of Torino, Torino, Italy, 2006).
[20] A. Becke, J. Chem. Phys. **98**, 5648 (1993).
[21] K. Burke, M. Enzerhof, and J. Perdew, Chem. Phys. Lett. **265**, 115 (1997).
[22] J. Binkley, J. Pople, and W. Hehre, J. Am. Chem. Soc. **102**, 939 (1980).
[23] W. Kraus and G. Nolze, J. Appl. Crystallogr. **29**, 301 (1996).
[24] F. Birch, Phys. Rev. **71**, 809 (1947).
[25] J. S. Loveday, R. J. Nelmes, W. G. Marshall, J. M. Besson, S. Klotz, and G. Hamel, Phys. Rev. Lett. **76**, 74 (1996).
[26] F. Datchi, S. Ninet, M. Gauthier, A. M. Saitta, B. Canny, and F. Decremps, Phys. Rev. B **73**, 174111 (2006).
[27] J. Liu, T. Sekine, and T. Kobayashi, Solid State Commun. **137**, 21 (2006).

Journal of Solid State Chemistry 182 (2009) 2535–2542

Contents lists available at ScienceDirect

Journal of Solid State Chemistry

journal homepage: www.elsevier.com/locate/jssc

Pressure-induced structural transformations of the Zintl phase sodium silicide

Raúl Quesada Cabrera [a], Ashkan Salamat [a], Oleg I. Barkalov [a,1], Olivier Leynaud [b], Peter Hutchins [a], Dominik Daisenberger [a], Denis Machon [c], Andrea Sella [a], Dewi W. Lewis [a], Paul F. McMillan [a,*]

[a] Department of Chemistry and Materials Chemistry Centre, Christopher Ingold Laboratories, University College London, 20 Gordon Street, London WC1H 0AJ, United Kingdom
[b] Department of Crystallography, Birkbeck College, Malet Street, London WC1E 7HX, United Kingdom
[c] Université de Lyon, F-69000, France Univ. Lyon 1, Laboratoire PMCN, CNRS, UMR 5586, F-69622 Villeurbanne Cedex, France

ARTICLE INFO

Article history:
Received 19 April 2009
Accepted 24 June 2009
Available online 30 June 2009

Keywords:
Sodium silicide
Zintl phase
High-pressure transition
Synchrotron X-ray diffraction
Pressure-induced amorphisation
Raman spectroscopy
Density functional calculation

ABSTRACT

The high-pressure behaviour of NaSi has been studied using Raman spectroscopy and angle-dispersive synchrotron X-ray diffraction to observe the onset of structural phase transformations and potential oligomerisation into anionic Si nanoclusters with extended dimensionality. Our studies reveal a first structural transformation occurring at 8–10 GPa, followed by irreversible amorphisation above 15 GPa, suggesting the formation of Si–Si bonds with oxidation of the Si^- species and reduction of Na^+ to metallic sodium. We have combined our experimental studies with DFT calculations to assist in the analysis of the structural behaviour of NaSi at high pressure.

1. Introduction

Alkali and alkaline earth silicides and germanides belong to the family of Zintl phases, in which polyanionic species, formed of the tetrelide atoms counterbalance the electropositive metal cations [1–3]. These compounds are interesting because the Si and Ge atoms occur with negative oxidation states and low coordination numbers, and they form unusual low-dimensional structures such as sheets, chains or isolated polyhedra. They are also important precursors for the synthesis of bulk amorphous semiconductors, including Si nanoparticles prepared by solution-phase routes or in the solid state [4], and also the expanded framework solids known as semiconductor clathrates that are isotypic with ice clathrate hydrates [5–7]. There are two main features of interest for high-pressure studies of Zintl phases containing anionic Si_n^{z-} units. First, the application of high pressure might cause a change of connectivity via redistribution of the Si–Si bonds within the anionic framework. Second, Si^- oxidation reactions might occur resulting in additional Si–Si bond formation with corresponding reduction of Na^+ and elimination of the elemental sodium (Na^0). Either of these outcomes would result in a new family of methods for producing Si_n clusters and nanoparticles with unusual coordination states, polymerisation and electronic properties, via solid state processing at low temperatures.

The alkali metal monosilicides and monogermanides (MSi, MGe) structures have been described previously [8–10]. The larger alkali silicides (KSi, RbSi, CsSi) exhibit a cubic arrangement of $[Si_4]^{4-}$ tetrahedra and alkali metal cations, with space group *P*-43*n*. Sodium silicide (NaSi) crystallises with a monoclinic structure (space group *C*2/*c*) containing isolated $[Si_4]^{4-}$ tetrahedra surrounded by Na^+ ions (Fig. 1) [8,9]. The $[Si_4]^{4-}$ anions present in the structure are analogous to the P_4 groups found in white phosphorus, reflecting the fact that Si^- is isoelectronic with P. By contrast, lithium silicide (LiSi) has a different structure to the other alkali metal silicides, in that the pyramidal 3-coordinated Si atoms are connected to provide alternating zig-zag chains, analogous to one of the black, high-pressure structures of phosphorus (Fig. 1).

Earlier studies aimed to prepare new alkali metal silicide or germanide compounds synthesised at high-pressure and high-temperature conditions followed by quenching to ambient conditions for analysis of the structures [11–16]. However, no high-density structural modifications have been reported for NaSi so far. Here we describe the room temperature compression of NaSi and the recovery of the resulting amorphous/nanocrystalline materials to ambient conditions.

* Corresponding author. Fax: +44 20 7679 7463.
E-mail address: p.f.mcmillan@ucl.ac.uk (P.F. McMillan).
[1] Permanent address: Institute of Solid State Physics, Russian Academy of Sciences, 142432 Chernogolovka, Moscow District, Russia.

0022-4596/$ - see front matter © 2009 Elsevier Inc. All rights reserved.
doi:10.1016/j.jssc.2009.06.037

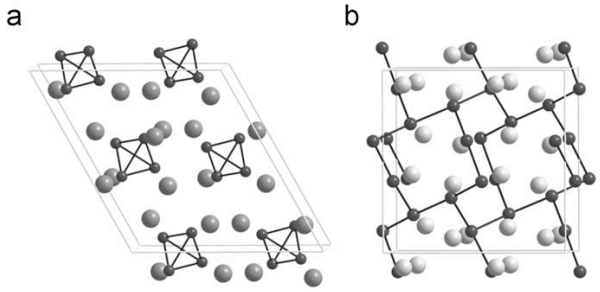

Fig. 1. (a) Representation of the crystal structure of NaSi at ambient pressure. NaSi is isoelectronic with white phosphorus, containing $[Si_4^4\ ]$ ions arranged in isolated distorted tetrahedra. (b) The crystal structure of LiSi at ambient pressure, related to black phosphorus *Cmca* structure, is formed by three-fold coordinated Si anions arranged along chains, forming eight-membered rings.

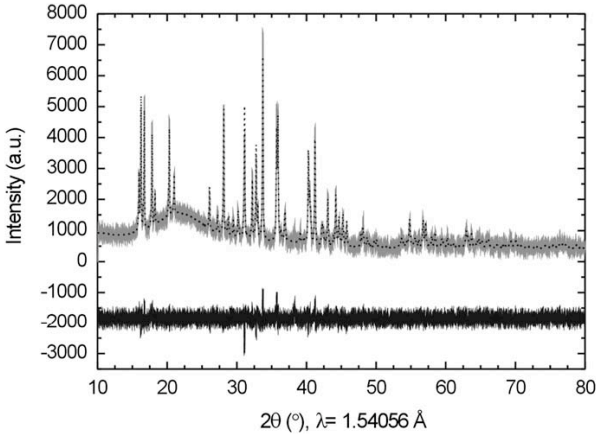

Fig. 2. X-ray diffraction pattern obtained at ambient conditions after the synthesis of NaSi. Rietveld refinement confirms the monoclinic *C*2/*c* structure. Reliability factors are $R_p = 16.1$, $R_{wp} = 16.0$, $R_{exp} = 8.58$, Bragg *R*-factor = 3.56.

2. Experimental

NaSi is highly reactive to moisture, and therefore all syntheses and DAC loading experiments were carried out in either a Schlenk vacuum line or a glove box with H_2O/O_2 content typically of less than 1 ppm. For NaSi syntheses from sodium and silicon, an excess of Na metal of about 6 at% comparing to the equiatomic composition of the final NaSi product was added to counteract loss due to evaporation and reaction with the inner surface of the reaction vessel. The elements were placed together in a Ni crucible and placed inside a steel autoclave fitted with a screw top and annealed Cu gasket [17]. The sealed autoclave was placed inside a furnace for 30–40 h at 650 °C. After the reaction was complete, the autoclave was cooled to room temperature and opened inside a dry-box. The sample was crushed in a mortar and placed in into a Pyrex sublimation tube equipped with a Young's valve. The sublimation tube was then attached to a vacuum system and evacuated using a turbomolecular pump. The sample was then heated to 240 °C for 15–20 h to remove the excess of Na from the sample. The purity of the sample was checked by X-ray diffraction using a Stoe diffractometer ($CuK\alpha_1$ radiation). The diffraction patterns indicated that complete reaction to form NaSi had occurred [9] (Fig. 2).

NaSi samples were loaded into the DAC in a glove box, prior to the high-pressure experiments. The diamond culet faces were typically 300 μm in diameter, and 80-μm-diameter holes were drilled in pre-indented rhenium gaskets (30–50 μm indent thickness) to contain the sample. Raman experiments were carried out using a mechanically driven opposed 4-screw symmetric diamond anvil cell [18]. Synchrotron X-ray diffraction studies were carried out using a N_2-driven membrane cell from Diacell (now EasyLab). No pressure-transmitting medium was added to avoid potential reactions with the sample. Ruby chips were added for pressure measurement by the ruby fluorescence method [19]. The narrow width of the ruby fluorescence peaks indicated approximately hydrostatic pressure conditions below 10 GPa. Above this pressure the ruby lines became broadened, but differences in the pressure indicated by different ruby chips within the sample chamber did not exceed 2 GPa.

The in-house Raman system at UCL consisted of an optical system based on Kaiser supernotch filters, an Acton spectrograph and a liquid-N_2 cooled back-thinned CCD detector. Spectra were excited using the 514.5 nm line of an Ar^+ laser focused onto the sample using a 50× long working distance Mitutoyo objective (numerical aperture = 0.42). Raman scattering was collected in 180° geometry through the same lens. The laser power was maintained at ~1 mW to avoid excessive heating of the sample. Subsequent data analysis and peak fitting were carried out using the PeakFit v4 software. Angle-dispersive X-ray diffraction data were collected at the UK Synchrotron Radiation Source (SRS, Daresbury Laboratory, station 9.5HP). Two-dimensional (2D) X-ray patterns were obtained and then integrated around the diffraction rings and converted into 1D plots using the FIT2D software [20]. FullProf [21] was used with the WinPlotr GUI interface [22] to carry out LeBail and Rietveld analyses of the data. The known structure of NaSi at ambient pressure and temperature conditions was used as a starting model for refining the high-pressure structure. Cell parameters were first approximately refined manually before performing subsequent LeBail and Rietveld refinements. Further Rietveld refinements of the high-pressure structure were also performed using the DFT calculated results as starting models.

Initial DFT optimisations were performed using the DMol^3 code with a double numeric basis set and the PWC functional [23,24]. The unit cell parameters were fixed at the initial values suggested from refinements of the experimental data and the atom positions optimised. We then undertook an initial series of compressions and expansions around these initial cell sizes to explore the potential energy surface (those results are not reported here, but are available from the authors on request). In each case, the cell was compressed (or expanded) by 5% along each cell dimension, initially with a fixed β angle and then by scanning the angle in steps of 5°. These studies were carried out to provide suitable starting geometries for the subsequent full structural optimisations. In order to achieve these, the CASTEP code was used, with ultrasoft norm-conserving pseudopotentials, the PWC functional and a plane-wave cut-off of 330 eV [25]. Each structure was fully optimised (cell parameters and atomic positions) with a specified applied external pressure. We considered two starting geometries obtained from the (constant volume) DMol^3 calculations: one obtained starting from the ambient pressure experimental unit cell (with a monoclinic angle of 117°), and another obtained from the high-pressure phase, where we found a local minimum with a monoclinic angle of 105°. The first model was fully optimised under applied external pressures ranging from 0 to 40 GPa, and the second was fully optimised over a more limited sample of the pressure range.

3. Results

3.1. Raman spectroscopy

The isolated Si_4^{4-} anion is isostructural with the P_4 molecule and exhibits T_d point group symmetry (-43 m). The vibrational modes of the cluster anion and their Raman (R) or infrared (IR) activities are $A_1(R)+E(R)+T_2(R, IR)$. The A_1 mode corresponds to a symmetric breathing vibration of the tetrahedral molecule, the E mode is a doubly degenerate symmetric deformation, and the T_2 vibration involves both stretching and bending components. These modes give rise to three peaks of approximately equal intensity at 474–482 cm^{-1} (A_1), 351–356 cm^{-1} (T_2), and 285 cm^{-1} (E) in the Raman spectra of the solid silicides with cubic symmetry, CsSi, K_3LiSi_4 and K_7LiSi_8 [26]. In these materials, the Si_4^{4-} groups are slightly distorted from tetrahedral symmetry, and this gives rise to weak additional peaks and small splitting of the main bands. Lattice modes and vibrations associated with the heavy metal cations occur at low frequency below 150 cm^{-1}, although it has been suggested that Li^+ cations may contribute to the higher frequency modes for K_3LiSi_4 and K_7LiSi_8 samples [26].

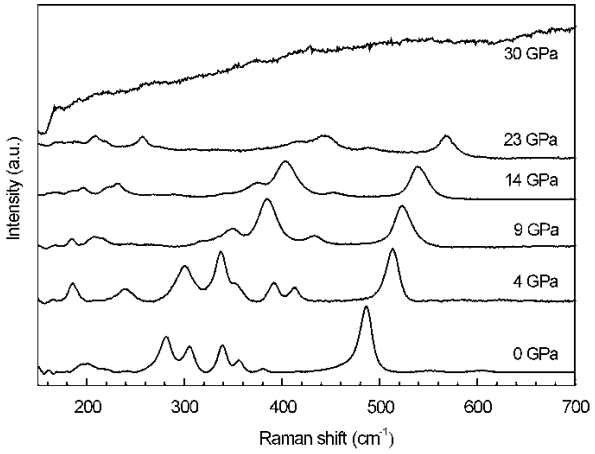

Fig. 3. Raman spectra of NaSi upon compression at room temperature. The distortion of Si_4^{4-} groups in the $C2/c$ structure gives rise to Raman-active vibrational bands at 480 cm^{-1} (A_1), 280 and 300 cm^{-1} (E) and 339.5, 355.7 and 380.5 cm^{-1} (T_2) at normal pressure.

The Raman spectrum for NaSi at ambient conditions is quite different from those of the other alkali monosilicides (Fig. 3). The strong A_1 mode is easily recognised at 480 cm^{-1}; however, the E mode is split to give a pair of medium intensity peaks at 280 and 300 cm^{-1}, and the T_2 mode gives rise to a group of three peaks centred near 350 cm^{-1}. This is a result of the site distortion of the Si_4^{4-} anions within the monoclinic crystal structure. Carrying out a symmetry analysis for the $C2/c$ structure (point group C_{2h}) with $Z = 8$ Na_4Si_4 units in the equivalent primitive cell leads to a prediction of $\Gamma_{normal} = 12A_g+12A_u+12B_g+12B_u$, where the A_g and B_g species are Raman active. Each Si_4^{4-} unit is associated to 3 internal modes, ν_1 (480 cm^{-1}), ν_2 (280 cm^{-1}) and ν_3 (350 cm^{-1}) and 6 external modes (3 rotations and 3 translations). In our Raman spectra, we expect 6 bands associated to the internal modes: 1 at 480 cm^{-1}, 2 around 280 cm^{-1} and 3 around 350 cm^{-1}. Rotations and translations are expected at low wavenumbers and only a few are often observed with our spectrometer. This is also the case for the modes related to translation of Na atoms ($6A_g+6A_u+6B_g+6B_u$).

During the first compression steps, changes in the Raman spectra indicate how the sample accommodates to pressure in non-hydrostatic conditions. This is evidenced by the appearance of two modes at 350 and 185 cm^{-1} at 4 GPa (Fig. 3). However, noticeable structural transformations occurring within the Si_4^{4-} units during compression result in a rapid increase in the intensity of a band near 370 cm^{-1}, in the region of the T_2 vibration, above 8 GPa. This observation coincides with a reduction in the number of peaks observed in the spectrum. Both changes are consistent with a transition into a phase with higher symmetry. The spectral features of crystalline NaSi remain recognisable up to 23 GPa. However, further compression results in a dramatic broadening of all modes, indicating pressure-induced amorphisation (Fig. 3). The onset of the amorphisation process is preceded by a noticeable reduction in intensity of the Si_4^{4-} stretching and bending vibrations, suggesting that the amorphisation may be associated with changes in the Si–Si bonding. During further compression to

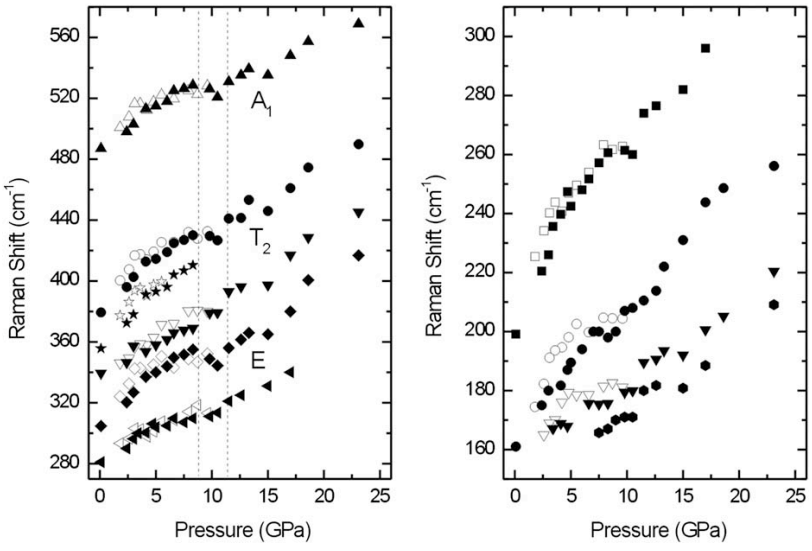

Fig. 4. Raman shifts plotted vs. pressure for crystalline NaSi. Full and empty symbols stand for compression and decompression runs respectively. Softening of certain bands is observed in between 8 and 12 GPa (highlighted by vertical dashed lines).

50 GPa the Raman scattering signal from the sample consists of a broad featureless signal extending to above 600 cm^{-1} that could barely be distinguished from the background (Fig. 3).

On examination of the Raman data at elevated pressures (Fig. 4), a linear increase of about 4 cm^{-1} GPa^{-1} is observed for most modes up to 8 GPa. The Si–Si stretching mode at 482 cm^{-1} is the most resistant to compression, with a coefficient of 2.81 cm^{-1} GPa^{-1}. Between 8 and 12 GPa, some of the lattice and vibrational modes show a small shift to lower wavenumber. The softening is largest in the case of the A_1 and E symmetry modes: −3.24 and −4.71 cm^{-1} GPa^{-1} respectively and it indicates the occurrence of a phase transition. The transformation is fully reversible upon decompression but it occurs with some hysteresis, indicating a first order transition (Fig. 4). A second vibrational mode softening at around 15 GPa suggests the initiation of the pressure-induced amorphisation observed. This will be discussed further below in the context of X-ray diffraction data.

During decompression from 50 GPa (Fig. 5), the sample remained mainly amorphous with a broad maximum near 470 cm^{-1} at 1 GPa. Some regions of the sample probed within the cell exhibited broad features that are similar (but not identical) to Raman bands reported for metastable silicon phases such as Si-III [27]. It is not known whether the partial metastable recrystallisation occurs spontaneously during decompression or whether it is due to the laser irradiation.

Once the sample was recovered to ambient conditions and the DAC opened, a vigorous reaction with atmospheric O_2 or H_2O took place, either with the highly reactive amorphous NaSi phase or with perhaps nanocrystalline Na metal produced during the amorphisation process.

3.2. *X-ray diffraction studies and density functional theory calculations*

Our Raman studies were complemented with *in situ* X-ray diffraction. Upon initial compression, all the peaks are observed to broaden due both to internal strains developed at grain boundaries (in the absence of a pressure-transmitting medium) within the compressed polycrystalline sample, and also the 1–2 GPa pressure gradients, indicated by the different ruby chips placed within the sample chamber (Fig. 6). The monoclinic NaSi structure remains recognisable up to about 8 GPa (Fig. 6). Changes in the pressure variation of individual reflections reveal evidence for a structural or phase transformation occurring in the 8–12 GPa range (Fig. 7). The new diffraction pattern is dominated by two strong reflections at 2.4 and 2.9 Å ($2\theta = 10.6°$ and 11.9°) at 14 GPa (Fig. 6). Substantial peak broadening did not allow an accurate structural refinement of the high-pressure phase structure, so we carried out DFT calculations in order to obtain models to be used in our LeBail and Rietveld refinements (Table 1).

The calculated cell volume matched that obtained by LeBail extraction (Fig. 8). Changes in the tetrahedral Si–Si distances and angles calculated upon compression are also shown in Fig. 8. Our initial constrained minimisations indicated that, as the cell was compressed, the monoclinic angle would be reduced. Full optimisation of the approximate high-pressure phase at 12 GPa resulted in a structure with $\beta = 106°$, compared with $\beta = 120°$ at ambient conditions. This structure is close to one obtained by

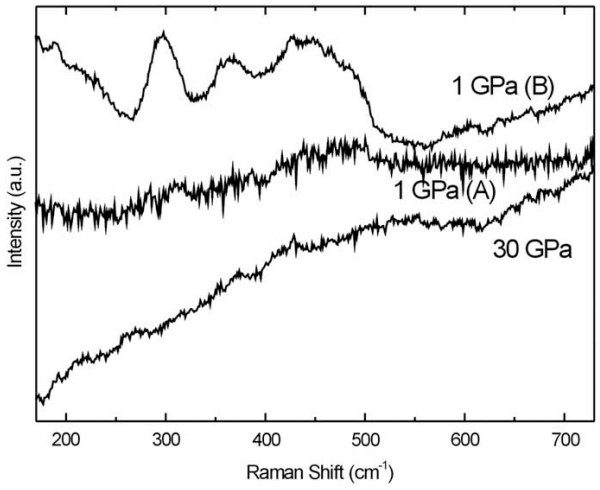

Fig. 5. Raman spectra of the amorphous sample obtained in the diamond anvil cell at 30 GPa and following decompression to 1 GPa. Two different spectra were obtained from regions of the sample recovered to 1 GPa. Spectra (A) and (B) correspond to different spots across the sample in the DAC.

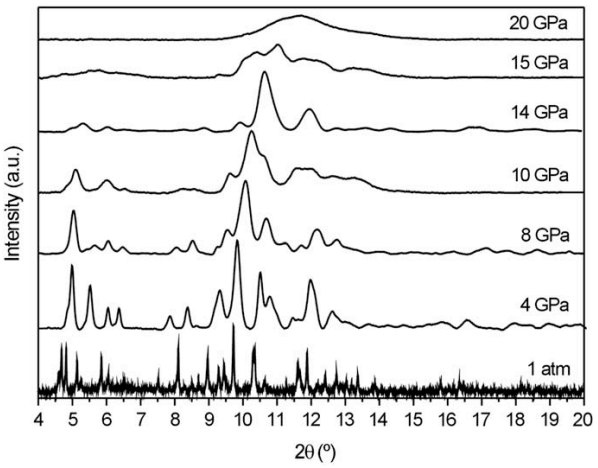

Fig. 6. Synchrotron X-ray diffraction patterns on NaSi upon compression at room temperature. The pattern at 1 atm was obtained using a Stoe diffractometer ($CuK\alpha_1$), however, it has been calculated for the synchrotron radiation at SRS 9.5HP ($\lambda = 0.443970$ Å) to be compared with the patterns at high pressure. A first crystal-to-crystal transformation of NaSi is observed above 8 GPa followed by pressure-induced amorphisation of the sample at 15 GPa.

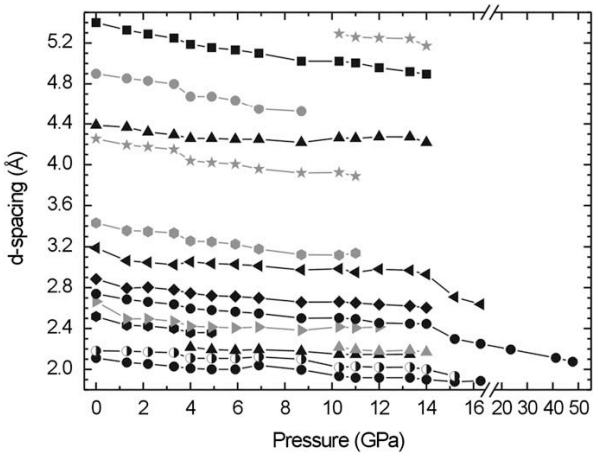

Fig. 7. Variation of interplanar spacings (d) of NaSi upon compression. The reflections affected by the transformation occurring between 8 and 12 GPa are highlighted (grey symbols).

taking the ambient phase and re-optimising it at an applied pressure of $P = 12$ GPa. However, it was not possible to optimize the high pressure structure directly from that at ambient conditions directly. Rather it was necessary to increase the pressure in steps of 2 GPa, re-optimizing the structure each time, in order to obtain a reliable high pressure structure. This behaviour is consistent with the presence of an energy barrier in the system that is likely associated with a first order phase transition into a high-pressure NaSi phase. One example of a Rietveld refinement using the calculated structure of NaSi at 12 GPa as a starting model is shown in Fig. 9. Experimental and calculated cell and atomic parameters are given in Table 2. The observed data (dots) fit quite well with the calculated curve (line), with reliability factors of $R_p = 9.21$, $R_{wp} = 10.9$, $R_{exp} = 2.27$ and the Bragg R-factor = 2.20.

Diffraction evidence for pressure-induced amorphisation (PIA) of the sample, as recorded by the Raman scattering measurements is shown by peak broadening and disappearance of most of the diffraction peaks beyond ~15 GPa. Although this pressure is much lower than that determined for the onset of PIA in the Raman experiments, this is not surprising in view of the longer correlation length required for crystalline X-ray diffraction features to be observed. The diffraction pattern corresponding to the amorphous modification is dominated by a single broad reflection. The initiation of PIA in the X-ray diffraction data indicates that the onset of the amorphisation process is associated with loss of long range order beginning at 15 GPa but the Raman data indicate that the local order of the $[Si_4]^{4-}$ units is maintained until 23 GPa. No recrystallisation of the amorphous modification occurs during further pressurisation to 50 GPa (Fig. 7). On decompression, it was possible to follow a continuous shift in the position of the broad amorphous reflection down to nearly ambient pressure, but the diffraction pattern changed abruptly in the last stages just before opening the DAC, with the appearance of two very weak broad reflections at 2.3 and 3.7 $Å^{-1}$ that are reminiscent of the pattern produced by amorphous silicon [28] (Fig. 10). We carried out a further experiment at high pressure using CO_2 laser heating in the diamond anvil cell to anneal the amorphous sample held at 30 GPa. To our surprise, this resulted in the appearance of sharp crystalline peaks due to *bcc* Na metal (Fig. 11). However, the broad features of the amorphous $Na_{1-x}Si$ material remained in the patterns.

Table 1
Correlation analysis for NaSi.

Ion movement			$G_M \rightarrow G_S \rightarrow G_F$			
Transl.	Libr.	Int.	T_d	C_2	C_{2h}	
Si_4						
		1	A_1	A	A_g	$\nu_1, 2\nu_2, \nu_3$, lib., trans.
		1	E		B_g	$2\nu_3$, 2lib., 2trans.
	1		T_1	B	A_u	$\nu_1, 2\nu_2, \nu_3$, lib., trans.
1		1	T_2		B_u	$2\nu_3$, 2lib., 2trans.
Na(1) and Na(2)						
				C_1		
					A_g	6 trans.
					B_{1g}	6 trans.
6				A		
					A_u	6 trans.
					B	6 trans.

There are three internal modes for each Si_4 group, υ_1 (482 cm^{-1}), υ_2 (285 cm^{-1}) and υ_3 (356 cm^{-1}) and 6 external modes (3 rotations and 3 translations). A_g and B_g modes are Raman active.

4. Discussion

The ambient pressure structure of NaSi is analogous to that of white phosphorus that forms a body-centered cubic lattice with discrete P_4 tetrahedra with intra-tetrahedral P–P distances of 2.21 Å [29]. The black orthorhombic modification that is

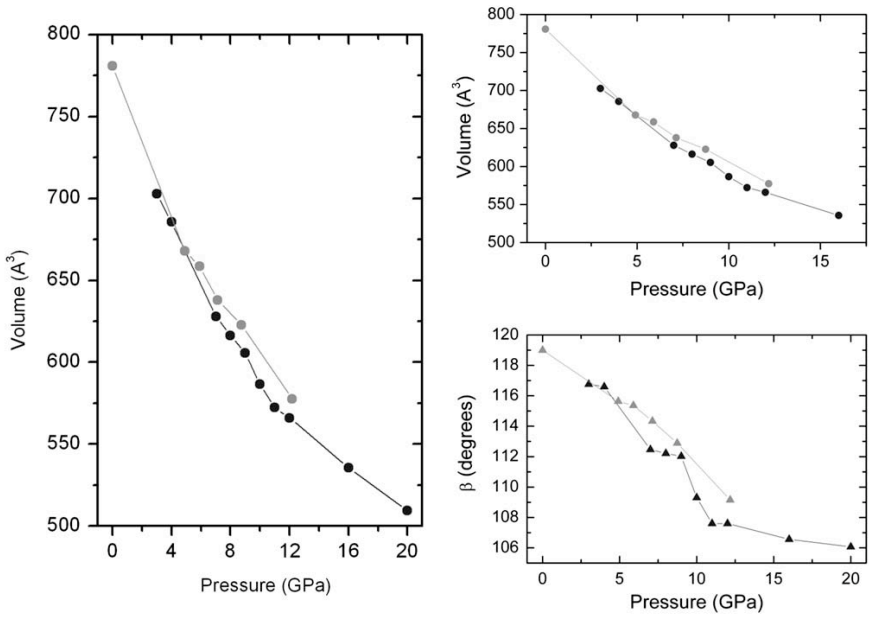

Fig. 8. Experimental (grey symbols) and calculated (black symbols) changes in unit cell volume as a function of pressure (*left*). Changes with pressure in Si–Si distances and angles calculated for $[Si_4]^4$ tetrahedra in the NaSi structure during compression (*right*).

analogous to the Si sublattice arrangement in LiSi is formed by puckered layers of phosphorus atoms, with P–P distances of 2.22 and 2.24 Å within the same layer, which fall within the same range as in the white modification [30,31]. The longest Si–Si bonds in the 3D LiSi structure are at around 2.4–2.5 Å, which are shorter than the first-nearest neighbour distance between tetrahedra calculated in this study for NaSi at 15 GPa (3.39 Å). The latter result indicates it is unlikely that the high-pressure transition observed for NaSi is simply a transformation into a LiSi-related 3D network. Instead, our experimental results and calculations suggest that the two NaSi structures are related through a translation of the $[Si_4]^{4-}$ tetrahedral layers accompanied by a rearrangement of the Na^+ positions and a relaxation of the $[Si_4]^{4-}$ tetrahedra towards a more highly symmetric structure (Fig. 12).

It has been reported that NaGe, which is also monoclinic at ambient conditions, undergoes a phase transition into the tetragonal *NaPb* structure at 4 GPa and 700 °C [13]. This structure contains isolated $[Si_4]^{4-}$ tetrahedral anions and it is also adopted by the cubic alkali monosilicides and monogermanides containing large cations (K, Rb, Cs) at conditions around 4 GPa and 600–700 °C [16]. However, the Rietveld refinements carried out using the *NaPb* structure as a starting model did not fit the diffraction patterns accurately and the minimum value for the monoclinic β-angle in NaSi was calculated to be 106°.

The formation of the amorphous ($Na_{1-x}Si$) material at high pressure is an intriguing observation. The featureless Raman spectra and broad X-ray diffraction pattern resemble those recorded for the metallic high-density amorphous phase (HDA) of elemental a-Si [28,32,33]. It is therefore possible that a high-density metallic amorphous form of NaSi has been produced in our experiments. Such an amorphous phase could contain a mixture of separated Si_4^{4-} units as well as tetrahedra linked by Si–Si bonds, by analogy with those that occur among varieties of "red" phosphorus. However, the appearance of diffraction peaks due to metallic Na following heating experiments at high pressure indicates that redox reactions can occur, producing Na^0 by $Na^+ + e^-$. The corresponding oxidation of silicon species involves $Si^- = Si^0 + e^-$, with the formation of new Si–Si bonds. The result is a progressive cross-linking of the silicide network to form nanoclusters of partially polymerised $(Si_x)^{y-}$ units, that can

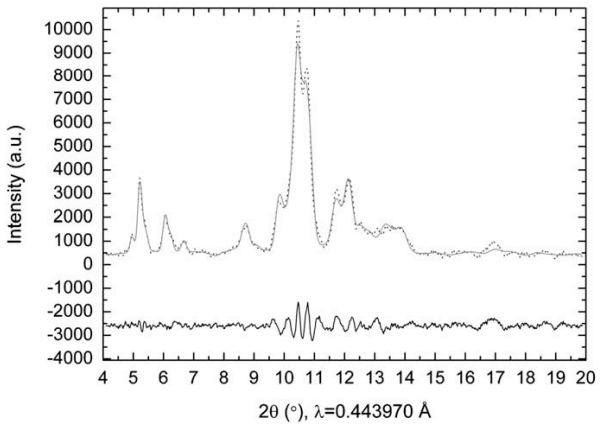

Fig. 9. Rietveld refinement carried out for an X-ray diffraction pattern of the high-pressure phase of NaSi at 12 GPa ($\lambda = 0.443970$ Å). The NaSi *C2/c* structure calculated at 16 GPa was used as a reference model for the refinement. Reliability factors are $R_p = 9.21$, $R_{wp} = 10.9$, $R_{exp} = 2.27$, Bragg *R*-factor = 2.20.

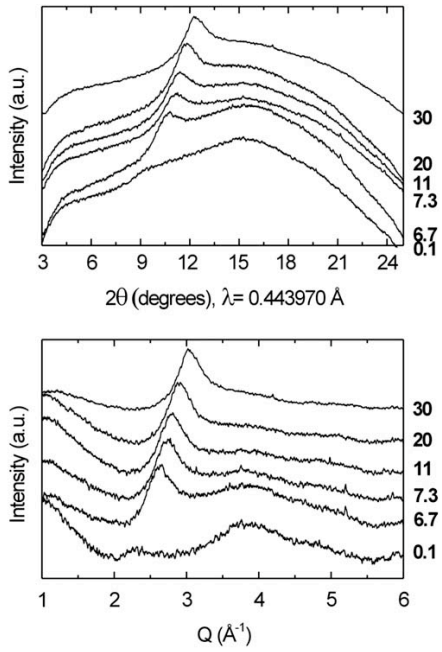

Fig. 10. X-ray diffraction patterns of NaSi obtained upon decompression from 30 GPa. Raw data (*above*) and corresponding baseline-subtracted data in Q space (*below*). Corresponding pressure values are given on the right-hand side of the plot in bold.

Table 2
Experimental and calculated cell parameters and atomic positions for NaSi at high pressure.

Cell parameters						
a	9.62272	10.18991	0.00846			
b	6.08230	6.07541	0.00479			
c	9.62272	9.96378	0.00739			
α	90.00000	90.00000	0.00000			
β	105.76357	109.38072	0.04078			
γ	90.00000	90.00000	0.00000			
	DFT			Ref.		
	x	*y*	*z*	*x*	*y*	*z*
Atomic positions						
Na(1)	0.11991	−0.76442	−0.38827	0.12336 (3)	−0.80632 (2)	−0.37622 (2)
Na(2)	0.82457	−0.58583	−0.40665	0.84174 (2)	−0.55910 (2)	−0.42675 (1)
Si(1)	0.11334	−1.04175	−0.15849	0.10155 (1)	−1.04640 (2)	−0.13803 (1)
Si(2)	−0.07563	−1.30006	−0.16588	−0.08363 (1)	−1.31807 (2)	−0.16523 (1)

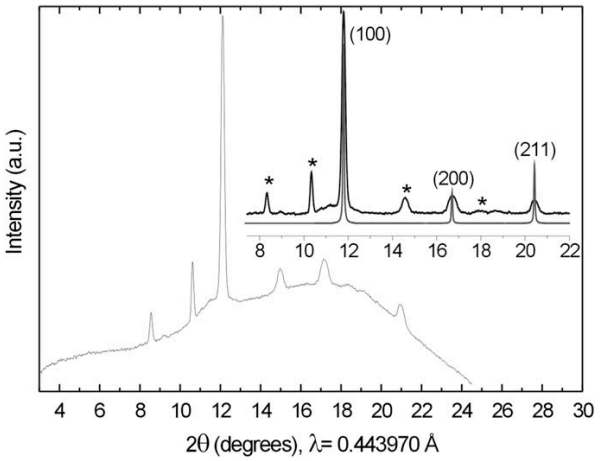

Fig. 11. X-ray diffraction pattern obtained after laser annealing of the amorphous NaSi sample at 30 GPa. The sample was loaded in dried NaCl and heated indirectly with a CO_2 laser, using ruby chips to transmit heat to the sample. The inset shows the pattern obtained after baseline subtraction, with characteristic lines from *bcc* Na metal (1 0 0), (2 0 0) and (2 1 1) reflections (grey) and peaks corresponding to the B2 phase of NaCl used as the pressure-transmitting medium (marked by asteriks).

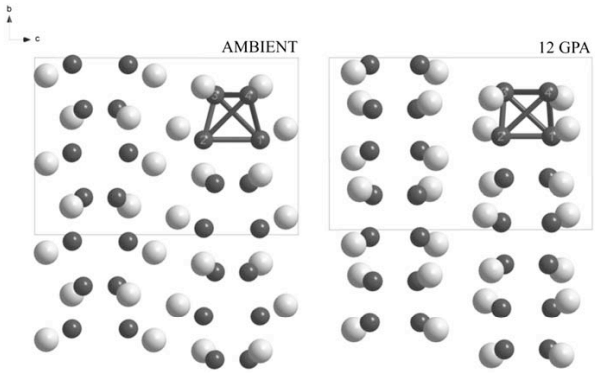

Fig. 12. Representation of the crystal structure of NaSi at ambient and high pressure (view along [1 0 0] plane). The structures are related by a slip of the $[Si_4]^{4}$ tetrahedral layers along with a rearrangement of the Na^+ cations and reduced distortion of the $[Si_4]^{4}$ units.

contain both $Si(Si)_3$ and $Si(Si)_4$ sites. These could have interesting and unusual electronic and optical properties. High-pressure treatment of alkali metal silicides may provide a new route to synthesise and control the polymerisation state of silicon-based nanoclusters.

Our results also have implications for the occurrence of high-density/low-density (HDA, LDA) polyamorphic transitions in Si- and Ge-based systems [28,32–35]. Amorphous Si and Ge are known to undergo a semiconductor–metallic transformation at high pressure that maps onto an expected density-driven liquid–liquid phase transition that appears quite general among elemental and other simple liquids [36]. It is interesting to explore how the observed PIA in NaSi and other alkali metal-containing alloys and compounds relate to the HDA-LDA behaviour. Recently, Machon et al. [37] studied amorphisation of the semiconductor clathrate phase Rb_6Si_{46}, and suggested that the large Rb atoms remain trapped within the a-Si structure at high pressure. They indicated that the high-density amorphous structure resembled that of HDA a-Si, and that a polyamorphic transition to an LDA phase resembling a-Si occurred during decompression. Our diffraction data indicate that the situation for NaSi is different, and that chemical diffusion accompanied by Na^+/Na^0 and Si^-/Si^0 redox processes occurs at high pressure or during decompression. In contrast to Rb, the smaller Na atoms appear to diffuse more easily through an a-Si network; as occurs during the formation of Si clathrates from the thermal decomposition of NaSi [38]. We expect that nanocrystalline *bcc* Na may form readily at high pressure causing the production of new Si–Si bonds between $[Si_4]^{4-}$ units and forming nanoscale clusters. Our computational studies indicate that the amorphisation process could originate in the ready distortion of the tetrahedral $[Si_4]^{4-}$ groups, indicated by our vibrational spectroscopy results at high pressure.

Consideration of the molar volumes gives useful insights into the nature of the chemical processes occurring in these systems. Under ambient conditions, the molar volume of NaSi is calculated to be 29.34 $cm^3\,mol^{-1}$, whereas the sum of the molar volumes of elemental Na and Si is 35.74 $cm^3\,mol^{-1}$. When the pressure is increased to 15 GPa, the molar volume calculated for NaSi decreases to 20.69 $cm^3\,mol^{-1}$. At this pressure, the volume of Na metal is 12.05 $cm^3\,mol^{-1}$ [39]. On the other hand, under these conditions, silicon can exist in either of three possible phases: in its high-density amorphous (HDA) modification, as the *β-Sn* type, or simple hexagonal (*sh*) phase. The molar volumes for *β-Sn* and *sh*-Si are known to be 20.36 [40] and 20.15 $cm^3\,mol^{-1}$ [41], respectively. The molar volume of HDA-Si, however, is unknown, but must be smaller than that of LDA-Si, 24.36 $cm^3\,mol^{-1}$ [42]. What this implies is that the molar volume of NaSi at 15 GPa must be slightly greater than the sum of volumes of its elemental components, a situation that therefore favours the otherwise unexpected decomposition of the intermetallic to its elements upon compression. Furthermore, we note that diffraction peaks of sodium become visible, whereas no evidence is observed for crystalline silicon. This is in stark contrast to our previous experiments in which *β*-Sn silicon crystallises spontaneously in the X-ray beam at 17 GPa and suggests that the presence of sodium may play a role in suppressing crystallisation, thereby extending the stability range of the amorphous silicon.

5. Conclusions

We have described the high-pressure behaviour of NaSi up to 50 GPa. As evidenced by both Raman and X-ray diffraction results, the solid adopts a higher-symmetry crystal structure in the range between 8 and 12 GPa. Density functional theory calculations showed that the ambient and high-pressure crystal structures are related by slipping of the planes of Si tetrahedra and rearrangement of the Na atoms. No evidence of a transformation of NaSi into a crystalline non-molecular network was recorded. However, random cross-linking between Si subunits has been suggested to result in irreversible loss of translational order. The nature of this amorphous modification has been discussed in terms of pressure-induced decomposition of the sample.

Acknowledgments

This work was supported by EPSRC Portfolio grant EP/D504782 (to C.R.A. Catlow, P. Barnes and PFM) and an EPSRC Senior Research Fellowship (GR/T00757) to PFM. Computer resource provided by EPSRC grant GR/S84415/01 (DWL). OIB also acknowledges support of Marie Curie Incoming International Fellowship (Project title "High-pressure phase transitions in

polyamorphic systems of semiconducting elements", contract number MIF2-CT-2006-008575). We thank A. Lennie (SRS Daresbury Laboratory, CCLRC) for assistance with the synchrotron experiments.

References

[1] S.M. Kauzlarich, Chemistry, Structure, and Bonding of Zintl Phases and Ions, Wiley-VCH Publishers, New York, 1996.
[2] R. Schäfer, Annu. Rev. Mater. Sci. 15 (1985) 1–41.
[3] R. Schäfer, Angew. Chem. Int. Ed. 12 (1973) 694–712.
[4] P.F. McMillan, J. Gryko, C. Bull, R. Arledge, A.J. Kenyon, B.A. Cressey, J. Solid State Chem. 178 (2005) 937–949.
[5] J.S. Kasper, P. Hagenmuller, M. Pouchard, C. Cros, Science 150 (1965) 1713–1714.
[6] A. San-Miguel, P. Toulemonde, High Pressure Res. 25 (2005) 159–185.
[7] G.K. Ramachandran, J. Dong, J. Diefenbacher, J. Gryko, R.F. Marzke, O.F. Sankey, P.F. McMillan, J. Solid State Chem. 145 (1999) 716–730.
[8] R. Schäfer, W. Klemm, Z. Anorg. Allg. Chem. 312 (1961) 214–220.
[9] J. Witte, H.G. Schnering, Z. Anorg. Allg. Chem. 327 (1964) 260–273.
[10] E. Busmann, Z. Anorg. Allg. Chem. 313 (1961) 90–106.
[11] J. Evers, G. Oehlinger, G. Sextl, Angew. Chem. Int. Ed. 32 (1993) 1442–1444.
[12] J. Evers, G. Oehlinger, G. Sextl, H.-O. Becker, Angew. Chem. Int. Ed. 26 (1987) 76–78.
[13] J. Evers, G. Oehlinger, G. Sextl, A. Weiss, Angew. Chem. Int. Ed. 24 (1985) 500–501.
[14] J. Evers, G. Oehlinger, A. Weiss, J. Solid State Chem. 20 (1977) 173–181.
[15] J. Evers, G. Oehlinger, A. Weiss, Angew. Chem. Int. Ed. 17 (1978) 538–539.
[16] J. Evers, G. Oehlinger, G. Sextl, A. Weiss, Angew. Chem. Int. Ed. 23 (1984) 528–529.
[17] E. Hohmann, Z. Anorg. Chemie 257 (1948) 113–126.
[18] H.K. Mao, G. Shen, R.J. Hemley, T.S. Duffy, in: M. H. Manghnani, T. Yagi (Eds.), X-ray diffraction with a double hot-plate laser-heated diamond cell, Properties of Earth and Planetary Materials at High Pressure and Temperature, American Geophysical Union, Washington DC, 1998, pp. 27–34.
[19] R.A. Forman, G.J. Piermarini, J.D. Barnett, S. Block, Science 176 (1972) 284–285.
[20] A.P. Hammersley, S.O. Svensson, M. Hanfland, A.N. Fitch, D. Häusermann, High Pressure Res. 14 (1996) 235–248.
[21] J. Rodríguez-Carvajal, FULLPROF: A Program for Rietveld Refinement and pattern matching analysis, Abstracts of the Satellite Meeting on Powder Diffraction of the XV Congress of the IUCr, Toulouse, 1990, p. 127.
[22] T. Roisnel, J. Rodríguez-Carvajal, in: R. Delhez, E.J. Mittenmeijer (Eds.), WinPLOTR: A Windows tool for powder diffraction patterns analysis, Materials Science Forum, Proceedings of the Seventh European Powder Diffraction Conference (EPDIC 7), 2000, pp. 118–123.
[23] DMol^3 Software, Accelrys, Inc., San Diego, CA, 2006.
[24] J. Perdew, Y. Wang, Phys. Rev. B: Condens. Matter Mater. Phys. 46 (1992) 12947–12954.
[25] S.J. Clark, M.D. Segall, C.J. Pickard, P.J. Hasnip, M.I.J. Probert, K. Refson, M.C. Payne, Z. Kristallog. 220 (2005) 567–570.
[26] G. Kliche, M. Schwarz, H.G. Schnering, Angew. Chem. Int. Ed. 26 (1987) 349–351.
[27] M. Hanfland, K. Syassen, High Pressure Res. 3 (1990) 242–244.
[28] D. Daisenberger, M. Wilson, P.F. McMillan, R. Quesada Cabrera, M.C. Wilding, D. Machon, Phys. Rev. B: Condens. Matter Mater. Phys. 75 (2007) 224118.1–224118.11.
[29] D.E.C. Corbridge, E.J. Lowe, Nature 170 (1952) 629.
[30] R. Hultgren, N.S. Gingrich, B.E. Warren, J. Chem. Phys. 3 (1935) 351–355.
[31] A. Brown, S. Rundqvist, Acta Cryst. 19 (1965) 684–685.
[32] S.K. Deb, M. Wilding, M. Somayazulu, P.F. McMillan, Nature 414 (2001) 528–530.
[33] P.F. McMillan, M. Wilson, D. Daisenberger, D. Machon, Nat. Mater. 4 (2005) 680–684.
[34] E. Principi, A. Di Cicco, F. Decremps, A. Polian, S. De Panfilis, A. Filipponi, Phys. Rev. B: Condens. Matter Mater. Phys. 69 (2004) 201201.1–201201.4.
[35] F. Coppari, A. Di Cicco, A. Congeduti, J.C. Chervin, F. Baudelet, A. Polian, High Pressure Res. 29 (2009) 103–107.
[36] P.F. McMillan, J. Mater. Chem. 14 (2004) 1506–1512.
[37] D. Machon, P. Toulemonde, P.F. McMillan, M. Amboage Castro, A. Munoz, P. Rodriguez-Hernandez, Phys. Rev. B: Condens. Matter Mater. Phys. 79 (2009) 184101.
[38] A. San-Miguel, P. Kéghélian, X. Blase, P. Mélinon, A. Pérez, J.P. Itié, A. Polian, E. Reny, C. Cros, M. Pouchard, Phys. Rev. Lett. 83 (1999) 5290–5293.
[39] M. Hanfland, I. Loa, K. Syassen, Phys. Rev. B: Condens. Matter Mater. Phys. 65 (2002) 184109.1–184109.8.
[40] A. Werner, J.A. Sanjurjo, M. Cardona, Solid State Commun. 44 (1982) 155–158.
[41] J.Z. Hu, L.D. Merkle, C.S. Menoni, I.L. Spain, Phys. Rev. B: Condens. Matter. Mater. Phys. 34 (1986) 4679–4684.
[42] J.S. Custer, M.O. Thompson, D.C. Jacobson, J.M. Poate, S. Rooda, W.C. Sinke, F. Spaepen, Appl. Phys. Lett. 64 (1994) 437–439.

High-Pressure Behavior and Polymorphism of Titanium Oxynitride Phase $Ti_{2.85}O_4N$

Ashkan Salamat, Geoffrey Hyett, Raul Quesada Cabrera, Paul F. McMillan,* and Ivan P. Parkin*

Materials Research Centre, Christopher Ingold Laboratory, University College London, 20 Gordon Street, London, WC1H 0AJ, United Kingdom

Received: January 26, 2010; Revised Manuscript Received: March 18, 2010

We report a crystallographic study of $Ti_{2.85}O_4N$, a new titanium oxynitride phase discovered using chemical vapor deposition and combinatorial chemistry techniques, under high-pressure conditions. Synchrotron X-ray diffraction was used to monitor structural changes in the material during compression up to 68 GPa. The data indicate that the orthorhombic (*Cmcm*) ambient-pressure phase ($K_0 = 154 \pm 22$ GPa with $K_0' = 5.2 \pm 0.5$) undergoes a first-order transition at 18 GPa to a new orthorhombic ($Pmc2_1$) structure. This new high-pressure polymorph remains stable up to 42 GPa, after which the emergence of a second high-pressure monoclinic ($P2_1/c$) phase is observed.

Introduction

A new titanium oxynitride phase, $Ti_{2.85}O_4N$, was recently discovered using the synthetic route of atmospheric pressure chemical vapor deposition combined with combinatorial materials exploration:[1] this new material was shown to be an active photocatalyst under UV illumination.[2] Chemical vapor deposition (CVD) is a technique more normally associated with thin film synthesis and industrial-scale deposition processes than with exploratory materials discovery research.[3] Recent studies conducted within the UCL group are now establishing the technique as a method for synthesizing new solid-state compounds and materials that may have technologically important properties, including photocatalysis. This work has focused recently on synthesis of novel semiconducting titanium oxynitride polymorphs that are poorly represented in the database at present. These are of primary interest for exploration because of the known optoelectronic and photocatalysis properties of TiO_2 and its N-doped equivalents, combined with predictions of new Ti_3N_4 and related oxynitrides based on ab initio theoretical studies combined with high-pressure−high-temperature synthesis studies.[4−6] Such new metal nitride and oxynitride compounds and their crystalline polymorphs are of great interest for development of new materials for photocatalysis, including water-splitting for energy applications, fine chemical production, and water decontamination and disinfection procedures.[7−9] Two main groups of titanium oxynitride materials have been investigated so far: first, TiO_xN_y phases that exist as a solid solution between the rock-salt structured end members TiN and TiO ($x + y \sim 1$) and N-doped TiO_2N_x phases, with the nitrogen doping <1−5%.[10,11] These latter materials have been identified as potential visible light photocatalysts.[12] Here, we have adopted the novel technique of using the CVD-synthesized material as a precursor for high-pressure studies to investigate the formation and recovery of new crystalline polymorphs. We predicted that this approach would result in higher-density titanium oxynitride structures with useful optoelectronic properties that could be developed for photocatalytic applications.[13,14]

The archetype Ti_3O_5 material for our investigations is a member of the Magnéli series of Ti_nO_{2n+1} phases with $n = 3$. It occurs at room temperature as an insulator with a monoclinic structure (β-Ti_3O_5). It undergoes a phase transition at 450 K to a second monoclinic structure (β') with a sharp 6% increase in unit cell volume. Further heating to 500 K leads to a second phase transition to the orthorhombic α-Ti_3O_5 structure.[15] The phase transition and volume increase at 450 K are associated with an insulator−metal transition. In the low T β phase, the titanium d electrons are localized within a metal−metal bond, which, above the transition temperature, become delocalized: breaking the metal−metal bond results in a relaxation of the structure and unit cell expansion. Previous work has found that reduction of the Fermi level by substituting Ti^{4+} with cations of lower charge causes a lowered transition T to be observed.[16−18] Hyett et al. demonstrated that a similar effect can be observed using anionic substitution in the new compound $Ti_{2.85}O_4N$ prepared by CVD, comparable with that achieved in α-Ti_3O_5 at $T > 500$ K.[1] High-pressure techniques provide a powerful tool for investigation of polymorphism and synthesis of new materials.[19] There have been a few previous studies of titanium oxides and nitrides under high-pressure conditions.[20,21] The polymorphism in TiO_2 has been investigated extensively, including studies of nanomaterials.[22−24] Åsbrink et al. investigated β-Ti_3O_5 (*C*2/*m* structure) up to 40 GPa but were unable to identify any pressure-induced phase transitions.[25] Here, we report high-pressure polymorphism of the new oxynitride compound $Ti_{2.85}O_4N$ using synchrotron X-ray diffraction techniques in a diamond anvil cell.

Experimental Techniques

A thin film of $Ti_{2.85}O_4N$ was synthesized via atmospheric pressure chemical vapor deposition (APCVD) from the reaction between gaseous titanium(IV) chloride, ethyl acetate, and ammonia deposited onto a glass surface. Titanium(IV) chloride (Aldrich, 99.9%) and ethyl acetate (Fisher, Reagent grade) were heated in bubblers to 82 and 39 °C, respectively, to generate vapors of these precursors, which were then transported to a mixing chamber with N_2 gas (BOC), with flow rates of 2 and 0.5 L min^{-1} through the titanium(IV) chloride and ethyl acetate, respectively. Ammonia vapor was transported to the mixing

* To whom correspondence should be addressed. E-mail: p.f.mcmillan@ucl.ac.uk (P.F.M.), i.p.parkin@ucl.ac.uk (I.P.P.).

10.1021/jp100769r
Published on Web 04/20/2010

chamber using its own room temperature vapor pressure. In the mixing chamber, the precursor gases were combined with a plain N_2 flow of 12 L min^{-1} and carried into the reaction chamber. All gas transport pipes and the mixing chamber were heated to 200 °C to avoid precursor condensation. The reaction chamber consisted of a 330 mm long silica tube with a diameter of 105 mm, containing a half-cylinder graphite block on which rested the glass substrate (220 × 90 × 3 mm^3). Whatman heater catridges inserted into the graphite block heated the substrate to 660 °C, at which temperature the precursors reacted to form a thin film of the titanium oxynitride. The deposition was conducted for 5 min. Additional details of the synthesis experiments along with chemical and structural characterization of the samples have been given previously.[1]

For high-pressure experiments, the thin film sample was removed from the substrate and ground into a powder. The $Ti_{2.85}O_4N$ material was precompressed between tungsten carbide cubes before being loaded into a cylindrical diamond anvil cell. Runs were carried out both nonhydrostatically without any pressure-transmitting medium and also using nitrogen cryogenically loaded into the DAC as a quasi-hydrostatic medium over at least part of the pressurization range. Experiments were carried out up to 68 GPa using 200 or 300 μm diamond culets. Rhenium gaskets were preindented to 30 μm and drilled using electroerosion to provide 80 μm holes. Pressure was determined using ruby fluorescence.[26] X-ray diffraction data were obtained at station ID27 of the European Synchrotron Radiation Facility (Grenoble, λ_0 = 0.3738 Å) and at beamline I15 at Diamond Light Source (Didcot, λ_0 = 0.4441 Å). At the ESRF, the 2 × 3 μm beam permitted micrometer-scale mapping of the sample chamber, whereas at Diamond, the incident beam was collimated to 30 μm. Two-dimensional diffraction data were recorded using either a CCD detector or a MAR 345 image plate and then integrated and transformed to 1-D patterns using Fit2D[27] and analyzed using GSAS,[28,29] FullProf,[30] and PowderCell.[31]

Results and Discussion

The composition of the starting $Ti_{2.85}O_4N$ sample produced by APCVD synthesis was determined previously using a combination of chemical analysis methods and Rietveld refinement of the powder X-ray synchrotron diffraction data.[1] A minor impurity peak at 2.52 Å identified as TiC represented <0.5% of the sample.

In a first series of high-pressure runs, we loaded the sample using N_2 as the pressure-transmitting medium and obtained high-quality data in the low-pressure range that we could analyze using refinement methods (Figure 1). Above 16−18 GPa, the data quality was reduced dramatically. We can partly associate this with the $\delta-\varepsilon$ transition of crystalline N_2.[32,33] However, a phase transition occurring in the $Ti_{2.85}O_4N$ sample was also indicated from the X-ray data in the same pressure range (Figure 2). We carried out a second series of runs with no pressure-transmitting medium present. This clearly showed the same transition occurring within the titanium oxynitride compound at around 18 GPa.

The X-ray diffraction data were analyzed using Le Bail methods to provide information on unit cell and d_{hkl} spacing variations with pressure (see Table 1).[34] These clearly identified contributions from the N_2 pressure-transmitting medium and the TiC impurity (Figure 1). The X-ray diffraction patterns of $Ti_{2.85}O_4N$ could be modeled using the ambient-pressure structure until ~14 GPa: above 18 GPa, the diffraction pattern first showed the emergence of a second orthorhombic phase mainly characterized by the appearance of a new peak at 11.6° 2θ. The

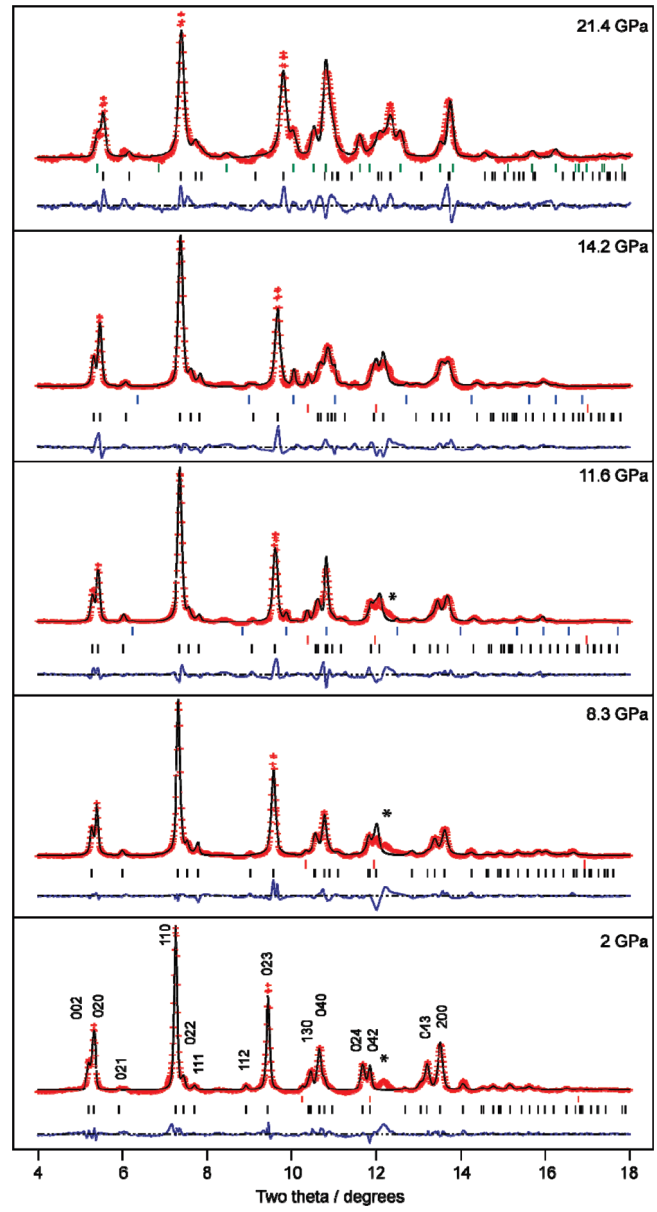

Figure 1. Le Bail refinements of diffraction data obtained up to 21.4 GPa in N_2 pressure-transmitting medium. Data points and Le Bail fits are overlaid in red and black, respectively, and difference plots are shown. The tick marks indicate peaks for the *Cmcm* $Ti_{2.85}O_4N$ structure (below), the high-pressure $Pmc2_1$ present at 21.4 GPa, and the TiC impurity and the δ- and ε-N_2 phases of the pressure medium. Asterisks (*) mark an identified broad peak that was assigned to an unknown impurity.

new structure could be refined within $Pmc2_1$ symmetry, based on systematic *hkl* absences. However, the low-pressure *Cmcm* phase could still be identified in the diffraction pattern until ~42 GPa, indicating that the transition must be first-order in nature. By 24 GPa, at least five peaks were observed due to the new high-pressure phase. These were indexed to an orthorhombic $Pmc2_1$ structure with a = 2.401 Å, b = 4.712 Å, and c = 6.019 Å (V = 68.10 $Å^3$) at a pressure of 24 GPa (see Table 2). This phase was found to be stable to beyond 42 GPa. By 68 GPa, at least two of the peaks develop shoulders, indicating a potential further phase change (Figure 3). Experiments conducted with no pressure-transmitting medium to above this pressure clearly revealed a potential second high-pressure phase transition. The second high-pressure phase is indexed as

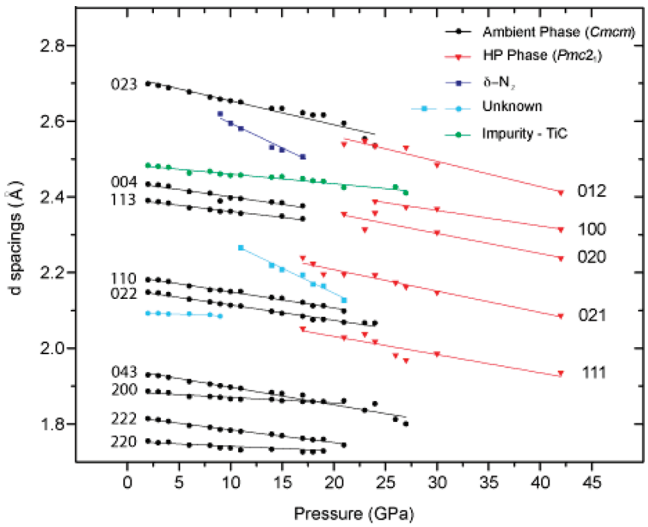

Figure 2. Positions recorded for diffraction peaks observed in the XRD data as a function of increasing pressure (GPa). The data indicate the appearance of a new phase (assigned by Le Bail refinement to $Pmc2_1$ symmetry) above 15−20 GPa. The low-pressure *Cmcm* phase persists to at least 23−27 GPa, indicating that the transformation is first-order. The d_{hkl} vs P data clearly reveal peaks due to e and δ phases of N_2 used as a pressure-transmitting medium as well as TiC and weak features due to an unidentified impurity phase.

TABLE 1: Cell Constants and Unit Cell Volume for $Ti_{2.85}O_4N$ (*Cmcm*) As Determined by Le Bail Refinement

pressure (GPa)	*a* (Å)	*b* (Å)	*c* (Å)	volume (Å^3)
2	3.7751(2)	9.577(1)	9.8053(8)	354.51(3)
3	3.7710(2)	9.5644(9)	9.7906(8)	353.12(3)
4	3.7636(3)	9.540(1)	9.767(1)	350.68(6)
5.3	3.7583(2)	9.520(1)	9.742(1)	348.53(5)
6.8	3.7474(3)	9.481(1)	9.730(1)	345.69(4)
8.3	3.7456(2)	9.455(1)	9.674(1)	342.58(4)
9.5	3.7364(3)	9.428(1)	9.665(1)	340.49(5)
10.2	3.7321(2)	9.409(1)	9.650(1)	338.84(5)
11.6	3.7272(2)	9.397(1)	7.638(1)	337.59(4)
12.4	3.7211(3)	9.373(2)	9.604(2)	334.95(7)
14.2	3.7207(3)	9.337(1)	9.585(1)	332.99(5)
15.6	3.7221(3)	9.325(1)	9.576(1)	332.39(5)
17.2	3.7156(4)	9.294(2)	9.530(2)	329.10(7)
18.4	3.7159(4)	9.268(2)	9.513(2)	327.63(7)
19.7	3.7149(5)	9.264(2)	9.499(2)	326.91(9)
21.4	3.7197(5)	9.190(2)	9.449(2)	323.0(1)
23.1	3.7245(5)	9.194(2)	9.442(2)	323.3(1)

TABLE 2: Cell Constants and Unit Cell Volume for the High-Pressure Phase of $Ti_{2.85}O_4N$ ($Pmc2_1$) As Determined by Le Bail Refinement

pressure (GPa)	*a* (Å)	*b* (Å)	*c* (Å)	volume (Å^3)
19	2.446(1)	4.799(1)	6.107(1)	71.686(3)
21.4	2.422(1)	4.714(1)	6.022(1)	68.755(3)
23.1	2.41(1)	4.692(1)	6.023(1)	68.106(3)
24	2.401(1)	4.712(1)	6.019(1)	68.096(3)
30	2.371(1)	4.612(1)	5.906(1)	64.582(3)
42	2.315(1)	4.481(1)	5.735(1)	59.492(3)

monoclinic ($P2_1/c$), corresponding to a distortion of the orthorhombic $Pmc2_1$ high-pressure phase. Le Bail analysis indicates a = 4.3456(5) Å, b = 5.177(3) Å, c = 2.872(1) Å, and β = 99.7(1)° at P = 68 GPa.

Figure 4 shows the variation of lattice parameters of $Ti_{2.85}O_4N$ structures during compression, beginning with the ambient T

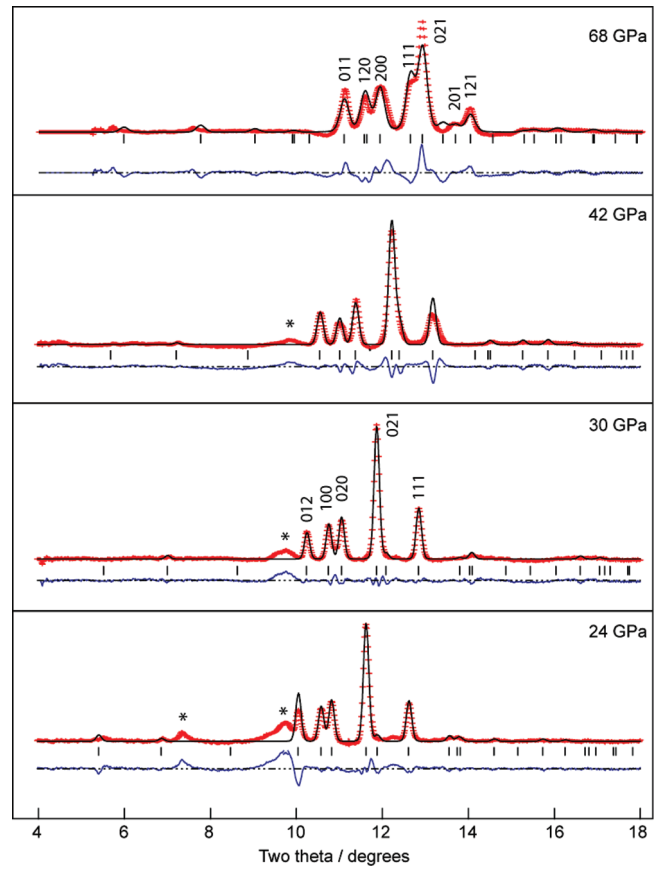

Figure 3. Nonhydrostatic compression data obtained with no pressure-transmitting medium at 24, 30, 42, and 68 GPa. The Le Bail refined X-ray diffraction patterns are of the $Pmc2_1$ high-pressure phase of $Ti_{2.85}O_4N$. Asterisks (∗) mark peaks resulting from remaining contributions from the ambient-pressure *Cmcm* phase. At 68 GPa, additional contributions indicating a second transformation into a monoclinic ($P2_1/c$) phase are observed.

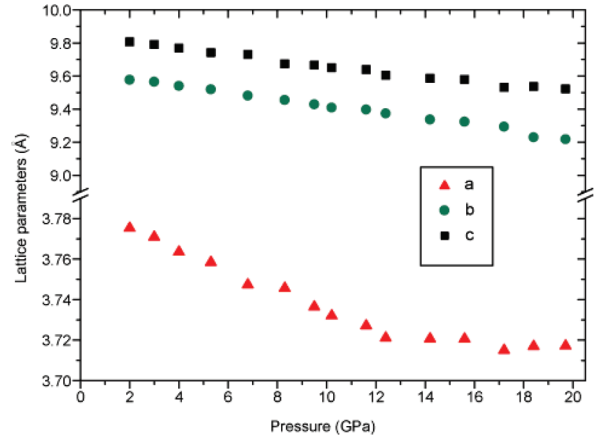

Figure 4. Plot of lattice parameters for the low- and high-pressure phases of $Ti_{2.85}O_4N$. The a, b, and c lattice parameters (Å) for the ambient phase of Ti_3O_4N (*Cmcm*) against pressure (GPa) are reported. The lattice parameters were determined using Le Bail refinement and are plotted with their corresponding y axis.

structure prepared by APCVD. The b and c parameters show an approximately linear decrease with pressure, corresponding to a 4% shortening in these parameters at a pressure of 20 GPa. However, a behaves differently: the initial compression is much lower (∼1%) and it completely ceases at ∼12 GPa. Interestingly, the same effect was observed previously for the monoclinic

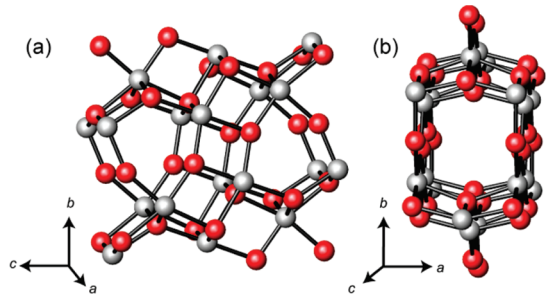

Figure 5. Representation of the unit cell of $Ti_{2.85}O_4N$, showing the titanium ions (gray) and anion sites (red). View of the (a) 100 face and (b) 001 face. From this can be seen the three coordinate anion sites between the tense titania layers that allow the relatively higher compressibility in the *b* and *c* directions.

β-Ti_3O_5 phase,[25] indicating that it does not depend on the presence of Ti vacancies or the degree of O/N substitution. In the case of Ti_3O_5, the *a* axis was found to have a linear compression of 0.8% that ceased at ~10 GPa compared with 6.7 and 5.4% for the *b* and *c* axes across the entire range up to 38 GPa. In both β-Ti_3O_5 and $Ti_{2.85}O_4N$ (Figure 5), the noticeably stiffer lattice direction is associated with dense columns of distorted edge-sharing TiO_6 octahedra along the 100 direction. These highly constrained structures have little possibility for angular distortion, and the linked Ti−O bonds resist compression along the axis. By 10−12 GPa, the maximum compressibility limit of the $(TiO_6)_n$ chains has been reached. The polyhedral compressibility for unlinked TiO_6 octahedra was estimated to be $\Delta V/V_o \sim 0.04$ GPa^{-1}, giving a maximum Ti−O bond compression at 10 GPa of ~1.5%. Along the 010 and 001 directions, the dense layers are interconnected by three coordinate anion sites that allow greater angular flexibility and, thus, the larger compressibility values recorded for the *b* and *c* dimensions over the entire pressure range, with no compression limit observed in the 10−12 GPa range. This observation indicates that the Ti_3O_5 and $Ti_{2.85}O_4N$ materials constitute remarkably rigid structures along one crystallographic direction.

The *V*(*P*) data were used to estimate the bulk modulus and its pressure derivative for the ambient-pressure $Ti_{2.85}O_4N$ compound as well as the new high-pressure phase. The compression data were analyzed using a finite strain Birch−Murnaghan equation of state (EOS) expression expanded to third order and the K_0 and K_0' values refined by constructing an Eulerian finite-strain reduced variable $F-f$ plot (Figure 6).[35] The data indicate a bulk modulus of $K_0 = 154 \pm 22$ GPa with $K_0' = 5.2 \pm 0.5$ for the ambient-pressure *Cmcm* phase of $Ti_{2.85}O_4N$. This is slightly lower than that obtained for β-Ti_3O_5 ($K_0 = 173$ GPa[25]) that can be attributed to the presence of cation vacancies in the oxynitride structure.

Recovery of the high-pressure phase to ambient conditions was studied during decompression from above 27 GPa, where the presence of the ambient phase was minimized in the X-ray diffraction pattern. The diffraction pattern of the high-pressure phase ($Pmc2_1$) is clearly visible during the first two pressure steps down to 25 GPa (Figure 7). Here, we have superposed the diffraction pattern obtained at 24 GPa for comparison. The peaks that are quite broad could indicate inhomogeneous strains present within the sample or structural disordering or even a nanocrystalline state. Although all of the diffraction peaks can be identified, there are marked changes in relative intensities between pressure points that could be due to changes in crystallite orientation relative to the incident beam. By 20 GPa, the main diffraction peaks become further broadened and new

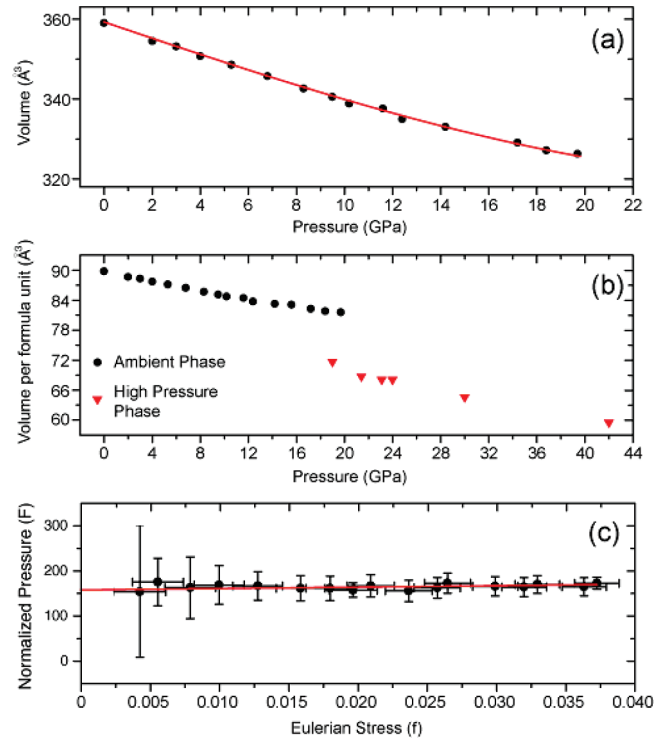

Figure 6. (a) A *V*(*P*) plot of compression data for the *Cmcm* phase of $Ti_{2.85}O_4N$. A Birch−Murnaghan equation of state reduced to the third order is fitted to the single phase. (b) The volume per formula unit is plotted as a function of pressure. A discontinuity is observed between the ambient phase (*Cmcm*) of $Ti_{2.85}O_4N$ and that of the first high-pressure phase ($Pmc2_1$). (c) Normalized pressure (*F*) vs Eulerian strain (*f*).

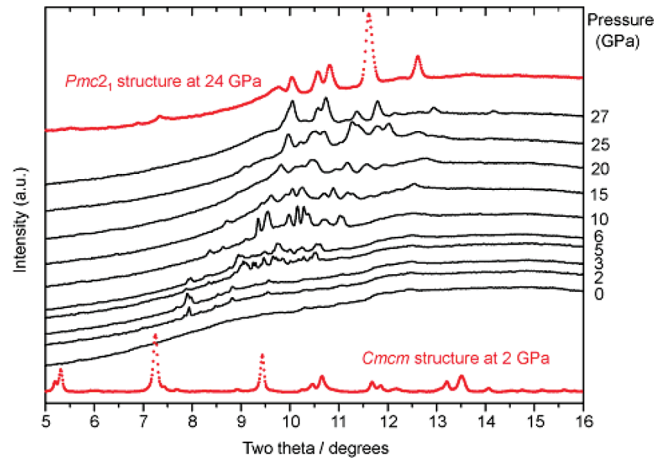

Figure 7. X-ray diffraction patterns of the decompression of the high-pressure phase of Ti_3O_4N from 27 to 0 GPa. Patterns shown in red are for reference and from the compression data sets at 2 and 24 GPa showing the patterns of the ambient structure and high-pressure structure, respectively.

features begin to appear in the pattern. At 15 GPa, below the first-order transition observed during the compression run, the broad diffraction peaks of the high-pressure phase can still be discerned in the pattern, but now a series of additional sharper peaks are clearly present that become better defined as the pressure is lowered to 10 GPa (Figure 7). A further new set of peaks is observed in the 5−6 GPa region that disappear by 2−3 GPa to be replaced by a simple peak pattern superimposed on a broad amorphous background. None of these series of peaks

correspond to structures identified within the $Ti_xO_yN_z$ system to date, and they likely correspond to metastable phases occurring as the highly metastable high-density $Ti_{2.85}O_4N$ structure is decompressed beyond its low-pressure stability limit. Upon complete decompression to a pressure of 1 atm, only weak broad bands indicating an amorphous or high disordered nanocrystalline material remain in the pattern. The results indicate that, following its formation at high pressure, the orthorhombic $Pmc2_1$ phase is not recoverable to ambient conditions, and decompression in the diamond anvil cell at room temperature results in recovery of amorphous material. We also carried out preliminary experiments using a multianvil apparatus, heating the $Ti_{2.85}O_4N$ at a pressure greater than 20 GPa to attempt to obtain a better crystallized sample that might be recoverable to ambient conditions. However, all of these investigations resulted in formation of a mixture of TiO_2 and TiN that is likely to be thermodynamically stable under the high-pressure−high-temperature conditions.

Conclusion

An investigation of the high-pressure behavior of $Ti_{2.85}O_4N$ was carried out using a diamond anvil cell and with synchrotron X-ray powder diffraction techniques. The diffraction pattern of the ambient-pressure *Cmcm* phase could be analyzed up to a pressure of 20 GPa to study its compressional behavior. The *b*- and *c*-axis parameters showed a near-linear decrease throughout the pressure range. The *a* parameter had a much smaller compressibility, and this stopped above 12 GPa. This behavior is similar to that of β-Ti_3O_5, and it can be explained by the relative incompressibility of edge-sharing chains of TiO_6 octahedra along the (100) direction.[36] The appearance of a new phase is indicated in the diffraction data above 18 GPa. The new compound can be indexed as an orthorhombic $Pmc2_1$ structure. However, the ambient-pressure *Cmcm* phase can still be recognized in the diffraction pattern up to a pressure of 42 GPa, indicating that the transition is first-order. The compressibility parameters of the two phases were analyzed using a third-order Birch−Murnaghan equation of state. Further compression to above 65 GPa indicates a further transition into a phase with $P2_1/c$ symmetry. During decompression experiments, the $Pmc2_1$ phase was not recoverable to 1 atm. At least three new metastable crystalline phases were observed to occur during decompression that have not yet been identified. The material recovered to ambient conditions was amorphous. High-pressure, high-temperature synthesis experiments resulted in transformation of the material into a mixture of TiO_2 and TiN phases that are thermodynamically stable under these conditions.

Acknowledgment. This work was supported by EPSRC Portfolio Grant EP/D504782 and a Senior Research Fellowship (EP/D07357X) to P.F.M. G.H. thanks the Ramsay Memorial Trust for a research fellowship, and I.P.P. is a Wolfson-Royal Society Research Merit Award fellow. We thank Nicholas A. Spencer, Edward Bailey, and Rachael Hazael for assistance with high-pressure synthesis and synchrotron experiments.

References and Notes

(1) Hyett, G.; Green, M. A.; Parkin, I. P. The use of combinatorial chemical vapor deposition in the synthesis of Ti_3-δO_4N with $0.06 < \delta < 0.25$: A titanium oxynitride phase isostructural to anosovite. *J. Am. Chem. Soc.* **2007**, *129*, 15541.

(2) Hyett, G.; Green, M. A.; Parkin, I. P. Ultra-violet light activated photocatalysis in thin films of the titanium oxynitride, Ti_3-δO_4N. *J. Photochem. Photobiol., A* **2009**, *203*, 199.

(3) Choy, K. L. Chemical vapour deposition of coatings. *Prog. Mater. Sci.* **2003**, *48*, 57.

(4) Kroll, P. Hafnium nitride with thorium phosphide structure: Physical properties and an assessment of the Hf-N, Zr-N, and Ti-N phase diagrams at high pressures and temperatures. *Phys. Rev. Lett.* **2003**, *90*, 4.

(5) Zerr, A.; Miehe, G.; Serghiou, G.; Schwarz, M.; Kroke, E.; Riedel, R.; Fuess, H.; Kroll, P.; Boehler, R. Synthesis of cubic silicon nitride. *Nature* **1999**, *400*, 340.

(6) Zerr, A.; Miehe, G.; Riedel, R. Synthesis of cubic zirconium and hafnium nitride having Th_3P_4 structure. *Nat. Mater.* **2003**, *2*, 185.

(7) Maeda, K.; Domen, K. New non-oxide photocatalysts designed for overall water splitting under visible light. *J. Phys. Chem. C* **2007**, *111*, 7851.

(8) Sato, J.; Saito, N.; Yamada, Y.; Maeda, K.; Takata, T.; Kondo, J. N.; Hara, M.; Kobayashi, H.; Domen, K.; Inoue, Y. RuO_2-loaded β-Ge_3N_4 as a non-oxide photocatalyst for overall water splitting. *J. Am. Chem. Soc.* **2005**, *127*, 4150.

(9) Ebbinghaus, S. G.; Abicht, H.-P.; Dronskowski, R.; Mller, T.; Reller, A.; Weidenkaff, A. Perovskite-related oxynitrides - Recent developments in synthesis, characterisation and investigations of physical properties. *Prog. Solid State Chem.* **2009**, *37*, 173.

(10) Dunnill, C. W.; Parkin, I. P. N-doped titania thin films prepared by atmospheric pressure CVD using *t*-butylamine as the nitrogen source: Enhanced photocatalytic activity under visible light. *Chem. Vap. Deposition* **2009**, *15*, 171.

(11) Morikawa, T.; Asahi, R.; Ohwaki, T.; Aoki, K.; Taga, Y. Band-gap narrowing of titanium dioxide by nitrogen doping. *Jpn. J. Appl. Phys., Part 2* **2001**, *40*, L561.

(12) Kuroda, Y.; Mori, T.; Yagi, K.; Makihata, N.; Kawahara, Y.; Nagao, M.; Kittaka, S. Preparation of visible-light-responsive $TiO_{2-x}N_x$ photocatalyst by a sol−gel method: Analysis of the active center on TiO_2 that reacts with NH_3. *Langmuir* **2005**, *21*, 8026.

(13) Lowther, J. E. Metal oxides. *MRS Bull.* **2003**, *28*, 189.

(14) Dubrovinsky, L. S.; Dubrovinskaia, N. A.; Swamy, V.; Muscat, J.; Harrison, N. M.; Ahuja, R.; Holm, B.; Johansson, B. Metal oxides. *Nature* **2001**, *410*, 653.

(15) Onoda, M. Phase transitions of Ti_3O_5. *J. Solid State Chem.* **1998**, *136*, 67.

(16) Grey, I. E.; Li, C.; Madsen, I. C. Phase-equilibria and structural studies on the solid-solution $MgTi_2O_5$-Ti_3O_5. *J. Solid State Chem.* **1994**, *113*, 62–73.

(17) Grey, I. E.; Ward, J. X-ray and Mossbauer study of $FeTi_2O_5$-Ti_3O_5 system. *J. Solid State Chem.* **1973**, *7*, 300.

(18) Kellerman, D. G.; Zhilyaev, V. A.; Perelyaev, V. A.; Shveikin, G. P. Effect of doping on the phase-transition in Ti_3O_5. *Inorg. Mater.* **1983**, *19*, 221–224.

(19) Schettino, V.; Bini, R. Constraining molecules at the closest approach: Chemistry at high pressure. *Chem. Soc. Rev.* **2007**, *36*, 869.

(20) Mattesini, M.; de Almeida, J. S.; Dubrovinsky, L.; Dubrovinskaia, N.; Johansson, B.; Ahuja, R. High-pressure and high-temperature synthesis of the cubic TiO_2 polymorph. *Phys. Rev. B* **2004**, *70*, 4.

(21) Muscat, J.; Swamy, V.; Harrison, N. M. First-principles calculations of the phase stability of TiO_2. *Phys. Rev. B* **2002**, *65*, 15.

(22) Jamieson, J. C.; Olinger, B. High-pressure polymorphism of titanium dioxide. *Science* **1968**, *161*, 893.

(23) Zhang, W. F.; He, Y. L.; Zhang, M. S.; Yin, Z.; Chen, Q. Raman scattering study on anatase TiO_2 nanocrystals. *J. Phys. D: Appl. Phys.* **2000**, *33*, 912.

(24) Swamy, V.; Kuznetsov, A.; Dubrovinsky, L. S.; McMillan, P. F.; Prakapenka, V. B.; Shen, G.; Muddle, B. C. Size-dependent pressure-induced amorphization in nanoscale TiO_2. *Phys. Rev. Lett.* **2006**, *96*, 4.

(25) Asbrink, S.; Gerward, L.; Olsen, J. S. A high-pressure study of Ti_3O_5 by X-ray diffraction and synchrotron radiation. Pressures up to 38.6 GPa. *J. Appl. Crystallogr.* **1989**, *22*, 119.

(26) Mao, H. K.; Bell, P. M.; Shaner, J. W.; Steinberg, D. J. Specific volume measurements of Cu, Mo, Pd and Ag and calibration of ruby R1 fluorescence pressure gauge from 0.06 to 1 MBar. *J. Appl. Phys.* **1978**, *49*, 3276.

(27) Hammersley, A. P.; Svensson, S. O.; Hanfland, M.; Fitch, A. N.; Hausermann, D. Fit2D. *High Pressure Res.* **1996**, *14*, 235.

(28) Larson, A. C.; Dreele, R. B. V. General Structure Analysis System (GSAS). *Los Alamos National Laboratory Report LAUR 86-748*; Los Alamos National Laboratory: Los Alamos, NM, 2000.

(29) Toby, B. H. EXPGUI for GSAS. *J. Appl. Crystallogr.* **2001**, *34*, 210.

(30) Rodriguez-Carvajal, J. FullProf98 and WinPLOTR. *Physica B* **1993**, *192*, 55.

(31) Kraus, W.; Nolze, G. PowderCell software. *J. Appl. Crystallogr.* **1996**, *29*, 301–303.

(32) Schiferl, D.; Buchsbaum, S.; Mills, R. L. Phase-transitions in nitrogen observed by Raman spectroscopy from 0.4 to 27.4 GPa at 15 K. *J. Phys. Chem.* **1985**, *89*, 2324.

(33) Bini, R.; Ulivi, L.; Kreutz, J.; Jodl, H. J. High-pressure phases of solid nitrogen by Raman and infrared spectroscopy. *J. Chem. Phys.* **2000**, *112*, 8522.

(34) Bail, A. L.; Duroy, H.; Fourquet, J. L. Ab-initio structure determination of $LiSbWO_6$ by X-ray powder diffraction. *Mater. Res. Bull.* **1988**, *23*, 447.

(35) Salamat, A.; Woodhead, K.; McMillan, P. F.; Cabrera, R. Q.; Rahman, A.; Adriaens, D.; Cora, F.; Perrillat, J. P. Tetrahedrally bonded dense C_2N_3H with a defective wurtzite structure: X-ray diffraction and Raman scattering results at high pressure and ambient conditions. *Phys. Rev. B* **2009**, *80*, 104106.

(36) Hazen, R. M.; Finger, L. W. Bulk modulus-volume relationship for cation-anion polyhedra. *J. Geophys. Res.* **1979**, *84*, 6723.

JP100769R